THE UNIVERSITY *of* EDINBURGH

This thesis has been submitted in fulfilment of the requirements for a postgraduate degree (e.g. PhD, MPhil, DClinPsychol) at the University of Edinburgh. Please note the following terms and conditions of use:

- This work is protected by copyright and other intellectual property rights, which are retained by the thesis author, unless otherwise stated.
- A copy can be downloaded for personal non-commercial research or study, without prior permission or charge.
- This thesis cannot be reproduced or quoted extensively from without first obtaining permission in writing from the author.
- The content must not be changed in any way or sold commercially in any format or medium without the formal permission of the author.
- When referring to this work, full bibliographic details including the author, title, awarding institution and date of the thesis must be given.

An Angular Analysis and Search for CP Violation in the Decay $B^0 \to J/\psi K^{*0}$

Ailsa Sparkes

A thesis submitted in fulfilment of the requirements
for the degree of Doctor of Philosophy
to the
University of Edinburgh
July 2012

Abstract

LHCb is a precision heavy-flavour experiment at the Large Hadron Collider and in 2011 collected just over 1 fb^{-1} of data at a centre-of-mass energy of $\sqrt{s} = 7$ TeV. The Ring Imaging Cherenkov (RICH) detectors allow LHCb to identify charged hadrons by measuring their velocity. The system uses Hybrid Photon Detectors to detect rings of single photons emitted by particles travelling through the RICH radiators. The performance-monitoring of these photon detectors whilst data-taking is presented and discussed. LHCb aims to perform precise measurements of Charge-Parity violation in B and D mesons. The final state of $B^0 \to J/\psi(\to \mu^+\mu^-)K^*(\to K^+\pi^-)$ is an admixture of parity-odd and parity-even final states, which are either longitudinally or transversely polarized. These contributions can be separated by performing an angular analysis. The polarization amplitudes and phases of the final state are measured. No difference is observed between the B^0 and $\overline{B^0}$ flavour eigenstates which indicates that Charge-Parity symmetry has been conserved. The ambiguity in the measurement of the strong phase has been resolved by studying the P-wave and S-wave interference in the K/π mass system. The deviation from zero or π in the measurement of the strong phases indicates that final state interactions have occurred. In addition, the prediction that the polarization amplitudes should be similar to those of $B_s^0 \to J/\psi\phi$ is confirmed.

Declaration

Except where otherwise stated, the research undertaken in this thesis was the unaided work of the author. Where the work was done in collaboration with others, a significant contribution was made by the author.

A.Sparkes
July 2012

Acknowledgements

Firstly, I would like to thank my supervisor, Steve Playfer for his constant support and guidance throughout my PhD. Due to his extremely helpful comments and meticulous proof-reading during the writing stage, I can say I am proud of this thesis. My second supervisor Stephan Eisenhardt introduced me to the RICH detectors, and gave me invaluable support for the work I did with them. A special thanks is required for Stephan for talking me out of giving up in my first year- this thesis would not exist if it weren't for that pep-talk! Franz Muheim and Peter Clarke deserve a huge thanks for always having time for a physics question, and for constant support.

I would like to acknowledge the LHCb RICH group for their support, particularly Thierry Gys, who helped me understand the inner workings of a photo detector. Thanks to Ross Young who bequeathed to me his code and spent hours and many emails tutoring me in it. Alexander Bien's collaboration has greatly benefited the analysis presented here. I would like to thank Greig Cowan who put up with my stupid questions long after he was required to and never complained. Conor Fitzpatrick who could always be relied on for help, no matter how busy he was. Rob Currie who has contributed considerably to my analysis, through the growing genius that is RapidFit. Ben Wynne who helped me through my first C++ troubles and listened and sympathised with my working-woes.

Thanks the "Omniladder" crew and hangers on for giving me sanity in and outside JCMB. Also the "LTAers" of CERN, where I spent some of the best times of my life. The "Physics Girlies" who I have missed hugely but are always on the end of the phone/facebook. Thanks to Vicky who is always there for me, despite living on the other side of the world. Particular thanks goes to Katherine, who I was able to share this final year with and who kept me sane and smiling. I am also very grateful to Sophie, who gave me a godson during my PhD, who I can spend more time with now. Nick deserves a truly massive thank you, for listening, for knowing what to say and for putting up with me through my most stressed times. Finally, I am eternally grateful to my parents who have both given me unfailing support in my career and every other aspect of my life, and my sister Cat who is my mirror, witness and partner in crime.

Contents

List of Figures

List of Tables

Chapter 1

Theoretical Introduction

1.1 Motivation

Approximately 10^{-6} s after the big bang, a quark-gluon plasma was formed in which free quarks and gluons were travelling at relativistic speeds. Particle-antiparticle pairs were continuously created and annihilated, causing photons to travel uniformly across the universe. This provides us with a visible remnant of the beginning of the universe called the Cosmic Microwave Background (CMB). Satellite probes of the CMB shown in Figure 1.1 have led to the estimation that the universe is 13.75 ± 0.11 billion years old [1]. At some point after the CMB was formed, one of the quantum numbers *baryon number* was violated, causing more particles to exist than antiparticles. This unknown process named *baryogenesis* means that the universe today is entirely made up of matter.

In 1967, Sakharov[2] explained that this lack of antimatter requires three conditions: non-conservation of baryon number, the universe cooling with a lack of thermal equilibrium, and a difference between matter and antimatter due to CP (Charge-Parity) violation during baryogenesis. The Standard Model of particle physics (SM) predicts some CP violation but at a level much too small to explain the observed asymmetry. Models beyond the SM must play an important role in explaining the lack of antimatter in the universe.

The presence of antimatter was first suggested by Dirac when he proposed a solution of Relativistic Quantum Mechanics. The positron, the antiparticle partner of the electron, was discovered experimentally by Anderson in 1933 [3] and the antiproton was discovered in 1955 [4]. Feynman [5] and Stueckelberg [6]

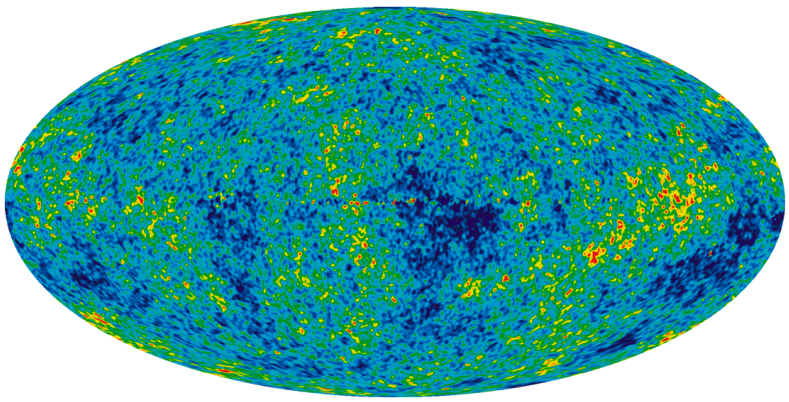

Figure 1.1: Cosmic Microwave Background of the visible universe using WMAP data. Credit: NASA / WMAP Science Team.

suggested an interpretation of antimatter in which antiparticles could either be seen as a duplicate set of particles with opposite additive quantum numbers, or as the same particles but travelling with a reversed arrow of time. CPT symmetry - a combination of Charge, Parity and Time reversal symmetry, is required in the SM to be a valid symmetry. If this is held, and the universe is symmetric under the reversal of time, it is required also to be matter-antimatter symmetric. This is known not to be the case so T-symmetry (time reversal symmetry) must be broken. More generally, CPT symmetry is required for any local Lorentz invariant quantum field theory, and predicts that particles and antiparticles have the same masses and lifetimes.

To understand more about these fundamental predictions, the basic model of our universe as it stands today must be introduced. The rest of this chapter will give an outline of our current understanding of the fundamental particles and forces of the universe, as well as introducing the concept of CP violation and how it is measured. Chapter 2 will give an outline of the LHCb detector which is the basis for this work. Chapter 3 gives a detailed overview of the RICH sub-detectors and the monitoring which has been carried out on them whilst data-taking. Chapters 4, 5 and 6 present the analysis of $B^0 \to J/\psi K^{*0}$ and the

search for CP violation in that channel.

1.2 The Standard Model

Particle physics deals with the most elementary constituents of matter. Interactions are studied at increasingly smaller ranges, involving heavier particles and therefore larger accelerators and detectors. With the results of such experiments, it has been possible to classify particles and their interactions into categories and identify a number of rules by which their behaviour can be described. These rules have led to theories of the properties of the weakly and electromagnetically interacting particles, *Electroweak theory*, as well as strongly interacting particles, *Quantum Chromodynamics* (QCD). Grand Unified Theories exist which combine the theories of the strongly interacting particles, the *quarks* and the weakly interacting particles, the *leptons*. These have not yet been verified experimentally. However it has been possible to combine the weak and electromagnetic interactions. It is assumed that the fourth force gravity will eventually be incorporated into a Quantum Theory of Gravity.

Particles fall into several major categories. The *gauge bosons* mediate the four fundamental forces shown in Table 1.1. Their relative strengths, ranges and masses are also shown. Gravity is included but its mediator, the graviton is only hypothetical at the current time. The *leptons* shown in Table 1.2 consist of the charged electron, muon and tau, and the corresponding neutrinos ν_e, ν_μ and ν_τ, each of which has a antiparticle partner. They are fermions which means they have spin $1/2$. They do not interact strongly and appear to be identical to one another in the weak and electromagnetic interactions. The only observed differences among the charged leptons are in mass and properties related to mass. It is possible that there are heavier pairs of leptons which have not yet been discovered. For each of the three types of leptons (e, μ, τ) there is a quantum number called a lepton number assigned. $L = +1$ for leptons, and $L = -1$ for antileptons. Total lepton number is separately conserved for each type of lepton in all particle interactions and decays. Any decay that does not conserve lepton number is forbidden (neutrino oscillations are a currently unexplained exception). The lepton numbers are shown in the Table 1.2.

Mesons are strongly interacting composite $(q\bar{q})$ particles with integer spin,

Interaction	Mediator	Relative Strength	Range [m]	Mass [GeV] [7]
Strong	gluon, g	1	∞	0
Electromagnetic	photon, γ	10^{-3}	∞	0
Weak	$W^{\pm}/Z^0$	10^{-16}	10^{-18}	$W^{\pm} = 80.399 \pm 0.023$ $Z^0 = 91.1876 \pm 0.0021$
Gravitation	graviton? g^0	10^{-41}	∞	?

Table 1.1: Fundamental forces of nature, their relative strengths, their range and the particle they are mediated by. The graviton is hypothetical at the current time.

Name	Spin	Baryon Number B	Lepton Number L	Charge Q	Mass [MeV] [7]
Leptons					
e (electron)			$L_e = 1$	-1	0.511
ν_e (e neutrino)				0	0^{SM}
μ (muon)	$1/2$	0	$L_\mu = 1$	-1	105.66
ν_μ (μ neutrino)				0	0^{SM}
τ (tau)			$L_\tau = 1$	-1	1776.82
ν_τ (τ neutrino)				0	0^{SM}
Quarks					
u (up)				$+2/3$	$0.7 - 3.1$
d (down)				$-1/3$	$4.1 - 5.7$
c (charm)	$1/2$	$1/3$	0	$+2/3$	1290^{+50}_{-110}
s (strange)				$-1/3$	100^{+30}_{-20}
t (top)				$+2/3$	$(172.9 \pm 1.08) \times 10^3$
b (bottom)				$-1/3$	4190^{+180}_{-60}

Table 1.2: Standard Model Particles and Quantum Numbers. 1st Generation, 2nd Generation and 3rd Generation. In the Standard Model, the neutrinos are are predicted to be massless, but have been discovered to oscillate between their flavours, implying they have some mass - hence the superscript "SM".

an example being the pion. Baryons are also strongly interacting composite (qqq) particles but have half-integer spins, the lightest ones being the proton and neutron. Both meson and baryons fall under the class of hadrons, and there is a large number of possible states. Quarks (see Table 1.2) are the fundamental particles that make up hadrons, bound by the mediators of the strong force, gluons. There are three generations of quarks, as there are for leptons. The up and down quarks are the lightest and make up protons and neutrons. The charm and strange are the second generation, and the top and bottom are the third, and heaviest generation. Each quark is assigned an additive Baryon number of $1/3$ and $-1/3$ for the antiquark. This means that all baryons (which consist of three quarks) have a total baryon number of 1, and all mesons (which consist of combinations of quark and antiquark pairs) have a total baryon number of 0. As far as it is known, all decays and interactions conserve the total baryon number. Although some New Physics models predict the violation of baryon number, this has not yet been observed.

The electromagnetic and weak forces The electromagnetic (EM) force is mediated by the exchange of photons. Heisenberg's Uncertainty Principle dictates the length of time that virtual photons can exist in relation to the distance from the mass shell $\Delta E \Delta t \approx \hbar$. The EM force has an infinite range as virtual photons can be very close to the mass shell which results in a very long lifetime. Quantum Electrodynamics (QED) is the relativistic quantum field theory of the electromagnetic force developed by Feynman [8], Schwinger [9] and Tomonaga [10]. An example of an emission of a photon by an electron is shown in Figure 1.2 with a Feynman diagram. This is the lowest order diagram to describe the electromagnetic interaction, but there are many possible contributions. This representation allows the calculation of the probabilities for decay processes by applying a set of rules called the Feynman rules. The rules for QED diagrams are:

- Each *photon - charged particle* vertex gives a factor of fermion charge Q, and strength of the coupling at the vertex $\sqrt{\alpha} = \sqrt{e^2/4\pi\hbar c}$
- Each *photon* gives a propagator term of $1/q^2$, where q is the photon four-momentum

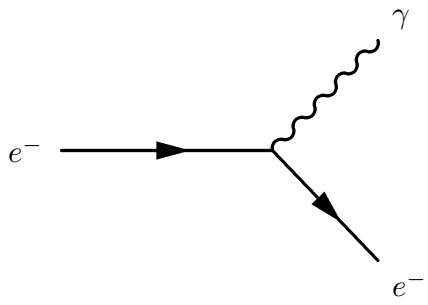

Figure 1.2: Feynman diagram representing the emission of a photon by an electron, the direction of time is left to right.

- The matrix element $\mathcal{M}$ for calculating scattering and decay amplitudes is proportional to the vertex and propagator terms

Feynman diagrams can also be used to describe weak processes involving the mediation of $W^{\pm}$ or Z^0 vector bosons. An example is shown in Figure 1.3 of a neutron decay to a proton mediated by a virtual W^- boson, which then decays into an electron and an anti-neutrino. For charged currents involving the $W^{\pm}$ boson, the Feynman rules are similar to those of QED, except the coupling strength is given by the weak charge, $\sqrt{\alpha_W}$, and the propagator term is $1/(q^2 - m_W^2)$. The existence of the weak bosons was proposed by S.Weinberg [11] and A. Salam [12] in 1967 who combined the electromagnetic and weak forces into a single theory. This theory postulated that at very high energies the electromagnetic and weak forces become equivalent. At this point of unification, the so-called *electroweak* force would be mediated by four massless particles of spin-1, a triplet W (of charges +1, 0 and -1) and a singlet B (of no charge). At lower energies, the symmetry between weak and electromagnetic forces is broken, the triplet and singlet mix to give three heavy bosons, the $W^{\pm}$ and Z^0 and a fourth massless particle, the photon.

The electroweak theory makes experimentally testable predictions. According to the model the coupling constant for associated with the W-boson g_W is related to the strength parameter α_W by:

$$g_W sin\theta_W = \sqrt{4\pi\alpha_W} \tag{1.1}$$

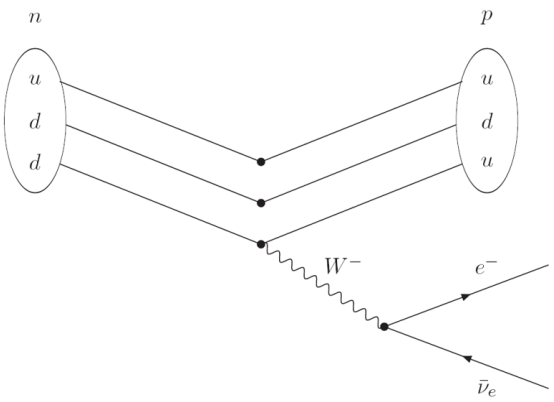

Figure 1.3: Feynman diagram of a weak process where a neutron decays to a proton.

where θ_W is called the Weinberg angle and has been determined from many different experiments to be [7]:

$$sin^2\theta_W = 0.23146 \pm 0.00012 \tag{1.2}$$

In the low energy limit the charged current reactions are characterized by the Fermi constant:

$$\frac{G_F}{\sqrt{2}} = \frac{g_W^2}{M_W^2} \tag{1.3}$$

By substituting in g_W from Equation 1.1 we obtain:

$$M_W^2 = \frac{\sqrt{2}g_W^2}{G_F} = \frac{4\sqrt{2}\pi\alpha_W}{G_F \sin^2\theta_W} \tag{1.4}$$

Since G_F can be measured in muon decay, the mass of the $W^\pm$ can be determined:

$$\mathrm{m_W} \approx 80 \text{ GeV} \tag{1.5}$$

In addition:

$$m_Z = \frac{m_W}{cos\theta_W} \approx 90 \text{ GeV} \tag{1.6}$$

The $W^\pm$ and Z^0 bosons decay via:

$$W^{\pm} \rightarrow q\bar{q} \text{ or } l^{\pm}\nu_l \tag{1.7}$$
$$Z^0 \rightarrow q\bar{q} \text{ or } l^{+}l^{-} \tag{1.8}$$
$$\tag{1.9}$$

where $l = e, \mu, \tau$. Generally, the mass of the Z^0 is determined by the channels $Z^0 \rightarrow e^+e^-,\ \mu^+\mu^-$ and the channels $W^+ \rightarrow e^+\nu_e,\ \mu^+\nu_\mu$ are used to determine the mass of the W boson. They have been very precisely measured to be [7]:

$$W^{\pm} = 80.399 \pm 0.023 \text{ GeV} \tag{1.10}$$
$$Z^0 = 91.1876 \pm 0.0021 \text{ GeV} \tag{1.11}$$

The initial discovery of these bosons and the agreement with the predicted values was a huge success for the electroweak theory and Carlo Rubbia, who led the experimental team and Simon van der Meer, who developed the accelerator technology which made the measurement possible, received the 1984 Nobel Prize.

The weak interactions that involve the $W^{\pm}$ boson are called *charged-current* interactions. Another testable prediction of electroweak theory was to observe *neutral current* interactions involving the exchange of the Z^0. An example is neutrino scattering which is shown in Figure 1.4. At CERN in the 1970s beams of high-energy neutrinos became available and it was possible to observe these neutrino scattering events using a heavy-liquid bubble chamber called Gargamelle [13]. This gave the first confirmation of the electroweak model.

The Strong Force Before the strong force can be understood, first some properties of quarks must be described. In addition to the lepton and baryon quantum numbers, there are also numbers named after the quark flavours, *strangeness*, *charm*, *beauty* and *truth*. Strangeness was required to explain the observation that strange particles are produced in pairs in the strong interaction of non-strange hadrons - they had to contain a new quark s and antiquark $\overline{s}$. This also explained the fact that certain decays that would otherwise be expected to occur in a strong interaction time of 10^{-22} s, actually occur in a weak interaction time of 10^{-10} s. It was postulated that strangeness is conserved in strong and

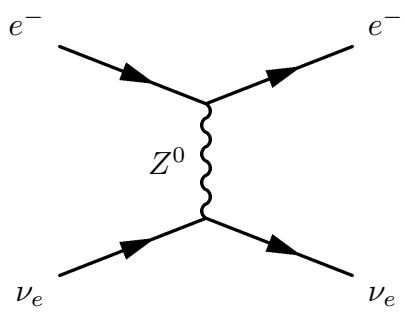

Figure 1.4: Feynman diagram showing neutrino scattering via neutral current weak interaction.

EM processes, but can change by one unit in weak processes which resolves this discrepancy. Then, for example the decay $\Lambda^0 \to p + \pi^-$ is allowed, even though it has a strangeness number of 1 in the initial state, and zero in the final state. Similarly the other internal quantum numbers of charm, beauty and truth are all assigned to hadrons containing the corresponding c, b and t quarks, and are all conserved in strong and EM interactions but not in weak interactions.

Hadrons are grouped into isospin multiplets, which have the same spin and parity, and almost identical masses e.g. (p, n), (π^+, π^0, π^-), $(\Delta^{++}, \Delta^+, \Delta^0, \Delta^-)$ etc. The isospin quantum number I_3 is used as a way of labeling the members of the multiplet:

$$I_3 = \frac{(N_u - N_d)}{2} \tag{1.12}$$

where N_u is the number of u quarks and N_d is the number of d quarks. I_3 is the third component of the vector I in isospin space. For triplets $I = 1$, for singlets $I = 0$, and for multiplets of four $I = \frac{3}{2}$. I must be conserved in strong interactions, but is violated in weak and EM interactions. I_3 is conserved in EM and strong interactions but not in weak interactions.

It was observed that the underlying structure of hadrons could be seen in a diagram of I_3 plotted against strangeness. This diagram for spin-0 mesons is shown in Figure 1.5(a). I_3 is on the x-axis and strangeness is on the y-axis. The K^0, K^+ and their antiparticles lie at $S = \pm 1$ and $I_3 = \pm\frac{1}{2}$ and the π^-, π^0 and π^+ lie at $S = 0$ and $I_3 = -1, 0$ and 1 respectively. They form a hexagonal shape which reveals that their quark composition is just a repeated simple structure

of u, d and s which are the quarks they are composed of. A similar diagram is shown for three quark couplings of baryons (see Figure 1.5(b)). From these observations, it is deduced that the quarks must have fractional charge in order to reproduce the known charges of the hadrons. Up quarks must have charge $+\frac{2}{3}$, and down and strange quarks must have $-\frac{1}{3}$ with the antiquarks having opposite charges.

Another observation from Figure 1.5(b) is that quark configurations such as sss, ddd or uuu exist. These baryons contain identical quarks, all with the same quantum numbers, and in a state with a total spin of $\frac{3}{2}$ which means they have to each have spin $\frac{1}{2}$ in the same configuration. This violates the Pauli Exclusion principle that no two fermions may share a quantum state. This difficulty is resolved by the introduction of a new quantum number called *colour*. Each quark in the baryon state has different colour of *red*, *green* or *blue* and the antiquarks have the corresponding anti-colours. Each hadron must be *colourless* - meaning it contains one quark of each colour, or has colour-anticolour combinations. As it stands only mesons and baryons have been confirmed to exist, but the search for hadrons containing more quarks is ongoing. It is proposed that tetraquarks (containing four quarks) or pentaquarks (containing five) may exist. The X(3872) discovered at Belle in 2003 [14] has been proposed to be a tetraquark [15].

Gluons carry colour between quarks, and so each have colour-anticolour properties. Figure 1.6 shows a gluon $R\overline{B}$ (with red-antiblue properties) being exchanged by red and blue quarks. The red quark emits its redness into a gluon and acquires blueness by also emitting anti-blueness. The blue quark absorbs the $R\overline{B}$ gluon, canceling its blueness and acquiring a red colour. One would expect nine possible gluons: $R\overline{R}$, $R\overline{B}$, $R\overline{G}$, $B\overline{R}$, $B\overline{B}$, $B\overline{G}$, $G\overline{R}$, $G\overline{B}$, $G\overline{G}$ but the three colourless combinations are actually coupled as:

$$\frac{1}{\sqrt{2}}(R\overline{R} - G\overline{G}) \qquad \frac{1}{\sqrt{6}}(R\overline{R} + G\overline{G} - 2B\overline{B}) \qquad \frac{1}{\sqrt{3}}(R\overline{R} + G\overline{G} + B\overline{B}) \quad (1.13)$$

Of these the first and second can transmit colour but the third cannot because it is colour neutral so there are only eight gluons.

There are some interesting effects of the quark model. Quarks are bound within hadrons, they have never been observed in a free state and it is postulated that no amount of energy can free a quark. In addition, the results of deep

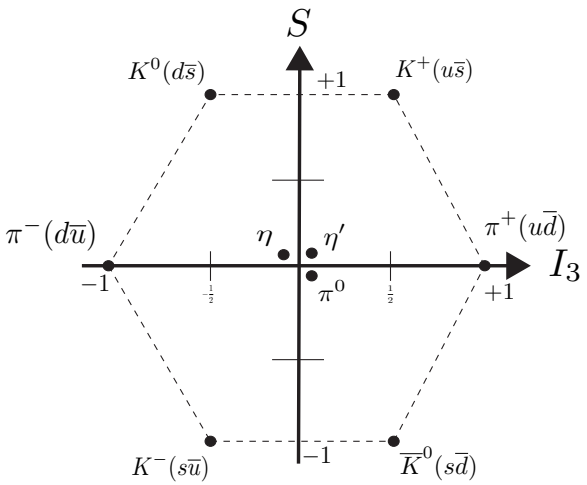

(a) spin-0 mesons

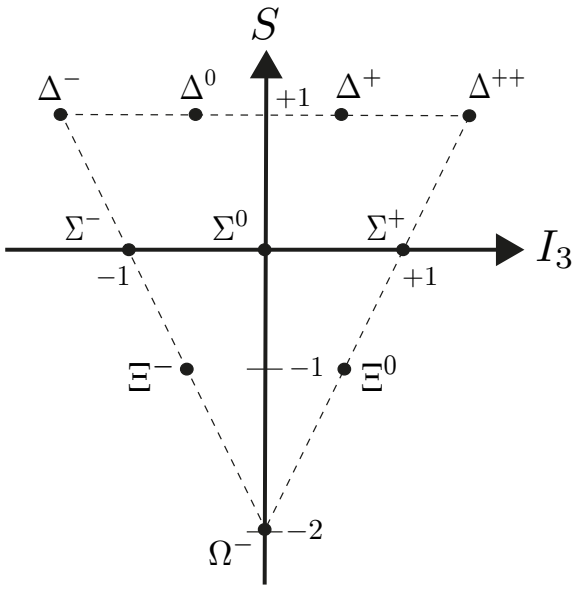

(b) spin-3/2 baryons

Figure 1.5: Isospin I_3 vs strangeness, S charts.

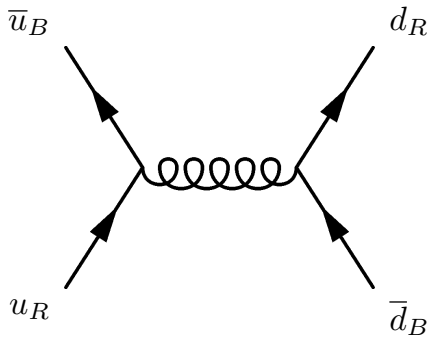

Figure 1.6: A red up-quark emits a $R\overline{B}$ gluon, which is absorbed by the blue down quark.

inelastic scattering experiments reveal that when the quarks are probed at very short distances using electron or neutrino scattering, quarks seem to move almost freely, as if they were not bound. These properties are called *confinement* and *asymptotic freedom*, respectively. The theory used to explain this behaviour and the colour field is Quantum Chromodynamics (QCD), analogous to QED for the EM force.

In QED, the photons are the carriers of the EM field, exactly as the gluons are the carriers of the strong colour field. However, photons themselves carry no electric charge and are unaffected by electric fields. Gluons carry a net colour-anticolour charge and interact directly with the quarks as well as self-interact. A quark can emit a gluon and then interact with it and create additional gluons. An electron emitting a virtual photon does not change its charge whereas a quark emitting a virtual gluon must change its colour charge. The colour charge of a quark is therefore spread out over a sphere of the order of the size of a hadron. If another quark penetrates this sphere, the spread-out colour charge would cause a considerably reduced quark-quark interaction. If we measure the quark's interactions over a small radius only a small fraction of its overall colour charge is observed and it appears to be in an almost free state.

At larger separations between quarks, the interactions between the exchanged gluons means the density of the colour field lines is high, compared to the field lines between two electrons. The density of the field lines stays approximately constant as the separation is increased. At large distances, the work done will cause the creation of a quark-antiquark pair, and a hadron. At high energies

such as the LHC, a chain reaction can occur, with many quark pairs and hadrons being created which causes cone-shaped jets. The first observation of these jets at Stanford Linear Collider in 1975 was a triumph for quark theory [16].

Mixing and the CKM Matrix The weak interactions of hadrons depends on how the W bosons are absorbed or emitted by quarks. It is observed that the lepton pairs (e^-, ν_e), (μ^-, ν_μ) and quark pairs (u, d) couple approximately with coupling constant G_F. When this is extended to the heavier quarks (c, s) this is observed to be not quite correct. For example, the decay $K^+ \to \mu^+\nu_\mu$ is observed in nature, and because the K^+ contains u and $\overline{s}$ quarks there must be a weak current between them. This contradicts the assumption that only coupling can occur between u and d quarks and c and s quarks. In 1963 Cabibbo introduced the concept of quark mixing [17]. This idea is that the d and s quarks participate in the weak interactions in the linear combinations:

$$d' = d\cos\theta_c + s\sin\theta_c \tag{1.14}$$

$$s' = -d\sin\theta_c + s\cos\theta_c \tag{1.15}$$

where d' and s' are the weak eigenstates and d and s are the mass eigenstates of the quarks. θ_c is called the *Cabibbo angle*, and allows lepton-quark symmetry to apply to u, d' and c, s'.

When the third generation is included in quark mixing, and the linear combination is written in matrix form, the interactions can be described as:

$$\begin{pmatrix} d' \\ s' \\ b' \end{pmatrix} = \begin{pmatrix} V_{ud} & V_{us} & V_{ub} \\ V_{cd} & V_{cs} & V_{cb} \\ V_{td} & V_{ts} & V_{tb} \end{pmatrix} \begin{pmatrix} d \\ s \\ b \end{pmatrix} \tag{1.16}$$

Where the 3×3 matrix is called the CKM Matrix (V), after Cabibbo, Kobayashi and Maskawa [18] and must be unitary to ensure that d', s' and b' are complete and orthonormal states. The CKM matrix maps the mass eigenstates to the weak eigenstates. Each matrix element relates to the probability of a flavour changing process:

$$P(i \to j) \propto |V_{ij}|^2 \tag{1.17}$$

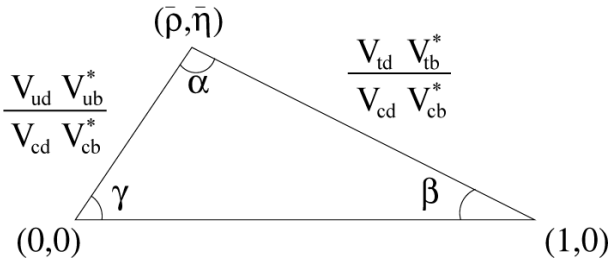

Figure 1.7: Unitarity Triangle.

These are all measurable although the smaller off-diagonal terms $|V_{td}|$ and $|V_{ub}|$ are more difficult to determine. Nine unitarity relationships can be constructed from this matrix, six of which sum to zero and can therefore be represented by a triangle in the complex plane. The most interesting orthogonality condition is between the first and third columns:

$$V_{ud}V_{ub}^* + V_{cd}V_{cb}^* + V_{td}V_{tb}^* = 0 \tag{1.18}$$

The corresponding triangle is shown in Figure 1.7 where each term is the length of a side divided by $|V_{cd}V_{cb}^*|$. To explain the coordinate system an alternative parameterisation of the matrix is presented. When it was realised that the bottom quark mostly decays to the charm quark ($|V_{cb}| >> |V_{ub}|$) Wolfenstein noticed that $|V_{cb}| \sim |V_{us}|^2$ and introduced a parameterization for the matrix, which is only approximately unitary but contains useful experimental information.

$$V = \begin{pmatrix} 1-\lambda^2/2 & \lambda & A\lambda^3(\rho - i\eta) \\ -\lambda & 1-\lambda^2/2 & A\lambda^2 \\ A\lambda^3(1-\rho-i\eta) & -A\lambda^2 & 1 \end{pmatrix} + O(\lambda^4) \tag{1.19}$$

The four parameters λ, A, ρ and η are all of order 1 ($\lambda \sim 0.23, A \sim 0.82, \rho \sim 0.22, \eta \sim 0.34$), so it is clear from the number of powers of λ in each element how large it is. From the Wolfenstein parameterisation it can be deduced that as well as $|V_{cb}| \sim |V_{us}|^2$, also $V_{td} << V_{ts}$ and $|V_{ub}| << |V_{cb}|$. It is clear that the CKM matrix has a *hierarchical* structure: up-type quarks preferably couple with down-type quarks of the same family. They also couple to quarks of other families although the couplings get smaller the more distant the family. The off-diagonal

elements are of order λ between generations 1 and 2, λ^2 between 2 and 3, and λ^3 between 1 and 3. An approximation to unitarity is achieved in a series expansion in which the following parameters are used:

$$\overline{\rho} = \rho(1 - \lambda^2/2) \tag{1.20a}$$
$$\overline{\eta} = \eta(1 - \lambda^2/2) \tag{1.20b}$$

In addition to leading order:

$$\frac{V_{ud}V_{ub}^*}{|V_{cd}V_{cb}|} = \rho + i\eta, \tag{1.21}$$
$$\frac{V_{cd}V_{cb}^*}{|V_{cd}V_{cb}|} = -1, \tag{1.22}$$
$$\frac{V_{td}V_{tb}^*}{|V_{cd}V_{cb}|} = 1 - \rho - i\eta \tag{1.23}$$

This is where the coordinates of the unitarity triangle in Figure 1.7 come from. The angles in the triangle are defined by:

$$\alpha \equiv arg\left(-\frac{V_{td}V_{tb}^*}{V_{ud}V_{ub}^*}\right) \tag{1.24}$$
$$\beta \equiv arg\left(-\frac{V_{cd}V_{cb}^*}{V_{td}V_{tb}^*}\right) \tag{1.25}$$
$$\gamma \equiv arg\left(-\frac{V_{ud}V_{ub}^*}{V_{cd}V_{cb}^*}\right) \tag{1.26}$$
$$\tag{1.27}$$

Each of the six triangles that represent the orthogonality relations for the CKM matrix has a different shape but have the same area. The Unitarity triangle shown in Figure 1.7 is one of the most interesting of the six because all three sides are similar in length, which means the angles (relative phases) are large. Many different B and D decays can contribute towards precise measurements of the angles of the triangle. The current constraints on the unitarity triangle are shown in Figure 1.8. This figure is a plot of the measurements of $\overline{\rho}$ and $\overline{\eta}$ defined in equations 1.20a and 1.20b. The unitarity triangle is shown in the middle and

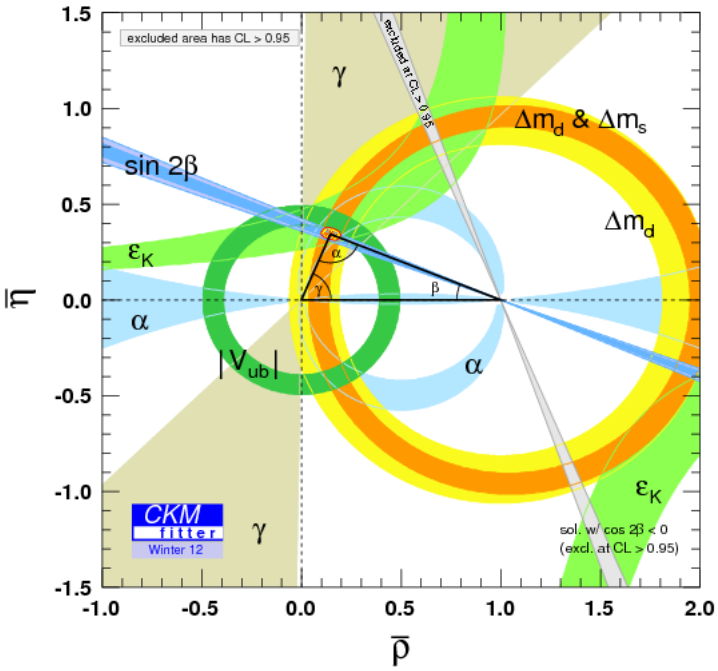

Figure 1.8: The constraints on the unitarity triangle from experiments so far (2012) [19] The coloured bands correspond to constraints on $\overline{\rho}$ and $\overline{\eta}$ from various measurements. α, β and γ are the three angles of the unitarity triangle shown in the centre. Δm_s and Δm_d are mass differences from $B^0_{s,d}$ mixing, ϵ_K is a CP violating parameter from the kaon sector.

the current constraints on its angles are shown by the coloured bands.

1.3 Charge-Parity violation

Charge conjugation relates to the existence of an antiparticle for every particle. As already mentioned this was predicted in 1928 by Dirac in his relativistic quantum theory. A charge (C) transformation corresponds to a reversal of charges such as electric charge, baryon and lepton number, and flavour quantum numbers, i.e. all additive quantum numbers. If C symmetry is conserved, antiparticles behave in the exact same way as their corresponding particles. In the weak interaction the charge conjugation of a left handed neutrino ν_L gives a left handed antineutrino $\overline{\nu_L}$, and a right handed antineutrino gives a right handed neutrino:

$$C\,|\nu_L\rangle \rightarrow \overline{\nu_L} \tag{1.28}$$

$$C\,|\overline{\nu_R}\rangle \rightarrow \nu_R \tag{1.29}$$

Neither $\overline{\nu_L}$ or ν_R are observed in nature, so C-parity is maximally violated in weak interactions.

Parity symmetry is also called space-inversion or left-right symmetry. It involves the invariance of physics under a transformation of the sign of the space coordinates. The three coordinate axes are inverted through the origin, which changes the handedness of the system. It is often called mirror symmetry because it may occur in two steps: a mirror reflection followed by a rotation by an angle π around the axis perpendicular to the same plane. From angular momentum conservation, physics must be invariant under a rotation, therefore whether physics is invariant under reflection is the important question. The parity transformation changes the sign of the position vector of a particle, and therefore the velocity and momentum also change sign (these are called polar vectors).

$$P\,|\psi(r)\rangle \rightarrow \psi(-r) \tag{1.30}$$

Angular momentum is invariant under P because both the position and momentum change sign (and is called an axial vector). Parity conservation is also violated in the lepton sector:

$$P\,|\nu_L\rangle \rightarrow \nu_R \tag{1.31}$$

$$P\,|\overline{\nu}_R\rangle \rightarrow \overline{\nu}_L \tag{1.32}$$

Parity violation was first observed in the β decay of ^{60}Co by C.S Wu [20]. Following this discovery that proved that Parity was not conserved in weak interations it was soon suggested that the particle charges must also be inverted when the parity transformation was implemented. So that the mirror image of a particle would actually be an antiparticle, and this would restore the symmetry. In 1957, Landau proposed that the combined symmetry operator CP was the one that mattered [21]. Weak interactions are parity asymmetric, however after

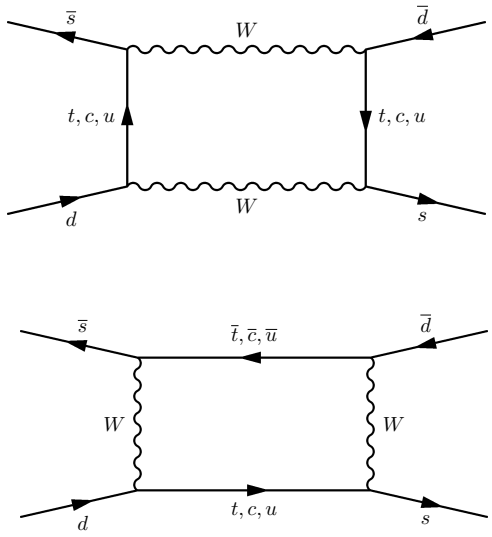

Figure 1.9: Feynman box diagrams showing the mixing of neutral kaons.

simultaneous C and P transformations, they remain identical. The neutrino system is invariant under CP asymmetry:

$$CP\,|\nu_L\rangle \rightarrow |\overline{\nu_R}\rangle \tag{1.33}$$

$$CP\,|\overline{\nu_R}\rangle \rightarrow |\nu_L\rangle \tag{1.34}$$

The first observation of CP violation was in neutral kaon decays. These are interesting because they oscillate between particle and antiparticle before decaying. There are two neutral kaon states: K^0 and $\overline{K}^0$ which have strangeness numbers $S = +1$ and $S = -1$ respectively. Oscillations would usually be forbidden with a change in strangeness, but in weak interactions this is allowed. They convert to each other via box diagrams (see Figure 1.9). Similar mixing occurs in neutral B and D meson states.

There are two CP eigenstates for the neutral kaon:

$$\left|K_1^0\right\rangle = \frac{1}{\sqrt{2}}\{\left|K^0\right\rangle + \left|\overline{K}^0\right\rangle\} \tag{1.35}$$

$$\left|K_2^0\right\rangle = \frac{1}{\sqrt{2}}\{\left|K^0\right\rangle - \left|\overline{K^0}\right\rangle\} \tag{1.36}$$

where

$$CP|K_1^0\rangle = |K_1^0\rangle \quad (1.37)$$
$$CP|K_2^0\rangle = -|K_2^0\rangle \quad (1.38)$$

Assuming CP is conserved K_1^0 should decay to states with CP = 1 (CP even) and K_2^0 should decay into states with CP = -1 (CP odd). This leads to the prediction that the decays $K_1^0 \to \pi^+\pi^-$, $\pi^0\pi^0$ and $K_2^0 \to \pi^+\pi^-\pi^0$, $\pi^0\pi^0\pi^0$ are allowed by CP conservation, whereas $K_1^0 \to \pi^+\pi^-\pi^0$, $\pi^0\pi^0\pi^0$ and $K_2^0 \to \pi^+\pi^-$, $\pi^0\pi^0$ are forbidden.

The two neutral kaons that are experimentally observed are called K_S^0 and K_L^0 because they have such different lifetimes ($0.89 \times 10^{-10}\,s$ and $0.53 \times 10^{-7}\,s$ respectively). It has been shown that the K_S^0 principally decays to two pions whereas the K_L^0 prefers to decay to three pions. This suggests that $K_S^0 = K_1^0$ and $K_L^0 = K_2^0$. However, experimentally it has been shown that the K_L^0 meson also decays to two pions with a branching ratio $\approx 10^{-3}$ [22]. This is clear evidence of CP-violation. Until 2001, the evidence for CP violation was confined to the kaon system, however since then many more examples have been discovered.

1.4 CP violation in Beauty sector

Analogous to the $K^0 - \overline{K}^0$ mixing system, neutral B mesons also mix. These occur through similar diagrams, shown in Figure 1.10. The B^0 meson contains quarks $d\bar{b}$ and has two CP eigenstates B_L^0 and B_H^0, for light and heavy. They have almost the same masses and lifetimes of approximately 1.5×10^{-12} s, and are linear combinations of B^0 and $\overline{B^0}$ mesons:

$$|B_L\rangle = p\left|B^0\right\rangle + q\left|\overline{B^0}\right\rangle \quad (1.39)$$
$$|B_H\rangle = p\left|B^0\right\rangle - q\left|\overline{B^0}\right\rangle \quad (1.40)$$

the complex parameters p and q are normalised:

$$|q|^2 + |p|^2 = 1 \tag{1.41}$$

The time evolution can be determined by a 2×2 effective Hamiltonian $\mathbf{H}$ which can be written in terms of Hermitian matrices $\mathbf{M}$ and $\mathbf{\Gamma}$ as:

$$\mathbf{H} = \mathbf{M} - \frac{i}{2}\mathbf{\Gamma} \tag{1.42}$$

A pure flavour eigenstate will evolve with time such that:

$$\left|B^0(t)\right\rangle = g_+(t)\left|B^0\right\rangle + \frac{q}{p}g_-(t)\left|\overline{B^0}\right\rangle \tag{1.43}$$

$$\left|\overline{B^0}(t)\right\rangle = \frac{p}{q}g_-(t)\left|B^0\right\rangle + g_+(t)\left|\overline{B^0}\right\rangle \tag{1.44}$$

where

$$g_\pm(t) = \frac{1}{2}\left(e^{-m_H t - \frac{1}{2}\Gamma_H t} \pm e^{-m_L t - \frac{1}{2}\Gamma_L t}\right) \tag{1.45}$$

where Γ_H, Γ_L, m_H and m_L are the widths and masses of the B_H and B_L mesons. This means:

$$|g_\pm(t)|^2 = \frac{e^{-\Gamma_0 t}}{2}[\cosh\frac{\Delta\Gamma t}{2} \pm \cos(\Delta M t)] \tag{1.46}$$

with $\Gamma_0 = (\Gamma_H + \Gamma_L)/2$, $\Delta\Gamma = \Gamma_H - \Gamma_L$, $\Delta M = m_H - m_L$.
The following time-dependent decay rates are obtained:

$$\Gamma(B^0(t) \to f) = |A_f|^2 \left[|g_+(t)|^2 + \left| \frac{q}{p} \frac{\overline{A}_f}{A_f} \right|^2 |g_-(t)|^2 + 2\Re \left(\frac{q}{p} \frac{\overline{A}_f}{A_f} g_+^*(t) g_-(t) \right) \right] \tag{1.47}$$

$$\Gamma(B^0(t) \to \overline{f}) = |\overline{A}_f|^2 \left| \frac{q}{p} \right|^2 \left[|g_-(t)|^2 + \left| \frac{p}{q} \frac{A_f}{\overline{A}_f} \right|^2 |g_+(t)|^2 + 2\Re \left(\frac{p}{q} \frac{A_f}{\overline{A}_f} g_+(t) g_-^*(t) \right) \right] \tag{1.48}$$

$$\Gamma(\overline{B}^0(t) \to f) = |A_f|^2 \left| \frac{p}{q} \right|^2 \left[|g_-(t)|^2 + \left| \frac{q}{p} \frac{\overline{A}_f}{A_f} \right|^2 |g_+(t)|^2 + 2\Re \left(\frac{q}{p} \frac{\overline{A}_f}{A_f} g_+(t) g_-^*(t) \right) \right] \tag{1.49}$$

$$\Gamma(\overline{B}^0(t) \to \overline{f}) = |\overline{A}_f|^2 \left[|g_+(t)|^2 + \left| \frac{p}{q} \frac{A_f}{\overline{A}_f} \right|^2 |g_-(t)|^2 + 2\Re \left(\frac{p}{q} \frac{A_f}{\overline{A}_f} g_+^*(t) g_-(t) \right) \right] \tag{1.50}$$

where A_f and $\overline{A}_f$ are the amplitudes for the decay and its conjugate, $\Delta\Gamma$ and ΔM are the differences between the width and mass of the two states, and:

$$g_+^*(t) g_-(t) = \frac{e^{-\Gamma_0 t}}{2} \left[\sinh \frac{\Delta\Gamma t}{2} + i \sin(\Delta M t) \right] \tag{1.51}$$

These expressions give the probability that a state that is a B^0 or $\overline{B}^0$ at $t = 0$ decays to f or $\overline{f}$ at time t. If the decay is a CP eigenstate - i.e. the final state of both B^0 and $\overline{B^0}$ is the same (such as the decays $B^0 \to J/\psi K^{*0}$ where $K^{*0} \to K_S^0 \pi^0$ or $B_s^0 \to J/\psi\phi$):

$$\frac{q}{p} \frac{\overline{A}_f}{A_f} = \frac{p}{q} \frac{A_f}{\overline{A}_f} \tag{1.52}$$

so that equations (1.47 and 1.48) and (1.49 and 1.50) become equivalent except for an interchange of $|g_-|^2$ and $|g_+|^2$.

CP violation in neutral mesons can be observed in three ways:

1. **Decay** (direct CP violation) - if an amplitude for a decay A_f and its conjugate process ($\overline{A_f}$) have different magnitudes this violates CP. The total amplitudes for a decay with contributions from two different processes can be written as:

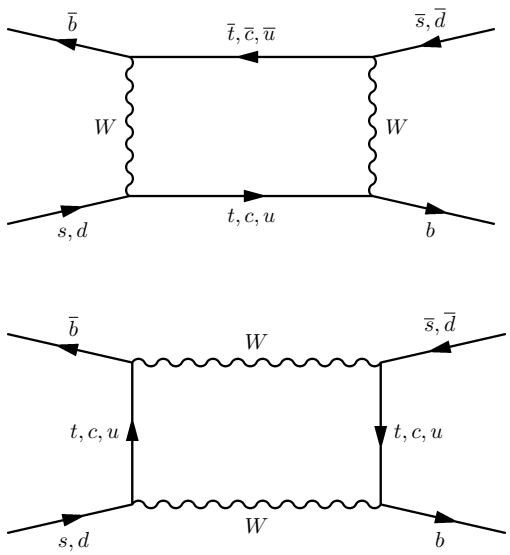

Figure 1.10: Feynman box diagrams of $B^0 - \overline{B}^0$ mixing.

$$A(B \to f) = ae^{-i\delta^a} + be^{i\phi}e^{i\delta^b} \tag{1.53}$$

$$\overline{A}(B \to f) = ae^{-i\delta^a} + b^{-i\phi}e^{i\delta^b} \tag{1.54}$$

where a and b are two different amplitude. The weak phase is set to zero for the first amplitude and ϕ for the second amplitude, because we are only interested in the relative phase. δ^a and δ^b are the strong phases. With no CP violation there is a relative weak phase between the amplitudes, but no strong phase which is depicted in Figure 1.11(a). If CP is violated there is also a relative strong phase which causes the magnitudes of the different amplitudes to differ, this is seen in Figure 1.11(b) where δ_b is the relative strong phase $(\delta_b - \delta_a)$.

$$|A_f/\overline{A}_f| \neq 1 \tag{1.55}$$

2. **Mixing** (indirect CP violation) - if the initial meson is neutral, it can oscillate before decaying. The quantity $\frac{q}{p}$ is the one related to mixing in Equations 1.47 to 1.50. When CP is violated, the mass eigenstates are not

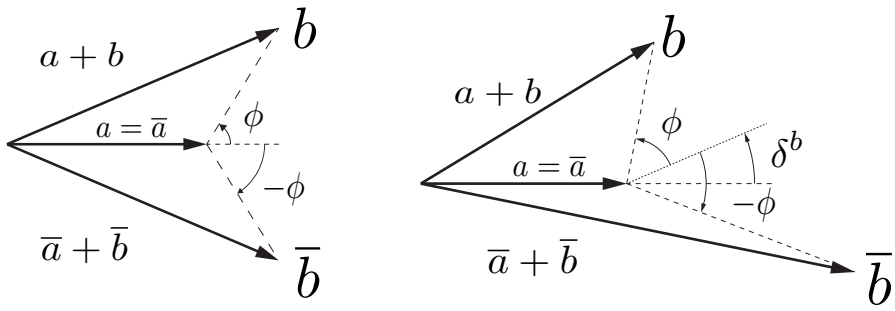

(a) CP conserved

(b) Direct CP violation

Figure 1.11: To demonstrate direct CP violation with two amplitudes a and b where $\overline{a}$ and $\overline{b}$ are the conjugate amplitudes. In (a) there is a relative weak phase between a and b but no strong phase. CP symmetry is conserved. In (b) there is both a relative weak phase and a relative strong phase δ^b, this means the overall magnitude of the decays are different and there is direct CP violation.

equal to the CP eigenstates and:

$$|q| \neq |p| \tag{1.56}$$

3. **Interference** - if both B^0 and $\overline{B^0}$ decay to the same final state, interference can occur between states where mixing has occurred and those where it has not. This is depicted in Figure 1.12. In terms of the time-dependent decay rates, it manifests if the imaginary terms in Equations 1.47 to 1.50:

$$\Im\left(\frac{p}{q}\frac{A_f}{\overline{A}_f}\right) \neq 0 \tag{1.57}$$

$$\Im\left(\frac{q}{p}\frac{\overline{A}_f}{A_f}\right) \neq 0 \tag{1.58}$$

History of B meson measurements In order to study CP violation in B mesons, B factories were constructed using e^+e^- colliders. They use the properties of the $\Upsilon(4S) = b\bar{b}$ bottomonium state, which has mass 10.58GeV and a width

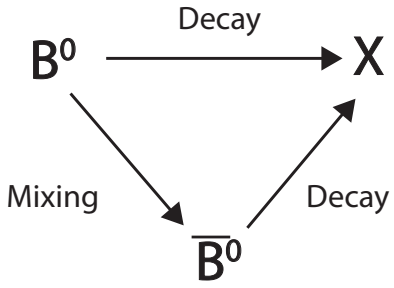

Figure 1.12: If both B^0 and $\overline{B^0}$ both decay to the same final state X, mixing can occur, as well as interference between mixing and decay.

of 20MeV. This means it is just heavy enough to decay to B^+B^- and $B^0\overline{B}^0$ pairs. The BaBar (at SLAC) and Belle (at KEK) detectors were unique in being able to measure the time between production and decay of the B mesons. Their accelerators KEK-B and PEP-II collide electron and positron beams with different energies. This ensures that the B mesons travel for a measurable distance before decaying and time dependent analyses can be carried out. They have both carried out many accurate measurements of the elements of the CKM matrix, confirming that only three families of quarks exist and that the SM accurately describes the electroweak interactions at the level of precision achieved. Many CP-violating effects have been observed in various channels. The effects are much larger than in the kaon system. LHCb has now joined the effort to search for CP-violating effects beyond the SM, not only in B^0_d mixing but also in B^0_s and D^0 meson mixing. The LHC collides protons onto protons which means there is a very large $b\bar{b}$ cross-section and all types of b hadrons are produced (see Chapter 2 for more details).

Potential ways in which CP violation can be measured include:

- **Decay Selection Rules:** A CP eigenstate decaying into an eigenstate with a different CP eigenvalue is a violation of CP symmetry. This is detected when a particle is observed to decay into two different states with opposite CP eigenvalues. The neutral kaon system as explained in section 1.3 is an example of this.

- **Decay rate differences:** differences in the decay energy distribution (for decays into more than two particles), or differences in the angular

distribution of the decay products between a particle and an antiparticle, are an indication of CP violation. An example of this is the decay described in Chapters 4, 5 and 6.

- **Triple products:** for decays with at least four particles in the final state, T-odd triple products can be formed. Any non-zero value or any difference between the magnitude of the triple products for particle and antiparticle decays indicates CP violation. These are described in more detail in Section 4.3.

Status of CP violation measurements at LHCb The LHCb collaboration has measured the first evidence of direct CP violation in charmless two-body decays of B_s^0 mesons as well as the first measurement of direct CP violation in B^0 decays at a hadron collider [23]. Using the $0.36\,\text{fb}^{-1}$ of data collected in 2010 the direct CP violating asymmetries in $B^0 \to K^+\pi^-$ and $B_s^0 \to K^-\pi^+$ decays were measured. The direct CP asymmetry in the B^0 or B_s^0 decay rate is defined as:

$$A_{CP} = \frac{\Gamma(\overline{B^0}_{(s)} \to \overline{f}_{(s)}) - \Gamma(B^0_{(s)} \to f_{(s)})}{\Gamma(\overline{B^0}_{(s)} \to \overline{f}_{(s)}) + \Gamma(B^0_{(s)} \to f_{(s)})} \tag{1.59}$$

where $\overline{f}_{(s)}$ denotes the charge conjugate of $f_{(s)}$. The results are as follows:

$$A_{CP}(B^0 \to K\pi) = -0.088 \pm 0.011 \pm 0.008 \tag{1.60}$$

$$A_{CP}(B_s^0 \to K\pi) = 0.27 \pm 0.08 \pm 0.02 \tag{1.61}$$

where the first uncertainty is statistical, and the second is systematic. The first result is the most precise measurement to date and in good agreement with the world average. The significance of the measured deviation from zero exceeds 6σ. The significance for the second result is 3.3σ.

Using $0.69\,\text{fb}^{-1}$ of data collected in 2011, a measurement of direct and mixing-induced CP violation in $B^0 \to \pi^+\pi^-$ and $B_s^0 \to K^+K^-$ decays [24] was performed. These are given by:

$$A_f^{dir} = \frac{|\lambda_f|^2 - 1}{|\lambda_f|^2 + 1} \tag{1.62}$$

$$\tag{1.63}$$

$$A_f^{mix} = \frac{2Im\lambda_f}{|\lambda_f|^2 + 1} \tag{1.64}$$

where λ_f is given by:

$$\lambda_f = \frac{q}{p}\frac{\overline{A}_f}{A_f} \tag{1.65}$$

The results are:

$$A_{\pi\pi}^{dir} = 0.11 \pm 0.21 \pm 0.03 \tag{1.66}$$

$$A_{\pi\pi}^{mix} = -0.56 \pm 0.17 \pm 0.03 \tag{1.67}$$

$$A_{KK}^{dir} = 0.02 \pm 0.18 \pm 0.04 \tag{1.68}$$

$$A_{KK}^{mix} = 0.17 \pm 0.18 \pm 0.05 \tag{1.69}$$

The measurements of the $\pi\pi$ final state are compatible with those from previous measurements and yield a 3.2σ evidence of mixing-induced CP violation, whereas those from the KK final state are measured for the first time.

LHCb has also carried out the world's best measurement on the CP violating phase ϕ_s using the decays $B_s^0 \to J/\psi\phi$ and $B_s^0 \to J/\psi\pi\pi$ [25]. The interference between the mixing and decay amplitudes gives rise to a weak phase, which is extracted by angular and time-dependent analysis. The result is:

$$\phi_s = (-0.001 \pm 0.101 \pm 0.027)\,\text{rad} \tag{1.70}$$

which is in good agreement with the SM prediction of (0.0363 ± 0.0017) rad [26].

An analysis of $B \to DK^\pm$ and $B^\pm \to D\pi^\pm$ was carried out where the D meson is reconstructed in $K^\pm\pi^\mp$, K^+K^-, $\pi^+\pi^-$ and $\pi^\pm K^\mp$. This uses $1.0\,\text{fb}^{-1}$ and measures several observables. CP violation in $B \to DK^\pm$ is observed with a significance of 5.8σ [27].

LHCb has also observed evidence of CP violation in charm decays $D^0 \to h^+h^-$ where the final state particles are both pions or both kaons. The difference in CP

asymmetry between these two decays is

$$\Delta A_{CP} = A_{CP}(K^- K^+) - A_{CP}(\pi^+ \pi^-) \tag{1.71}$$

and is measured to be

$$\Delta A_{CP} = (-0.82 \pm 0.21 \pm 0.11)\% \tag{1.72}$$

This differs from the hypothesis of CP conservation by 3.5 standard deviations, and could be evidence of physics beyond the SM [28].

Direct CP violation in $B^0 \to J/\psi K^{*0}$: A measurement of direct CP violation in $B^0 \to J/\psi K^{*0}$ is described in Chapters 4 through to 6.

Chapter 2

The LHCb Detector

2.1 The Large Hadron Collider

The 27 km long circular tunnel housing the Large Hadron Collider (LHC) is situated at CERN, 100 m underground on the borders of France and Switzerland. It is designed to collide protons onto protons at a centre of mass energy of 14 TeV at an unprecedented luminosity of $10^{34}\,\mathrm{cm}^{-2}\,\mathrm{s}^{-1}$. In 2011 the centre of mass energy was kept at 7 TeV and the luminosity was of order $10^{32}\,\mathrm{cm}^{-2}\,\mathrm{s}^{-1}$.

Protons are obtained from hydrogen gas and are firstly accelerated to 50 MeV with a linear accelerator called LINAC2. They are then passed to the Proton Synchrotron Booster where the energy is increased to 1.4 GeV. Following this they are injected into the Proton Synchrotron and accelerated to 25 GeV. The Super Proton Synchrotron (SPS) accelerates them to 450 GeV and they are finally injected into the LHC as bunches in two directions round the ring where they are accelerated further in a ramp phase. There are 1,232 superconducting dipole magnets with magnetic fields of up to 8.33 T which are used to bend and contain the protons. These are 14.2 metres long which is as long as reasonably possible. This minimises the amount of dead space between the magnets and maximises their bending power. There are 392 quadrupole magnets used to focus and squeeze the beams around the interaction regions.

Bunches are injected into the LHC in batches of trains. The nominal number of particles in each bunch is 1.15×10^{11}, and the number of bunches in the LHC is designed to be 2808 per beam. In 2011 there have been up to 1381 bunches per beam and this is expected to increase in 2012. The spacing between bunches

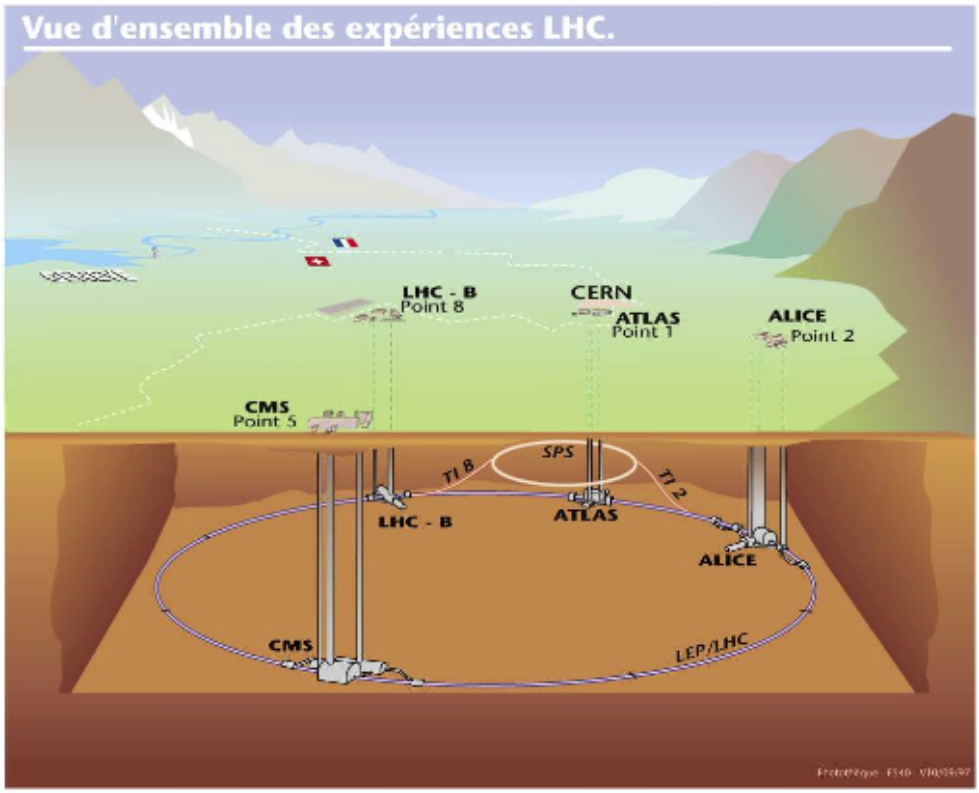

Figure 2.1: Diagram showing the SPS, LHC and the four largest detectors, ATLAS, CMS, ALICE and LHCb.

puts a constraint on the number of bunches possible. For example for a spacing of 75 ns, a maximum of 936 bunches is possible. In 2011 the smallest spacing was 50 ns which allows a maximum of 1440 bunches. After each train there is an abort gap of 3 μs which is necessary for safe beam dumps.

The four main detectors at the LHC: ATLAS, CMS, ALICE and LHCb, are located at the four collision points. Each has had an extensive design, construction, and commissioning lasting approximately 15 years. ATLAS and CMS are general purpose detectors and ALICE is designed to analyse lead-ion collisions that will take place at the LHC. Figure 2.1 shows the SPS, the LHC ring and the detectors.

2.2 The LHCb Experiment

The LHCb detector was built for the main purpose of studying the decays of B and D mesons. The LHC will have a $b\bar{b}$ production cross section of $\approx 500\,\mu$b at a centre of mass energy of 14 TeV. In 2011 running at a centre of mass energy of 7 TeV means the $b\bar{b}$ production cross section was measured to be $284\,\mu$b [29]. At these high energies, proton-proton interactions have highly boosted virtual gluons which interact to produce $b\bar{b}$ pairs at small angles, close to the beam pipe. For this reason the LHCb detector has a dedicated forward angular coverage from approximately 10 mrad to 300 mrad (see Figure 2.2).

At the collision point of LHCb the luminosity of the collisions can be adjusted by displacing the beams from head on collisions while keeping the same crossing angle. This allows the experiment to keep an approximately constant instantaneous luminosity as it deteriorates over the run. This also means that the average number of interactions per crossing (μ) can be limited as LHCb cannot cope with the interaction multiplicities that the ATLAS and CMS experiments work with. Reducing the particle occupancy through the detector also keeps radiation damage to a minimum. Since the LHC started colliding protons in November 2009 until the end of 2011, the instantaneous luminosity was at an average of $3.5 \times 10^{32}\,\mathrm{cm^2 s^{-1}}$, with a μ (number of visible interactions per crossing) of 1.5. At the end of 2011 LHCb had collected an integrated luminosity of $1.22\,\mathrm{fb^{-1}}$.

Other B physics experiments, like BaBar at the Stanford Linear Accelerator (SLAC), Belle at KEK and the Tevatron experiments have made accurate measurements in heavy flavour physics. All of these results have so far been consistent with the Standard Model (SM) predictions. As previously explained, the CP violation predicted by the SM does not explain the antimatter-matter asymmetry in the universe. LHCb has begun to make the most precise measurements in heavy flavour physics and may find CP violation beyond the SM prediction.

The LHCb detector, shown in Figure 2.3 has certain qualities that make it optimal for measuring CP violating parameters and observing rare decays. It provides precise vertexing and momentum resolution which are crucial for measurements involving oscillating B mesons, and for obtaining a high mass resolution. The identification of charged particles i.e. protons, kaons and pions,

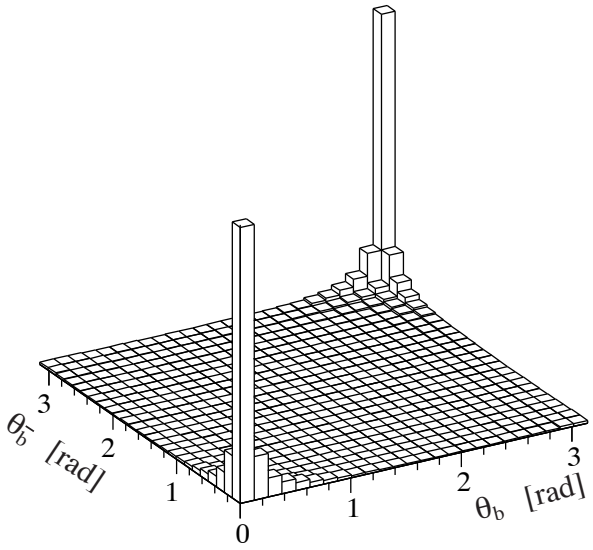

[30]

Figure 2.2: Polar production angles for b and $\bar{b}$ mesons.

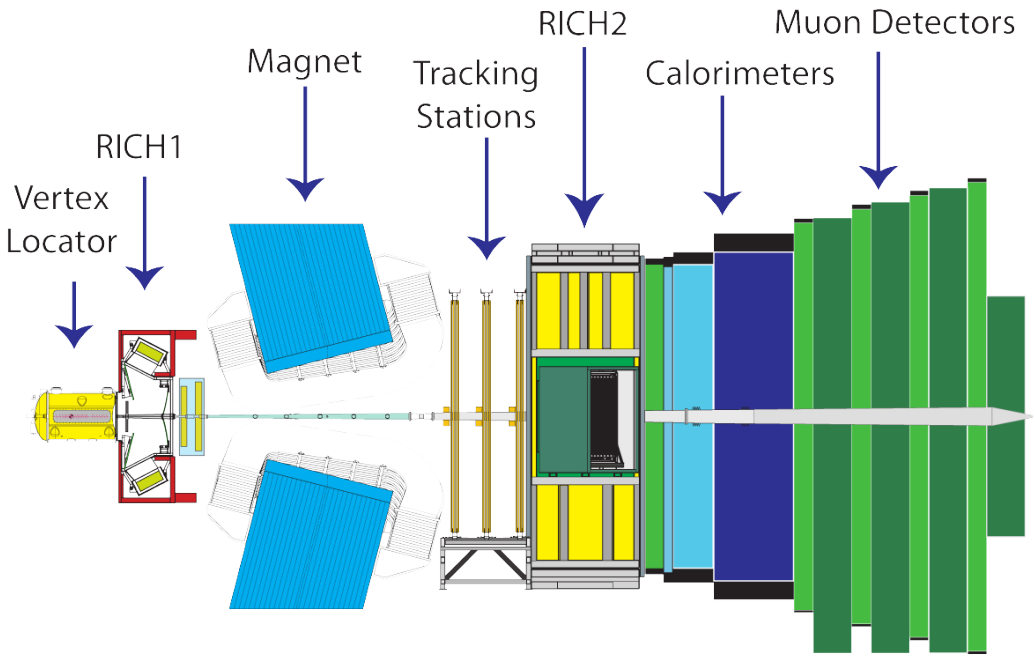

Figure 2.3: Schematic of the LHCb detector and its subdetectors.

is also required for the reconstruction of many B meson channels. In addition, the ability to detect photons, electrons and muons precisely is necessary for many physics goals. The various subdetectors, and the trigger system, all contribute towards these requirements and are explained in the following sections. The majority of the subdetectors are designed to reduce the amount of material in the acceptance range of the detector as much as possible. This maximizes the detection efficiency of the particles from the collision, especially for electrons and photons. In addition, multiple scattering of charged particles interferes with the pattern recognition and reduces the momentum resolution, so this needs to be kept to a minimum.

The LHCb coordinate system is a right-handed system with positive z running along the beam-line away from the interaction point and positive y is in an upward direction from z. The *rapidity* depends on the longitudinal momentum along the direction of the path of the particle, and the energy of the particle.. *Pseudorapidity* η, is a variable used to approximate the rapidity if the mass and momentum of the particle are not known. It is defined by:

$$\eta = -\log\tan(\theta/2) \tag{2.1}$$

where θ is the angle between the particle momentum and the beam axis.

2.3 Particle Tracking

The tracking system is made up of the Vertex Locator (VeLo), and 4 tracking stations: the Tracker Turicensis (TT) which is located upstream of the magnet and T1, T2 and T3 which are downstream of the magnet. Charged particle tracks are bent horizontally in the magnetic field and when these are reconstructed the momentum of the particles can be measured - a necessary step towards particle ID and more importantly towards reconstructing B and D mesons.

2.3.1 The Vertex Locator

B mesons have lifetimes of approximately 1.5 ps. In the LHC, this means they travel about 1 cm before decaying at a displaced vertex. It is therefore important to be able to separate the particles produced at the primary proton-proton vertex

and the B decay vertex. The VeLo accurately measures positions of tracks close to the interaction point so that production and decay vertices of bottom and charm hadrons can be reconstructed. This is essential for making an accurate measurement of the decay lifetimes of B and D mesons.

The VeLo is made up of 21 staggered silicon modules which surround the beam axis and are positioned from $z = -18\,\text{cm}$ to $+80\,\text{cm}$ (see Figure 2.4). It is able to detect particles with a pseudorapidity of $1.6 < \eta < 4.9$ and those from primary vertices with $|z| < 10.6\,\text{cm}$. The sensitive region of the VeLo starts at an inner diameter of 8mm from the beam axis, but is retracted by 30 mm during injection to protect it from damage. The VeLo is housed in its own vacuum vessel of thin aluminium foil which protects the vacuum of the beam pipe from any outgassing of the VeLo. The vacuum pressure in the VeLo box is carefully balanced with that of the beam pipe. The sides of the vessel act as Radio Frequency (RF) shields, so that the VeLo is protected from RF pickup from the beam. The inside of the box is coated with polyamide-imide which is radiation resistant and electrically isolates the aluminium from the rest of the VeLo.

VeLo stations consist of two modules, and each has two types of sensor: the ϕ sensor which measures the azimuthal position around the beam, and the R-sensor which measures the radial distance from the beam axis. The sensors are $300\,\mu\text{m}$ thick, approximately semicircular and are positioned on either side of the beam axis. Each sensor has a radius of 42 mm, and they overlap when they are inserted for physics running. To ensure that they cover the full azimuthal angle the right-side module is placed 1.5 cm behind the left-side module on the z-axis. There is a minimum requirement that tracks with a production angle from 15 mrad up to 390 mrad must pass through as least three stations. This explains the density of the stations near the interaction point, and further away (see Figure 2.4). The optimisation of the sensor positions did not include the single sensor between the cluster near the interaction point and further away, this was added to reduce the large gap in z. This improves the performance of the pattern recognition, which is not optimal if there were two hits in neighboring sensors and one far away. There are two modules which cover the backward direction and were used as a veto for multiple interactions in 2011. This is called the pileup veto.

The R sensor has strips in concentric semi-circles with their centre at the nominal beam position. Each strip is divided into four regions to reduce

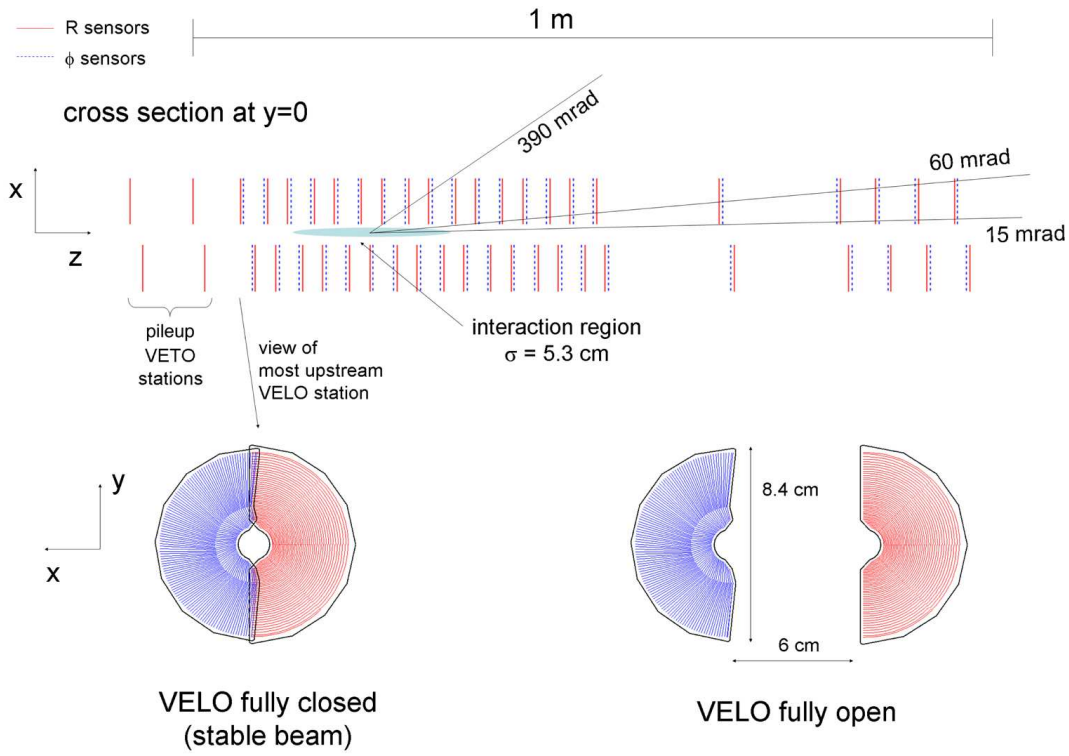

Figure 2.4: A cross-section of the VeLo silicon sensors in the (x,z) plane, while VeLo is fully closed. Below, the front of the modules are shown in their open and closed positions [31].

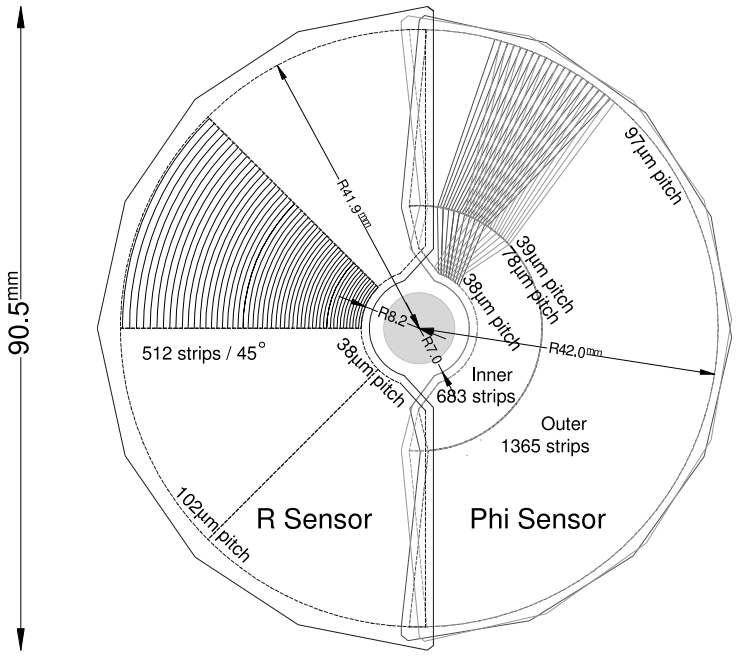

Figure 2.5: Geometry of the VeLo sensors. Only portions of the strips are shown [31].

occupancy. The inner region has a pitch up to 38 μm, which increases outwards to 101.6 μm at the outer edge. The ϕ sensor would ideally have strips running radially outwards from the beam position, but the occupancies of the strips would be too high; therefore the sensor is divided into an inner and outer region at a radius of 17.25 mm. The pitch of the outer region starts at 39.3 μm which is roughly half of the pitch at the end of the inner region which is set to 78.3 μm. There is a skew used in the strips of the ϕ sensor to improve pattern recognition. The inner strips have a $\sim 20°$ angle to the radial whereas the outer strips have one of $\sim 10°$. The modules are then placed so that adjacent ϕ sensors have opposite skew (i.e. the angles are reversed for inner and outer regions). This means that ghost hits can be distinguished from true hits. The strip and pitch layers can be seen in Figure 2.5.

The VeLo is required to have a high signal to noise (S/N) ratio and before installation this was found to be between 17 and 25. This is now measured using clusters on tracks in data, and the noise is measured in non zero-suppressed data. The S/N ratio is shown in Figure 2.6 for a typical R and ϕ sensor as a function of

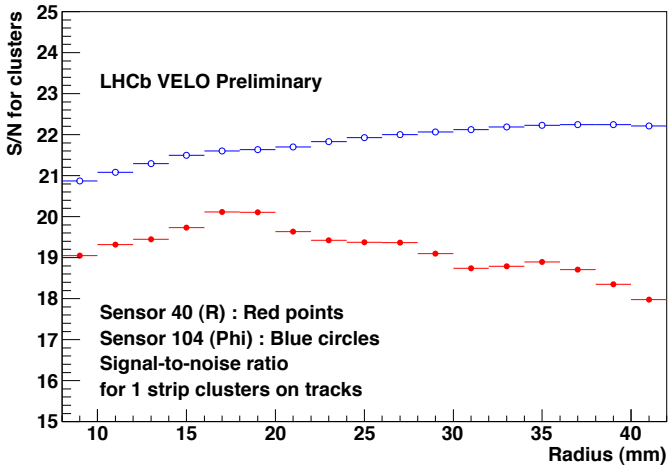

Figure 2.6: Signal/Noise of a typical R and ϕ VeLo sensor as a function of its radius.

the radius. This confirms that the performance of these modules is in agreement with the test studies and exceeds the design specification.

A high efficiency is also required of the VeLo. In 2011 the fraction of strips that cannot be used to detect particles is less than 0.5 %. The cluster finding efficiency is greater than 99 % [32]. The single hit resolution is found by comparing the position of the VeLo clusters with the fitted intercept of the track which uses the rest of the tracking system. In the range $4 - 28\,\mu m$, the resolution depends linearly on the strip pitch as well as the projected angle as can be seen in Figure 2.7. The projected angle is the angle perpendicular to the strip direction. The best resolution is $4\,\mu$m for a $40\,\mu$m strip pitch.

The Primary Vertex (PV) resolution is measured by dividing all tracks in an event randomly into two groups and finding the difference between the reconstructed PV position. The PV resolution using this method is shown in Figure 2.8. A typical PV has 35-40 tracks. The Impact Parameter (IP) is the distance of closest approach between a track and the reconstructed vertex. The IP resolution as a function of the inverse transverse momentum is linear as shown in Figure 2.9 with MC10 and data from 2011. The resolution degrades because of multiple scattering and so depends on the amount of material in the detector, the discrepancy between the data and simulation is thought to be because of simplifications in the material simulations, or the modelling of multiple scattering.

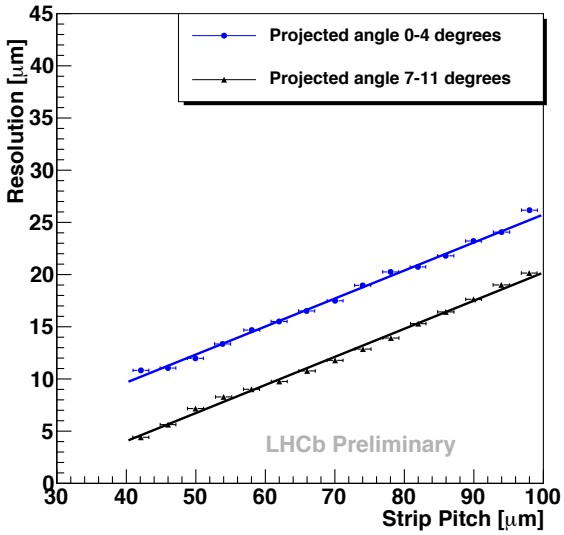

Figure 2.7: Hit Resolution as a function of strip pitch for 2 bins of the projected angles for an R sensor using long tracks in 2010 data.

The difference is corrected in the Monte Carlo before it is used for analysis and so no systematic uncertainty is assigned.

2.3.2 The Magnet

The LHCb dipole magnet enables momentum measurements to take place by bending the path of charged particles. It is comprised of two coils supported on an iron yoke and is wedge-shaped to fit the LHCb angular acceptance. It is a warm magnet so can be ramped easily and the field can be reversed periodically. It provides a bending power of $\int \mathrm{B}\, dl = 4\,\mathrm{Tm}$ for tracks that come from the interaction point.

2.3.3 The Tracking Stations

The tracking system includes the Tracker Turicensis (TT) and the tracking stations (T1-T3), which are positioned further downstream at equal distances apart along the beam pipe. The Inner Tracker (IT) is classed as all of the inner regions of the tracking stations. The IT and TT both use silicon microstrip detectors and are combined in a common project called the Silicon Tracker (ST). Straw tubes are used in the outer regions of the tracking stations which together

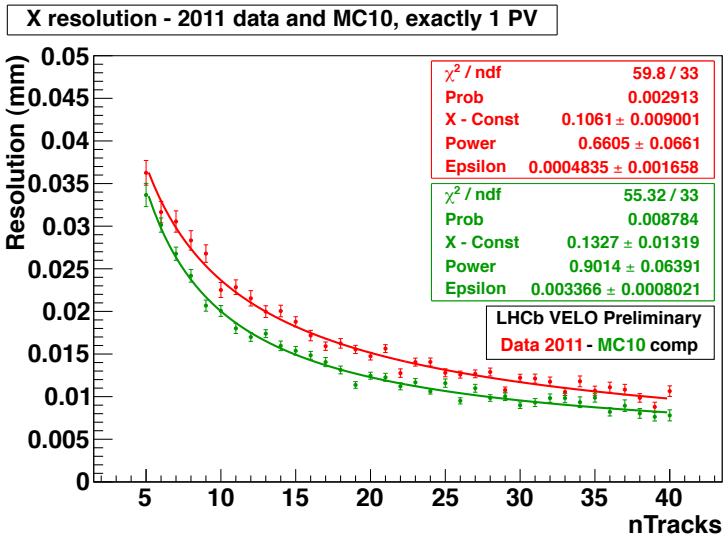

Figure 2.8: PV resolution in x direction comparing 2011 data and MC10, events with only one PV.

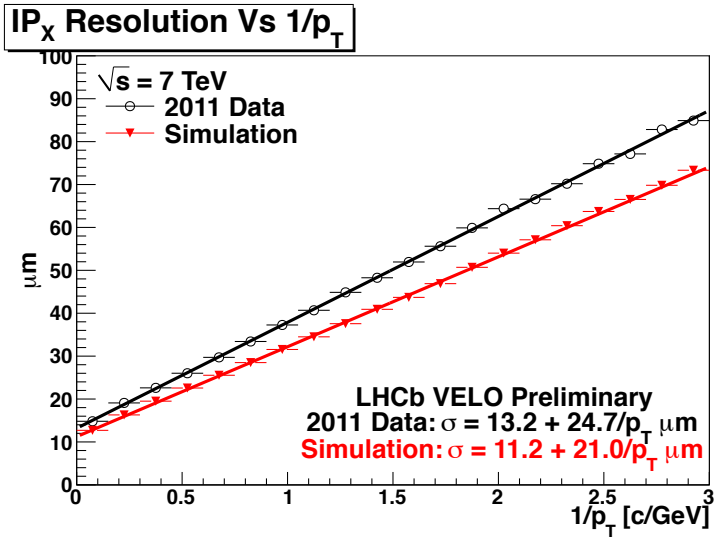

Figure 2.9: Impact parameter in X as a function of inverse transverse momentum measured with 2011 data compared to MC10.

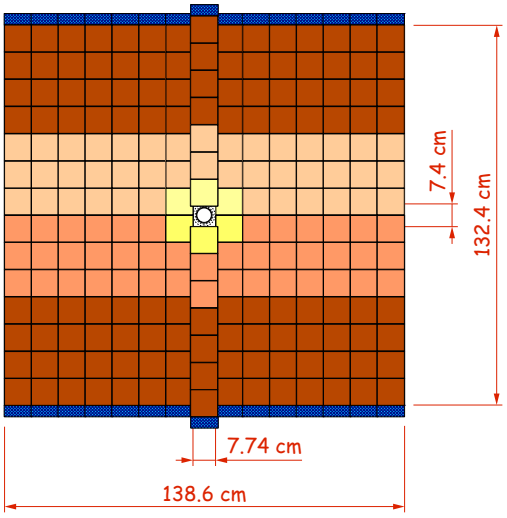

Figure 2.10: One layer of the Tracker Turicensis. The beam line goes through the centre.

are called the Outer Tracker (OT). The IT has a finer granularity than the OT because of the higher flux of particles nearer the beam pipe.

Each ST station has four detection layers, the first and last being vertical, measuring the track position in x. The second and third layer are rotated by a stereo angle of $+5°$ and $-5°$ which allows the y-coordinate to be measured. The ST sensors are housed in light-tight boxes which are thermally and electrically insulated. They are cooled to $< 5°$C to slow down radiation damage and the associated increase in leakage currents. The sensors are also flushed with nitrogen continuously to prevent condensation.

The TT is placed before the magnet which allows reconstruction of the tracks from low-momentum particles which are swept out of the downstream acceptance. It also provides transverse momentum measurements for tracks with a large IP which is used for triggering. The four TT layers are made up of modules which cover the entire LHCb acceptance height. Each module is made up of fourteen silicon sensors, each 500 μm thick carrying 512 readout strips with a pitch of 183 μm. The modules are staggered by about 1 cm in z and overlap by a few millimetres in x to cover the acceptance. Figure 2.10 shows one of the layers without stereo angle.

Each of the three IT stations consists of four detector boxes which are arranged

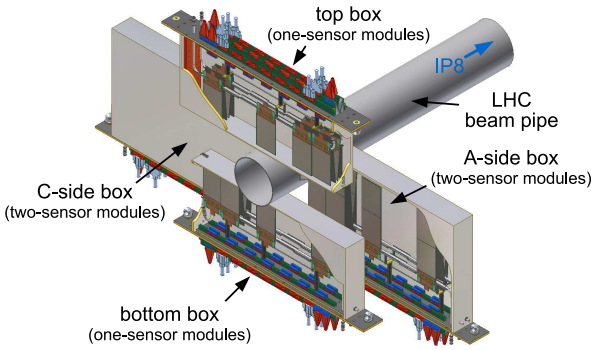

Figure 2.11: Four IT detector boxes around the beampipe.

around the beam pipe as seen in Figure 2.11. Each box contains the four detection layers which consist of seven detector modules which are staggered to leave no gaps. The modules contain single silicon sensors in the upper and lower boxes, and double sensors in the boxes either side of the beampipe. The one-sensor modules are 320 μm thick and the two-sensor modules are 410 μm thick to ensure high signal-to-noise ratios for each module type. Each sensor carries 384 readout strips with a pitch of 198 μm.

The OT consists of gas-filled carbon-doped polyimide straw tubes (a heat and chemical resistant plastic). The counting gas consists of Argon, CO_2 and O_2 in the ratio 70 : 28.5 : 1.5 which optimises the drift time [31]. There is a negative high voltage on the outside surface of each tube and an anode sense wire running along the centre which is at virtual ground. When charged particles travel through they ionise the gas producing electrons which drift to this anode wire. The electric field near the wire causes multiplication of the electrons which amplifies the signal making a detectable pulse. The drift time of the electrons reveals the position of the original particle. The IT and OT modular layout can be seen in Figure 2.12.

In order to reconstruct high-multiplicity B decays, a very high single hit efficiency for minimum ionising particles is required. Both TT and IT have a single-hit detection efficiency $> 99.8\%$ provided the signal-to-noise ratio stays above 10.

The track efficiency for any tracking subsystem is measured using a tag-and-probe method. The system in question is excluded from the track reconstruction.

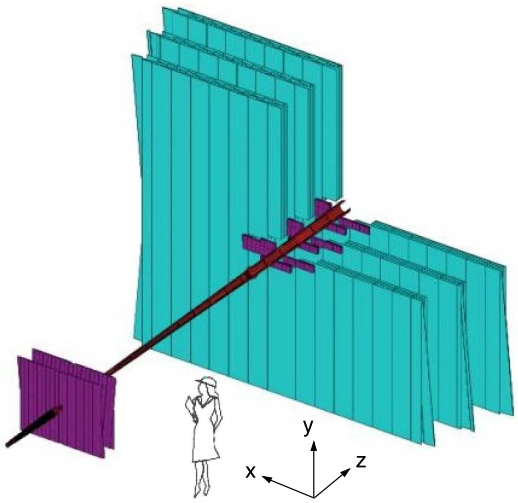

Figure 2.12: Arrangement of the Outer (blue) and Inner (purple) tracking stations.

In this study the decays $K_s \to \pi\pi$ and $J/\psi \to \mu\mu$ are used for measuring the efficiency of the ST. One of the daughters in the decay is reconstructed by the complete tracking system, and the other is reconstructed using only the VeLo and a cluster in the calorimeter- this is called the 'probe' particle. The efficiency of the T-station is then calculated by checking the matching of the 'probe' track. The overall hit efficiency for the IT in 2011 was 99.65% and 99.30% for the TT [33].

The hit resolution is dependent on the strip pitches and the projected angle of the track. In the ST it is also affected by cross-talk which is the coupling of a strip to its neighbours when it gets a hit. When the magnetic field is perpendicular to the electric field in the sensor, the charge carriers will follow through the silicon at an angle rather than following the electric field lines. This Lorentz effect biases the reconstructed position of a cluster and this is taken into account for the hit resolution. The single hit resolution is measured to be $58\,\mu m$ for the IT and $62\,\mu m$ for the TT [34]. This is seen in Figure 2.13 and is in good agreement with Monte Carlo expectations and does not affect the use of MC in any analyses.

The OT modules were designed to withstand a large irradiation dose during operation. However in laboratory tests they showed a rapid gain-loss under mild irradiation. This was due to the deposition of a small insulating layer of a substance containing hydrocarbons onto the anode wire. In addition, there

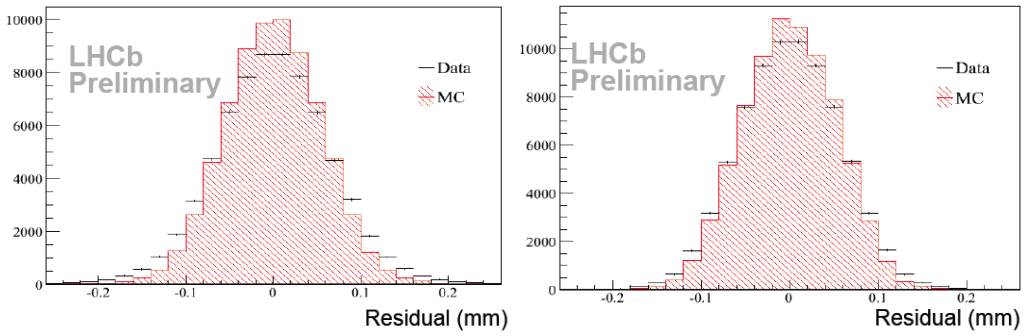

Figure 2.13: Hit Resolutions for IT (left) and OT (right) with 2011 data.

was some unexpected aging damage caused by contamination of the gas due to the outgassing of a plastifier used in the construction of the detector. This was extensively studied in the laboratory, and some preventative actions were taken to reduce the effect. The modules were heated for 2 weeks at 40°C to outgas the material, and oxygen was added to the counting gas.

A system for monitoring the aging of the modules in the detector cavern was devised using sources of radiation to measure the detector response which is carried out at every technical stop (about once a month). The gain is also measured with regular threshold scans where the amplifier threshold is varied and the hit efficiency is measured with tracks. A typical response from October 2011 is shown in Figure 2.14. In 2011 running no gain-loss was observed [35] [36].

2.4 Particle Identification

Particle identification in LHCb is carried out in various ways. The calorimeter detects particles with high transverse momentum, the muon chambers identify muons, and the Ring Imaging Cherenkov (RICH) detectors identify heavier charged particles. The calorimeters and the muon system are described here, the RICH system is described in Chapter 3.

2.4.1 The Calorimeters

The main purpose of the calorimeter system is to determine the energy and position of the particles traversing the detector. The material in the calorimeter

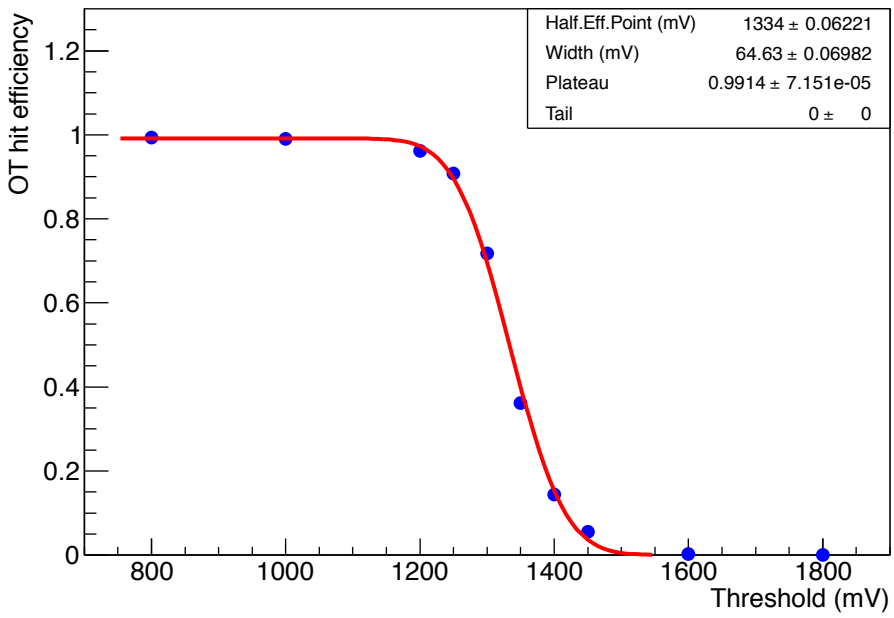

Figure 2.14: Threshold scan for the OT.

system is layered with *absorber* and *signal generator*. The absorber produces a cascade of interactions which initially multiply quickly, and are finally absorbed. The signal generator consists of scintillating volumes where the light detected is approximately proportional to the number of deposited particles. Calibration is then used to calculate the deposited energy. The calorimeter system is essential for flavour tagging because it identifies electrons. In addition, it is required for accurately reconstructing π^0 particles and prompt photons which are both needed for the study of B-meson decays. Crucially it is used for triggering on events containing electrons, photons, neutral pions or hadrons (see section 2.5).

LHCb's calorimeter system consists of the Scintillator Pad Detector (SPD), the Pre-Shower Detector (PS) as well as the Electromagnetic Calorimeter (ECAL) and the Hadronic Calorimeter (HCAL). The layout of the detectors is shown in Figure 2.15. All four detectors transmit scintillation light via wavelength-shifting fibres to photo-multiplier tubes (PMTs). The SPD/PS cells are read out with MAPMTs (Multi-anode PMTs) located outside the LHCb acceptance. These are 64-channel PMTs with bi-alkali photocathodes and fast readout. The ECAL and HCAL have individual MAPMTs located on the modules. The scintillator consists of polystyrene tiles which are treated with wavelength shifting (WLS)

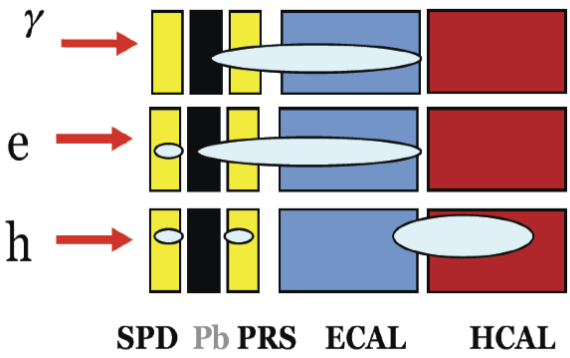

Figure 2.15: The layout of the SPD, PS, ECAL and HCAL detectors and examples of photon, electron and hadron signatures.

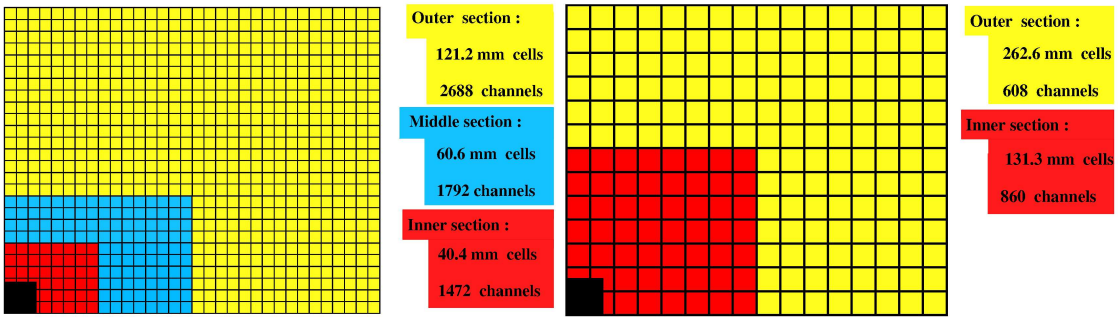

Figure 2.16: Lateral segmentation of the SPD/PS and ECAL (left) and the HCAL (right). One quarter of the detector face, the area closest to the beam is in black.

dopants in varying concentrations. The concentrations are chosen so that that the scintillation light is almost saturated, and is tuned to match the absorption spectrum of the WLS fibres.

All four detectors vary the segmentation of their cells according to the distance from the beam pipe. The ECAL and the PS/SPD have an inner, middle and outer region which are each divided into square cells of length 4, 6 and 12 cm respectively. The HCAL is divided into two sections only (inner and outer) with larger cells due to the size of the hadronic showers. The segmentation of the detectors is shows in Figure 2.16.

The purpose of the SPD and PS is to separate the electrons from a high background of neutral and charged pions produced in the collisions. This is done

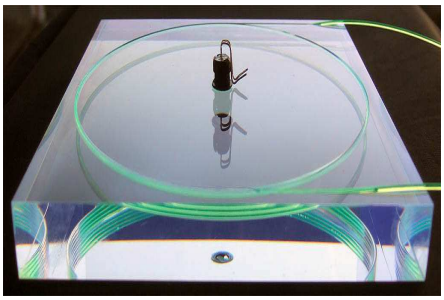

Figure 2.17: Individual scintillator pad with WLS fibre layout. There is a groove in the cell in which the fibres are placed, exiting on the right side. The LED housing is in the middle [31].

by using a longitudinal segmentation. Both the PS and the SPD are single layers of high granularity scintillator tiles separated by a lead sheet which is 2.5 radiation lengths (X_0) thick. Together they have an active area of $7.6 \times 6.2\,\mathrm{m}$. Both planes are divided into two halves so they can be removed for service work. An individual scintillator pad with the WLS fibre layout is shown in Figure 2.17. The fibres are coiled and placed into a groove in the cell, exiting at the side to transport the scintillator light to the PMTs. The PMTs used (MaPMTs) have a bialkali photocathode segmented into 64 pixels of $2 \times 2\,\mathrm{mm}^2$, and were extensively tested for gain, crosstalk and behaviour under magnetic field before installation [31].

To obtain the highest energy resolution the showers from high energy photons must be fully absorbed. For this reason the ECAL has a thickness of 25 radiation lengths. It can therefore reconstruct the kinematical parameters of photons and identify electrons and positrons. The trigger requirements on the HCAL resolution do not depend on the containment of the hadron showers as much as for the ECAL, so due to a limit on space, its thickness is only 5.6 interaction lengths.

Both the ECAL and the HCAL have rectangular walls with a solid angle coverage of $300 \times 250\,\mathrm{mrad}$ excluding a central 30 mrad area in the centre for the beam pipe. The ECAL uses the 'shashlik' design which consists of alternate layers of lead and scintillator which are perpendicular to the beam direction. The scintillators are read out by plastic WLS fibres which are threaded through holes in the sandwich structure. The lead layers are 2 mm thick and there is a $120\,\mu m$ thick layer of TYVEK paper before the 4 mm thick scintillator tiles. In

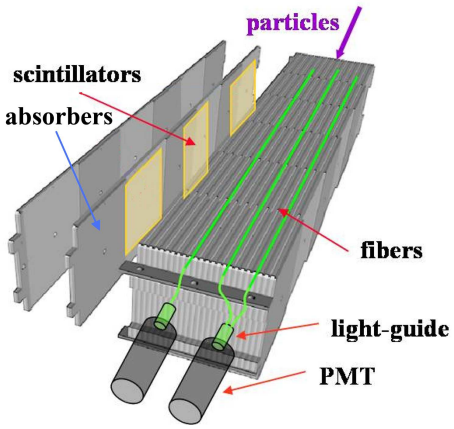

Figure 2.18: Exploded view of scintillator and absorber layers of the HCAL.

total there are 66 layers with a total thickness of 46 cm, wrapped with light-tight black paper. The light from the tiles is absorbed, re-emitted and transported by WLS fibres of 1.2 mm diameter through the module, and is read-out with the phototubes.

The HCAL is made up of tiles, unusually layered parallel to the beam direction as can be seen in Figure 2.18. This orientation has been shown to have a good sampling homogeneity and allows a simplification of the readout fibre path and their coupling with the scintillators. The tiles consist of alternate layers of scintillator and 1 cm thick iron. In the longitudinal direction the tiles are interspersed with steel absorbers corresponding to the hadron interaction length. Two 6 mm thick steel plates are glued in two layers to several 4 mm thick spacers, leaving gaps for the 3 mm thick scintillator tiles. The steel plates are are again wrapped in TYVEK paper. The light is again collected by WLS fibres running along the detector towards the back where the PMTs are housed. The gain of the phototubes of the ECAL and HCAL are set depending on their distance from the beampipe to ensure a constant gain throughout.

The ECAL is calibrated with data using the energy flow method. This allows the improvement of calibration between cells using a relatively small number of events. The average transverse energy for a given cell is computed and compared to its neighbours assuming a smooth energy flow. It involves smoothing the map of transverse energy depositions at the surface of the detector. For each cell a correction factor is calculated with respect to the average deposit over eight

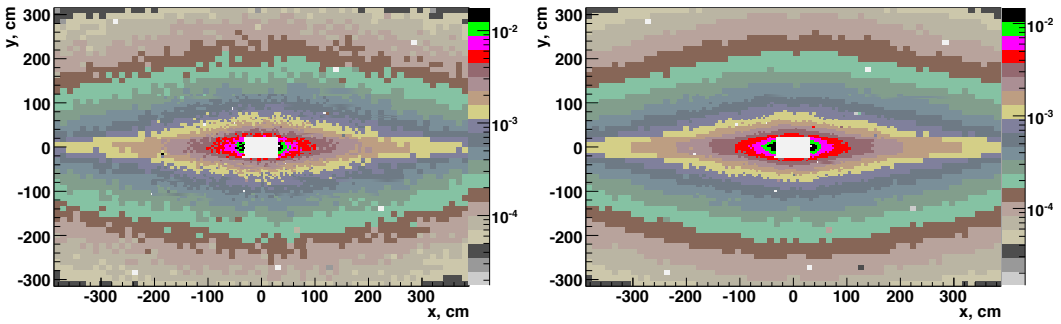

Figure 2.19: ECAL cluster occupancy before and after energy flow calibration.

neighbouring cells. This is normalised using the position of net invariant mass peaks associated with the decays $\pi^0 \to \gamma\gamma$ and $\eta \to \gamma\gamma$. Figure 2.19 shows the cluster occupancy maps for the ECAL before and after energy flow calibration. Improvement of the width of the π^0 invariant mass peak was from 9.1% to 7.5% and for the η peak width from 6.1% to 5.4%.

The ECAL is then finely calibrated using $\pi^0 \to \gamma\gamma$ decays. This uses a set of invariant mass distributions for combinations of two photons constructed for each detector cell. The shift of the position of the peak with respect to 135 MeV (PDG mass [7]) is used to correct the energy scale of that cell. For the ECAL calibration the PS is also used for reconstruction of neutral pions. This energy calibration accuracy is now $2 - 2.5\%$ [37].

A radioactive caesium source calibration system is installed in the HCAL. The sources are moved across each scintillator tile and the PMT response is measured. The anode current of each PMT is measured with a dedicated integrator board approximately 500 times per second. The relation between the anode current and the measured particle energy is known from calibration from test beam runs. The method allows a calibration level of $2 - 3\%$ and is done when there is a technical stop.

The performance of the calorimeters is obtained from the offline analysis. For electron ID pure electron samples come from photon conversion $\gamma \to e^+e^-$. For pure hadron samples the decay $D \to K\pi$ is used. On data a 4% mis-identification rate at 90% efficiency is obtained. The γ/π^0 separation is important for radiative decay studies. The algorithm is based on cluster shape variables. The separation efficiency is $> 90\%$ for each zone of the ECAL [38]. The $\pi^+\pi^-\pi^0$ invariant mass

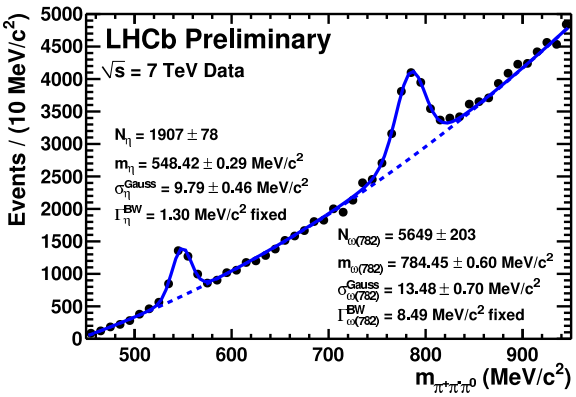

Figure 2.20: The $\pi^+\pi^-\pi^0$ invariant mass distribution reconstructed using the whole LHCb detector including the ECAL. The η and ω resonances are clearly visible.

distribution reconstructed using the whole LHCb detector including the ECAL is shown in Figure 2.20 where η and ω are clearly visible.

It is very important that there is a high resolution and powerful shower separation for background rejection and efficiency for B decays. Radiative B meson decays particularly require the calorimeter system to have an excellent photon energy resolution. CP violating decays which involve a π^0 require the calorimeters to have an excellent resolution on the mass and energy of the π^0.

2.4.2 The Muon Detector

It is essential for many of the key physics analyses to be able to identify muons in the final state. This includes the analysis described in Chapter 4 where the J/ψ decays to two muons. Muons are also used to tag the flavour of semi-leptonic B decays. The rare decay modes $B_d/B_s \to \mu^+\mu^-$ also require good resolution from the muon detectors.

Muons are the most penetrating particles that can be detected by LHCb, so the muon chambers are the final subdetectors. There are five stations (M1 - M5), the first one being located before the calorimeter PS detector to improve the p_T measurements for the trigger. The remaining four lying behind the HCAL (see Figure 2.21) are distanced 1.2 m from each other, and are interleaved with iron block filters 80cm thick. The filters absorb hadrons, electrons and photons to ensure that only muons reach the final muon station. Only muons that have a

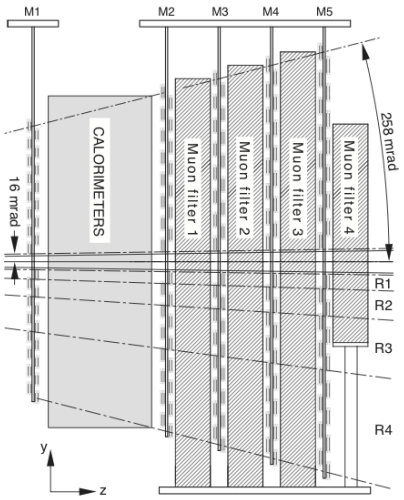

Figure 2.21: Layout of the Muon Stations.

minimum momentum of $\sim 6\,\text{GeV}$ traverse all of the five stations. Each station has a detection efficiency of at least 95%. It is noted that in other subdetectors the minimum momentum of a particle can be larger than 6 GeV.

The detectors provide position measurements of tracks with binary information to the trigger. This is done by separating the chambers into logical pads. The size of the muon stations scale with the distance from the interaction point in order to cover the full acceptance of the detector. Since there is a larger particle flux towards the beam pipe, the stations are divided into four concentric rectangular regions (R1-R4), their size increasing according to the ratio $1 : 2 : 4 : 8$ as seen in Figure 2.22, where the segmentation of the logical pads is also shown. This means that there is a similar channel occupancy over the four regions.

All of the muon stations use Multi Wire Proportional Chambers (MWPC) except for the inner region of station M1 where the particle flux is too high. In this region triple-GEM detectors are used instead because they have better aging properties. For positive identification of a muon the trigger requires there to be a signal in each of the five stations. This means that the chambers must have an efficiency of $> 99\%$ within the 25 ns gate between bunches. The required time resolution is ensured by using a fast gas mixture and suitable charge-collection geometry for the MWPC and GEM detectors.

The 1368 MWPCs in the muon system contain four gas gaps filled with a

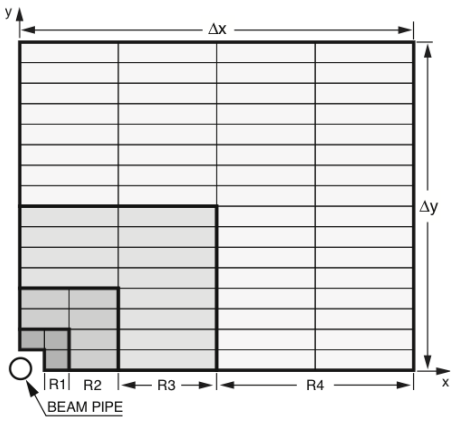

Figure 2.22: Segmentation of each Muon Chamber.

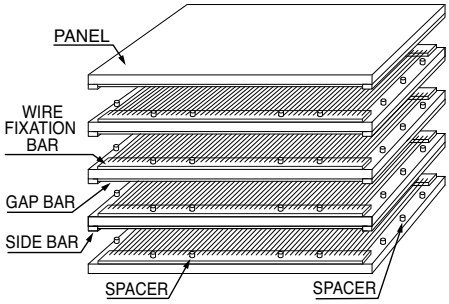

Figure 2.23: Exploded view of one muon chamber.

mixture of Argon, CO_2 and CF_4 in the ratio 40:55:5 [31]. This means a time resolution of 5 ns can be achieved in a 5 mm gas gap with a wire plane of 2 mm spacing. The signals from two adjacent gas gaps are OR-ed and this gives an efficiency $> 90\%$ in a 20 ns window and a gas gain of $\approx 10^5$. The wire has a diameter of 30 μm and is made of gold-plated tungsten. In M2-M4 a chamber is made up of four gas gaps stacked together, with two OR-ed together. The M1 chambers only contain two gas gaps to minimize the material in front of the ECAL. Figure 2.23 shows the layers of a chamber. The panels are a 9 mm thick insulating plane between two conducting planes. The inner conducting planes form the cathodes while the outer ones are an electrical shield. Bars are used in between the layers to form the gas gaps. The general design is the same for all chambers.

The Gas Electron Multiplier (GEM) detectors in the inner region of M1 have

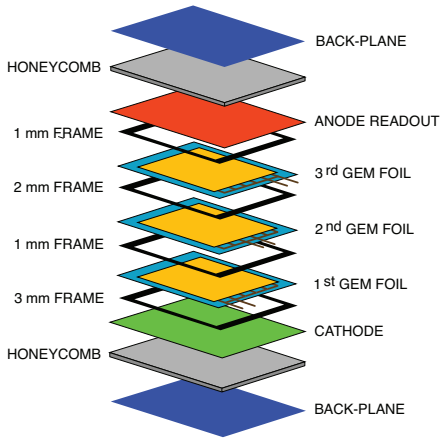

Figure 2.24: Exploded view of a triple-GEM detector.

to withstand a rate up to 500 kHz/cm^2 of charged particles [31]. The triple-GEM chambers have an active area of $20 \times 24\,\text{cm}^2$ and contain three GEM foils between anode and cathode planes. An exploded view of a triple-GEM detector can be seen in Figure 2.24. Particles traversing through the drift gap between the cathode and the first GEM foil produce ionisation electrons which are then attracted by electric fields though all of the GEM foils and they multiply. They then drift into the anode inducing a signal on the pads. A gas mixture of Argon, CO_2 and CF_4 (45:15:40) [39], is used to give a time resolution better than 3 ns. The size of the gaps between each foil have also been decided carefully to improve the time resolution. Each muon chamber holds two triple-GEM detectors superimposed which are logically OR-ed.

The overall efficiency for the muon detector is evaluated for each region separately, applying fiducial volume cuts. For each station, the efficiency is determined using muon tracks which are reconstructed using the other four stations.

The PID performance of the muon system is determined using muons from J/ψ decays. These are reconstructed using purely kinematic selections such as cuts on the momentum and transverse momentum, as well as the track goodness-of-fit. Figure 2.25 shows the identification efficiency as a function of a momentum of the track, when a loose muon ID requirement is applied to the muon from the J/ψ. The efficiency on average is 0.9774 ± 0.00013 where MC gives 0.9613 ± 0.0004 so there is good agreement.

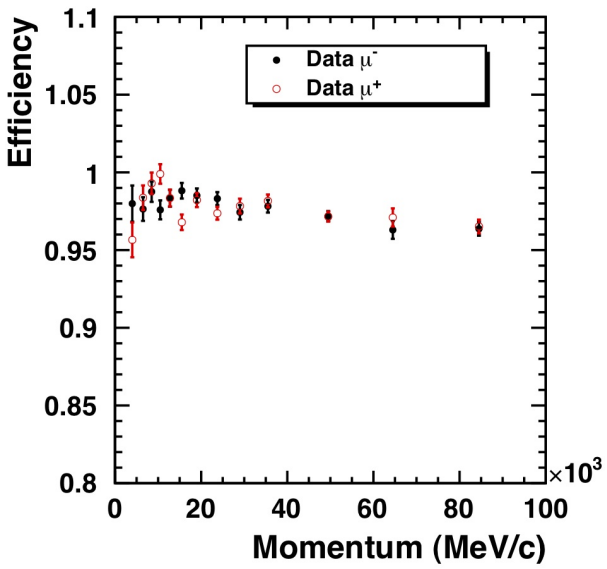

Figure 2.25: Muon identification efficiency as a function of track momentum.

2.5 The Trigger System

For an instantaneous luminosity of $2 \times 10^{32}\,\mathrm{cm}^{-2}\,\mathrm{s}^{-1}$, the crossing frequency of visible interaction is approximately 10 MHz for LHCb. This needs to be reduced to about 3 kHz at which rate the events are written to storage for offline analysis. Only about 15% of the total number of $b\bar{b}$ pairs produced will have at least one B meson with all of its decay products within the detector acceptance. In order to store as many interesting events as possible in an efficient way, the trigger is divided into different levels. The Level-0 (L0) trigger is implemented in hardware, and the High Level Trigger (HLT) is implemented in software, which makes it very flexible. The L0 reduces the rate of visible interactions from $\sim$ 10 MHz to a rate of 1 MHz. The HLT then reduces this to $\sim$ 3kHz. The trigger setup is shown in Figure 2.26.

To determine the trigger efficiencies on data, the so-called TISTOS method is used, described in detail in [40]. Events are categorised into two groups: *trigger independently of signal* (TIS) where the event would also have been triggered without the signal under study and *trigger on signal* (TOS) where the signal under study is used to trigger the event. The total trigger efficiency ϵ^{TRIG} for a given channel is given by:

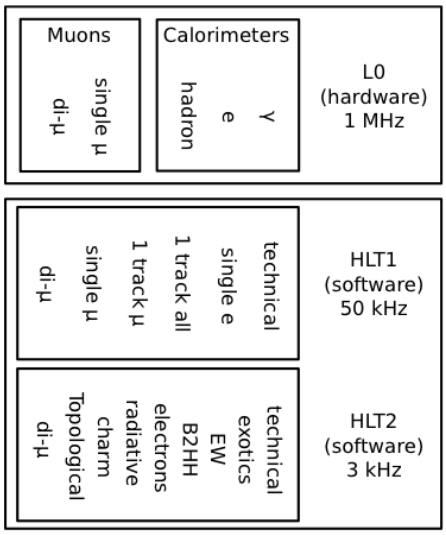

Figure 2.26: Diagram of the different levels of the trigger.

$$\epsilon^{TRIG} = \epsilon^{TIS} \times \frac{N^{TRIG}}{N^{TIS}} = \frac{N^{TIS\&TOS}}{N^{TOS}} \times \frac{N^{TRIG}}{N^{TIS}} \tag{2.2}$$

where ϵ^{TIS} is the efficiency of the TIS trigger, N^{TRIG} is the total number of triggered events and N^{TIS}, N^{TOS}, $N^{TIS\&TOS}$ are the number of TIS, number of TOS and number of events where both triggers were fired, respectively.

In the analysis of $B^0 \to J/\psi K^{*0}$, described in Chapters 4, 5 and 6 the decay channel $B^+ \to J/\psi K^+$ is used to find the trigger efficiency. A simultaneous fit of two different samples is performed. One sample is exclusively TIS and one is TIS&TOS. The fit is done in two dimensions - in the invariant mass of the B and that of the J/ψ. This yields three categories of candidates: signal, background with a J/ψ, and combinatorial background.

2.5.1 Level-0 Trigger

The L0 trigger uses information from the Muon detectors and the Calorimeters to reduce the readout rate. B mesons regularly decay into particles with large transverse momentum (P_t) and energy(E_t). Therefore, particles that meet the following requirements are triggered on:

1. At least one cluster in the HCAL with $E_t > 2.5\,\text{GeV}$

2. At least one cluster in the ECAL with $E_t > 2.5\,\text{GeV}$

3. A muon candidate in the muon chambers with $p_t > 1.48\,\text{GeV/c}$ or two muons (dimuon trigger) with $p_t^{\mu_1} + p_t^{\mu_2} > 1.3\,\text{GeV/c}$ [41]

In addition to this, to avoid reconstruction of events with a large number of tracks and primary vertices, events with a certain number of hits in the SPD are rejected. In the 2011 run, the L0 global event cut was set to < 900 hits for the dimuon trigger and < 600 hits for all other triggers [41]. The pile-up system estimates the number of primary proton-proton interactions in each bunch crossing. It is located upstream of the VeLo behind the interaction point and uses the same silicon sensors as used in the VeLo. In the 2011 run, if multiple interactions were detected the crossing was vetoed. The pile-up system, the calorimeter trigger and the muon trigger are all connected to the Level-0 Decision Unit (DU) which collects all the information for the final decision (see section 2.5.1).

For the L0 calorimeter trigger the HCAL and ECAL are divided into 2×2 cells. It is assumed that the section will contain most of the energy from the shower of a single particle. The E_T of all showers contained in the section is summed up. Information from each calorimeter detector is used to identify clusters from electrons, photons or hadrons.

The Muon System is divided into 192 towers pointing towards the interaction point for the L0 trigger, as seen in Figure 2.27. A Processing Unit (PU) is connected to a tower of logical pads across the five stations. At every bunch crossing each PU runs 96 track finding algorithms in parallel, one for each pad of M3 in the tower. For each hit in M3 a track passing through is extrapolated to the other stations. Hits are looked for within a Field of Interest (FoI) of the track. The size of the FoI depends on the station, the level of background and the minimum-bias retention allowed. If a hit is found in each station this is flagged as a muon track. The p_T of the track is determined from hits in M1 and M2.

For $B^0 \to J/\psi K^{*0}$, the L0 efficiencies are measured with the TISTOS method described above, requiring TIS on the full trigger chain and TOS only at L0. The efficiencies for $\text{B}^+ \to J/\psi K^+$ of the global L0 as well as for the muon and dimuon decision calculated with $330\,\text{pb}^{-1}$ is given in Table 2.1 [41].

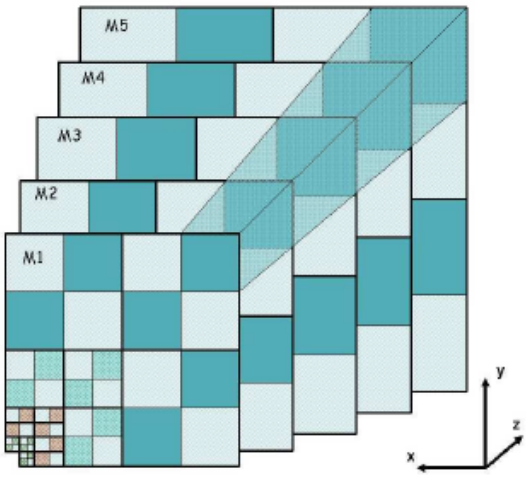

Figure 2.27: Towers layout for the Muon system used for the trigger.

	Global	all muons	L0 Muon	L0 Dimuon
$B^+ \to J/\psi K^+$	$92.5 \pm 0.7\%$	$91.6 \pm 0.7\%$	$91.0 \pm 0.7\%$	$63.3 \pm 2.6\%$

Table 2.1: L0 trigger efficiency measured using the TISTOS method.

2.5.2 High Level Trigger

HLT1 reconstructs VeLo tracks for all events that pass the L0 trigger. The VeLo tracks are matched to hits in the muon station assuming that the minimum momentum is 6 GeV. The tracks are fitted and a hard cut on the track χ^2 of 25 is performed. Then L0 candidates are divided into independent lines depending on the L0 decision output. About 15% of events will have been selected by multiple L0 triggers and therefore will go through more than one HLT1 line. The lines are called 'alleys' and include: μ, $\mu + hadron$, *hadron, ECAL*, and *inclusive* and *exclusive* selection alleys. The particles in the VeLo and Tracking stations are reconstructed corresponding to the L0 objects (or in the case of γ and π^0 candidates to confirm that no charged particle was present). This is called L0 confirmation and reduces the rate to $\sim$ 50kHz. The most important trigger for the $B^0 \to J/\psi K^{*0}$ described in Chapter 4, are the HLT1 Muon and Dimuon lines.

The logical OR of an L0 Muon and an L0 Dimuon is taken for the HLT1 dimuon trigger. They are separated into *high mass* and *detached* muons, both of which are used for $B^0 \to J/\psi K^{*0}$. A detached muon is separated from the parent particle. The high mass have a dimuon vertex with an invariant mass at or above the J/ψ mass. The detached dimuons can also have lower masses but there is also a IP χ^2 cut with respect to the best primary vertex. The efficiencies as a function of transverse momentum for the *HLT1 dimuon high mass*, and the *HLT1 detached muon* triggers are shown in Figure 2.28. The reduced efficiency in the low p_T region is due to an dependence of the muon identification efficiency on the p_T [41].

HLT2 selects composite particles using the full event information and requirements such as the invariant mass or the lifetime of the particle. It is designed to be as similar as possible to the offline selection. A set of tracks are initially selected based on loose momentum and IP cuts, then composite particles are formed such as $K^* \to K^+\pi^-$ or $J/\psi \to \mu^+\mu^-$, which are then used for all selections to avoid duplication in reconstruction of final states. The inclusive and exclusive selections reduce the rate to $\sim$ 2kHz, and data is written to storage. The inclusive triggers select partial decays (such as $B_d \to J/\psi X$). The exclusive triggers look for specific decay channels.

The inclusive dimuon triggers have both *prompt* and *detached* sections. The prompt ones uses the mass and muon ID to distinguish between signal and

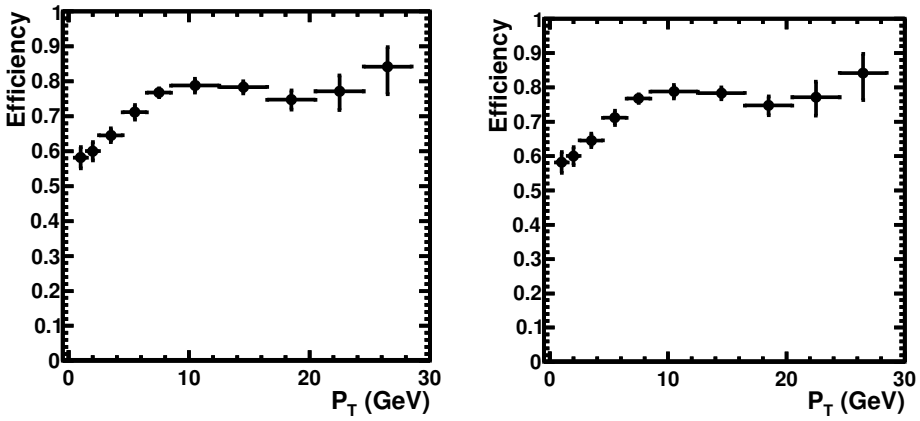

(a) HLT1 dimuon high mass (b) HLT1 detached muon

Figure 2.28: The dimuon trigger efficiency as a function of transverse momentum for the dimuon high mass and detached muon lines with $330\,\mathrm{pb}^{-1}$.

background and includes the HLT2 dimuon J/ψ line which is used for the $B^0 \to J/\psi K^{*0}$ analysis. They have a mass window of 120 MeV around the J/ψ mass, and requires a good track quality (track χ^2/ndof < 5 and a vertex $\chi^2 < 25$). The detached sections are based on the decay length significance of the dimuon vertex and include the HLT2 dimuon detached J/ψ line which is relevant for $B^0 \to J/\psi K^{*0}$. It enhances the efficiency inside the J/ψ mass window, where the vertex separation requirement is reduced compared to the other detached lines. The efficiency of this line as a function of p_T can be seen in Figure 2.29 and the rate is $88.9 \pm 0.8\%$ [41].

The triggers described have been used successfully in 2011 to collect the data used in the $B^0 \to J/\psi K^{*0}$ analysis described in Chapter 3 and 4.

2.6 The LHCb Software

Gaudi is the Object Oriented framework which provides a common infrastructure and environment for the different software applications of LHCb. This includes simulation, reconstruction, analysis, and the steps in between. Each step in the analysis corresponds to a different application and the main ones are briefly described here:

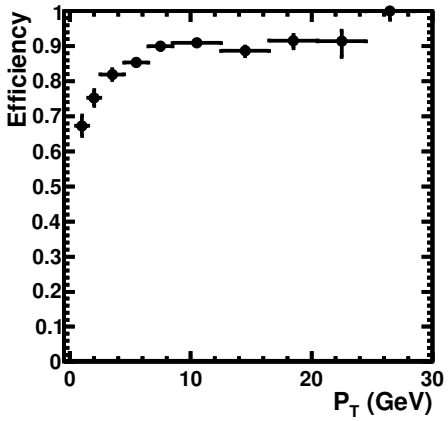

Figure 2.29: Efficiency as a function of transverse momentum for the HLT2 dimuon detached J/ψ line.

- Gauss - for Monte Carlo Simulation. This includes the initial event generation, and the interactions within the detector. Proton-proton collisions are simulated with PYTHIA [42] and the decays of B mesons are simulated with EvtGen [43]. The detector simulation uses GEANT 4 [44]
- Moore - all packages for the trigger are included here
- Boole - simulates detector responses and their digitization to produce data in the same format as the electronics and data acquisition systems
- Brunel - performs subdetector and global reconstruction using pattern recognition for MC and data. It can process the output from Boole and from data
- DaVinci - analysis framework used for offline physics selection on both MC and data which have been fully reconstructed. It also provides tools to allow the evaluation of the performance of the code

2.7 RapidFit

RapidFit is a fitting program that has been used extensively for the $B^0 \to J/\psi K^{*0}$ analysis. It was developed at Edinburgh University and uses probability density

functions (PDFs) to perform a negative log-likelihood fit using Minuit [45] to extract values of parameters of interest. It uses simple configuration files to make it easy to generate events, carry out toy studies, produce pull plots, and fit contributions of signal and background models to data in the form of ROOT [46] nTuples or ASCII files. It also has the functionality to do sPlot [47] fits.

Chapter 3

Particle Identification using the RICH system

3.1 The Ring Imaging Cherenkov (RICH) Detectors

The RICH system measures the velocity of charged particles which emit Cherenkov light as they travel through the radiators. Combining this information with momentum information from the Tracking system (see Section 2.3), gives the mass of the particle.

3.1.1 Cherenkov Radiation

As charged particles travel through a medium, the electric field distorts the atoms so they become polarized, behaving like dipoles. If the velocity of the particle is larger than the phase velocity of light in the medium, the waves from each position of the particle can be in phase with one another so there will be a resultant wavefront at a distant point, this is depicted in Figure 3.1. The particle track goes from A to C, with wavelets going from arbitrary points on the track. If the particle travels this length in the same time that the light travels from A to B, the waves will be coherent. This radiation is only observed at a particular angle θ, at which the waves combine to form a plane wave front BC, this is called the Cherenkov angle.

If the velocity of the particle is βc where c in the velocity of light in vacuum,

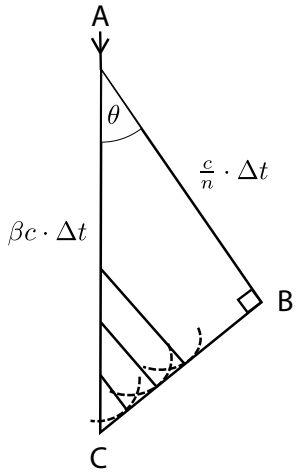

Figure 3.1: Huygens construction to illustrate coherence. The particle track goes from A to C, with wavelets going from arbitrary points on the track. If the particle travels this length in the same time that light travels from A to B, the waves will be coherent.

and n is the refractive index of the medium, in time Δt the particle will travel a distance $AC = \beta c \cdot \Delta t$, and the light will travel a distance $AB = \Delta t \cdot (\frac{c}{n})$. Thus the 'Cherenkov relation' is obtained:

$$cos\theta = \frac{1}{\beta n} \tag{3.1}$$

Figure 3.1 is only for one plane, but there will be a symmetry about the axis of the particle, so the light originating from each point on the track is propagated as a wavefront which becomes the surface of a cone as in Figure 3.2. The cones of photons produced from a charged particle travelling through a medium can be focused into rings. If the refractive index of the medium is known as well as the Cherenkov angle, then the velocity of the particle can be deduced.

3.1.2 RICH detectors

The two RICH detectors in LHCb take advantage of the way Cherenkov light is produced in cones to measure the velocity of charged particles. RICH 1 (see Figure 3.3(a)) is situated before the magnet in order to cover a large angular acceptance. Its purpose is to enable particle identification over the

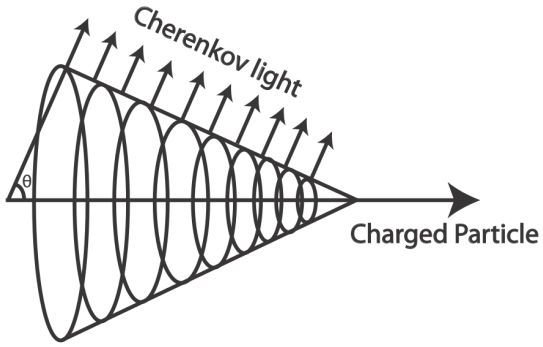

Figure 3.2: Cherenkov cone emitted by a charged particle. θ is the Cherenkov angle.

momentum range $1 \rightarrow 70\,\mathrm{GeV/c^2}$ with a polar angle acceptance from ± 25 to $\pm 300\,\mathrm{mrad}$ horizontally and $\pm 250\,\mathrm{mrad}$ vertically. It uses two radiators, C_4F_{10} covers the momentum range $\sim 5 \rightarrow 70\,\mathrm{GeV/c^2}$, and silica aerogel which covers $1 \rightarrow 10\,\mathrm{GeV/c^2}$. The saturated Cherenkov angle (for particles with $\beta = 1$) for C_4F_{10} is 53 mrad, and for the aerogel is 242 mrad. RICH 2 (see Figure 3.3(b)) is situated after the magnet and tracking stations. It identifies higher momentum particles from approximately $20\mathrm{GeV/c^2}$ up to beyond $100\,\mathrm{GeV/c^2}$ using CF_4 in the radiator, and has a reduced angular acceptance of ± 15 to $\pm 120\,\mathrm{mrad}$ horizontally and $\pm 100\,\mathrm{mrad}$ vertically. The saturated Cherenkov angle for C_4F_{10} is 32 mrad. The RICH detectors use radiators of a well known refractive index through which the particles traverse and produce photons in cones. Figure 3.4 shows that the momentum and acceptance range covered by each radiator compliment each other well.

The Cherenkov light produced when charged particles travel through the radiators, is reflected and focused using flat and spherical mirrors which are tilted so that the ring image is reflected onto arrays of photo-detectors (see Figure 3.5). The radius of the ring becomes equivalent to the opening angle of the Cherenkov cone because of the known geometry. The photo-detectors, called Hybrid Photon Detectors (HPDs) are located outside of the LHCb acceptance in order to reduce the amount of material that the particles have to traverse. They image and read-out the position of the Cherenkov photons. There are 196 HPDs in RICH 1 and

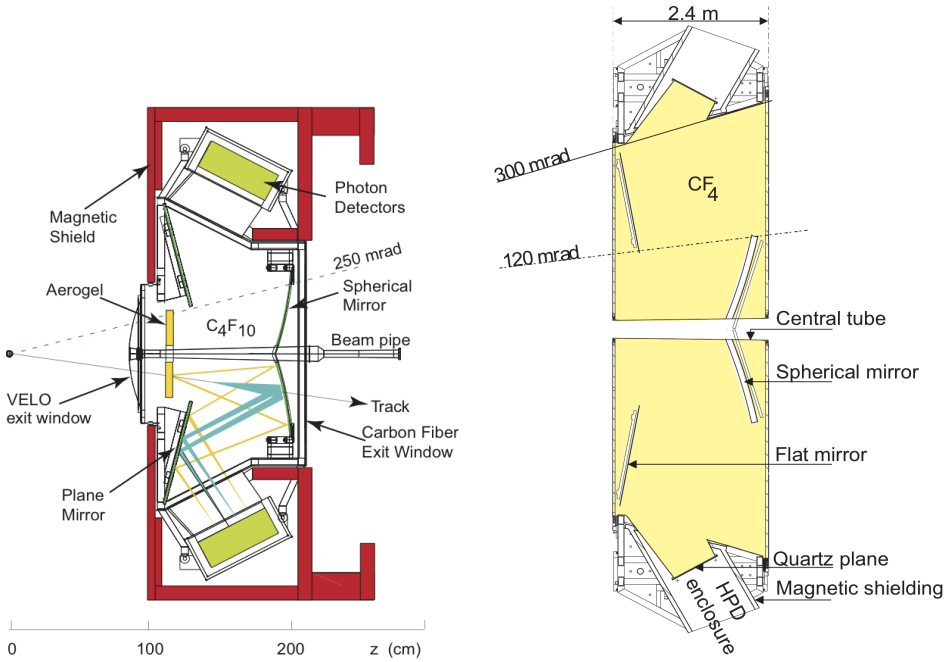

(a) RICH 1 Schematic layout (b) RICH 2 Schematic layout

Figure 3.3: Schematic layout of RICH 1 and RICH 2.

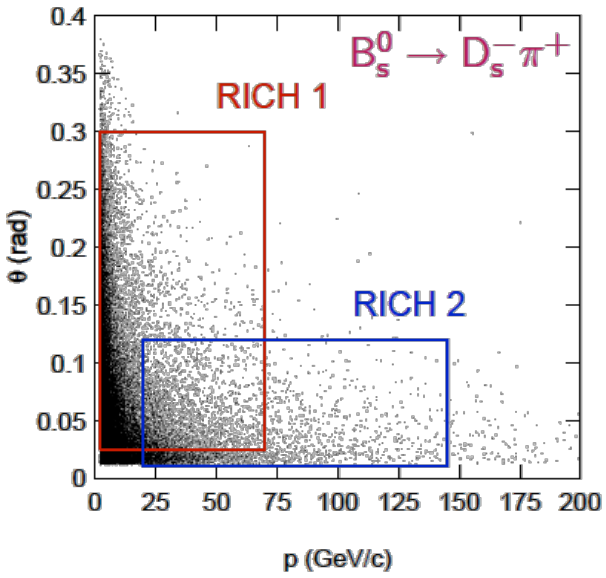

Figure 3.4: Acceptance of the RICH radiators. The momentum coverage for each RICH radiator is plotted against the acceptance range for the decay $B_s^0 \to D_s^- \pi^+$. Together they cover a large range in both parameters.

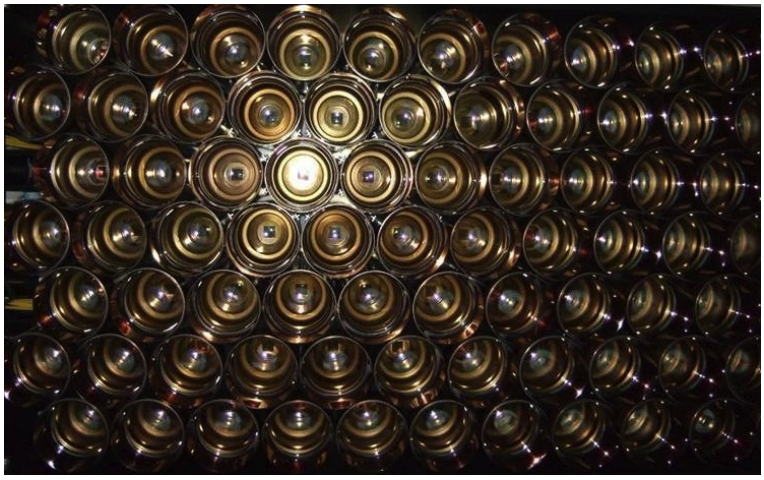

Figure 3.5: Photograph of the array of RICH 1 HPDs.

288 in RICH 2 covering a total area of $3.3\,\mathrm{m}^2$.

3.1.3 Cherenkov ring reconstruction

Pattern recognition algorithms are used to reconstruct the Cherenkov rings. A ring on the HPD plane will be approximately elliptical, with a degree of distortion that depends on the track position and direction. The reconstruction procedure is based on a maximal likelihood approach.

A particle type hypothesis is assigned to each charged particle track found in the tracking stations. Initially the hypothesis is for a pion, which is the most common particle type. The corresponding expected number and Cherenkov radii of the resulting photons are calculated and the likelihood is calculated. The hypothesis is then changed and the likelihood is recalculated. This is done iteratively for the whole detector plane and for each radiator. The change with the largest increase in likelihood is kept.

To study the performance of the RICH system, the ratio of log-likelihood between two particle hypotheses is determined:

$$\Delta ln\mathcal{L}_{K\pi} = ln\mathcal{L}(K) - ln\mathcal{L}(\pi) = ln\frac{\mathcal{L}(K)}{\mathcal{L}(\pi)} \tag{3.2}$$

This delta log-likelihood (DLL) can be used as a selection cut to improve the purity of the sample, which decreases the efficiency, or vice-versa.

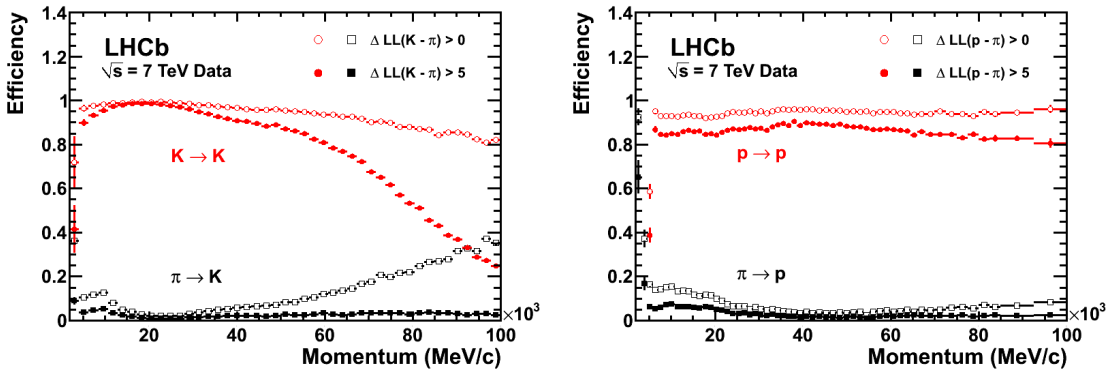

(a) Kaons (b) Protons

Figure 3.6: Identification and misidentification efficiencies for kaons and protons as a function of momentum. The solid markers are for DLL>0 and the hollow markers are for DLL>5.

To calculate the identification and mis-identification efficiencies, pure samples of pion, kaons and protons are required. The decays $K^0_s \to \pi^+\pi^-$ and $\Lambda \to p\pi^-$, as well as the charm decay $D^{*+} \to D^0(\to K^-\pi^+)\pi^+$ can be selected with a high purity using kinematic cuts only. These channels provide the information for the identification efficiency plots shown in Figure 3.6. The two curves represent the two different DLL cuts, $DLL > 0$ and $DLL > 5$. The first is used to measure the cut efficiency, the second to select a high purity data sample. A drop in efficiency for kaons at high momentum will improve during the reprocessing of the current data when the updated alignment will have been fully implemented.

3.1.4 Calibration of the RICH detectors

There are four main contributions to the limit on the precision of the Cherenkov angle θ_c:

- Emission point: the tilt of the spherical mirrors leads to a translation of the photon image on the detector plane dependent on its emission point along the particle track. This is not taken into account in the reconstruction, in which photons are assumed to originate at the mid-point of a track through a radiator.

- Chromatic Dispersion: The refractive index varies with wavelength, and since Cherenkov photons are emitted with a wide distribution of wave-

	Aerogel	C_4F_{10}	CF_4
Emission	0.4	0.8	0.2
Chromatic	2.1	0.9	0.5
HPD	0.5	0.6	0.2
Track	0.4	0.4	0.4
Total	2.6	1.5	0.7

Table 3.1: Single photoelectron resolutions for the three RICH radiators. All numbers are in mrad.

lengths, θ_c is also spread.

- HPD pixel size: Each pixel covers a $2.5 \times 2.5\,\text{mm}^2$ area on the HPD window. It is especially limiting in RICH 1 (fewer HPDs and smaller acceptance region for rings from C_4F_{10}).

- Tracking: Since θ_c is calculated with information from the tracking, track precision must be taken into account.

The resulting resolution for each contribution on simulated data are shown in Table 3.1 [31]. The resolution is largest for the aerogel, dominated by the chromatic dispersion and smallest for CF_4.

The detector simulation is used in the reconstruction process for tracks and particles, therefore any discrepancy between the simulation and the detector will introduce inaccuracies. This simulation must therefore be corrected (or 'aligned'). The aim is that any contribution to the resolution of the Cherenkov angle from the simulation is small compared to the dominant sources listed above.

After the initial alignment of the mirrors and HPDs within the RICH detectors following installation, the alignment is regularly improved and updated using collision data. The flat and spherical mirrors are aligned using an iterative method which minimises the distortion of the Cherenkov angle distribution. Alignment parameters are automatically updated for every fill of the LHC. Cherenkov angle resolutions of 1.59 mrad (C_4F_{10}) and 0.66 mrad (CF_4) have been achieved for the two gas radiators (see Figure 3.7). This meets the expectation from the LHCb detector Monte-Carlo of 1.53 mrad (C_4F_{10}) and 0.66 mrad (CF_4).

In the HPDs, photoelectron trajectories are affected by the residual stray magnetic field of the LHCb dipole magnet. Magnetic Distortion Correction

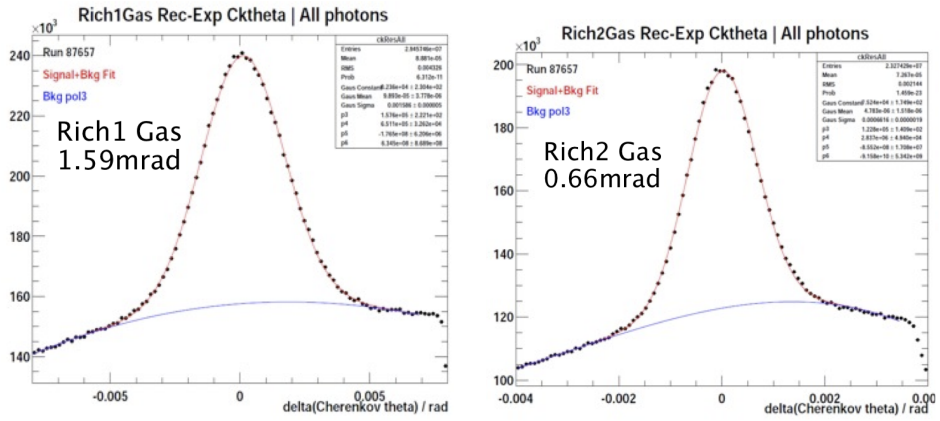

(a) RICH 1 (b) RICH 2

Figure 3.7: Cherenkov angle resolution for the RICH detectors in 2011.

Systems have been implemented in both RICH detectors. They project a known pattern of light spots onto the HPDs. From the recorded responses with the two polarities of the bending magnet and without magnetic field, magnetic distortion maps are extracted and automatically fed into the detector database, so it can be corrected for. For more details see [48].

3.1.5 RICH performance

The RICH detectors have been running successfully since collisions began in November 2009. Despite a larger instantaneous luminosity than originally planned, their excellent performance has enabled many interesting physics analyses to take place. Whilst the RICH detectors are running, the comprehensive online monitoring system allows shifters to monitor their behaviour and the environmental conditions. It enables problems to be identified and resolved quickly. The data quality is constantly monitored during collisions. Figure 3.8 shows the main screen that RICH shifters see when collisions are taking place. Hit maps of the RICH 1 and RICH 2 detector planes are seen during collisions, showing accumulated hits for all channels. There are a few missing HPD images, this is explained later.

LHCb was designed to run with a mean number of visible interactions per bunch crossing (μ) of 0.4. In 2011 it has been running with a typical μ of 1.5 and a maximum of 4. Multiple primary vertices lead to a reduction in PID efficiency.

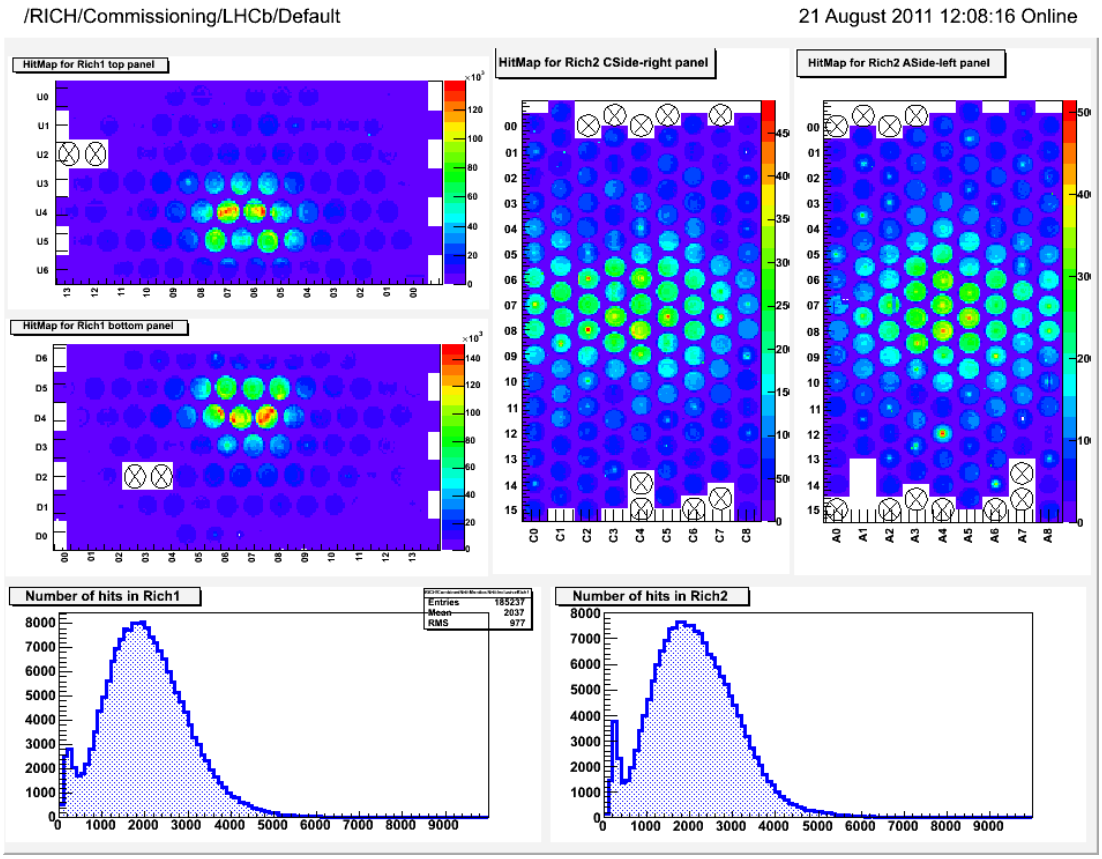

Figure 3.8: HPD Hit Map from 21/08/2011. This is the screen the RICH shifters see when monitoring their behaviour. RICH 1 occupancies are on the left, and those for RICH 2 are on the right. A histogram of the number of hits for both RICH detectors is shown at the bottom.

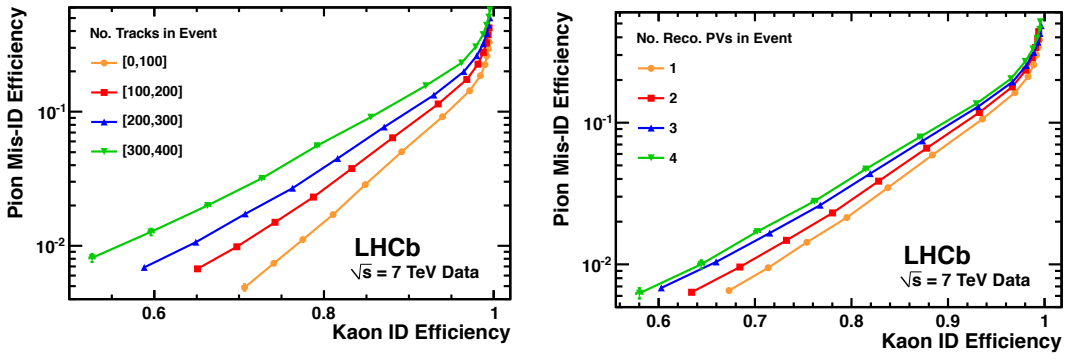

Figure 3.9: Identification efficiency as a function of track multiplicity and multiple primary vertices.

Figure 3.9 shows the pion misidentification fraction against the kaon identification efficiency as a function of track multiplicity as well as the number of reconstructed primary vertices, as the requirement on the likelihood difference $\Delta log\mathcal{L}(K-\pi)$ is varied. As expected some degradation in PID performance occurs with increased interactions. However it is evident that the K/π separation is robust up to the highest multiplicities in 2011.

Plotting the Cherenkov angle against the momentum as in Figure 3.10, illustrates the particle separation power of the combined RICH detectors. This is essential for many LHCb physics analyses including the analysis $B^0 \to J/\psi K^{*0}$ (described in Chapters 4 - 6), for which the final state includes a pion and a kaon. Figure 3.11 shows the DLL distribution for K/π separation for fully simulated $B^0 \to J/\psi K^{*0}$ data (MC11a) for the truth matched sample, and reflection background (where the kaon has been misidentified as a pion or vice-versa). Cutting on the DLL distribution at zero eliminates a large proportion of the reflection background, whilst preserving the majority of the signal.

3.2 Hybrid Photon Detectors

Figure 3.12 shows a photograph of a single HPD, and a schematic diagram. They are called 'Hybrid' because they combine a silicon pixel sensor and readout chip with a vacuum tube. Each HPD has a 7 mm-thick quartz window coated with an S20 multi-alkali photocathode on the inside which converts the incoming

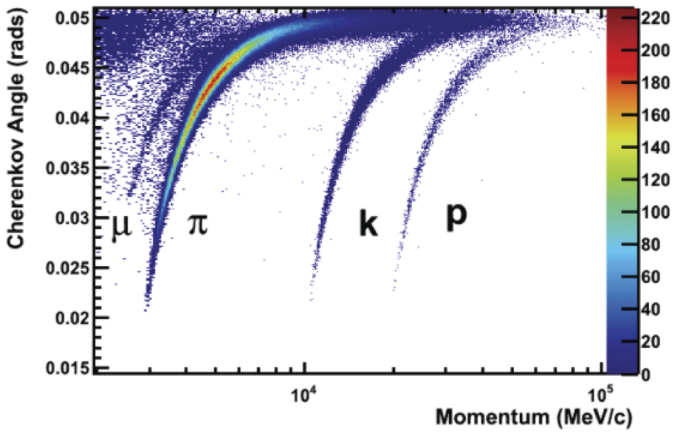

Figure 3.10: Cherenkov angle as a function of Momentum.

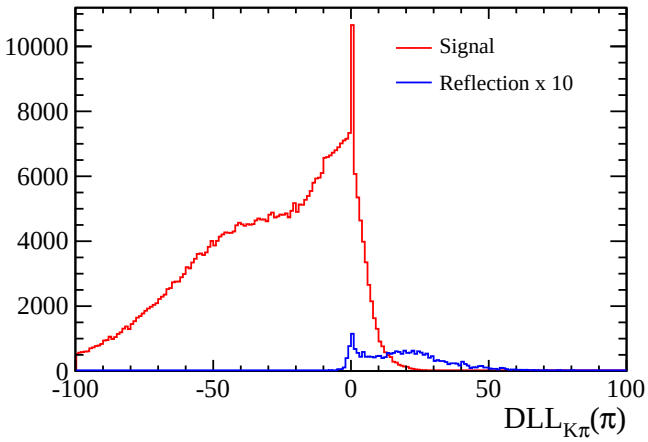

Figure 3.11: Delta Log Likelihood (DLL) distribution for K/π separation from fully simulated MC11a $B^0 \to J/\psi K^{*0}$ with truth matched events (red) and reflection background (blue) which has been multiplied by 10 to make it visible. There is a peak at zero which are events for which the mass hypothesis was below the Cherenkov threshold, and the algorithm therefore returns zero by default. Since the signal selection involves a DLL cut at 0, these events are not included in the selection.

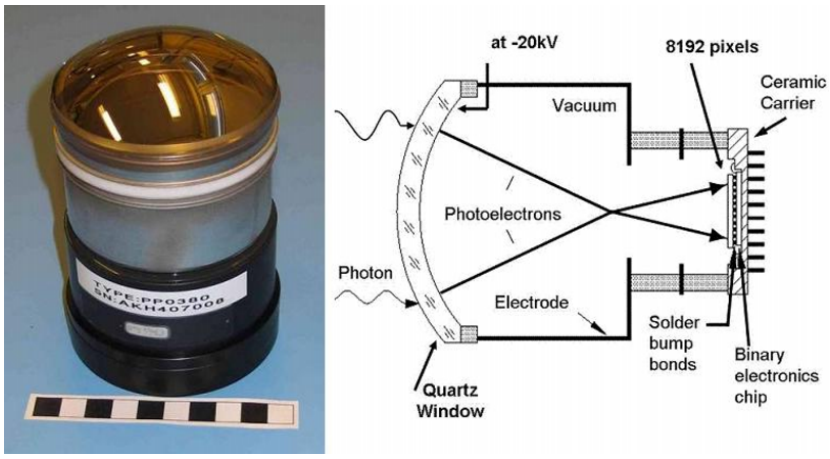

Figure 3.12: Photograph of a single HPD, and a schematic diagram showing the acceleration of the photoelectrons on to the pixel chip.

Cherenkov photons to photoelectrons by the photoelectric effect. These are accelerated through the vacuum tube by a high voltage bias of up to 18kV. The cross-focusing electrostatic field projects the photoelectrons onto the pixel anode at the base, with a demagnification factor of approximately 5. The anode consists of a 300 μm thick 32×256 pixel detector array. These pixels are called 'ALICE' pixels. The HPD can also be read-out in LHCb mode where eights pixels are grouped together, effectively creating one square 'LHCb' pixel. The sensor chip is bump-bonded to the binary readout chip, which can operate at 40 MHz. This is glued and wire-bonded to a ceramic carrier and encapsulated in the vacuum tube. When a photoelectron hits the sensor up to 5000 electron-hole pairs are released in the silicon. The silicon sensor is reversely biased at 80V, over-depleting the p-n junctions and allowing the charge collection within the 25 ns between each proton bunch crossing [49] [50] [51]. The external L0 trigger causes the signals to be read out at 1 MHz from a total of 500,000 pixels.

3.3 HPD testing

The HPDs were chosen for LHCb for a number of reasons. They have a very low noise, a good active-to-total area ratio, and good time resolution. Their high spatial resolution and low noise allow the accurate pattern recognition of Cherenkov rings. In order to check that each meets the specifications defined by

the LHCb collaboration, they are shipped to Edinburgh and Glasgow Universities after production at *Photonis* and tested before installation. In Edinburgh there are two test stations, one for standard testing of the HPDs, and one for testing their quantum efficiency (QE). The configuration, monitoring and data taking are fully automated. The standard test programme quantifies every function and property of an HPD: the parameters characterising the photocathode, the electron optics, the state of the tube body and exterior, the characteristics of the silicon sensor and the functionality of the readout chip [52].

The QE is defined as the probability that an incoming photon of a given wavelength produces a photoelectron that is detected. This takes into account any inefficiencies due to reflections at the air-quartz or quartz-cathode boundaries, as well as the thickness, absorptive qualities and work function of the photocathode. The QE is tested at Edinburgh by comparing ratios of current readings between a calibrated photo-diode (PD) and the HPD from a stable light source:

$$\eta_q^{HPD}(\lambda) = \eta_q^{PD}(\lambda)\frac{I_{HPD}(\lambda)}{I_{PD}(\lambda)} \tag{3.3}$$

where η_q is the QE and λ is the wavelength. LHCb requires a QE of $> 20.0\%$ at $\lambda = 270\,\text{nm}$, and $> 15.7\%$ at $400\,\text{nm}$. The HPDs were found to have an average QE $\sim 30\%$ for $270\,\text{nm}$ and $\sim 25\%$ for $400\,\text{nm}$ [53] [54].

3.3.1 Ion Feedback of the HPDs

The HPD vacuum has been observed to degrade over time, through a process called Ion Feedback (IFB). Residual gas molecules in the vacuum tubes get ionised by the incoming photoelectrons and are accelerated onto the photocathode where they generate secondary electrons. If the HPD vacuum is poor, these secondary photoelectrons will further ionise gas molecules, resulting in a chain reaction. Many photoelectrons hitting the photocathode over a prolonged period of time can cause it to degrade and emit light which may interfere with the detection of photons from Cherenkov rings. The HPDs must be replaced well before they start to degrade and are therefore monitored closely. They can be repaired a limited number of times, carried out by the manufacturers. The time an HPD spends in the detector before it has to be replaced varies hugely, but an HPD with a medium rate of IFB is likely to need replacing after one year.

The rate of IFB can be measured accurately since it gives characteristic signal clusters of five or more adjacent pixel hits, $200 - 300$ ns after the primary signal photoelectron has hit. The IFB rate is defined as the ratio of the number of large clusters to all of the clusters detected. It is initially measured in the test stations at Edinburgh, where a strobe-scan method has been developed. The decay between light pulses from a light emitting diode (LED) and the readout of the HPD is systematically varied while the rate of pixel clusters are recorded. The ratio of the number of delayed (IFB) clusters to the initial signal gives the IFB rate.

The rate of Ion Feedback is also monitored closely once the HPDs are installed in the RICH detectors. There is a continuous-wave (CW) laser installed in the LHCb cavern for this purpose. Studies have been carried out to ensure that data from the strobe-scan method can be compared directly with data from the CW laser [54]. The monitoring of the IFB using the CW laser is explained in more detail in next section.

3.3.2 Monitoring of Ion Feedback

The CW laser is installed in the LHCb cavern behind the shielding walls, and therefore does not need to be radiation hard. Optical fibres are used to transport the light to illuminate the HPD planes. Figure 3.13(a) shows all of the hits from a CW laser in run 75910 in July 2010. Figure 3.13(b) shows all of the hits classed as IFB hits in this run (those with 5 adjacent pixel hits). From these hitmaps it is clear that HPDs D0_10, D1_5 and U2_6 have a high IFB. In particular D1_5 is showing signs of a degrading photocathode which is clear from the lower occupancy in the centre of the image. All of the HPDs mentioned were replaced soon after this run was taken.

An IFB CW laser run can only be taken when the LHC is not running. Approximately once a month there will be a 'technical stop' in which test runs and various other maintenance can be carried out. This opportunity is taken for an IFB run, which can be analysed afterwards to extract the IFB rate at that time for each HPD.

The first IFB measurement is taken as soon as an HPD reaches Edinburgh to be tested, and is measured regularly over its lifetime. The IFB rate for each measurement is plotted on a timeline. For the majority of HPDs, the IFB rate

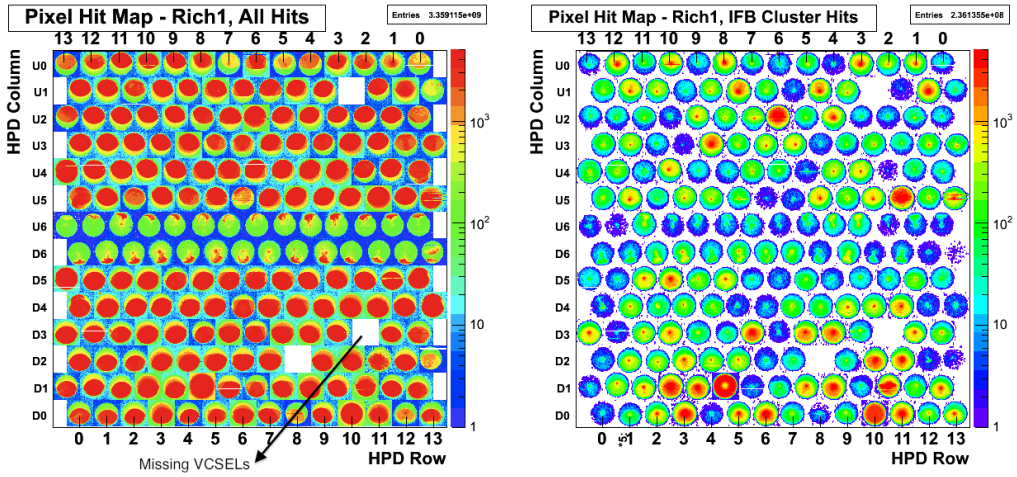

(a) All Hits (b) IFB Hits

Figure 3.13: Map of hits in RICH 1 during a laser run in July 2010, all clusters, and IFB hits.

of the HPDs increases approximately linearly over time (see for example Figure 3.14). Studies have shown that degradation of the photocathode begins when the IFB rate reaches approximately 5% [53]. By fitting a straight line to the timeline and extrapolating this to 5%, the date that the HPD is predicted to start degrading can be estimated. This has been shown to be a accurate and reliable prediction. Those HPDs soon to reach the 5% rate, are called 'at-risk'. The prediction enables the removal of at-risk HPDs from the RICH detectors before they start to degrade.

The RICH 2 detector can easily be accessed for the replacement of HPDs. This can be done within 2 days during any of the technical stops throughout the year. However, RICH 1 is harder to access and needs approximately 2 weeks for replacement of the HPDs. This can only be done at the yearly Christmas shutdown of the LHC which is specifically used for repair and maintenance of the detectors. The replacement plan is worked out according to the number of HPDs available to replace current HPDs. These are usually HPDs that have been repaired by being baked out at 300°C in vacuum, which removes most stray gas molecules. This can only be done a maximum of three times, before the anode may be damaged [53]. The replacement strategy gives priority to HPDs in the high occupancy region of the RICH detectors (the centre of the HPD plane). If

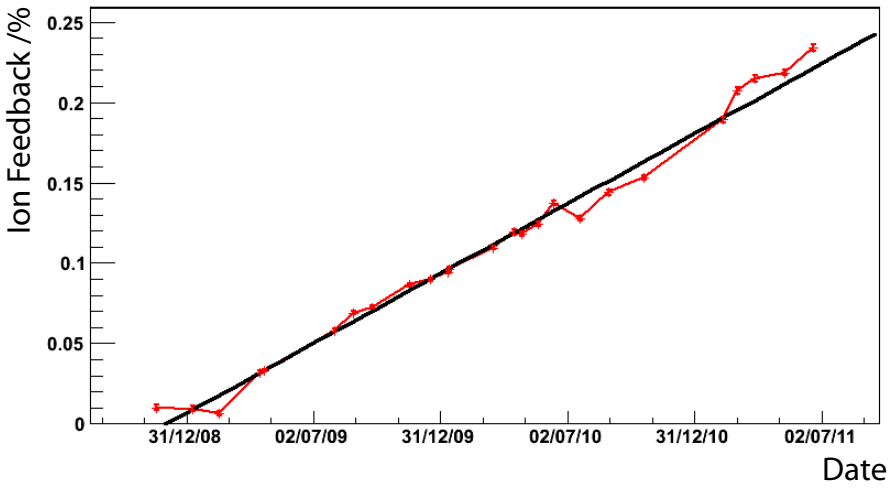

Figure 3.14: IFB timeline for HPD H714006. The y-axis is absolute date, and the x-axis is the rate of Ion Feedback. The black line is a linear best-fit line.

there are not enough HPDs to replace all of the at-risk IFB HPDs in the RICH detectors, anodes can be used to replace an HPD in the low occupancy area (the outside of the RICH 2 HPD plane) without significant loss to the PID performance of the RICH detectors. At the end of 2010, 18 HPDs were replaced in RICH 1 and 13 were replaced in RICH 2. At the end of 2011, 13 HPDs were replaced in RICH 1 and 22 HPDs were replaced in RICH 2. In RICH 2 there have been replacements of HPDs with anodes around the periphery due to there not being enough replacement HPDs.

3.3.3 Increased IFB gradient

As already mentioned an accurate prediction can be made of when the HPDs will begin to degrade, relying on the increase in IFB rate being linear. However approximately 20% of the total number of HPDs installed in the RICH detectors, when reviewed in May 2010, seemed to have experienced an increased IFB gradient in 2009, compared to 2008. An extreme example of such behaviour is shown in Figure 3.15. In order to study this behaviour, timelines for many HPDs were overlaid using two different schemes. The first plotting the absolute date and the second plotting the time elapsed since the HPD was manufactured. Depending on the behaviour in each graph, two things could be deduced:

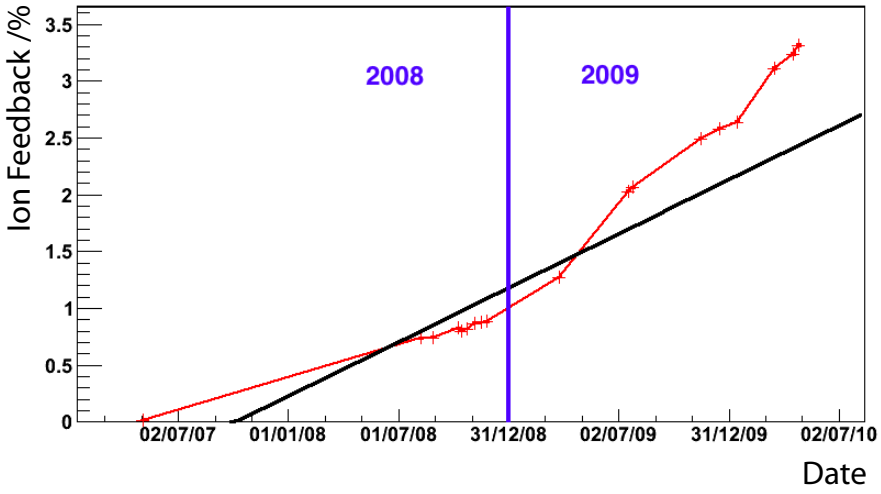

Figure 3.15: IFB timeline for HPD H708015. This is an extreme case where the IFB gradient increases from 2008 to 2009. The blue vertical line indicates the end of 2008. The black line is a linear best fit line.

- If a common pattern was seen in the absolute time plots, it could be deduced that the change in gradient was due to environmental effects within the detector,
- If a common pattern was seen in the elapsed time plots, it could be deduced that the absolute age of the HPD affects the IFB gradient.

Environmental stress in the LHCb pit is much worse than whilst the HPDs were being stored in Edinburgh at room temperature in a nitrogen-filled environment. In the LHCb cavern they are also in a nitrogen-filled environment but they are close to other subdetectors whose electronics are warm whilst in operation. Conversely, it has been shown that a high particle occupancy can decrease the IFB rate.

The HPDs were divided into RICH 1 and RICH 2, then into groups of approximately 20, each group having a certain range of IFB (measured in May 2010). These groups were then plotted together on the same graph. The timelines were plotted up until the technical shutdown at the end of 2010- when some HPDs were replaced. The 196 HPDs in RICH 1, HPDs were divided into 10 groups of HPDs, each increasing in the most recent IFB measurement. RICH 2 has 14 groups of a similar number.

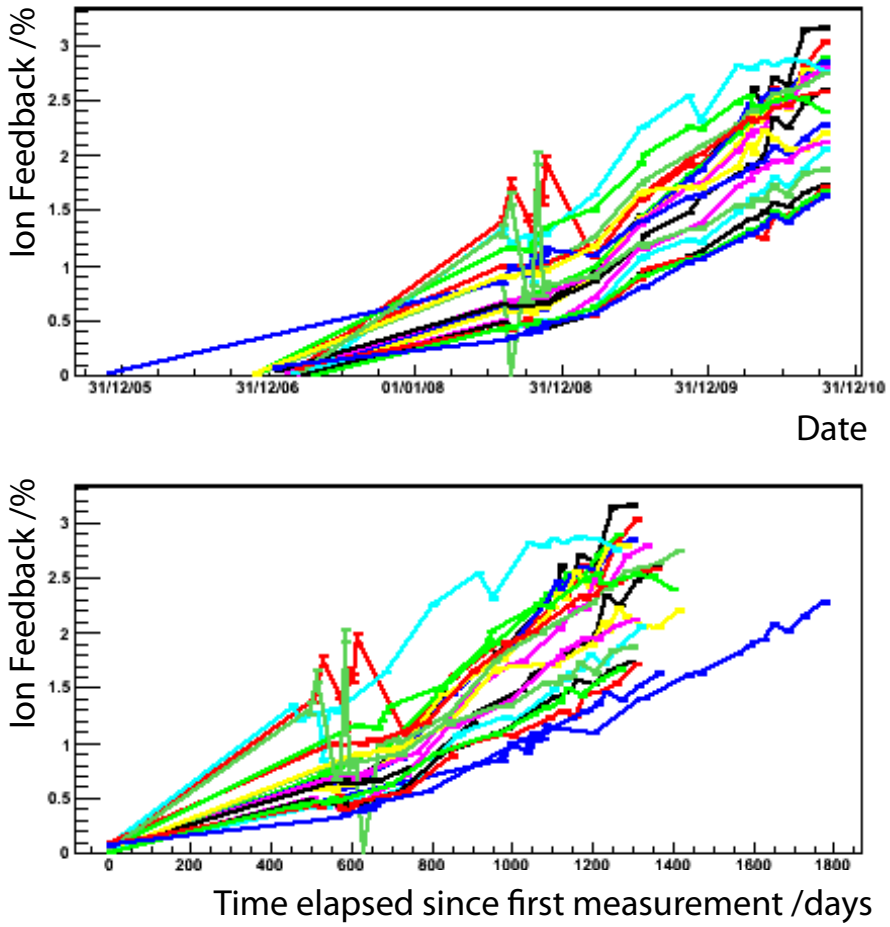

Figure 3.16: Showing IFB timelines of a high IFB group of HPDs, the upper plot against absolute date, and the lower showing time elapsed since the HPD was manufactured.

Figure 3.16 is typical of the timelines for High IFB HPDs. The upper plot, against absolute date shows two different gradients for the IFB increase. The first shows a steady increase until about the end of 2008, and the second has a relatively larger gradient until the end of 2010. The lower plot shows the IFB rate against the time elapsed since the first measurement was made. This is approximately equal to the time the HPD was manufactured, since they were sent to Edinburgh and measured for IFB soon after. The plots shows an approximately steady and linear increase in IFB as the HPD ages.

Groups of lower IFB HPDs were also studied, and the corresponding plots are shown in Figure 3.17 for one group. For this group, the increase in IFB is much less, and any patterns are harder to see. For most HPDs, there is not an obvious difference between the upper and lower plots. However there is still a hint that the gradient has increased after 2008. The RICH 2 timelines show a similar behaviour, for both high and low IFB HPDs. The rest of the timelines for the other IFB groups, and the RICH 2 timelines can be seen in Appendix A.

The HPD timelines for both of the RICH detectors, suggest that the increase in gradient that is seen in some HPDs, is more pronounced in higher IFB HPDs. In addition, the increased gradient is seen in the absolute time plots rather than the HPD age plots. This suggests that of the two scenarios hypothesised, the first is more likely: that the increased gradient in some of the HPDs is due to environmental or beam effects in the RICH detector.

3.3.4 Long IFB laser runs

Most IFB measurements are calculated using the first 3 million events from a laser run. Some extra long IFB laser runs were carried out, to verify this method. The dates and length of the runs studied are shown in Table 3.2. Several studies have been done using these long runs to gain some insight into the behaviour of the HPDs in the LHCb cavern.

- An initial study was carried out to check that the measurement of IFB made with the first 3 million events in a run was similar between different long laser runs. The logarithm of the IFB measurement for each HPD in two different runs were plotted against each other. This was done for all of the long runs. An example of these plots is shown in Figure 3.18 and it

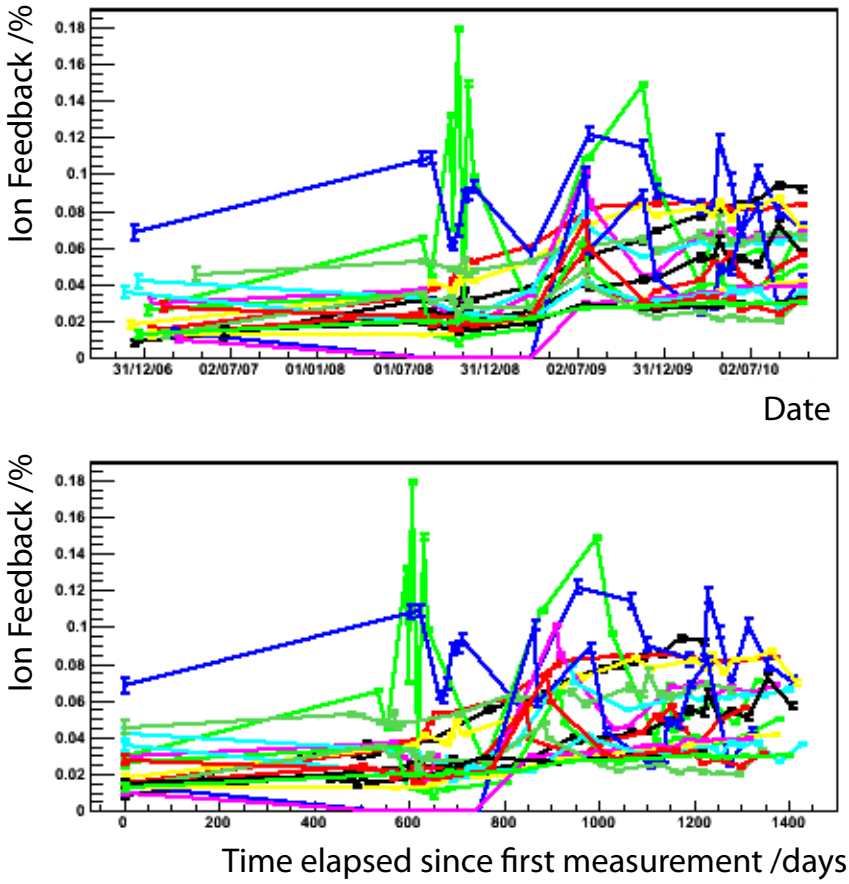

Figure 3.17: Showing timelines of a low IFB group of RICH 1 HPDs, the upper plot against absolute date and the lower showing time elapsed since the HPD was manufactured.

Run Number	Date Taken	Approximate Length /hours
35170	14/10/2008	16
36569	15/11/2008	46
37219	24/11/2008	20
48902	25/4/2009	23
61738	15/11/2009	15
73264 (plus preceding runs)	11/6/2010	89

Table 3.2: The run number of each Long laser run taken, the date of the run, and the length of it.

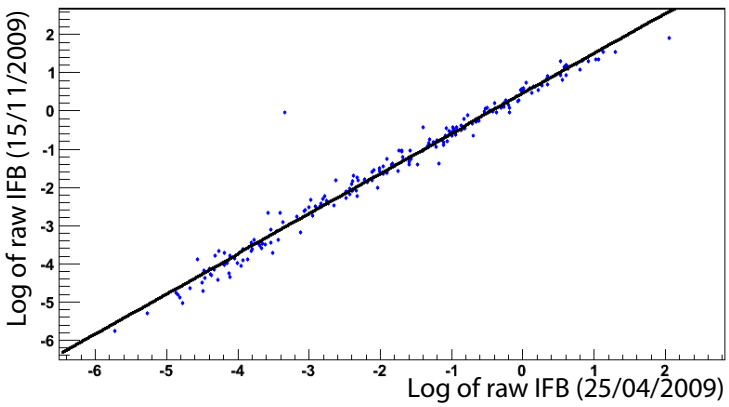

Figure 3.18: The logarithm of IFB measurements for two different runs in RICH 1 - run 48902 and 61738.

shows a high correlation, as expected. Plots for the other runs are shown in Appendix B. This helps to verify the method for calculating the IFB measurement.

- The IFB rate was then measured using separate slices of 3 million events across the run. For the majority of HPDs, the variation observed in measurements was small as expected. A typical timeline from run 73264 is shows in Figure 3.19. It was found however, that for some HPDs the IFB rate seemed to vary more than expected across these long runs. This variation is not conceivable for 'real' IFB change in such a limited amount of time, so there must be another cause. Typical HPDs with low IFB may increase in IFB by 0.5% per year. Over these long laser runs IFB appears to change by as much as 0.6% for a few HPDs. Studies were done for RICH 1 to see if a cause for this could be found. Figure 3.20 shows the range (difference between maximum and minimum value) of IFB for HPDs during run 37219. The majority of HPDs show a relatively small change in IFB of less than 0.02%. This is a typical histogram for all of the long laser runs taken (the rest of which can be seen in Appendix B).

- The IFB value across the long laser runs are plotted as a function of time and fitted linearly as in Figure 3.19. The gradient of this fit provides a means of quantifying the behaviour of the HPDs across the run. Despite many of the HPDs not showing a linear behaviour, it may show some insight into

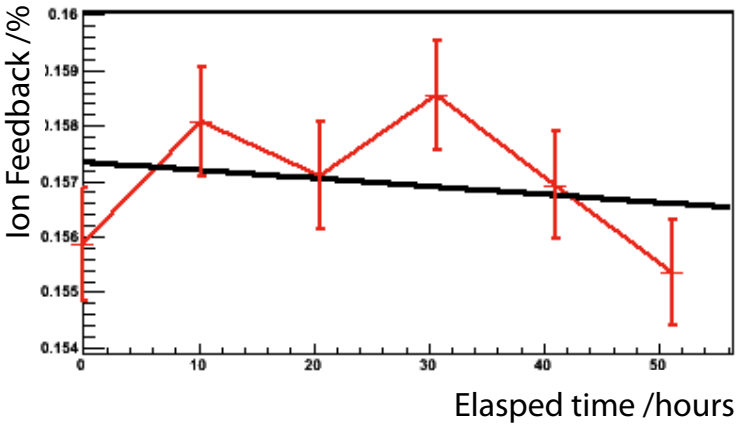

Figure 3.19: Typical IFB measurements taken over a long laser run 73264.

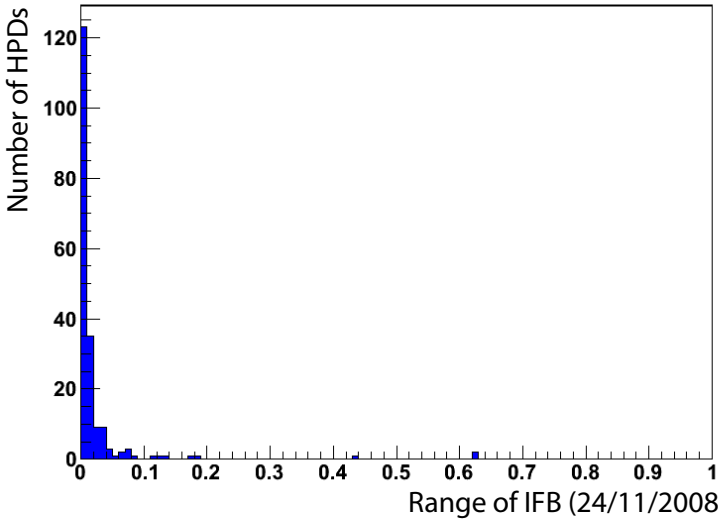

Figure 3.20: Histogram showing the range of IFB in RICH1 HPDs over run 37219 on 24/11/2008 which lasted approximately 20 hours.

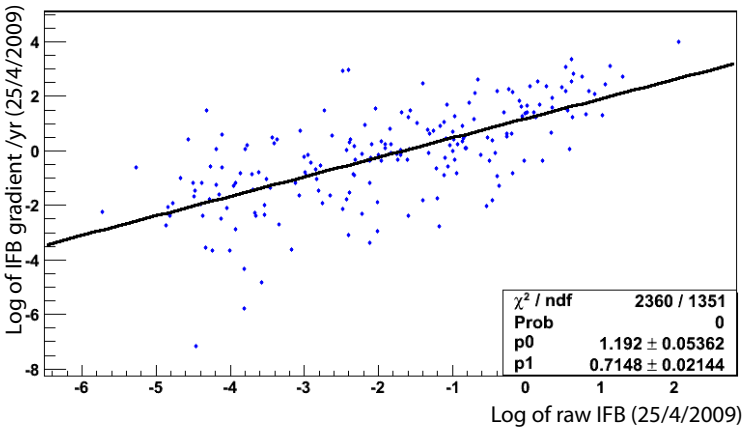

Figure 3.21: The logarithm of the IFB gradient against the logarithm of the IFB measurement in long run 48902.

Run	Gradient
35170	0.74
36569	0.68
37219	0.78
48902	0.71
61738	0.56
73264	0.53

Table 3.3: Gradient of the fit line when IFB is plotted against the IFB gradient for each long laser run in RICH 1.

the cause. The logarithm of the gradient was plotted against the logarithm of the IFB measurement from the same run, to see if the absolute value of the IFB has an effect on the change of IFB over a run. Such a plot is shown in Figure 3.21. There is a large variance but in general the high IFB HPDs seem to have a larger gradient value. Table 3.3 shows the gradient of the fit line for the same plot, for each long laser run separately. For example for run 48902, the gradient of the line in plot 3.21 is 0.71, as shown in the fourth column of Table 3.3. The values of the first four runs suggest there is some correlation between the amount the IFB changes over a long run, and the magnitude of the IFB itself. The final two runs do not show this correlation.

Run	#HPDs with +ve gradient	#HPDs with -ve gradient
35170	91	103
36569	104	90
37219	129	65
48902	107	89
61738	97	97
73264	85	108

Table 3.4: Number of HPDs with a negative or positing IFB gradient during long runs.

- Another interesting study was to look at whether HPDs have similar behaviour in each long laser run. In each run the number of HPDs with a positive/negative IFB gradient over the run was counted - see Table 3.4. However when looking in detail at these numbers it is clear that individual HPDs do not behave similarly in different long laser runs. For more details on this study see Appendix C.

- To investigate further whether the beam occupancy affects the IFB behaviour, the average cluster rate for each HPD was calculated and plotted. This is taken as a measure of the amount of light falling on the HPDs. Interestingly for some HPDs the IFB behaviour is directly correlated with the average cluster rate. Figure 3.22 shows the IFB rate and the average cluster rate over long run 35170 for two different HPDs. Figure 3.22(a) shows an HPD whose IFB seems to be correlated with the average cluster rate. Figure 3.22(b) shows an HPD that seems to have the opposite behaviour, and is anti-correlated with the average cluster rate. Table 3.5 shows how many HPDs out of 196 in each long laser run are either correlated or anti-correlated with the average cluster rate. On average approximately 30% of the HPDs are anti-correlated in each run, and only 6% are correlated. The remaining 64% are uncorrelated. A study was done to see whether for each long laser run, the same HPDs are correlated or anti-correlated with average cluster rate. The details of this study are in Appendix C and again suggest that HPDs do not seem to behave similarly between runs.

In conclusion, high IFB HPDs seem to be more likely to have a high gradient over a long laser run. However, no other patterns have yet been found to

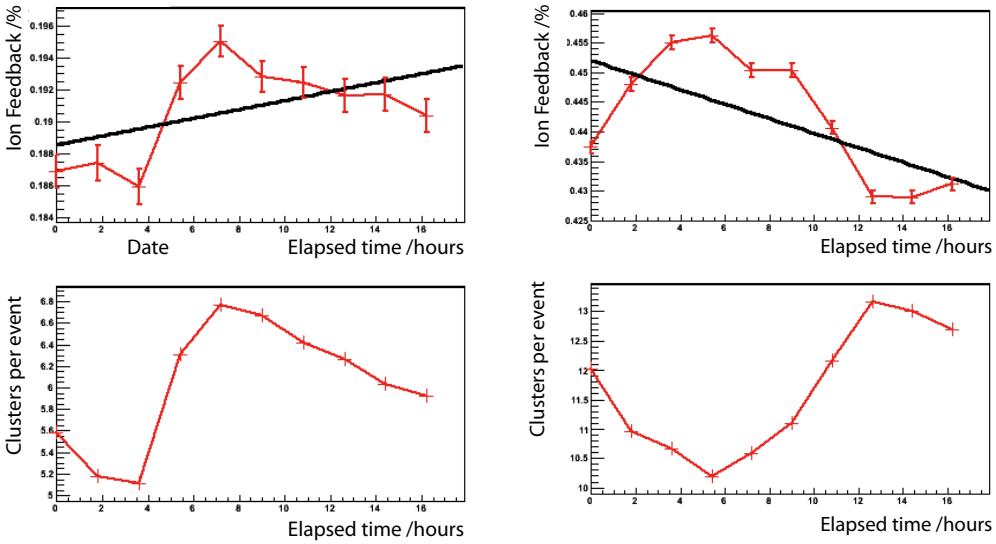

(a) HPD H703004 (b) HPD H627027

Figure 3.22: Behaviour of the IFB rate and the average cluster rate over a long run 35170 for two different HPDs.

Run	#HPDs varying with CR	#HPDs varying against CR
35170	11	81
37219	9	45
36569	12	51
48902	9	41
61738	19	51
73264	20	54

Table 3.5: Showing how many HPD's IFB is correlated or anti-correlated with the average cluster rate over each long-run.

explain the large change in measured IFB for some HPDs. HPDs do not seem to behave consistently between runs with respect to negative or positive gradients, or whether they are correlated with the occupancy level or not. Further work would include more investigation into the different conditions in the RICH detectors before and during the long laser runs, which may have an effect on the HPDs behaviour. Tests in laboratory conditions could be done with the strobe-scan method, whilst changing the environmental conditions to see if there was an effect on the IFB measurement.

3.4 Conclusions

The RICH detectors perform the essential task of identifying charged particles created from the proton-proton collisions of the LHC. Using radiators and arrays of Hybrid Photon Detectors they reconstruct the rings of photons produced and extract the velocity of the particles. They have been performing well in 2010 and 2011 with a good Cherenkov angle resolution and particle separation.

The monitoring of Ion Feedback using CW laser runs in the LHCb cavern enables the precise prediction of the degradation of HPDs so that they can be replaced when needed. Studies have been done to investigate the increased gradient that was seen in some HPDs between 2008 and 2009 and it was found to be due to the environment within the RICH detectors themselves. This highlights the importance of constant close monitoring of the HPDs.

Studies were also done into the unphysical behaviour for some HPDs when IFB measurements were taken over a long laser run. No obvious patterns were found over different runs to suggest that the HPDs themselves always behave in the same way. More investigation is needed to draw more conclusions from this. However, the reliability of taking the first 3 million events in an IFB run to predict the degradation of HPDs has been verified, and this method will continue to be used.

Chapter 4

Angular Analysis of $\mathbf{B^0 \to J/\psi(\mu^+\mu^-)K^{*0}(K^+\pi^-)}$

4.1 Introduction

An angular analysis of $B^0 \to J/\psi K^{*0}$ and its flavour conjugate is a sensitive probe of New Physics (NP). The Standard Model predicts that the amplitudes describing the decay are equal for the B^0 and $\overline{B}^0$ decays. Any deviation from this would be evidence for direct CP violation. Any limits found on CP violation would constrain extensions of the SM. In the following chapter the decay $B^0 \to J/\psi K^{*0}$ is described and the motivation for carrying out an analysis. The data sample and analysis methods are described in Chapter 5, and the results are presented and discussed in Chapter 6.

4.2 Description of $B^0 \to J/\psi K^{*0}$

$B^0 \to J/\psi K^{*0}$ is an interesting channel because it involves three kinds of mesons, one with a heavy quark and a light quark $B^0(d\bar{b})$, one with two heavy quarks $J/\psi(c\bar{c})$ and one with two light quarks $K^*(d\bar{s})$. $B^0 \to J/\psi K^{*0}$ is a colour-suppressed Cabibbo-favoured decay described primarily by the tree diagram shown in Figure 4.1(a). There is an internal W emission from a $\bar{b} \to \bar{c}$ transition, which produces a $c\bar{s}$ pair that associates with the $\bar{c}$ and d quarks to form colour singlets. There are also contributions from penguin amplitudes (see Figures 4.1(b) and 4.1(c)) but these are highly suppressed.

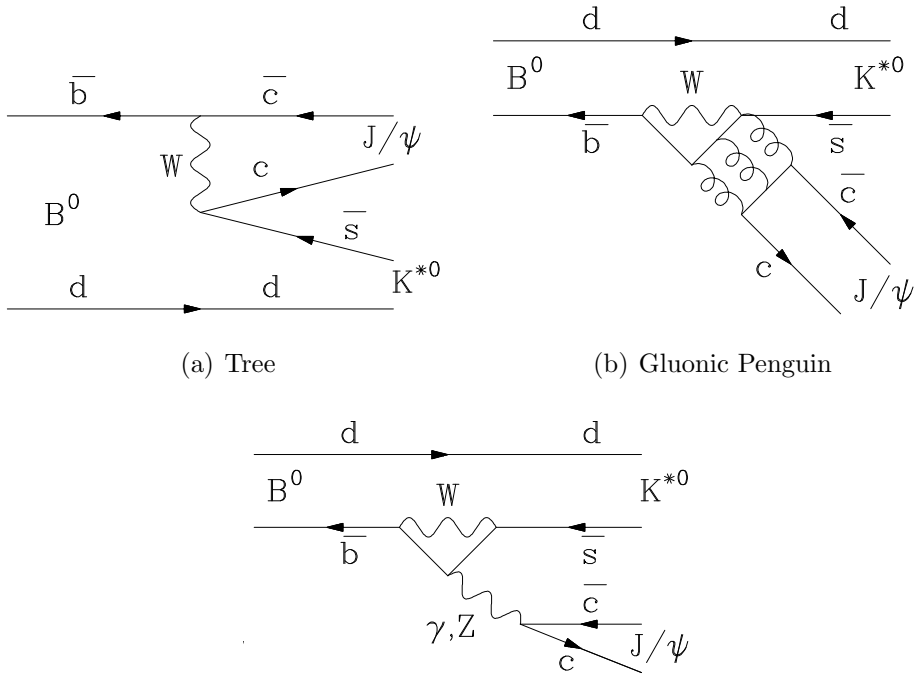

(a) Tree

(b) Gluonic Penguin

(c) Electroweak Penguin

Figure 4.1: Feynman diagrams contributing to $B^0 \to J/\psi K^{*0}$.

As already detailed in Chapter 1 (section 1.4) if the full decay amplitude of a decay is not equal to that of the conjugate, direct CP violation has occurred. It is possible to measure these amplitudes for $B^0 \to J/\psi K^{*0}$, but since the final state is an admixture of parity-odd and parity-even amplitudes a more sensitive probe of CP violation is to separate these out and measure them individually. The amplitude for any pseudoscalar to vector-vector decay can be written [55]:

$$A(B \to V_1 V_2) = A_0 \epsilon^{*L}_{V_1} \epsilon^{*L}_{V_2} - \frac{A_\parallel}{\sqrt{2}} \epsilon^{\vec{*}T}_{V_1} \cdot \epsilon^{\vec{*}T}_{V_2} - i \frac{A_\perp}{\sqrt{2}} \epsilon^{\vec{*}}_{V_1} \times \epsilon^{\vec{*}}_{V_2} \cdot \hat{\mathbf{p}} \qquad (4.1)$$

where $\epsilon^{\vec{}}_{V_2}$ and $\epsilon^{\vec{}}_{V_2}$ are the unit polarization vectors of V_1 and V_2 respectively and $\hat{\mathbf{p}}$ is the unit vector along the direction of motion of V_2 in the rest frame of V_1. The longitudinal unit polarization vector is $\epsilon^{*L}_{V_i} = \epsilon^{\vec{*}}_{V_i} \cdot \hat{\mathbf{p}}$ and the transverse unit polarization vector is $\epsilon^{\vec{*}T}_{V_i} = \epsilon^{\vec{*}}_{V_i} - \epsilon^{*L}_{V_i} \hat{\mathbf{p}}$. A_0 is for the case when both vectors have longitudinal polarization with respect to the direction of motion, and $A_\parallel$ and $A_\perp$ is when they are both transverse polarization, and are either parallel or perpendicular to each other. $A_\perp$ is therefore odd under the parity transformation because of the appearance of $\epsilon^{\vec{*}}_{V_1} \times \epsilon^{\vec{*}}_{V_2} \cdot \hat{\mathbf{p}}$, whereas $A_\parallel$ and A_0 are even. The amplitudes A_0, $A_\perp$ and $A_\parallel$ have relative orbital angular momentum $L = 0, 1, 2$ respectively, resulting in a zero total angular momentum to match the initial state.

The daughter K^* ($\overline{K^*}$) meson decays to $K^+\pi^-$ ($K^-\pi^+$), where this pair is an orbital P-wave amplitude. However in the vicinity of the K^* mass the $K\pi$ system can have contributions from the S-wave amplitude. This can be non-resonant or come from the tails of higher mass resonances. Only relative contributions of the amplitudes are measured so that $|A_0|^2 + |A_\parallel|^2 + |A_\perp|^2 + |A_S|^2 = 1$. The phases of the decay amplitudes are defined by: $A_j = |A_j| e^{i\delta_j}$ where $j = 0, \parallel, \perp, S$. Only the relative phase differences can be measured, so the convention $\delta_0 = 0$ is adopted.

The angular distributions of the decay products are different for each polarization amplitude, which means it is possible to separate them statistically. The angular distributions are described by three transversity angles [56]: θ, ψ and ϕ, which are defined in Figure 4.2. θ is the angle between μ^+ and the z-axis in the rest frame of the J/ψ meson. ϕ is the azimuthal angle of μ^+ in the same frame. ψ is the angle between the momentum vector of K^+ daughter and the negative momentum vector of the J/ψ in the K^* rest frame.

For a pseudoscalar to vector-vector decay, if there is no CP violation in mixing,

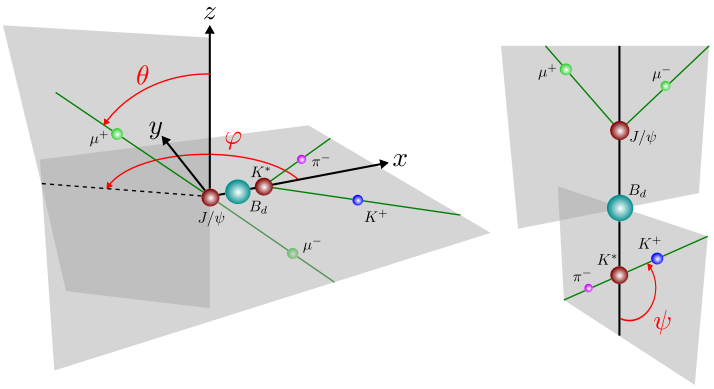

Figure 4.2: Shows the angular distribution of $B^0 \to J/\psi K^{*0}$. θ is the angle between the μ^+ and the z axis in the J/ψ rest frame. ϕ is the azimuthal angle of μ^+ in the same frame. ψ is the angle between the momentum of the K^+ and the negative momentum of the J/ψ in the $K^* \to K^+\pi^-$ rest frame.

$|p/q| = 1$, or in the decay, $A = \overline{A}$ (see equations 1.47 to 1.50), the time dependent decay rates can be expressed as [57]:

$$\frac{d^4\Gamma[B \to f]}{dtd\Omega} = |g_+(t)|^2 \times \{f_1|A_0|^2 + f_2|A_\parallel|^2 + f_3|A_\perp|^2 + f_4\Im(A_\parallel^* A_\perp) + f_5\Re(A_0^* A_\parallel) + f_6\Im(A_0^* A_\perp) + f_7|A_S|^2 + f_8\Re(A_\parallel^* A_S) + f_9(A_\perp^* A_S) + f_{10}(A_0^* A_S)\} \tag{4.2}$$

$$\frac{d^4\Gamma[\overline{B} \to \overline{f}]}{dtd\Omega} = |g_+(t)|^2 \times \{f_1|A_0|^2 + f_2|A_\parallel|^2 + f_3|A_\perp|^2 - f_4\Im(A_\parallel^* A_\perp) + f_5\Re(A_0^* A_\parallel) - f_6\Im(A_0^* A_\perp) + f_7|A_S|^2 + f_8\Re(A_\parallel^* A_S) - f_9(A_\perp^* A_S) + f_{10}(A_0^* A_S)\} \tag{4.3}$$

$$\frac{d^4\Gamma[B \to \overline{f}]}{dtd\Omega} = |g_-(t)|^2 \times \{f_1|A_0|^2 + f_2|A_\parallel|^2 + f_3|A_\perp|^2 + f_4\Im(A_\parallel^* A_\perp) + f_5\Re(A_0^* A_\parallel) + f_6\Im(A_0^* A_\perp) + f_7|A_S|^2 + f_8\Re(A_\parallel^* A_S) + f_9(A_\perp^* A_S) + f_{10}(A_0^* A_S)\} \tag{4.4}$$

$$\frac{d^3\Gamma[\overline{B} \to f]}{d\Omega} =$$
$$|g_-(t)|^2 \times \{f_1|A_0|^2 + f_2|A_\parallel|^2 + f_3|A_\perp|^2 - f_4\Im(A_\parallel^* A_\perp) + f_5\Re(A_0^* A_\parallel) - f_6\Im(A_0^* A_\perp)$$
$$+f_7|A_S|^2 + f_8\Re(A_\parallel^* A_S) - f_9(A_\perp^* A_S) + f_{10}(A_0^* A_S)\} \tag{4.5}$$

where $\Omega = (\cos\psi, \cos\theta, \phi)$. The amplitudes are time-independent as can be seen in Table 4.1. The angular dependent functions f_i are given in Table 4.2. The time dependent functions $|g_\pm(t)|^2$ are defined as:

$$|g_\pm(t)|^2 = \frac{e^{-\Gamma_0 t}}{2}\left[\cosh\left(\frac{\Delta\Gamma_d t}{2}\right) \pm \cos(\Delta m_d t)\right] \tag{4.6}$$

$\Gamma_d = 1/\tau_{B^0}$ is the total decay width of the B^0 meson, Γ_H and Γ_L are the decay widths of the heavy and light states. $\Gamma_d = (\Gamma_H + \Gamma_L)/2$, $\Delta\Gamma_d = \Gamma_H - \Gamma_L$, $\Delta m_d = m_H - m_L$. The decay width difference between the B^0 and $\overline{B}^0$ is negligible so the expressions simplify to:

$$\begin{aligned} |g_+(t)|^2 &= \cos^2\left(\frac{\Delta m_d t}{2}\right) e^{-\Gamma_d t} \\ |g_-(t)|^2 &= \sin^2\left(\frac{\Delta m_d t}{2}\right) e^{-\Gamma_d t} \end{aligned} \tag{4.7}$$

$B^0 \to J/\psi K^{*0}$ has a flavour specific final state and the analysis is performed untagged. The production asymmetry for pp collisions at the LHC for $B^0 \to J/\psi K^{*0}$ is expected to be negligible and has been measured to be approximately 1% [58], favouring the B^0 over the $\overline{B^0}$ decay. It has been verified that this does not have a significant effect on the measurement of the polarisation amplitudes. A production asymmetry was introduced to a fully simulated Monte Carlo sample, which included mixing, and the full analysis was performed on it. No significant differences were seen for either a 10% or 1% production asymmetry. It is therefore possible to take the sum of equations 4.2 to 4.5 to give the total time-dependent angular distribution:

$$\begin{aligned}
&\frac{d^4\Gamma(B \to J/\psi K^*(\to K^\pm\pi^\mp)}{dtd\Omega)} \\
&= e^{-\Gamma_d t}[f_1(\Omega)|A_0(0)|^2 + f_2(\Omega)|A_\parallel(0)|^2 + f_3(\Omega)|A_\perp(0)|^2 \\
&\pm f_4(\Omega)\Im(A_\parallel^*(0)A_\perp(0))) \\
&+ f_5(\Omega)\Re(A_0(0)A_\parallel(0)| \\
&\pm f_6(\Omega)\Re(A_0(0)A_\perp(0)) \\
&+ f_7(\Omega)|A_s(0)|^2 + f_8(\Omega)\Re(A_s(0)^*A_\parallel(0)) \\
&\pm f_9(\Omega)\Im(A_s(0)^*A_\perp(0)) + f_{10}\Re(A_S(0)^*A_0(0))]
\end{aligned} \tag{4.8}$$

The signs of the terms containing f_4, f_6 and f_9 change sign depending on whether the case is for B^0 or $\overline{B}^0$.

Amplitude term	Explicit expression
$\|A_0(t)\|^2$	$\|A_0(0)\|^2$
$\|A_\parallel(t)\|^2$	$\|A_\parallel(0)\|^2$
$\|A_\perp(t)\|^2$	$\|A_\perp(0)\|^2$
$\|A_s(t)\|^2$	$\|A_s(0)\|^2$
$\Im(A_\parallel^* A_\perp)$	$\|A_\parallel(0)\|\|A_\perp(0)\|\sin(\delta_\perp - \delta_\parallel)$
$\Re(A_0^* A_\parallel)$	$\|A_0(0)\|\|A_\parallel(0)\|\cos(\delta_\parallel)$
$\Im(A_0^* A_\perp)$	$\|A_0(0)\|\|A_\perp(0)\|\sin(\delta_\perp)$
$\Re(A_\parallel^* A_S)$	$\|A_\parallel(0)\|\|A_S(0)\|\cos(\delta_\parallel - \delta_S)$
$\Im(A_\perp^* A_S)$	$\|A_\perp(0)\|\|A_S(0)\|\sin(\delta_\perp - \delta_S)$
$\Re(A_0^* A_S)$	$\|A_0(0)\|\|A_S(0)\|\cos(\delta_S)$

Table 4.1: Explicit expressions of the polarization amplitude terms including the phases. δ_0 is set to zero, so is not included.

4.3 Motivation

This section will describe the motivations for an angular analysis of $\mathrm{B}^0 \to J/\psi K^*$, including those in the past and how they have changed. A summary of these is

i	$f_i(\Omega = \cos\psi, \cos\theta, \phi)$
1	$\frac{9}{32\pi} 2\ \cos^2\psi(1 - \sin^2\theta\ \cos^2\phi)$
2	$\frac{9}{32\pi}\ \sin^2\psi(1 - \sin^2\theta\ \sin^2\phi)$
3	$\frac{9}{32\pi}\ \sin^2\psi\ \sin^2\theta$
4	$-\frac{9}{32\pi}\ \sin^2\psi\ \sin 2\theta\ \sin\phi$
5	$\frac{9}{32\pi\sqrt{2}}\ \sin 2\psi\ \sin^2\theta\ \sin 2\phi$
6	$\frac{9}{32\pi\sqrt{2}}\ \sin\ 2\psi\ \sin\ 2\theta\ \cos\ \phi$
7	$\frac{3}{32\pi} 2(1 -\ \sin^2\psi\ \cos^2\theta)$
8	$\frac{3}{32\pi}\sqrt{6}\ \sin\psi\ \sin^2\theta\ \sin 2\phi$
9	$\frac{3}{32\pi}\sqrt{6}\ \sin\psi\ \sin 2\theta\ \cos\phi$
10	$\frac{3}{32\pi} 4\sqrt{3}\ \cos\psi(1 -\ \sin^2\theta\ \cos^2\phi)$

Table 4.2: Angular dependencies of the amplitudes.

Past motivation	Factorization hypothesis Ambiguity-free measurement of $\sin 2\beta$
Present motivation	Search for New Physics Triple Product asymmetries Control Channel for $B_s^0 \to J/\psi\phi$ Cross-check for $B_s^0 \to J/\psi\phi$

Table 4.3: Summary table of past and present motivation for the angular analysis of $B^0 \to J/\psi K^{*0}$

shown in Table 4.3.

4.3.1 History of the motivation for $B^0 \to J/\psi K^{*0}$

Factorization The angular analysis of $B^0 \to J/\psi K^{*0}$ was first performed in 1994 at the CLEO II experiment at CESR [59] and at the ARGUS experiment at DORIS II [60]. At this time the main motivation for this analysis was a test of the factorization hypothesis in decays with an internal W emission. Naive factorization assumes that two body hadronic decays of B mesons can be expressed as the product of two hadronic currents. This was very successful for the prediction of decays where the products of the W^- are well separated from

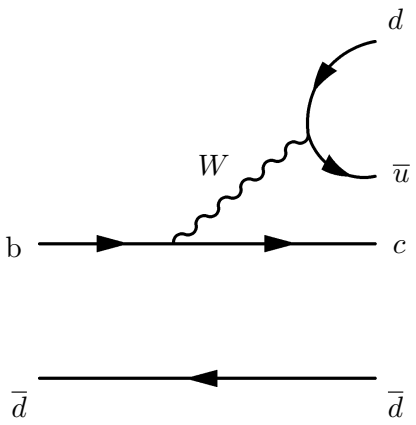

Figure 4.3: Feynman diagram of the decay $B^0(b\overline{d}) \rightarrow D^+(c\overline{d})\pi^-(d\overline{u})$. This decay is well described by naive factorization because the decay products are well separated and do not interact with each other.

the other decay products [61]. An example of this is the $B^0 \rightarrow D^+\pi^-$ decay shown in Figure 4.3. In this decay the π^+ is formed from the quarks of the W boson (the $d\overline{u}$ quarks) and the D^+ meson is formed from the converted b quark and the spectator $\overline{d}$. For colour-suppressed decays, one of the mesons is formed from the converted $\overline{b}$ quark and a quark from the W, and the other is formed from the remaining quark from the W combined with the spectator quark. In this case the decay products are not well separated, final state interactions can occur, which would mean naive factorization would not describe the decay well [62]. This is the case for $B^0 \rightarrow J/\psi K^{*0}$ as seen in Figure 4.1(a). If there are no final-state interactions, the P-wave and S-wave phases are simply phase shifts in $K\pi$ scattering at the appropriate invariant mass (taking the $K\pi$ scattering to be inelastic in that range). The measured phases would be equal 0 or π [63] which provides a test of the factorization hypothesis. It can also be tested through the measurement of Branching Ratios which are affected by QCD corrections such as $R = \mathcal{B}(B \rightarrow J/\psi K^*)/\mathcal{B}(B \rightarrow J/\psi K)$, or through measuring the longitudinal polarization fraction ($|A_0|^2$) in decays to two vector mesons.

The first measurements done by CLEO and ARGUS for $B^0 \rightarrow J/\psi K^{*0}$ observed a value of $0.80 \pm 0.08 \pm 0.05$ for $|A_0|^2$ (CLEO) [59]. In 1997 CLEO updated this measurement, reducing it to $0.52 \pm 0.07 \pm 0.04$, becoming more consistent with the naive factorization hypothesis. However, the branching ratio

Model	$\|A_0\|^2$	R
Neubert et al (1991). [64]	0.35	1.61
Deandrea et al (1993). [65]	0.36	1.50
Aleksan et al (1995). [66]	0.45	2.15
CLEO [67]	$0.52 \pm 0.07 \pm 0.04$	$1.45 \pm 0.20 \pm 0.17$

Table 4.4: Predicted values of the longitudinal polarization fraction as well as the ratio $R = \mathcal{B}(B \to J/\psi K^*)/\mathcal{B}(B \to J/\psi K)$, using various models of Naive factorization. The CLEO experimental result is also shown.

$R = \mathcal{B}(B \to J/\psi K^*)/\mathcal{B}(B \to J/\psi K)$ calculated was inconsistent with the same prediction models. Both of these observed values from CLEO are shown in Table 4.4 along with the prediction of three slightly different models for $|A_0|^2$ and R[1]. They all use form-factor models and include heavy meson to light meson scaling. The model by Neubert et al appears to predict $|A_0|^2$ to be too small, and R to be too large. Deandrea et al use experimental data as input to their calculations and have a result closer to the experimental one. Aleksan et al introduce further corrections and get a prediction closer to the experimental value of the longitudinal polarisation, but which deviates from the value for R.

The CLEO measurement of the strong phases deviated slightly from π which indicated that final state interactions were occurring to some extent. By 2002 CDF [68], BaBar [69] and Belle [70] had also done measurements of the angular amplitudes and phases of the decay. The results confirmed the existence of final state interactions, but $|A_0|^2$ seemed to be again deviating further from naive factorization predictions ($0.597 \pm 0.028 \pm 0.024$ [69]).

Papers began to emerge which incorporated QCD corrections into the factorization hypothesis. These took into account non-factorizable terms which are dependent on the polarization of the final state [71] [72]. The values predicted using QCD factorization with one particular model [73], along with the most recent experimental values are shown in Table 4.5. Other form factor models have very similar values to this [74]. All of the experimental results shown are consistent with one another, supporting their reliability. The predicted value for $|A_0|^2$ is not dissimilar to the naive factorization values and is inconsistent with the most precise measured value from BaBar of $0.556 \pm 0.009 \pm 0.010$. $|A_\parallel|^2$ is

[1]Note these are quoted for historical reasons and are not the most recent calculations

close to the measured values but $|A_\perp|^2$ is still inconsistent. The strong phases are consistent with the predicted values, showing that the final state interactions have been taken into account. It has been suggested that one of the charm quarks in the final state could emit a gluon before forming the J/ψ meson which may fragment into a parton of the K meson. The gluon would be longitudinally polarized and contribute to $|A_0|^2$, improving the prediction [71].

There are new models for factorization available for example using perturbative QCD which may improve predictions for this decay. Calculations have been carried out for other channels such as $B \to K^\pm\pi^\mp$ but not yet for $B^0 \to J/\psi K^{*0}$.

Ambiguity free measurement of $\sin 2\beta$ Another goal was to resolve the ambiguity in the CP violating parameter $\sin 2\beta$ using the decay $\mathrm{B}^0 \to J/\psi(\to \mu^+\mu^-)K^{*0}(\to K_S\pi^0)$. Both the B^0 and $\overline{B}^0$ decay to the same final state which makes it a CP eigenstate. As described in section 1.4 this means there could be interference between mixing and decay. The time dependent angular distribution is similar to that of $B^0 \to J/\psi K^{*0}$ ($K^* \to K^+\pi^-$). The S-wave component has been neglected in analyses of this channel due to limited statistics, so only the first six terms are relevant:

$$\begin{aligned}\frac{d^4\Gamma(B \to J/\psi K^*(\to K_S\pi^0))}{dt\,d(\cos\theta)\,d\phi\,d(\cos\psi)} = \\ = e^{-\Gamma_d t}[f_1(\Omega)|A_0(t)|^2 + f_2(\Omega)|A_\parallel(t)|^2 + f_3(\Omega)|A_\perp(t)|^2 \\ \pm f_4(\Omega)\Im(A_\parallel^*(t)A_\perp(t)) \\ + f_5(\Omega)\Re(A_0(t)A_\parallel(t)) \\ \pm f_6(\Omega)\Re(A_0(t)A_\perp(t))]\end{aligned} \tag{4.9}$$

The amplitude terms are given in Table 4.6. They are now time dependent due to the interference between mixing and decay. Note the presence of $\cos 2\beta$ in the interference terms between the amplitudes of opposite parity. This can be extracted via an angular analysis which has been carried out by BaBar [80] and Belle [79]. The ambiguity in the measurement of $\sin 2\beta$ needed to be resolved to check that the results were consistent with the SM. The interference between the S-wave and P-wave amplitudes in the decay channel $B^0 \to J/\psi K^{*0}$ ($\to K^+\pi^-$) was also used by BaBar to resolve this ambiguity. This method is explained

	MS [73]	CDF Result (2007) [76]	D0 Result (2009) [77]	BaBar Result (2007) [78]	Belle Results (2005) [79]	LHCb Result [75] (2011)
$\lvert A_\parallel \rvert^2$	0.25	$0.211 \pm 0.012 \pm 0.006$	$0.230 \pm 0.013 \pm 0.025$	$0.211 \pm 0.010 \pm 0.006$	$0.231 \pm 0.012 \pm 0.008$	$0.253 \pm 0.020 \pm 0.016$
$\lvert A_\perp \rvert^2$	0.35	$0.220 \pm 0.015 \pm 0.011^*$	$0.183 \pm 0.017 \pm 0.028^*$	$0.233 \pm 0.010 \pm 0.005$	$0.195 \pm 0.012 \pm 0.008$	$0.191 \pm 0.019 \pm 0.017$
$\lvert A_0 \rvert^2$	0.40	$0.569 \pm 0.009 \pm 0.009$	$0.587 \pm 0.011 \pm 0.013$	$0.556 \pm 0.009 \pm 0.010$	$0.574 \pm 0.012 \pm 0.009$	$0.556 \pm 0.028 \pm 0.023^*$
$\delta_\parallel$	-3.05	$-2.96 \pm 0.08 \pm 0.03$	-	$-2.93 \pm 0.08 \pm 0.04$	$-2.887 \pm 0.090 \pm 0.008$	$-2.87 \pm 0.11 \pm 0.10$
$\delta_\perp$	3.08	$2.97 \pm 0.06 \pm 0.01$	-	$2.91 \pm 0.05 \pm 0.03$	$2.938 \pm 0.064 \pm 0.010$	$3.02 \pm 0.09 \pm 0.07$

Table 4.5: Previous results for polarization amplitudes and phases. None include the S-wave contribution, but do include it as a systematic uncertainty. The measurements with a * have been calculated from results of the other amplitudes, the errors have been propagated.

Amplitude term	Time dependent expression
$\|A_0(t)\|^2$	$\|A_0\|^2 e^{-\Gamma_d t}\left[1 \pm \sin(2\beta)\sin(\Delta m_d t)\right]$
$\|A_\parallel(t)\|^2$	$\|A_\parallel\|^2 e^{-\Gamma_d t}\left[1 \pm \sin(2\beta)\sin(\Delta m_d t)\right]$
$\|A_\perp(t)\|^2$	$\|A_\perp\|^2 e^{-\Gamma_d t}\left[1 \mp \sin(2\beta)\sin(\Delta m_d t)\right]$
$\Im(A_\parallel^* A_\perp)$	$\pm\|A_\parallel\|\|A_\perp\| e^{-\Gamma_d t}\left[\sin(\delta_\perp - \delta_\parallel)\cos(\Delta m_d t) - \cos(\delta_\perp - \delta_\parallel)\cos(2\beta)\sin(\Delta m_d t)\right]$
$\Re(A_0^* A_\parallel)$	$\|A_0\|\|A_\parallel\|\cos(\delta_\parallel) e^{-\Gamma_d t}\left[1 \pm \sin(2\beta)\sin(\Delta m_d t)\right]$
$\Im(A_0^* A_\perp)$	$\pm\|A_0\|\|A_\perp\| e^{-\Gamma_d t}\left[\sin(\delta_\perp)\cos(\Delta m_d t) - \cos(\delta_\perp)\cos(2\beta)\sin(\Delta m_d t)\right]$

Table 4.6: Amplitude terms for $B^0 \to J/\psi K^{*0}$ ($K^* \to K_S\pi^0$). δ_0 is set to zero by convention.

further later in this Chapter. The measurements by BaBar and Belle of $\sin 2\beta$ are so far consistent with the SM-based fits of the CKM triangle (see the current constraints in Figure 1.7).

Even though the understanding of the factorization could still be improved, it is no longer a main motivation for the analysis of this decay channel, nor is the resolution of the ambiguity in $\cos 2\beta$. The present motives for studying this channel are detailed in the following sections.

4.3.2 Current Motivation for $B^0 \to J/\psi K^{*0}$

Searching for New Physics As already mentioned, in the SM $B^0 \to J/\psi K^{*0}$ is assumed to be dominated by a tree-level diagram and to have a negligible contribution from electroweak and gluonic penguin decays (see Figure 4.1). The penguin contributions can be calculated from Wilson coefficient functions and non-pertubative hadronic matrix elements. When calculated with the former a negligible contribution is found, however the latter is associated with large uncertainties. From an analysis of $B^0 \to J/\psi\pi^0$ decays, penguin uncertainties in $B_s \to J/\psi\phi$ as large as $\mathcal{O}(10\%)$ are not ruled out [81]. This would be similar for $B^0 \to J/\psi K^{*0}$.

New Physics (NP) could affect the decay amplitude at loop level. Examples of such NP models include non-minimal supersymmetric models, and models with Z-mediated flavour-changing neutral currents [82]. The observation of direct CP-violation in B-meson decays is crucial in establishing the mechanism of CP violation. Limits on this would constrain extensions to the SM [83]. Any large

asymmetries observed between the B^0 and $\overline{B}^0$ decays would be evidence for NP. The full amplitude of $B^0 \to J/\psi K^{*0}$ ($B \to f$) would become [84]:

$$A(B \to f) = ae^{-i\delta^a} + be^{i\phi}e^{i\delta^b} \tag{4.10}$$

where a and b are the two amplitudes and $\delta^{a,b}$ are the respective strong phases. The two amplitudes could be the tree and penguin amplitudes in the SM, or could be the SM tree and a larger NP amplitude. The weak phase is set to be zero for the first contribution, and ϕ for the second one, because only a relative phase is measured. For the CP conjugate decay $\overline{B} \to \overline{f}$ the amplitude is given by changing the sign of the weak phase ϕ. The direct integral asymmetry is then obtained by:

$$\begin{aligned} a_{dir}^{CP} &= \frac{\Gamma(B \to f) - \Gamma(\overline{B} \to \overline{f})}{\Gamma(B \to f) + \Gamma(\overline{B} \to \overline{f})} \\ &= \frac{2ab\sin(\delta^a - \delta^b)\sin(\phi)}{a^2 + b^2 + 2ab\cos(\delta^a - \delta^b)\cos(\phi)} \end{aligned} \tag{4.11}$$

It is clear from this that an observable direct asymmetry requires not only a non-zero weak phase difference between the two decay amplitudes, but also a non-zero strong phase difference. Since the b quark is relatively heavy, the strong phases are predicted to be quite small. If the different strong phases are close to equal there will be no observable signal of direct asymmetry, even if NP is present [85]. In order to observe NP effects it is possible to instead look at the helicity amplitudes. Analogous to equation 4.10:

$$\begin{aligned} A(B \to J/\psi K^*) &= a_\lambda e^{i\delta_\lambda^a} + b_\lambda e^{i\phi} e^{i\delta_\lambda^b} \\ A(\overline{B} \to J/\psi \overline{K}^*) &= a_\lambda e^{i\delta_\lambda^a} + b_\lambda e^{-i\phi} e^{i\delta_\lambda^b} \end{aligned} \tag{4.12}$$

where a_λ and b_λ are the two different amplitudes and $\delta_\lambda^{a,b}$ are their strong phases. The full amplitude becomes (not including the S-wave component):

$$\begin{aligned} A(B \to J/\psi K^*) &= A_0 g_0 + A_\parallel g_\parallel + iA_\perp g_\perp \\ A(\overline{B} \to J/\psi \overline{K}^*) &= \overline{A}_0 g_0 + \overline{A}_\parallel g_\parallel - i\overline{A}_\perp g_\perp \end{aligned} \tag{4.13}$$

Parameter	B^0	$\overline{B}^0$
$A_\parallel$	0.216 ± 0.017	0.244 ± 0.018
$A_\perp$	0.213 ± 0.017	0.178 ± 0.017
A_0	0.571 ± 0.015	0.578 ± 0.016
$\delta_\parallel$	-2.934 ± 0.134	-2.851 ± 0.114
$\delta_\perp$	2.878 ± 0.088	2.993 ± 0.089

Table 4.7: Polarization amplitudes for $B^0 \to J/\psi K^{*0}$ from Belle [79] for B^0 and $\overline{B}^0$ decays separately. No evidence of direct CP violation is observed.

where g_λ are the coefficients of the amplitudes. When no direct CP violation occurs [86]:

$$|A_0|^2 + |A_\perp|^2 + |A_\parallel|^2 = |\overline{A}_0|^2 + |\overline{A}_\perp|^2 + |\overline{A}_\parallel|^2 \tag{4.14}$$

but CP violation may be detected in decay rates for individual transversity amplitudes i.e. $|A_k|^2 \neq |\overline{A}_k|^2 (k = 0, \parallel, \perp)$. Any significant deviation from this would be a clear signal of NP [82] [87] [88].

Direct CP violation in $B^0 \to J/\psi K^{*0}$ has been studied by Belle, by measuring the polarization amplitudes between B^0 and $\overline{B}^0$ decays separately [79]. The results are shown in Table 4.7 where it can be seen that no direct CP violation was observed.

Triple Product asymmetries It has been pointed out [89] that as well as the individual polarization amplitudes, the quantities $\Im(A_\perp A_0^* - \overline{A}_\perp \overline{A}_0^*)$ and $\Im(A_\perp A_\parallel^* - \overline{A}_\perp \overline{A}_\parallel^*)$ are also CP violating, and do not require non-zero phases. These occur in triple product asymmetries [86].

The triple product correlation can be extracted from the measured decay amplitudes. They take the form $\vec{p} \cdot (\vec{v}_1 \times \vec{v}_2)$ in the B^0 rest frame where $\vec{p}$ is the momentum of the J/ψ or K^* and $\vec{v}_1(\vec{v}_2)$ is the polarization vector of $J/\psi(K^*)$ [89]. They are odd under time reversal (T-odd) and their asymmetries are sensitive to direct CP violation. The asymmetries are defined using the decay amplitudes as:

$A_T^{(1)}$	$0.091 \pm 0.034 \pm 0.007$
$A_T^{(2)}$	$-0.098 \pm 0.032 \pm 0.003$
$\overline{A}_T^{(1)}$	$0.047 \pm 0.031 \pm 0.007$
$\overline{A}_T^{(2)}$	$-0.089 \pm 0.029 \pm 0.003$
$\lvert A_T^{(1)} - \overline{A}_T^{(1)} \rvert$	0.044 ± 0.046
$\lvert A_T^{(2)} - \overline{A}_T^{(2)} \rvert$	0.009 ± 0.043

Table 4.8: Measured triple product asymmetries for $B^0 \to J/\psi K^{*0}$ from Belle [79]. The first error is statistical and the second is systematic.

$$A_T^{(1)} = \frac{\Im(A_\perp A_0^*)}{A_0^2 + A_\parallel^2 + A_\perp^2}$$
$$A_T^{(2)} = \frac{\Im(A_\perp A_\parallel^*)}{A_0^2 + A_\parallel^2 + A_\perp^2} \tag{4.15}$$

The corresponding asymmetries for $\overline{B}^0$ decays are defined as $\overline{A}_T^{(1)}$ and $\overline{A}_T^{(2)}$. The SM predicts no difference between B^0 and $\overline{B}$ mesons. Belle has measured the triple product asymmetries for $B^0 \to J/\psi K^{*0}$ and the results are shown in Table 4.8. All measured asymmetries are small. No difference between the asymmetries for B^0 and $\overline{B}^0$ mesons is observed, consistent with the absence of T-odd CP violation.

S-wave contribution Most previous experiments have not measured the S-wave fraction. BaBar however has done an analysis of $B_d \to J/\psi K\pi$ including the S-wave amplitude, and measuring the $K\pi$ mass dependence of its phase difference with respect to the P-wave. They show that including a $K\pi$ S-wave with a significant S-P interference is required to describe the data. Integrated over the range $0.8 < m_{K\pi} < 1.0\,\mathrm{GeV/c^2}$ they find an S-wave fraction of $(7.3 \pm 1.8\%)$ [80]. They also see a large variation of the S-wave phase in the K^* mass region and using this they resolve the ambiguity in the phase described in the following section.

Resolving the ambiguity in the phase The phases $\delta_\parallel$, $\delta_\perp$ and δ_s only appear in the differential decay rate as differences of each other. This can be seen in

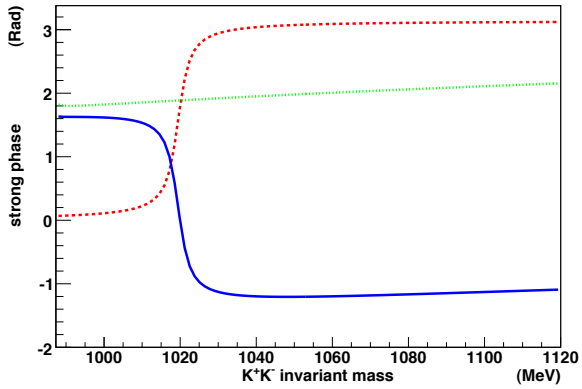

Figure 4.4: From [92] to demonstrate the phase changes across the K^+K^- invariant mass. The dashed red curve, dotted green, and solid blue curves are for δ_0, δ_S and $\delta_s - \delta_0$ respectively. The same behaviour applies to the $K\pi$ invariant mass.

Table 4.1. This means that the differential decay rate is invariant under the transformation:

$$(\delta_\parallel, \delta_\perp, -\delta_S) \longleftrightarrow (-\delta_\parallel, \pi - \delta_\perp, \delta_S) \tag{4.16}$$

This ambiguity must be resolved. For both $B^0 \to J/\psi K^{*0}$ and $B_s^0 \to J/\psi\phi$, according to Wigner's causality principle [90], the phase of a resonant amplitude increases with increasing invariant mass. The $K\pi$ P-wave phases increase rapidly in the vicinity of the K^* while the S-wave phase increases only gradually since it is far from a resonance. The relative phase difference $|\delta_S|$, is expected to fall rapidly with increasing $m_{K\pi}$ in this region. This allows, through a simultaneous fit in separate bins of $K\pi$ invariant mass, the resolution of the phase ambiguity for the P-wave phases. This behaviour is the same for the ϕ invariant mass distribution in $B_s^0 \to J/\psi\phi$ which is shown in Figure 4.4. This method has been used in the LHCb analysis for $B_s^0 \to J/\psi\phi$ [91], to resolve the ambiguity in physics parameter $\Delta\Gamma_s$ and CP violating phase ϕ_s. For the $B^0 \to J/\psi K^{*0}$ analysis, it also resolves the ambiguity in the phases, and is useful for a cross-check of the $B_s^0 \to J/\psi\phi$ analysis.

Control channel for $B_s^0 \to J/\psi\phi$ The decay $B_s^0 \to J/\psi\phi$ is of great interest in the search for CP violation. It is sensitive to the CP violation weak phase

ϕ_s. This is predicted to be small in the SM, being governed by the mixing phase $\Phi_M = -2\beta_s$ where β_s is one of the angles of one of the unitarity triangles from the CKM matrix:

$$\beta_s = arg\frac{(-V_{ts}V_{tb}^*)}{V_{cs}V_{cb}^*} = \lambda^2\eta \tag{4.17}$$

where $\lambda = 0.2253 \pm 0.0007$ [7] and $\eta \sim 0.3$ are parameters in the Wolfenstein parameterization of the CKM matrix. In the SM ϕ_s is predicted to be $-0.036 \pm 0.002\,\text{rad}$ [93]. Any additional NP could add a large phase. $B_s^0 \to J/\psi\phi$ is also a pseudoscalar to vector-vector decay and has a final state with an admixture of parity-odd and parity-even eigenstates. The measurement of ϕ_s is performed with a similar angular analysis which also extracts the same polarization amplitudes and strong phases as for the $B^0 \to J/\psi K^{*0}$ angular analysis.

The measurement of ϕ_s has been performed by CDF [94], and D0 [95] at the Tevatron collider. More recently it has been measured at LHCb [96] with $0.37\,\text{fb}^{-1}$ and with an update using $1\,\text{fb}^{-1}$, ϕ_s has been measured as $(-0.001 \pm 0.101 \pm 0.027)\,\text{rad}$, consistent with the SM prediction.

It is expected that the P-wave amplitudes and strong phases in $B_s^0 \to J/\psi\phi$ should be very similar (to within a few percent) to those in $B^0 \to J/\psi K^{*0}$ [97]. The reason for this is the similarities between the two processes. They are both dominated by the colour-suppressed tree diagram shown in Figure 4.1. They only differ by the substitution of the s spectator quark for the d, and they have similar branching ratios [7]:

$$\begin{aligned} \mathcal{B}(B^0 \to J/\psi K^*) &= (1.33 \pm 0.06) \times 10^{-3} \\ \mathcal{B}(B_s^0 \to J/\psi\phi) &= (1.3 \pm 0.4) \times 10^{-3} \end{aligned} \tag{4.18}$$

Electroweak and gluonic penguin amplitudes also contribute to both decays, these can been seen in Figure 4.1. As already discussed it is assumed that these contributions are very small, however this assumption needs to be tested. If any deviation in the measured polarization amplitudes or their phases is seen, it could be due to additional pollution by penguin contributions. This could create problems for the measurement of ϕ_s in $B_s^0 \to J/\psi\phi$, so it is important that this is checked. It has been shown in other decays that the strong phases and the

magnitudes of the amplitudes are approximately equal (to within a few percent) for $SU(3)$ related processes such as $B^0 \to J/\psi K^{*0}$ and $B_s^0 \to J/\psi\phi$ [97]. Results from the Tevatron and the B factories do show the amplitudes and phases of $B_s^0 \to J/\psi\phi$ and $B^0 \to J/\psi K^{*0}$ to be consistent within the errors. The results of $B^0 \to J/\psi K^{*0}$ from LHCb presented in Chapter 6 will be compared with the latest results from LHCb for $B_s^0 \to J/\psi\phi$.

Cross-check for $B_s^0 \to J/\psi\phi$ The analysis of $B_s^0 \to J/\psi\phi$ at LHCb uses the fitting program RapidFit which was developed at Edinburgh University (see section 2.7). The analysis described in Chapter 5 uses the same fitting program. Since $B^0 \to J/\psi K^{*0}$ has more backgrounds to include, a larger fraction of S-wave, and has been well measured by the B-factories, it is a very useful cross-check for the $B_s^0 \to J/\psi\phi$ analysis. Specifically it has been useful for noticing potential software bugs that may also have affected the $B_s^0 \to J/\psi\phi$ analysis.

4.3.3 Conclusion

It has been shown that an angular analysis of $B^0 \to J/\psi K^{*0}$ allows the separation of the parity-odd and parity-even final states by measuring the different polarization amplitudes. Previously, the motivation for this has been a test of the factorization hypothesis, which led to an improvement in the predictions for colour-suppressed decays. It also allowed the resolution of the ambiguity in the measurement of the CP violating parameter $\sin 2\beta$ measured in $B^0 \to J/\psi K^{*0}$ ($\to K_S\pi$). Since the first analysis of this channel, it has been well measured by previous experiments all of which are consistent in the polarization amplitudes and phases. A test of New Physics is possible by a direct CP violation measurement - comparing the amplitudes for the decay and its conjugate. The CP-violating triple product correlations can also be measured and compared with the SM prediction of zero. The S-wave contribution from the $K\pi$ resonance can be measured which leads to the resolution of the ambiguity in the phase, for both $B^0 \to J/\psi K^{*0}$ and $B_s^0 \to J/\psi\phi$, the latter also resolving the ambiguity in the CP-violating phase ϕ_s. The following Chapter describes the angular analysis of $B^0 \to J/\psi K^{*0}$ with the LHCb experiment.

Chapter 5

Methods for $B^0 \to J/\psi K^*$ Analysis

5.1 Data Samples and Event Selection

As described in Chapter 2, the data is selected in three stages. The Level-0 hardware trigger, the High Level Triggers HLT1 and HLT2, then the stripping and offline selection. The data used in this analysis were collected using two lines of the Level-0 (L0) hardware trigger: the single-muon line which requires one muon candidate with a transverse momentum $p_T > 1.4$ GeV, and the dimuon line which requires two muon candidates with $p_T > 0.56$ GeV and $p_T > 0.48$ GeV respectively. Next, the first stage HLT1 performs a partial event reconstruction which confirms or discards the L0 trigger decision. The HLT1 trigger used (*HLT1DiMuonHighMass*) requires events to have either two well-identified muons with an invariant mass above 2.7 GeV, or at least one muon or one high p_T track with a large impact parameter to any primary vertex. HLT2, the second stage performs a full event reconstruction and event selection. The trigger used (*HLT2DiMuonDetachedJpsi*) passes only those events with a muon candidate pair with invariant mass within 120 MeV of the nominal J/ψ mass [7]. This trigger line cuts on the decay length significance (DLS) of the J/ψ with respect to the best Primary Vertex, i.e. the one which has the smallest impact parameter of the J/ψ ($DLS > 3\sigma$). This trigger line introduces a bias for short B meson decay times but since the lifetime is not being specifically measured in this analysis it does not affect the systematic errors (for more details see section 5.3.2). At both

the HLT1 and HLT2 stage, we require the tracks from our signal B candidate to have fired the trigger (TOS). For more details about the trigger used in this analysis see Section 2.5.

Event selection is carried out after the events have been triggered on. Selections reduce the number of events by discarding candidate decays which fall outside of a given range in kinematic variable or PID information. Cuts are chosen in variables where the signal and background distributions differ such that they can be separated. This is done in two stages, the first being event stripping. Similar decay channels have the same stripping line to save CPU time. Reasonably loose event selection cuts are used in the stripping so that they can be altered at a later date, but they have to be tight enough to limit the amount of data that has to be stored. After events have been stripped they are then offline selected with tighter cuts that can be easily altered.

The stripping and offline selections are summarised in Table 5.1. They are chosen to increase the signal-to-background ratio, and are based on a "roadmap" selection which was developed on Monte Carlo [98]. The selection used here is the same as the "roadmap" selection and as the previous analysis in [75] except for the K^* p_T cut, the pion DLL cut and the trigger decision. It has been checked that these cuts are still appropriate for both data and MC.

One additional selection cut is made that is not in the table which is for multiple B candidates. It has been shown that there are 1.3 multiple candidates per event on average. If there are multiple B candidates per event only the candidate with the smallest vertex χ^2_{vtx}/n_{DoF} is kept. It has been verified that candidates removed are either duplicates of the selected candidates or are consistent with combinatorial background.

All daughter tracks ($\mu^\pm$, $K^\pm$,$\pi^\pm$) are required to have a track goodness-of-fit $\chi^2_{track}/nDoF$ (track χ^2 per number of degrees of freedom) to be less than 5 in the stripping and 4 in the final selection. This cut is effective at identifying tracks that are reconstructed from a spurious set of hits in the detector (ghosts), since they have a high $\chi^2_{track}/nDoF$. Clone tracks occur because several different tracking pattern algorithms are used for different types of tracks which can sometimes overlap. Two tracks are considered clones of each other if they share certain information. This is quantified using the Kullback-Leibler distance [99]. It measures the difference in information content between the two tracks. If small,

it indicates the tracks are likely to be clones. A cut on this quantity (which is unitless) at 5000 removes most of the clone tracks. For further information on the clone cut, see [100].

In order to select true J/ψ particles a number of cuts are placed on the stripped $\mu^{\pm}$ events. There is a PID delta log likelihood (DLL) cut on both of the muons of less than zero. For a description of this cut see section 3.1.3. There is also a minimum p_T cut on both of the muons of greater than 500 MeV which removes combinatorial background. A goodness-of-fit $\chi^2_{vtx}/nDoF$ is placed on the vertex of the J/ψ meson of less than 16. There is also a cut on the $\mu^+\mu^-$ invariant mass distribution around the Particle Data Group [7] value of the J/ψ invariant mass from 3030 to 3150 MeV.

Only events which survive the J/ψ selection are used as input for selecting $K^* \to K^{\pm}\pi^{\mp}$. This removes most of the background coming from prompt pions and kaons that could fake a K^* signal. There are then three DLL PID cuts performed. The first two are for the kaon selection and separate them from pions and protons ($DLL_{K\pi} > 0$, $DLL_{Kp} > -2$) and the third is for the pion selection and separates them from kaons ($DLL_{K\pi} < 0$). These PID cuts are very effective at selecting pure samples of charged particles as was seen in Figure 3.6 in Chapter 3. There is also a cut placed on the p_T of the K^* meson of greater than 2000 MeV which removes a large amount of combinatorial background. It is required that the event also falls within a $K\pi$ mass range from 826 to 966 MeV, and that the K^* vertex has a $\chi^2_{vtx}/nDoF$ of < 16.

For selecting the overall decay chain $B^0 \to J/\psi K^{*0}$ a cut is placed on the invariant mass window of the B meson around the Particle Data Group [7] value. Only events falling in the range from 5150 to 5400 MeV are accepted. A $\chi^2_{vtx}/nDoF$ cut of less than 10 is also placed on the B vertex. A tool developed by the BaBar collaboration called Decay Tree Fitter is used to calculate the decay time and a cut is placed on $\chi^2_{DTF}/nDoF$ at less than 5 [101]. A goodness-of-fit is carried out on the impact parameter of the B^0 meson and a cut is placed on $\chi^2_{IP}/nDoF$ at less than 25. A lower $\chi^2_{IP}/nDoF$ is also placed on the next best candidate. Finally a proper decay time cut > 0.3ps is placed to get rid of prompt background.

After these cuts are applied there are a total of 77285 events in the sample. The efficiencies for the proper time cut, the B mass window, the original selection

Decay mode	Cut parameter	Stripping 17	Final selection
all tracks	χ^2_{track}/nDoF	< 5	< 4
	KL divergence (clone)	–	> 5000
$J/\psi \to \mu\mu$	$DLL_{\mu\pi}$	> 0	> 0
	$min(p_T(\mu^+), p_T(\mu^-))$	–	> 0.5 GeV
	χ^2_{vtx}/nDoF(J/ψ)	< 16	< 16
	$\lvert M(\mu^+\mu^-) - M(J/\psi)\rvert$	< 80 MeV	$\in [3030, 3150]$ MeV
$K^* \to K\pi$	$DLL_{K\pi}(K)$	> -2	> 0
	$DLL_{Kp}(K)$	–	> -2
	$DLL_{K\pi}(\pi)$	–	< 0
	$p_T(\text{K}^{*0})$	> 1 GeV	> 2 GeV
	$\lvert M(K^+\pi^-) - M(K^*)\rvert$	$\in [826, 966]$ MeV	$\in [826, 966]$ MeV
	$\chi^2_{vtx}(K^*)/nDoF$	< 16	< 16
$B_d \to J/\psi K^*$	$M(B_d)$	$\in [5100, 5450]$ MeV	$\in [5150, 5400]$ MeV
	$\chi^2_{\text{vtx}}(B_d)$/nDoF	< 10	< 10
	$\chi^2_{\text{DTF(B+PV)}}(B_d)$/nDoF	–	< 5
	$\chi^2_{\text{IP}}(B_d)$/nDoF	–	< 25
	$\chi_{\text{IP,next}}(B_d)$	–	> 50
	$t(B_d)$	> 0.2 ps	> 0.3 ps

Table 5.1: $B^0 \to J/\psi K^{*0}$ cuts used for both stripping and final selections.

used in [75], as well as the cuts introduced for this analysis and the trigger requirement are shown in Table 5.2. The cut on the K^* p_T shows a nice increase in the S/B ratio, but cuts out a lot of events. However, this increases the stability and reliability of the fit and reduces systematic errors. The Monte Carlo (MC) simulation used in this analysis was called MC11a and was produced by a centrally managed production team on LHCb. They use a simulation of the LHCb detector and full reconstruction of the decays involved using Geant4 [44]. The MC is very useful for detector acceptance and background studies, as well as verifying analysis methods.

5.2 Background Studies

The main backgrounds that have to be considered are :

- Combinatorial background of random tracks

Cut	No. total events	ϵ_{cut} S+B (%)	Signal fraction (S/B) (%)	ϵ_{sig} (%)	ϵ_{bkg} (%)
Stripping Selection	1619115	-	-	-	-
Proper time cut	950119	59	-	-	-
B mass window cut	816998	86	19	-	-
*Selection from [75]	399626	49	36	93	34
K^* p_T	144014	36	69	69	17
π PID	101471	70	79	81	48
Trigger biased	77285	76	79	76	76

Table 5.2: Total number of events, total selection cut efficiency (ϵ_{cut}), signal fraction at each stage of selection, as well as the signal efficiency (ϵ_{sig}), and background efficiency (ϵ_{bkg}). Each efficiency is defined with respect to the previous cut. The signal fraction is the overall number of signal events compared to background events after each cut. T his is found from a fit to the B^0 mass distribution each time. This is only shown for the sample when the proper time cut and B mass window cut have already been applied because of the large combinatorial background before these cuts. For a more detailed efficiency study of the selection cuts included in the previous analysis, see [102].

- Backgrounds containing true J/ψ from non-signal $B \to J/\psi X$ events (J/ψ background)
- Background where the two reconstructed muons do not originate from a J/ψ (non-J/ψ background)

To investigate the non-J/ψ background, a simultaneous unbinned maximum likelihood fit was performed to both the B^0 and the J/ψ invariant mass distributions in data (see Figure 5.1) and sWeights were extracted [103], [47]. The sWeight technique was developed to obtain background subtracted distributions of variables which are uncorrelated with a certain discriminating variable. In this case a double Gaussian was used to fit to the B^0 invariant mass with an exponential for the background. A double Crystal Ball function (which is a Gaussian distribution convoluted with a power-law tail) was used to fit to the J/ψ invariant mass, with an exponential for the background. Using the sWeights the events were categorised into four categories which are shown in Table 5.3. Those that peak in the signal range in both distributions are classed as signal and have the highest percentage of events. Those that do not peak in either are defined as combinatorial background. Those that only peak in the J/ψ distribution are

Category	Peaks in B^0	Peaks in J/ψ	% of events
Signal	Yes	Yes	$78.5 \pm 2.9\%$
Combinatorial Background	No	No	$5.6 \pm 0.2\%$
J/ψ Background	No	Yes	$15.9 \pm 2.9\%$
Non- J/ψ Background	Yes	No	$0.0 \pm 0.03\%$

Table 5.3: Categorisation of events simultaneously fit in the B^0 and J/ψ invariant mass distributions.

classed as the J/ψ background, and those that do no peak in the J/ψ mass but do in the B^0 mass are classed as non-J/ψ background events. The combinatorial and the J/ψ background are the only backgrounds that need to be taken into account. The non-J/ψ background fraction is consistent with zero.

To study the backgrounds further an LHCb tool called *BKGCAT* [104] was used to separate the events into different categories. The relevant categories are listed in Table 5.4. MC11a $B^0 \to J/\psi K^{*0}$ signal events were selected from a sample of approximately 10 million candidates using the data selection described in section 5.1. The number of truth matched signal events selected as well as the number of events in each background category selected are listed in Table 5.5, as well as the percentage of the total events selected. The *reflection*, *partially reconstructed*, *ghost* and *low mass* are the backgrounds which peak in the B invariant mass distribution. Their invariant mass distributions are shown in Figures 5.2(a) to 5.2(h), along with the truth matched invariant mass.

The mass distribution of the *reflection* background is rather wide compared to the signal and is only 0.04% of it. This is low due to the effective PID cuts placed on the charged tracks and can be neglected in the fit. The *partially reconstructed physics* background is only 0.03% of the signal so this can also be neglected. The *low mass background* are those events where the J/ψ meson emits at least one photon which explains the radiative tail in Figure 5.2(d).

A significant proportion of this background exists in the dataset but the distribution of the transversity angles shown in Figure 5.3(b) is very similar to that of the signal (Figure 5.3(a)). A Kolmogorov-Smirnoff test [105] performed between the signal and the low mass background normalized angular distributions gives values of 0.459 for $\cos\psi$, 0.175 for $\cos\theta$ and 0.349 for ϕ, supporting the

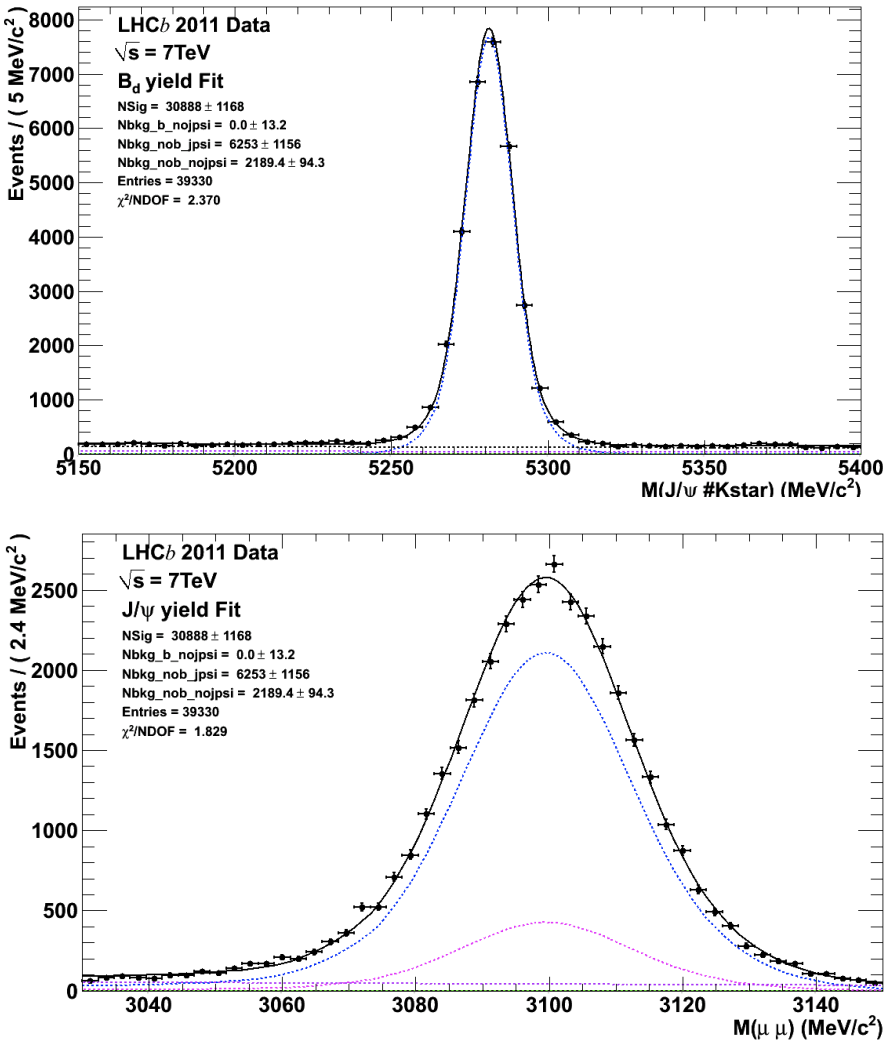

Figure 5.1: Invariant mass distributions of $J/\psi K^*$ and $\mu\mu$. The simultaneous fit lines are shown. The blue dotted line is the signal (peaks in both distributions), the pink dotted line is the J/ψ background (peaks in the J/ψ but not the B mass distribution) and the red is the combinatorial background (does not peak in either distribution).

BKGCAT	Definition
0	Signal
20 Fully Reconstructed Physics background	The decay topology is fully and correctly reconstructed but the mother particle is incorrectly identified e.g. $B_s \to J/\psi K^*$ is reconstructed.
30 Reflection	Caused by the misidentification of a final state particle. Usually a pion is misidentified as a kaon
40 Partially Reconstructed Physics background	A fragment of a decay occurring in the event is incorrectly identified as a signal decay.
50 Low Mass Background	Special case of the partially reconstructed physics background, where there is no misidentification and the reconstructed particle is found to have a mass systematically below the signal peak. This is due to radiative emission. This could mean that the sidebands do not well model the background under the peak
60 Ghost	One or more of the final state particles is found to have no associated MC particle. Protected against by kinematic cuts e.g. p_T or IP.
70 From PV	One or more of the final state particles come from the Primary Vertex. These will have high momenta
100 From Different PV	The final state particles come from more than one primary vertex
110 $b\bar{b}$	Does not fit into any previous category, but at least one of the final state particles has a mother with bottom content

Table 5.4: Description of each background category in the BKGCAT tool.

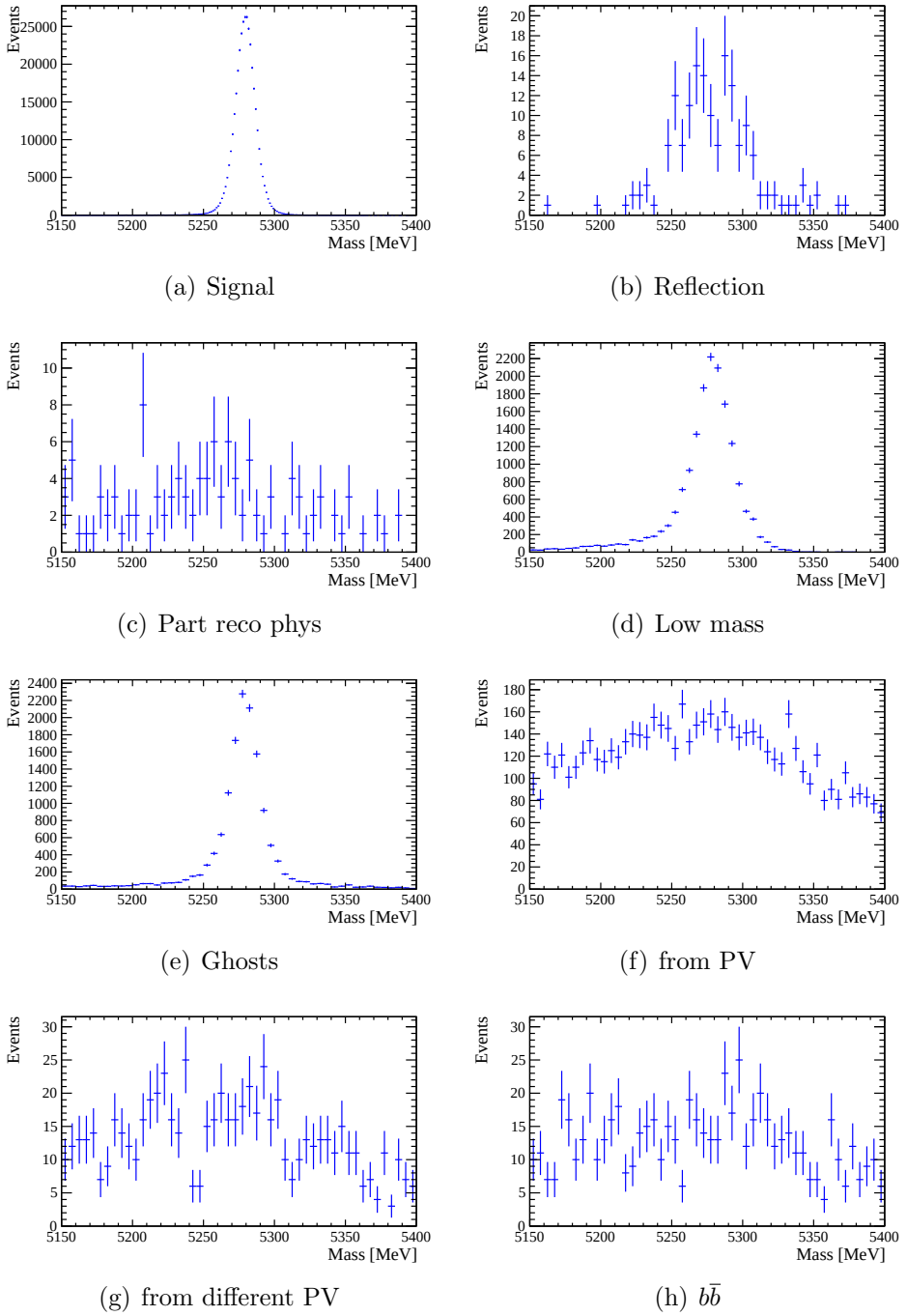

(a) Signal

(b) Reflection

(c) Part reco phys

(d) Low mass

(e) Ghosts

(f) from PV

(g) from different PV

(h) $b\bar{b}$

Figure 5.2: B^0 invariant mass of each background category in MC.

BKGCAT	Num events	Percentage of total
Total events	404624	-
0 Signal	366409	90.6
30 Reflection	162	0.04
40 Part Reco Phys Bkg	116	0.03
50 Low Mass Bkg	16497	4.41
60 Ghost	14076	3.48
70 From PV	6076	1.50
100 From Different PV	644	0.16
110 $b\bar{b}$	626	0.16

Table 5.5: Yield in each background category from $B^0 \to J/\psi K^{*0}$ MC11a.

case that these are similar[1]. The *ghosts* also contribute significantly to the selected events and their angular distribution is shown in Figure 5.3(c). The $\cos\psi$ distribution is significantly different to the signal, and the Kolmogorov-Smirnoff test returns a value of zero. When the *ghosts* are included in the fit it makes a small difference to the fit result. This difference is included as a systematic error. The invariant mass distribution of the remaining backgrounds are shown in Figures 5.2(f) to 5.2(h). The *from PV*, *from different PV* and $b\bar{b}$ backgrounds are mostly flat in the B^0 mass signal region so these are treated as combinatorial background in the fit.

The $B^0 \to J/\psi K^{*0}$ selection was also used to select events from a sample of inclusive $B \to J/\psi X$ Monte Carlo events in order to study the J/ψ background. A total of 1003 events were selected from approximately 20 million. The number of events in each category is shown in Table 5.6. The invariant mass distribution for the total selection of $B^0 \to J/\psi K^{*0}$ MC, inclusive $B \to J/\psi X$ MC and the data is overlayed in Figure 5.4. Overall the distribution of the $B \to J/\psi X$ inclusive MC seems to describe the background in the sidebands of the data well. Figure 5.4 also shows that the signal peak in data is slightly wider and shifted to a lower mass than the Monte Carlo signal peak. The shift to lower mass is a known issue with the alignment of the tracking stations in LHCb and will be improved with re-alignment. It will not affect this analysis since only the angular acceptance correction is dependent on the MC, detailed in Chapter 6. A mass

[1]In the Kolmogorov-Smirnoff test a value of 1 means the distributions are exactly the same, and 0 means they are completely different

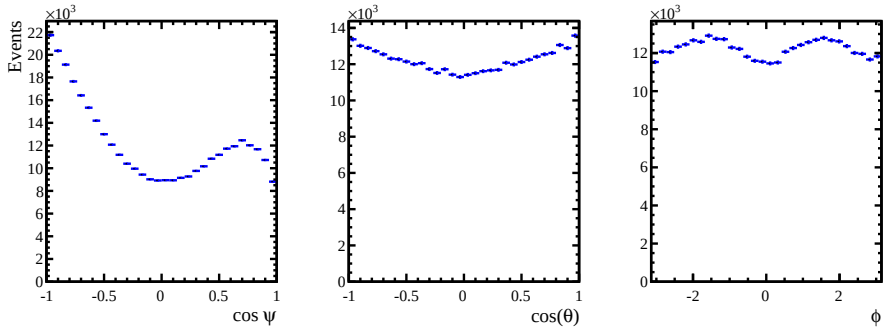

(a) Signal

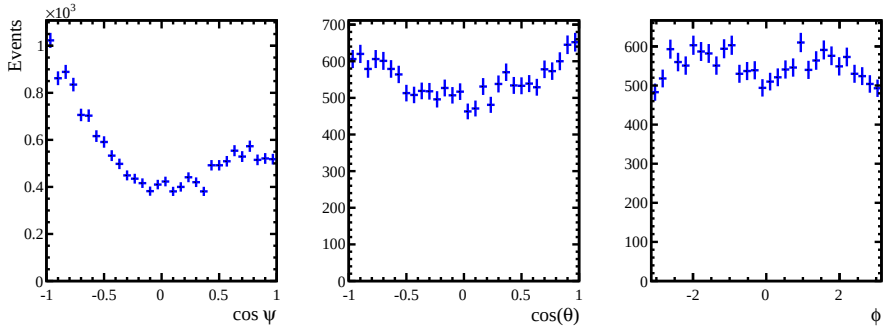

(b) Low Mass Bkg

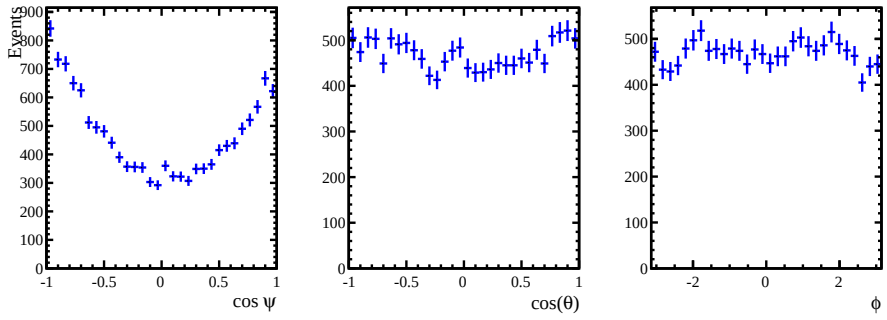

(c) Ghost

Figure 5.3: Transversity angle distribution of the signal and two types of peaking background in accepted signal MC.

BKGCAT	Num events	Percentage of total
Total	1003	-
0 Signal	804	80.16
20 Fully Reco Phys Bkg	2	0.20
30 Reflection	1	0.10
40 Part Reco Phys Bkg	7	0.70
50 Low Mass Bkg	34	0.30
60 Ghost	36	3.59
70 From PV	93	9.27
100 From Different PV	9	0.90
110 $b\bar{b}$	17	1.69

Table 5.6: Yield in each background category from inclusive $B \to J/\psi X$ MC11a.

Parameter	MC Fit	Data Fit
Fraction $f^{\sigma}_{\mathrm{m},1}$	0.866 ± 0.003	0.750 ± 0.020
$\sigma^{sig}_{\mathrm{m},1}$ [MeV]	6.75 ± 0.02	7.11 ± 0.09
$\sigma^{sig}_{\mathrm{m},2}$ [MeV]	16.89 ± 0.22	13.86 ± 0.38
mean [MeV]	5279.40 ± 0.012	5281.18 ± 0.037

Table 5.7: MC and data invariant mass fit parameters.

fit to the signal MC gives the parameters shown in Table 5.7. The first Gaussian width is increased by 0.36 MeV and the mass peak has been shifted by 1.8 MeV.

Cross contamination from other decays has been considered, in particular the two channels $B^+ \to J/\psi K^{*+}(K^{*+} \to K^+\pi^0)$ and $B^+ \to J/\psi K^{*+}(K^{*+} \to K_s\pi^+)$. Fully simulated MC11a was used to select $B^0 \to J/\psi K^{*0}$ candidates from these channels. Out of 1M generated events for each channel, 44 events were selected for $B^+ \to J/\psi K^{*+}(K^{*+} \to K^+\pi^0)$ and 80 events were selected for $B^+ \to J/\psi K^{*+}(K^{*+} \to K_s\pi^+)$. For both, the B^0 invariant mass distribution does not seem to peak in the signal region as can be seen in Figure 5.5, however there are limited statistics. However, it can be concluded that both of these channels will not affect the $B^0 \to J/\psi K^{*0}$ analysis significantly, so these backgrounds are neglected.

In addition, the channel $B^0_s \to J/\psi\phi$ may contaminate the $B^0 \to J/\psi K^{*0}$ sample if a kaon is mis-identified as a pion. The $B^0 \to J/\psi K^{*0}$ selection was used to select events from $B^0_s \to J/\psi\phi$ MC11a. Out of approximately 5 million

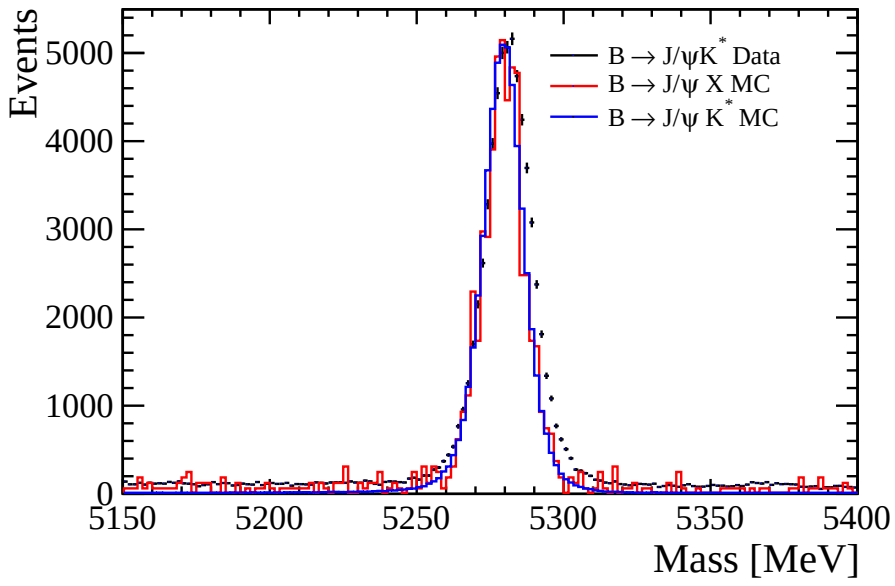

Figure 5.4: B^0 Invariant mass distribution for $B^0 \to J/\psi K^{*0}$ MC, inclusive $B \to J/\psi X$ MC and the data selections (scaled to match data).

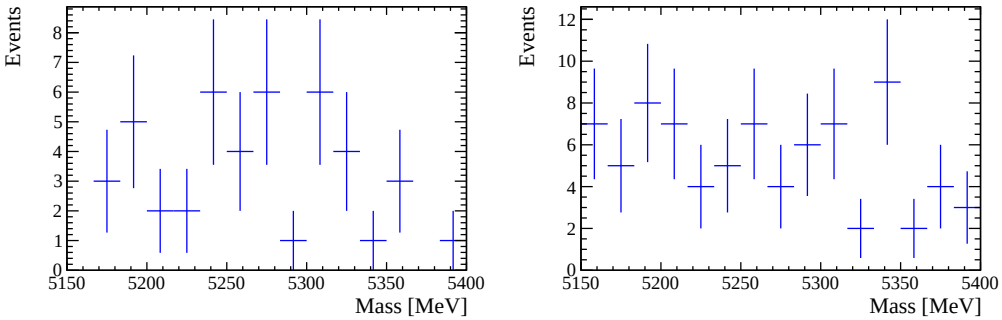

(a) $B^+ \to J/\psi K^{*+}(K^{*+} \to K^+\pi^0)$ (b) $B^+ \to J/\psi K^{*+}(K^{*+} \to K_S\pi^+)$

Figure 5.5: Invariant mass distributions in $B^+ \to J/\psi K^{*+}$ MC.

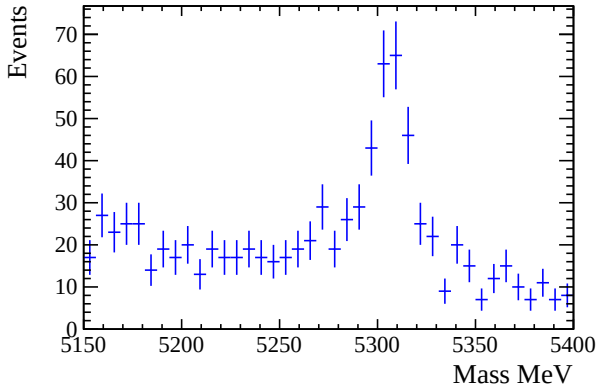

Figure 5.6: B^0 invariant mass for mis-identified $B_s^0 \to J/\psi\phi$ events. The $B^0 \to J/\psi K^{*0}$ selection was used to select events from $B_s^0 \to J/\psi\phi$ MC11a.

events, 850 events were selected and have the invariant mass distribution shown in Figure 5.6. When scaled to the number of events selected in $B_s^0 \to J/\psi\phi$ MC and data with the $B_s^0 \to J/\psi\phi$ selection (which is very similar to the $B^0 \to J/\psi K^{*0}$ selection, see [25]), there is an equivalent of 83 events occurring in the $B^0 \to J/\psi K^{*0}$ sample. This is 0.11% percent of the total number of events. When this sample was included in the fit, fixing its angular distribution and Crystal Ball shape to a fit performed on MC, it made no difference to the results for the measured amplitudes.

It is also clear from the invariant mass distribution of the selected signal candidates, that the $B_s \to J/\psi K^*$ decay is visible in the high mass sideband. This decay has been observed by both CDF [106] and LHCb [107]. When this is included in the fit as an extra Gaussian background as can be seen in Figure 5.7 (note the logarithmic scale), there is no difference made to the fit results.

5.3 Maximum Likelihood Fit

An unbinned maximum likelihood fit is performed to the invariant mass m_B, the decay time t, and the three decay angles $\Omega = (\cos\theta, \phi, \cos\psi)$. The mass factorizes as a separate component to the time and angles:

$$\frac{d}{d\lambda_k}\sum_e ln\frac{s(m_B|\vec{\lambda})s(t_e,\vec{\Omega}_e|\vec{\lambda})\epsilon(t,\vec{\Omega})}{\int\int s(m_B|\vec{\lambda})s(t,\vec{\Omega}|\vec{\lambda})\epsilon(t,\vec{\Omega})d\Omega dt} = 0 \tag{5.1}$$

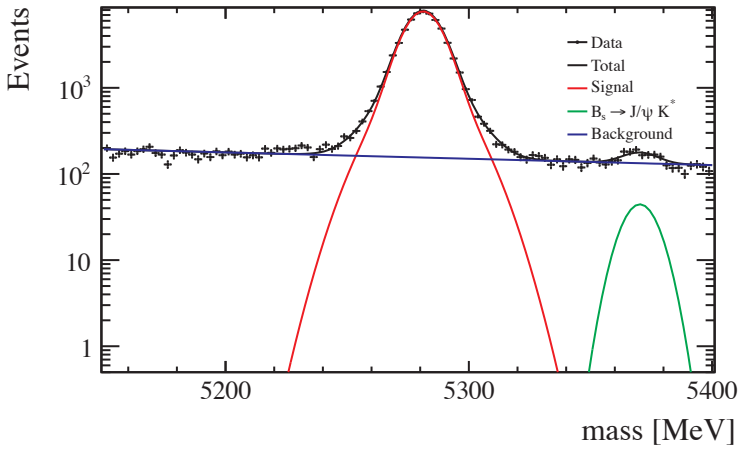

Figure 5.7: Fit to data including a fit to the $B_s \to J/\psi K^*$ decay in the high mass sideband. Note the logarithmic scale. Including this component in the fit makes no difference to the fitted parameters.

Where λ are the physics parameters, s is the unnormalized PDF, m_B is the invariant B^0 mass, t is the proper time, Ω the decay angles and the sum is over all events. ϵ is the decay angle and proper time acceptance which must be taken into account. The methods for doing this are explained in the following sections.

The probability density function consists of signal and background components which include detector resolution and acceptance effects. The signal PDF for time and angles is given by:

$$s(t_e, \vec{\Omega}_e|\vec{\lambda}) = \sum_{i=1}^{10} A_i(t_e|\vec{\lambda}) f_i(\vec{\Omega}_e) \tag{5.2}$$

where $A_i(t_e|\vec{\lambda})$ are the amplitudes given in Table 4.1 and $f_i(\vec{\Omega}_e)$ are the angular functions given in Table 4.2

The physics parameters determined in the fit are the decay width Γ_d of the B^0, the polarization amplitudes $|A_\parallel|^2$, $|A_\perp|^2$ and $|A_S|^2$ and the strong phases $\delta_\parallel$, $\delta_\perp$ and δ_S. $|A_0|^2$ is determined by $1-|A_\parallel|^2-|A_\perp|^2-|A_S|^2$ so that the proportion of each amplitude is measured only.

The signal m_B distribution is modeled as the sum of two Gaussian functions with a common mean. The mean and width of both Gaussians, and the fraction of the second Gaussian are fit parameters. The m_B distribution of the background

is described by an exponential function with a slope determined by the fit. The distribution of the signal decay time and angles is described by the differential decay width equation 4.8. The decay time is not correlated with any of the other observables, but it is used in the fit to help with signal-background separation. The decay width Γ_d is found to be consistent with the world average [7], but only statistical errors are quoted here. The systematic errors are being studied.

The fit is carried out by two separate fitting frameworks, one called RapidFit in Edinburgh (see section 2.7), and the other being the Heidelberg fitter. They have been written separately, and are crucial for cross-checking the results.

5.3.1 Time and angular resolution

The finite proper time resolution of the detector is taken into account by convolving the time dependent exponential terms in the differential decay rate (see Equation (4.8)) with a Gaussian model of width 60 fs. This resolution has been verified using prompt events from data. When the width of the Gaussian is varied from 30 fs to 100 fs in the fit, none of the physics parameters are affected. The effect of the finite angular resolution of the transversity angle distributions has been studied with fully simulated events with similar resolutions to those in the data. The systematic bias for 1 million $B_s^0 \to J/\psi\phi$ events due to neglecting the angular resolutions while fixing the strong phases is only significant for $A_\perp(0)$ and equals $(0.23 \pm 0.07) \times 10^{-3}$ [102]. This is negligible compared to the statistical errors with the current amount of data being used and is therefore ignored in the fit model.

5.3.2 Decay Time acceptance

There are two distinct decay time acceptance effects. The first is a decrease in reconstruction efficiency at large decay times. This effect is attributed to poor reconstruction efficiency in the VELO detector. It is parametrised by the efficiency function $\epsilon(t) = 1 + \beta t$, with $\beta = -0.0092 \pm 0.0008$ ps^{-1} determined from MC. Secondly, there is a trigger acceptance at small decay time which is caused by the use of the lifetime biasing trigger line. In previous analyses (e.g. [25]) a one-dimensional acceptance histogram has been used to account for this.

Both of these effects and how the efficiency corrections have been obtained

are explained in more detail in [25]. The main effect of the time acceptance is on Γ_d, the measurement of which is not the goal of this analysis. The decay time acceptance is not expected to have an effect on the measurement of the amplitudes. Indeed, when applying these corrections the amplitudes do not change. It will be shown in Chapter 6 that in the correlation matrix of the fit there is little correlation between the lifetime fit parameters, the polarisation amplitudes and the signal fraction.

5.3.3 Angular acceptances

The LHCb detector geometry and explicit selection cuts introduce an angular acceptance. Using Equation 5.2, the maximum likelihood in Equation 5.1 can be written:

$$\frac{d}{d\lambda_k}\sum_e ln\frac{A_i(t_e|\vec{\lambda})\epsilon(t)f_i(\vec{\Omega_e})\epsilon(\vec{\Omega})}{\int A_j(t|\lambda)\epsilon(t)\int f_j(\vec{\Omega})\epsilon(\vec{\Omega})d\Omega dt} = 0 \tag{5.3}$$

To correct for the efficiency in the numerator a 3-dimensional efficiency histogram is created from the ratio of the angular distributions of the accepted MC signal events, which have been fully reconstructed, triggered and selected, to the angular distribution of the original sample of signal MC events, which were generated according to Equation 4.8 using the previously measured angular amplitudes. In Figure 5.8 the 1D projections of the angular acceptance histogram can be seen. Note that the efficiencies are normalised to 1.

For the denominator, ten normalization weights are used:

$$\xi_j = \int f_j(\vec{\Omega})\epsilon(\vec{\Omega})d\vec{\Omega} \tag{5.4}$$

Whether an event is accepted or rejected depends on other observables such as momentum, impact parameter etc which we call z. So:

$$\epsilon(\vec{\Omega}) = \frac{\int \epsilon(\vec{\Omega},z)S(\vec{\Omega},z|\vec{\lambda})dz}{S(\vec{\Omega}|\vec{\lambda})} \tag{5.5}$$

which means that Equation 5.4 can be written:

$$\xi_j = \frac{1}{N_{gen}}\sum_e^{generated}\frac{f_j(\vec{\Omega}_e)}{S(\vec{\Omega}_e|\vec{\lambda})}\epsilon(\vec{\Omega}_e,z_e) \tag{5.6}$$

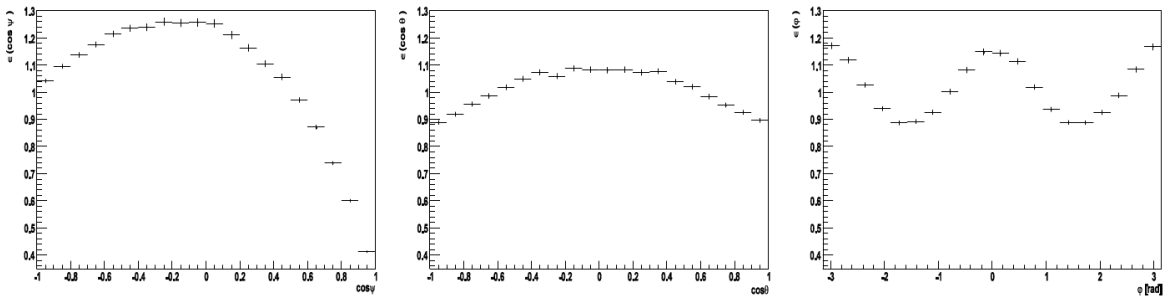

Figure 5.8: Normalised 1D projections of the angular acceptance histogram.

For each individual event the efficiency is a boolean because it is either accepted or rejected so:

$$\xi_j = \frac{1}{N_{gen}} \sum_{e}^{accepted} \frac{f_j(\vec{\Omega}_e)}{S(\vec{\Omega}_e|\vec{\lambda})} \tag{5.7}$$

This is just a sum of accepted events. For more details of this method see [108]. As a cross check, the Heidelberg fitter uses the same 3-dimensional efficiency histogram in the denominator and numerator, which is equivalent. The fact that the angular acceptance is determined completely using simulated events means that we must ensure that the angles and momenta distributions of the particles in MC are representative of the data. Some discrepancies are observed so some MC distributions are reweighted to calculate a systematic error. This is discussed further in Chapter 6.

5.3.4 Background Description

The combinatorial background is modeled as a single component by analysing the data in the sidebands of the B^0 mass distribution. The PDF describing the background contribution is assumed to factorize into a mass dependent, a time dependent and an angular dependent part. The mass distribution is described by an exponential with parameter $\alpha_{\mathrm{m}}^{\mathrm{LL}}$, which has a negative slope. Two exponentials with lifetimes τ_1^{LL} and τ_2^{LL} and relative fraction $f_{\tau,1}^{\mathrm{LL}}$ are used to describe the proper time distribution of the long lived background events. The background parameters are determined simultaneously with the physics parameters. The background events are correlated in the transversity angles, so

a three-dimension histogram is filled with background events from the B^0 mass sidebands to describe the background in the fit. The mass sidebands used are [5150;5230] and [5325;5400] MeV. It should be noted that the sidebands include the $B_s \to J/\psi K^*$ decay, but removing this has a negligible effect. The fit has been carried out excluding this region and no difference is observed.

5.3.5 sWeighted Fit

In addition to the nominal fit, an sWeighted fit [103] [47] is carried out and used as a cross check and for systematic error estimation. For this analysis the signal weight is obtained using the B^0 invariant mass as the discriminating variable. The correlation between the B^0 invariant mass and other variables such as the invariant mass of the K^*, the decay time, and the angular variables is negligible for both the signal and background components in the data. To distinguish between the regular fit and the sWeighted fit they will be called cFit (classic Fit) and sFit respectively in the following.

5.3.6 Validation of the fit methods

A fit to fully simulated truth matched $B^0 \to J/\psi K^{*0}$ signal MC has been performed for both the cFit and the sFit. The results and their deviation from the generated values are shown in Table 5.8. These results show that in the absence of backgrounds both the cFit and sFit are consistent with the generated values for the amplitudes and phases.

Another way to validate the fit is through *toy studies* using the PDF to generate datasets, which can then be fit to the same PDF. To quantify the fit stability and have confidence in the statistical errors a thousand toy studies were carried out using the signal PDF only, each toy containing the number of events in the dataset. The pull plots are shown in Figure 5.9. They show that the difference between the fitted and the generated values of the physics parameters are close to zero with a RMS of close to one. To further validate the fit procedure the signal and background PDFs were used to generate 700,000 events, with the same signal-to-background ratio as in data, and the angular background from the B^0 mass sidebands in data. These were then fit using the same PDFs. The generated values of the fit parameters and the fit results for the sFit and cFit are

Parameter	cFit Result	pull from generated value
$A_\parallel{}^2$	0.241 ± 0.0015	0.001
$A_\perp{}^2$	0.160 ± 0.0015	0.000
$\delta_\parallel$	2.503 ± 0.0083	0.001
$\delta_\perp$	-0.168 ± 0.0067	0.002

Parameter	sFit result	pull from generated value
$A_\parallel{}^2$	0.240 ± 0.0015	0.000
$A_\perp{}^2$	0.160 ± 0.0015	0.000
$\delta_\parallel$	2.506 ± 0.0082	0.006
$\delta_\perp$	-0.167 ± 0.0067	0.003

Table 5.8: cFit and sFit results for truth matched $B^0 \to J/\psi K^{*0}$ signal MC data.

Parameter	Generated Value	cFit Result	sFit Result
$A_\parallel{}^2$	0.24	0.241 ± 0.001	0.242 ± 0.001
$A_\perp{}^2$	0.16	0.160 ± 0.001	0.159 ± 0.001
$\delta_\parallel$	3.00	2.99 ± 0.009	2.99 ± 0.008
$\delta_\perp$	0.20	0.194 ± 0.007	0.196 ± 0.006
$A_s{}^2$	0.05	0.049 ± 0.001	0.050 ± 0.001
δ_s	-2.00	-2.01 ± 0.008	-2.01 ± 0.007

Table 5.9: Fit to data generated with the signal and background PDFs for both cFit and sFit. For both the angular acceptance was flat. For the cFit the data was generated with the angular background from the B^0 mass sidebands in data.

shown in Table 5.9. They are consistent with each other and consistent with the generated values within the uncertainties.

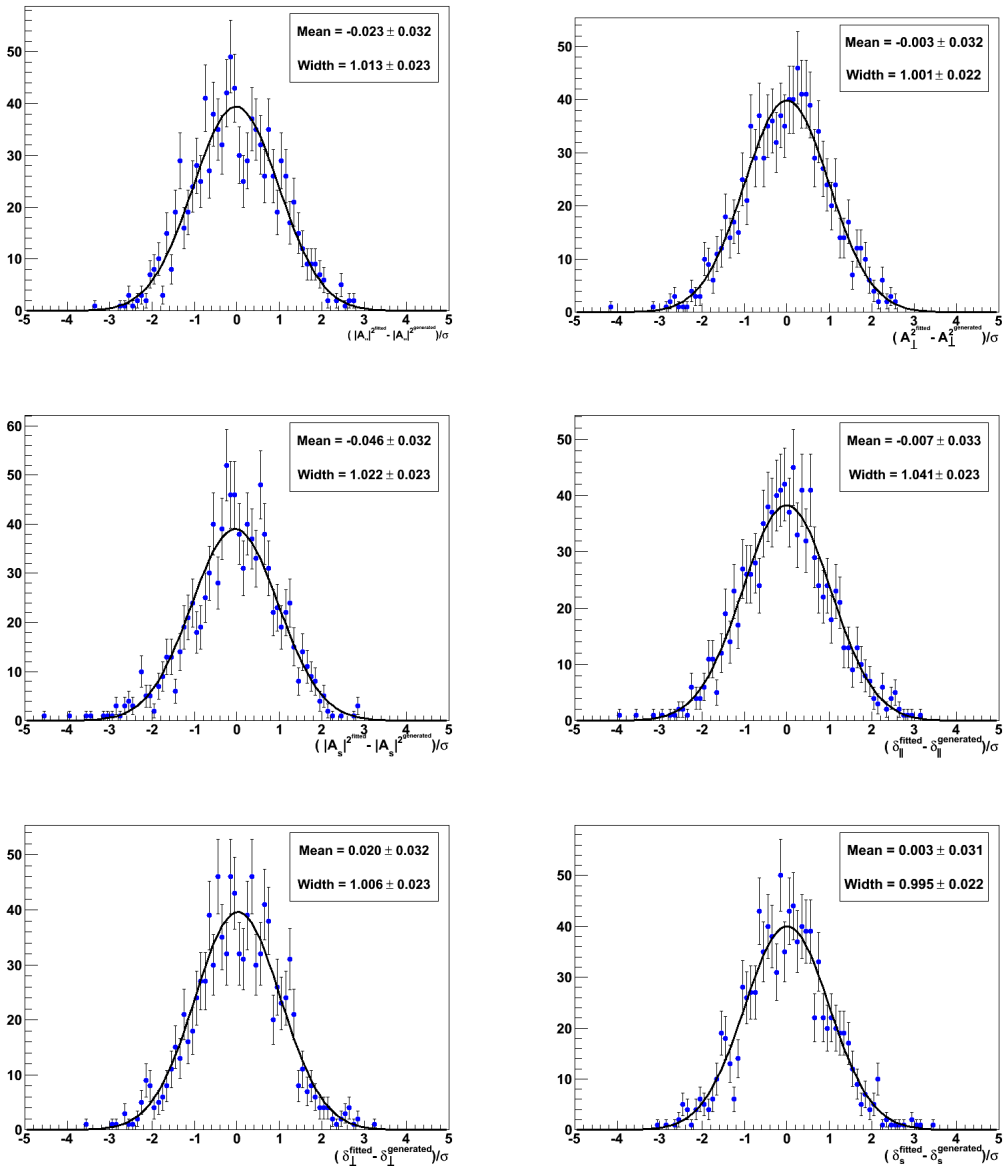

Figure 5.9: Pull distributions of the physics parameters (1000 toy experiments).

Chapter 6

Results of Angular Analysis of $B^0 \to J/\psi(\mu^+\mu^-)K^*(K^+\pi^-)$

In this Chapter the differences in the data and MC samples are described which leads onto the calculation of the systematic uncertainties for the results. The nominal fit to the angular amplitudes with and without S-wave, the resolution of the ambiguity in the phase, and the direct CP measurement are then presented and discussed.

6.1 Data/MC Comparison

As mentioned in Chapter 5 Monte Carlo is relied on for the determination of the acceptance. An extensive data/MC comparison has been carried out using the accepted signal Monte Carlo sample described in Section 5.2. For all plots in this section the MC categories are required to be classed as signal (the *low mass background* category is classed as signal because it has similar invariant B^0 mass and angular distributions - see Section 5.2) [1] The data has been background subtracted using sWeights from a fit to the B^0 invariant mass distribution. The transverse momentum and pseudorapidity of the B^0 are known to differ in the data compared to MC from analysis of other channels such as the J/ψ polarization analysis. It is thought that the difference in the pseudorapidity is due to the alignment of the tracking in the detector. They also differ here

[1] The *ghosts* background category is classed as background because the angular distribution is not signal-like (see Section 5.2 for more details). It is taken into account in the systematics for the final results, but excluded in this study.

and are shown with the ratio of the two distributions in Figure 6.1. The B^0 momentum has a discrepancy at low momenta < 80 GeV but becomes consistent at larger values, although there are larger statistical errors. The B^0 transverse momentum is inconsistent for the whole momentum range, but is approximately consistent at $> 20\,\text{GeV}$ (where there are fewer events). The pseudorapidity is shifted to larger values for data compared to MC. The B^0 transverse momentum and pseudorapidity will be reweighted in two dimensions to match the data for the calculation of the acceptance, and this will be taken into account in the systematic uncertainties. The reweighting is done iteratively by taking the ratio of the data and MC for each variable alternately. This reweighting does not improve the discrepancies in the daughter momentum distributions, which are described below.

There is a slight discrepancy in the momenta and transverse momenta distributions for the J/ψ as seen in Figure 6.2. The discrepancy is again larger at small momenta, but becomes close to one at approximately 40 GeV in momentum and 3 GeV for transverse momentum. There is a similar pattern for the momenta of the daughters of the J/ψ which are shown in Figures 6.3 and 6.4. When the momenta reaches around 20 GeV for both μ^+ and μ^- the data and MC distributions become consistent. The p_T distributions for the $\mu^\pm$ are approximately consistent even at low values. These small discrepancies are found to be negligible for the acceptance correction.

In Figure 6.5 the momenta and transverse momenta of the K^* meson is shown. There is a discrepancy at low momenta which again becomes consistent above approximately 25 GeV. The transverse momentum distribution for the K^* is consistent. The daughters of the K^* have large discrepancies between the data and MC in the momenta and transverse momenta distributions, particularly for the pion. Looking at the residual plots in 6.6 the difference in momenta for the kaon becomes more consistent at approximately 15 GeV but the momentum distribution for the pion (Figure 6.7) is inconsistent until about 70 GeV, although here the number of events are low. In addition the difference in the kaon transverse momentum is quite large at all values. The transverse momentum of the pion has a different shape in MC compared to data, there appears to be an additional shoulder below 1 GeV.

Reweighting the MC in the B^0 transverse momentum and pseudorapidity in

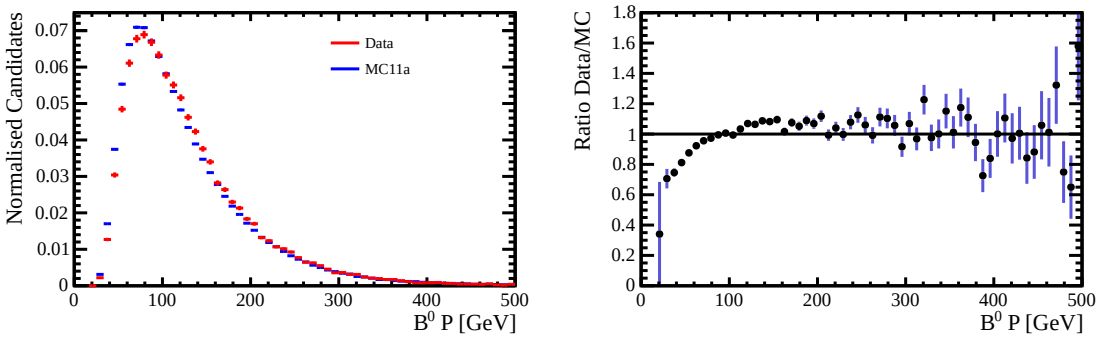

(a) B^0 momentum

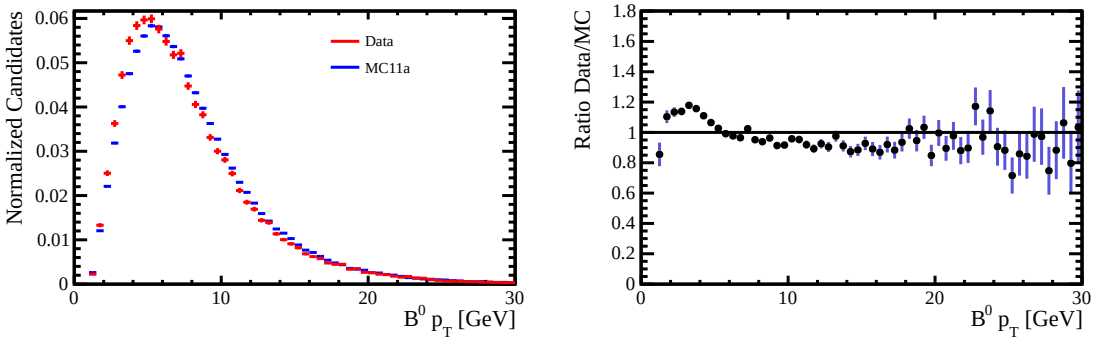

(b) B^0 Transverse momentum

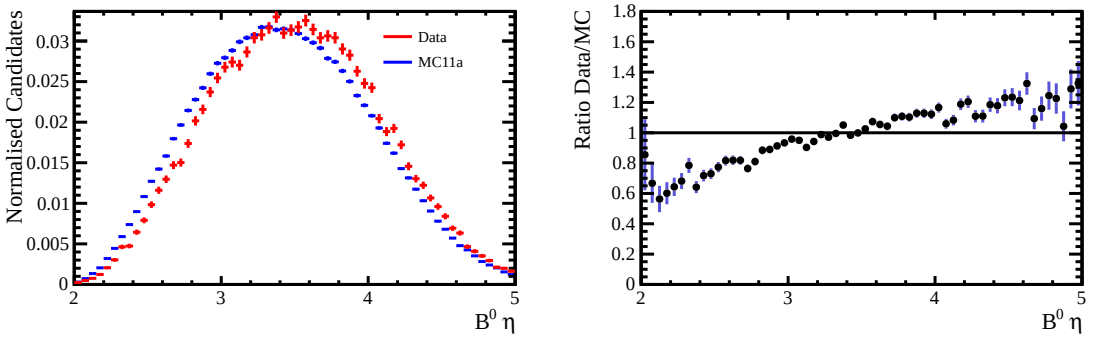

(c) B^0 Pseudorapidity

Figure 6.1: Transverse momentum and pseudorapidity of the B^0 meson in signal MC and sWeighted data, along with the ratio of the two distributions.

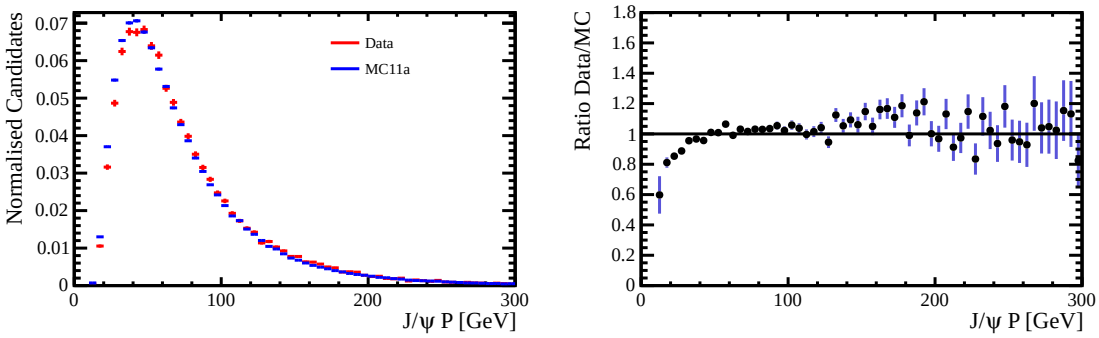

(a) J/ψ momentum

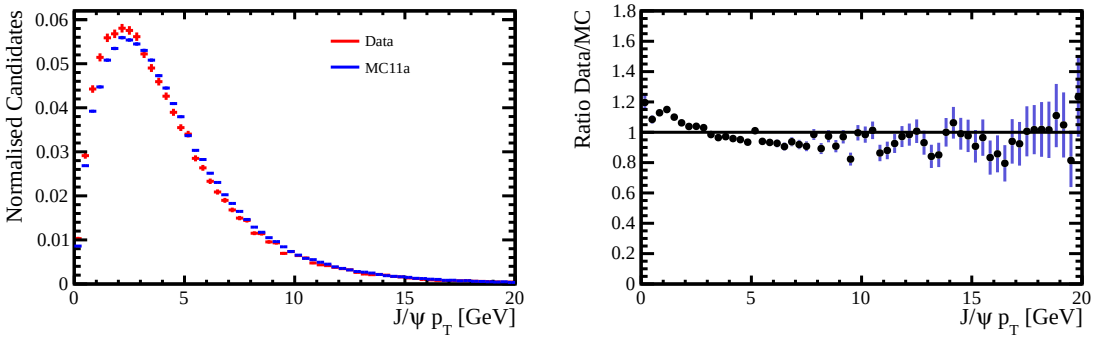

(b) J/ψ transverse momentum

Figure 6.2: Momentum and transverse momentum distributions for the J/ψ particle for signal MC and sWeighted data, with the ratio of the two distributions.

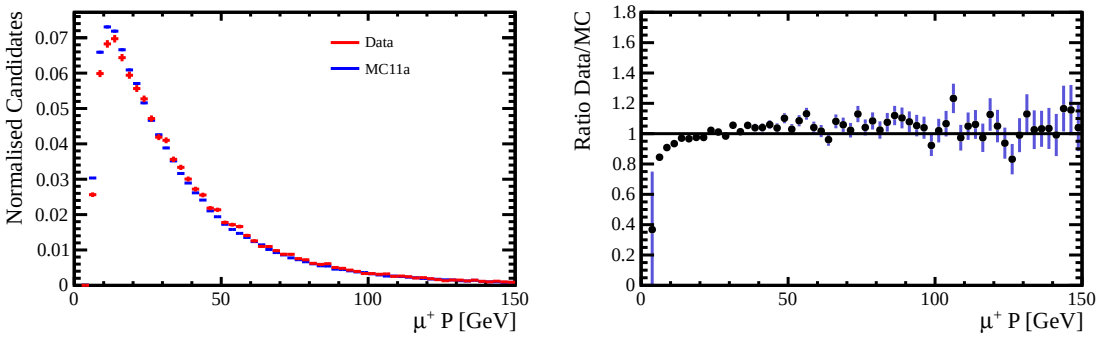

(a) μ^+ momentum

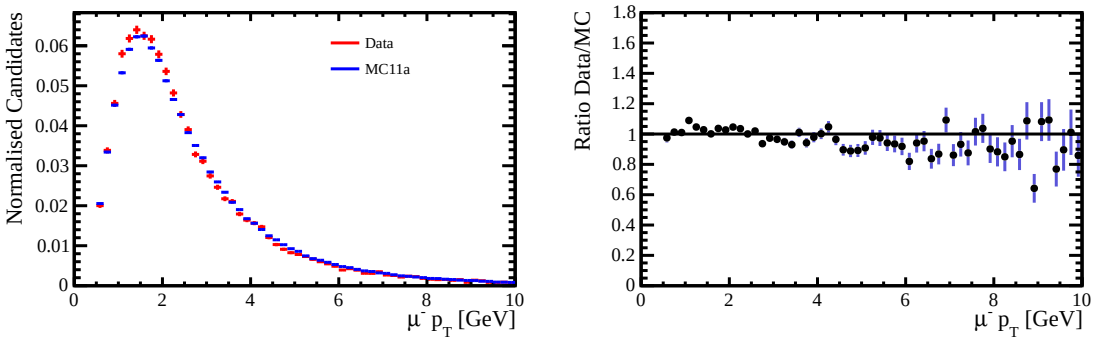

(b) μ^+ transverse momentum

Figure 6.3: Momenta and transverse momenta distributions for the μ^+ particle for signal MC and sWeighted data, with the ratio of the two distributions.

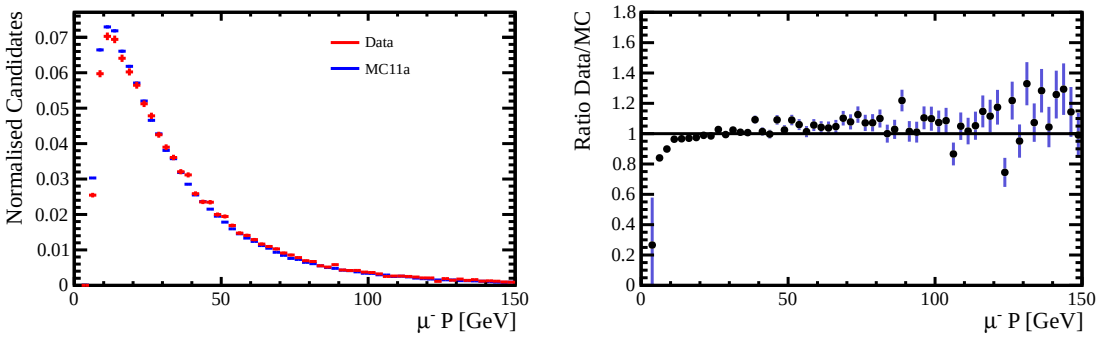

(a) μ^- momentum

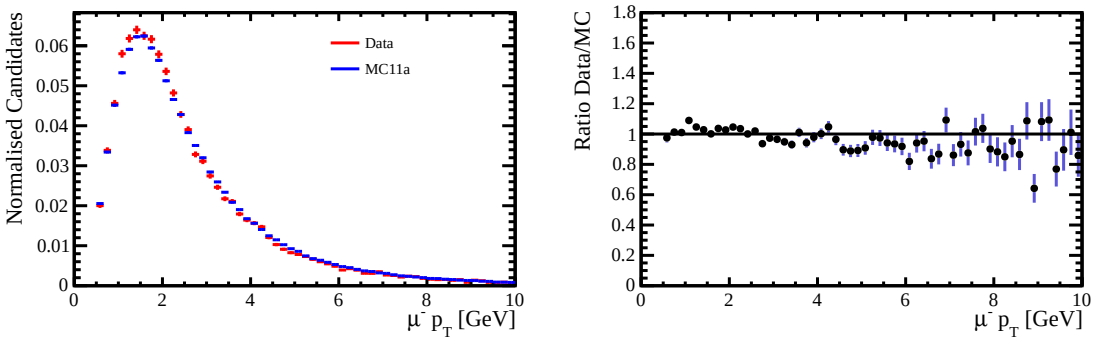

(b) μ^- transverse momentum

Figure 6.4: Momenta and transverse momenta distributions for the μ^- particle for signal MC and sWeighted data, with the ratio of the two distributions.

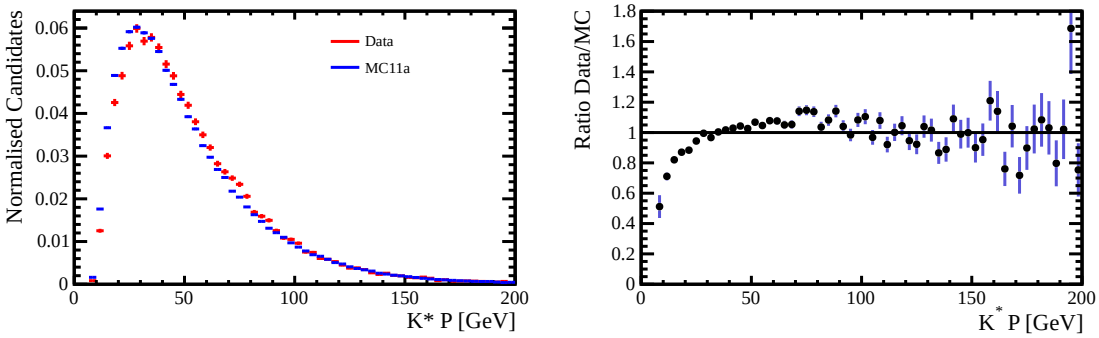

(a) K^* momentum

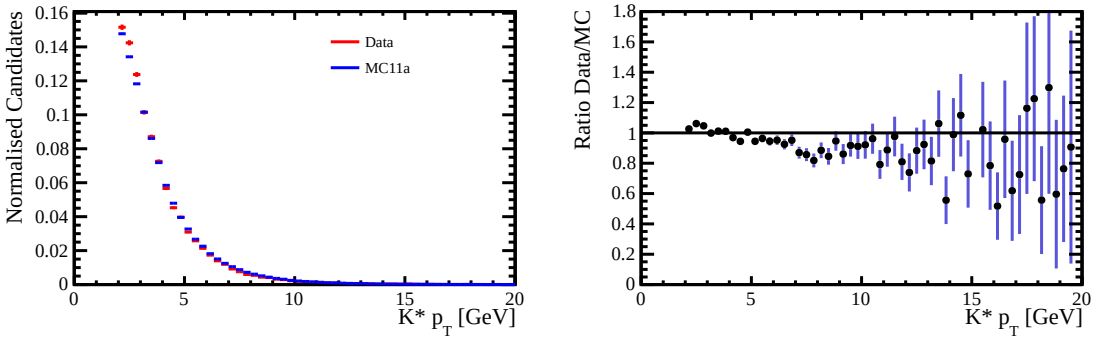

(b) K^* transverse momentum

Figure 6.5: Momentum and transverse momentum distributions for the K^* particle for MC11a and data, with the ratio of the two distributions. The cut at $K^* p_T > 2\,\text{GeV}$ is clear.

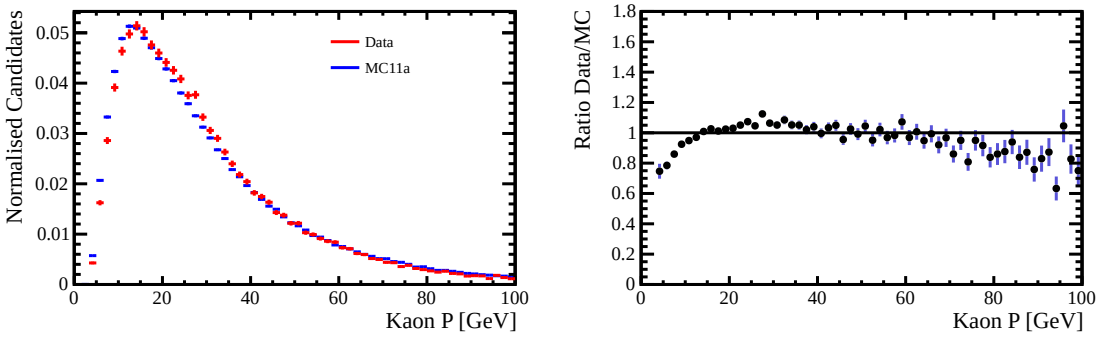

(a) Kaon momentum

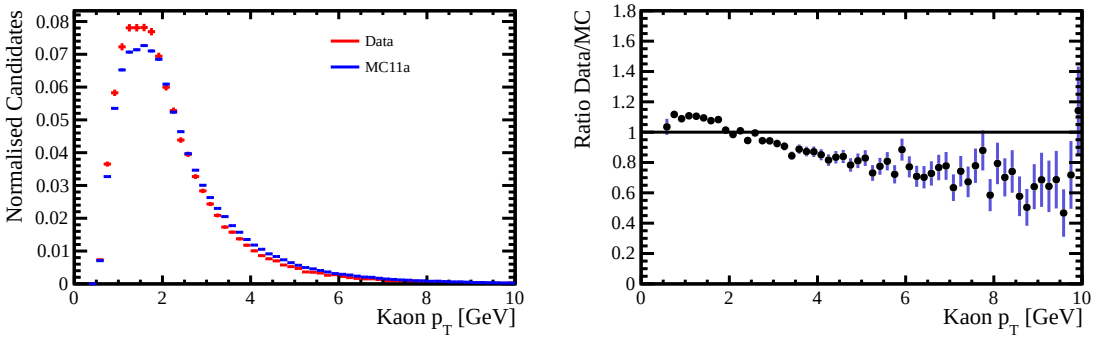

(b) Kaon transverse momentum

Figure 6.6: Momenta and transverse momenta distributions for the kaon for signal MC and sWeighted data, with the ratio of the two distributions.

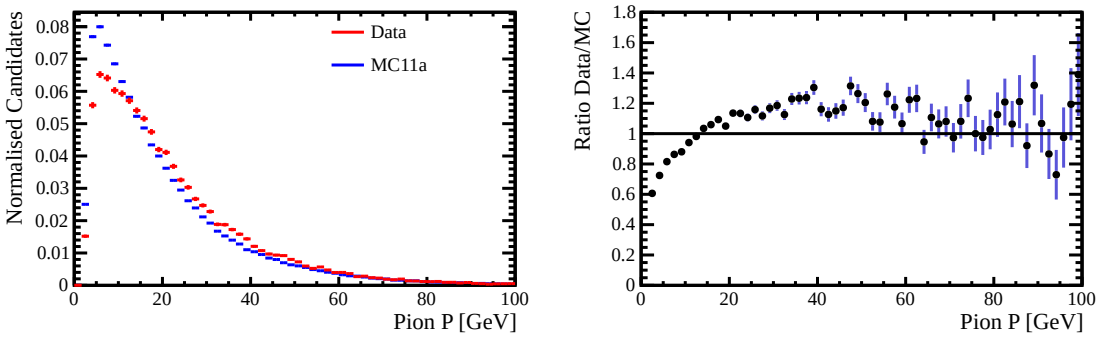

(a) Pion momentum

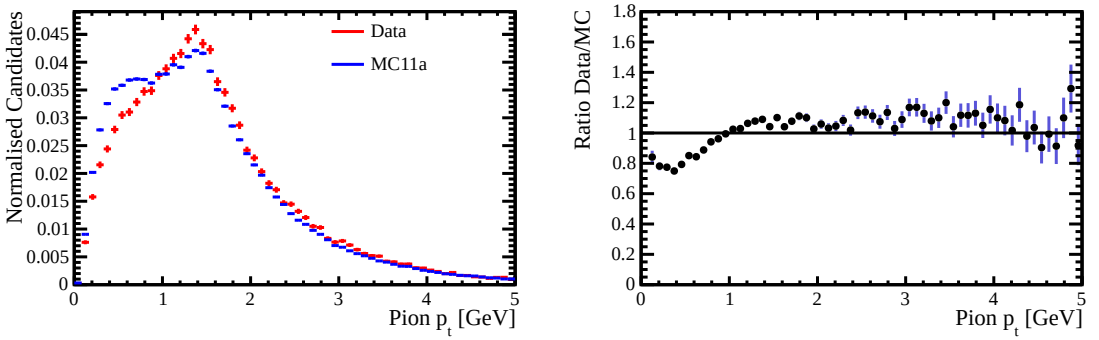

(b) Pion transverse momentum

Figure 6.7: Momenta and transverse momenta distributions for the kaon and pion particles for signal MC and sWeighted data, with the ratio of the two distributions.

two dimensions does not significantly improve the data/MC agreement in the distributions shown for the K^* daughter particles. Reweighting in the MC pion momentum distribution which is that with the greatest deviation from data, does significantly improve the discrepancy in the other K^* daughter variables. Figure 6.8 shows the kaon momentum and transverse momentum distributions as well as the pion transverse momentum, when the MC has been reweighted simultaneously in the B^0 transverse momentum, the pseudorapidity as well as in the pion momentum distribution.

All three MC and data distributions for the transversity angles are shown in Figure 6.9. A χ^2 test was performed for comparing the two distributions for each angle [109]. A p-value is calculated and the hypothesis is rejected if this value is lower than some singificance level. For the $\cos\psi$ distributions a $\chi^2/nDoF$ value of 13.6 with a p-value compatible with zero is found. For the ϕ distributions a $\chi^2/nDoF$ value of 2.7 with a p-value again consistent with zero is found. The hypothesis that either of these distributions are consistent with one another is therefore rejected. For the $\cos\theta$ distribution the test returns a $\chi^2/nDoF$ value of 1.16 and a p-value of 0.27 indicating that these distributions are consistent with each other for a significance level of 0.05.

The angle ψ shows the greatest deviation and is the one between the positive direction of the K^* meson in the K^* frame of reference, and the kaon. Is it therefore correlated with low momentum pions. Reweighting the MC to the pion momentum distribution in the data improves the agreement in the $\cos\psi$ distribution, but is still not ideal, as shown in Figure 6.10. A alternative solution to this is explained in the following.

As mentioned in Section 5.3.3 the angular acceptance correction is calculated using ten weights ξ_j as defined in Equation 5.7, as well as an efficiency histogram. In Table 6.1 the values of these weights are shown for the nominal MC, that which has been reweighted in the B^0 p_T and η, as well as that which has been reweighted in B^0 p_T, η and π momentum. The values are similar for the nominal and MC weighted in B^0 p_T and η. When the MC is reweighted in the pion momentum as well, the difference is larger especially for f_{10} which affects the fit results significantly, in particular for the S-wave contribution. The uncertainties shown in Table 6.1 are due to the available statistics for Monte Carlo.

Investigations into the reason for the large discrepancy between data and MC

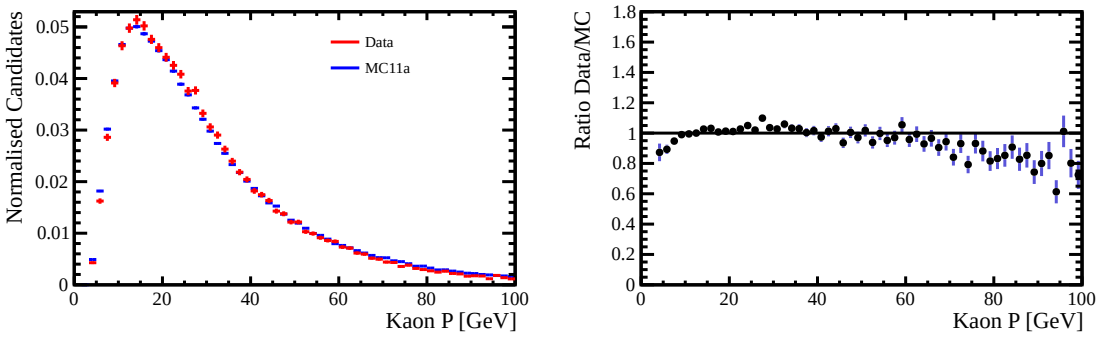

(a) Kaon momentum

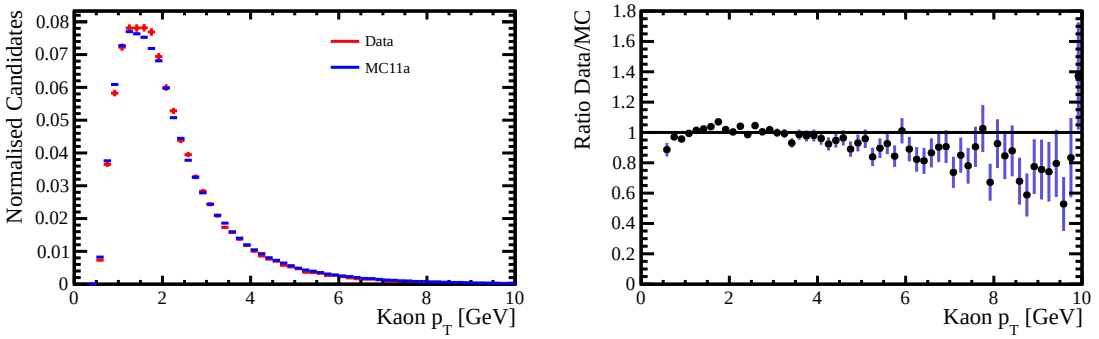

(b) Kaon transverse momentum

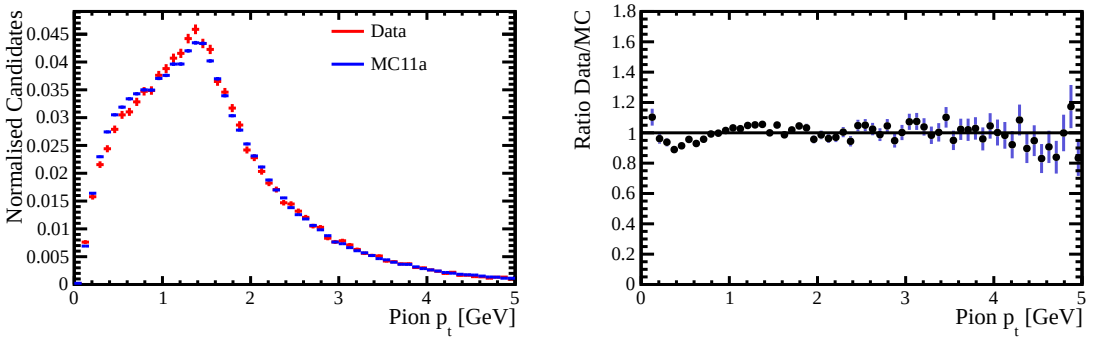

(c) Pion transverse momentum

Figure 6.8: Momenta and transverse momenta distributions for the K^* daughter particles, where the data is sWeighted, and the signal MC has been reweighted to match the data simultaneously in the B^0 transverse momentum, the pseudorapidity and the pion momentum distributions.

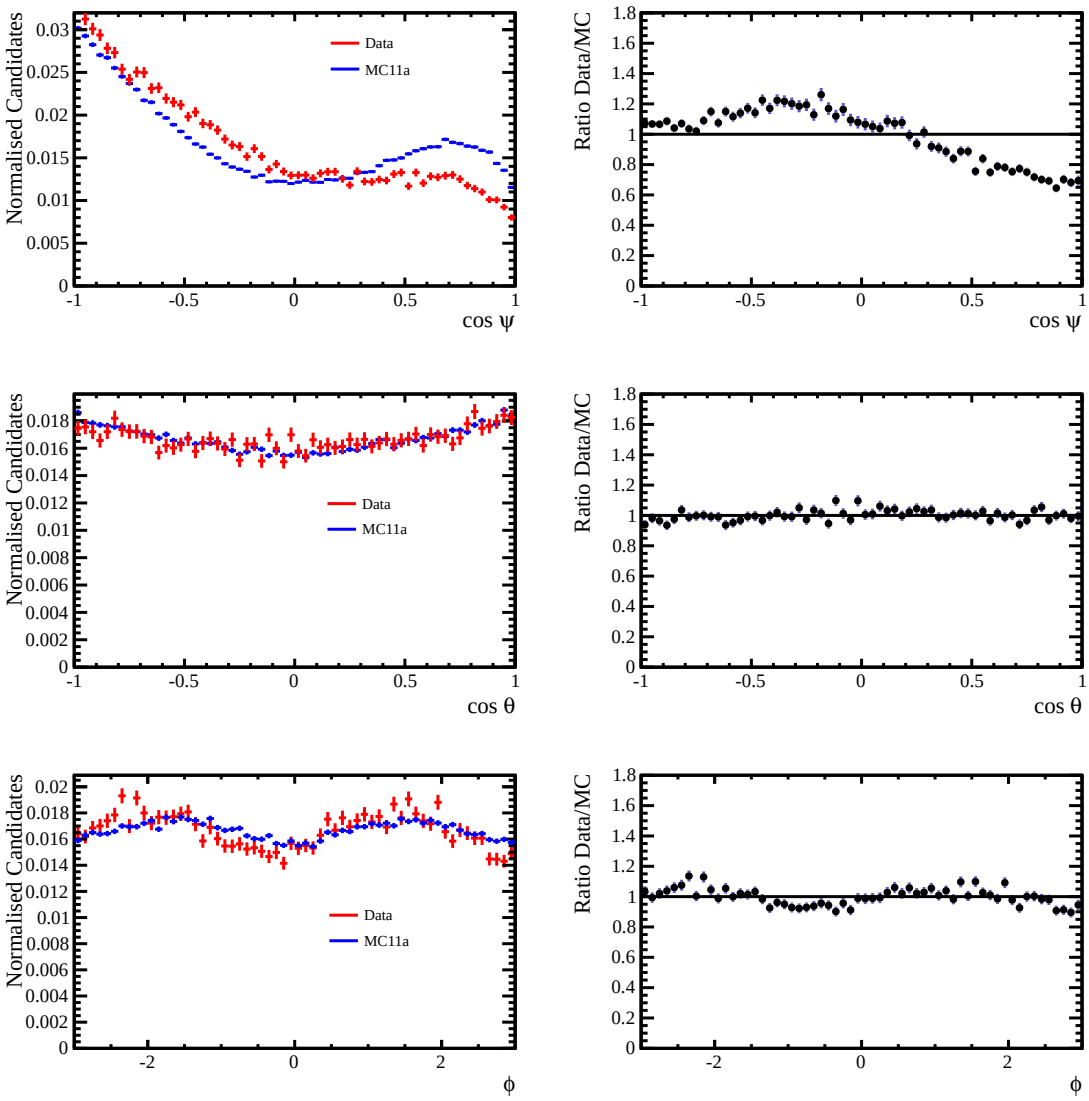

Figure 6.9: Distributions of the transversity angles for signal MC and sWeighted data with the ratio of the two distributions.

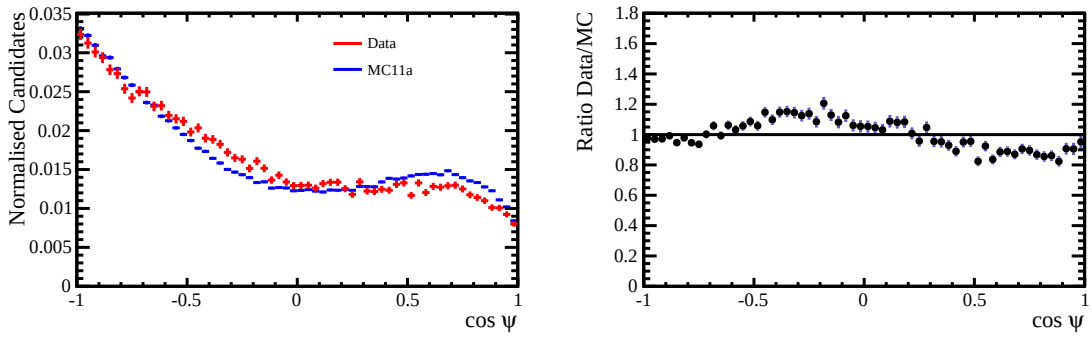

Figure 6.10: $\cos\psi$ distribution for signal MC and sWeighted data, where the MC has been reweighted to match the data simultaneously in B^0 transverse momentum, the pseudorapidity and the pion momentum distributions.

weight	before reweighting	$B^0 p_T$ & η reweight	$B^0 p_T$ & η & π p reweight
ξ_1	0.9002 ± 0.0010	0.8999 ± 0.0010	0.8948 ± 0.0010
ξ_2	1.1387 ± 0.0017	1.1387 ± 0.0017	1.1469 ± 0.0017
ξ_3	1.1443 ± 0.0019	1.1439 ± 0.0019	1.1515 ± 0.0019
ξ_4	0.0010 ± 0.0018	0.0012 ± 0.0018	0.0008 ± 0.0018
ξ_5	-0.0119 ± 0.0011	-0.0114 ± 0.0011	-0.0090 ± 0.0018
ξ_6	-0.0004 ± 0.0011	-0.0004 ± 0.0011	-0.0005 ± 0.0011
ξ_7	1.0092 ± 0.0011	1.0094 ± 0.0011	1.0123 ± 0.0011
ξ_8	-0.0114 ± 0.0017	-0.0135 ± 0.0017	-0.0162 ± 0.0017
ξ_9	0.0007 ± 0.0015	0.0010 ± 0.0015	0.0012 ± 0.0015
ξ_{10}	-0.2753 ± 0.0029	-0.2723 ± 0.0029	-0.4327 ± 0.0029

Table 6.1: Acceptance weights before and after pion momentum reweighting. The uncertainty is statistical only. For a flat angular acceptance the numbers would be: $\xi_1,\ \xi_2,\ \xi_3$ and $\xi_7 = 1$, and for $\xi_4,\ \xi_5,\ \xi_6,\ \xi_8,\ \xi_9$ and $\xi_{10} = 0$.

have been done in order to reduce the systematic uncertainty. The generated MC does not include the S-wave component or the interference between the P-wave and S-wave and it is thought that this may cause or partially cause the discrepancy in $\cos\psi$ and pion momentum. It is a complicated procedure to generate this data, which would have to include interference terms, dependent on $K\pi$ mass. This is not yet available. The S-wave component does not come from a $K^*(892)$ resonance, it is thought to be from the tail of the $K^*(1430)$.

Adding an S-wave component into the MC would have an effect on the shape of the $\cos\psi$ distribution, especially as it goes to 1. This has been shown by generating toys with different fractions of S-wave. A method to reduce the discrepancy in $\cos\psi$ and pion momentum distributions is described here. It is hoped that it provides a better solution than reweighting the MC directly in the pion momentum.

The method is to effectively add S-wave to the nominal MC and then calculate the acceptance iteratively. As a starting point the angular PDF is calculated on an event-by-event basis for two different scenarios: first with no S-wave (with the nominal MC values as input) and then with S-wave where the S-wave results from the nominal fit to data are used as input. This is considered as the best estimate of S-wave in the first instance. The ratio of the two scenarios is used to reweight the MC in the three transversity angles. This reweighting yields an MC sample which represents signal with both P and S-wave. However, when the acceptance weights are calculated by dividing a histogram of fully simulated events by a histogram of PDF generated events, then this reweighting has no effect. This is because the weights included per event in the numerator of the calculation are cancelled by the same change in the denominator of the calculation. It is emphasised that this reweighting is done not to change the acceptance factors but to reduce the discrepancy between data and MC by better inclusion of the underlying physics in the MC.

This method, of course, assumes that the S-wave fraction determined from data is correct (which a priori is not clear). Therefore an iterative method is used. The procedure is the following:

1. The MC is reweighted in the three angles as described above with the S-wave results from data as the best guess. The acceptance is not changed.

2. The remaining residual difference in the pion and kaon momentum is taken

weight	Nominal	Iteration 1	Iteration 2	Iteration 3	Iteration 4
ξ_1	0.9046	0.8951	0.8943	0.8942	0.8942
ξ_2	1.1447	1.1604	1.1607	0.1601	1.1596
ξ_3	1.1505	1.1663	1.1666	0.1659	1.1655
ξ_4	0.0004	0.0002	0.0001	0.0001	0.0001
ξ_5	-0.0107	-0.0106	-0.0105	-0.0104	-0.0104
ξ_6	-0.0007	-0.0008	-0.0008	-0.0008	-0.0008
ξ_7	1.0140	1.0202	1.0201	1.0197	1.0194
ξ_8	-0.0130	-0.0123	-0.0125	-0.0126	-0.0126
ξ_9	0.0015	0.0016	0.0016	0.0016	0.0016
ξ_{10}	-0.2739	-0.2938	-0.3045	-0.3108	-0.3145

Table 6.2: Nominal acceptance weights and after each iteration

to reweight the MC events even further to bring the momentum spectra into agreement. The acceptance factors calculated from these events will now be different as this weighting only applies to the numerator of the acceptance calculation. Note that the residual reweighting has to be performed in the pion and kaon momentum as both spectra are correlated and introducing S-wave to the MC has an effect on both variables.

3. This reweighted acceptance is used for a new fit to data.

4. The fit results are used as new input for 1.

5. The procedure is iterated until it converges.

In Table 6.2 the nominal acceptance weights and after each iteration are shown. It is observed that ξ_2, ξ_3 and ξ_{10} change significantly from the nominal conditions to to the first iteration, whereas the following iterations change the acceptance weights only by a small amount. This shows that the method described above converges quickly. The corresponding fit results can be seen in Table 6.3. Note that the reweighting in p_t and η of the B is performed simultaneously. The results after iteration 4 are taken as the true value for the amplitutes and phases.

As expected the most significant change is observed for the S-wave parameters from the nominal scenario to Iteration 1. The S-wave fraction is reduced to (3.7 $\pm$ 0.4)%. The pion momentum spectrum is improved after the final iteration compared to nominal MC (see Figure 6.7). Figure 6.11 shows the pion and kaon

	Nominal	Iteration 1	Iteration 2	Iteration 3	Iteration 4
$\|A_\parallel\|^2$	0.226 ± 0.004	0.221 ± 0.004	0.220 ± 0.004	0.221 ± 0.004	0.221 ± 0.004
$\|A_\perp\|^2$	0.202 ± 0.004	0.198 ± 0.004	0.198 ± 0.004	0.198 ± 0.004	0.198 ± 0.004
$\delta_\parallel$ (rad)	-2.98 ± 0.03	-2.98 ± 0.03	-2.99 ± 0.03	-2.99 ± 0.03	-2.99 ± 0.03
$\delta_\perp$ (rad)	2.93 ± 0.02	2.93 ± 0.02	2.92 ± 0.02	2.92 ± 0.02	2.92 ± 0.02
$\|A_S\|^2$	0.044 ± 0.004	0.039 ± 0.004	0.038 ± 0.004	0.037 ± 0.004	0.037 ± 0.004
δ_S(rad)	2.18 ± 0.03	2.15 ± 0.03	2.14 ± 0.03	2.13 ± 0.03	2.12 ± 0.03

Table 6.3: Corresponding fit results for the iterative method

momentum distributions after the final iteration, after step 1 has been carried out again. Effectively this shows the Monte Carlo with the amount of S-wave the final iteration gives back. A residual difference can still be observed which is attributed to detector effects. The kaon momentum distribution discrepancy is slightly worsened compared to nominal MC, but after reweighting for the S-wave fraction we believe the physics behind the MC is improved, so that this remaining discrepancy is really due to residual geometry effects.

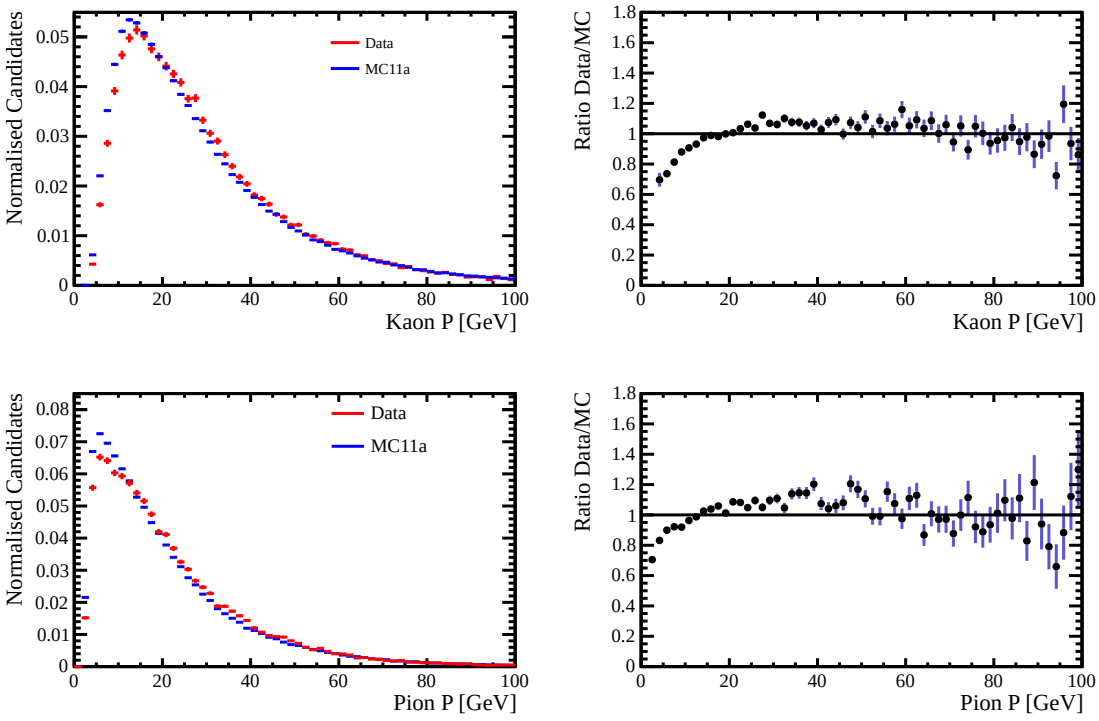

Figure 6.11: Kaon (top) and pion (bottom) momentum spectra after adding S-wave to the MC with the iterative method

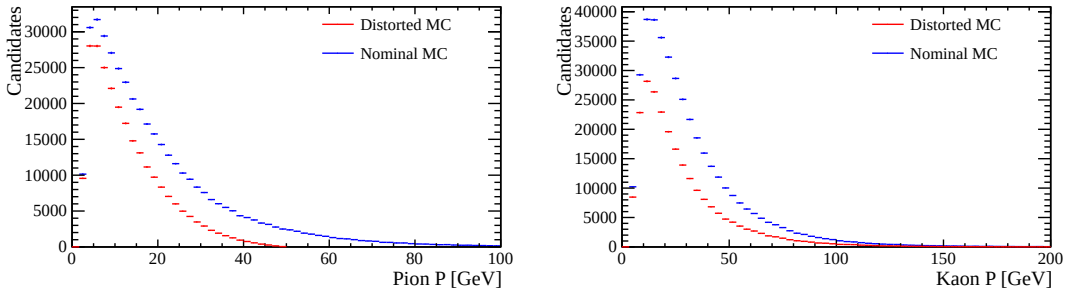

Figure 6.12: The pion and kaon momentum distributions of the nominal MC (blue) and the distorted MC to test the iterative method

To verify this approach two crosschecks have to be made:

- The first crosscheck is to use part of the MC sample, distort the pion momentum distribution for low momenta (which also affects the kaon momentum distribution due to correlations) and use this as if it were real data for the iterative method described above. If this method is correct, the S-wave fraction after the last iteration step should be compatible with 0 as the MC sample does not include S-wave.

- The second crosscheck is to reweight the pion momentum in the three angles at generator level so that no cuts are applied. If the pion momentum is not affected by the reweighting, then the S-wave cannot be the reason for the observed discrepancy.

To perform the first crosscheck, the MC sample is artificially distorted by weighting each event with $w = 1 - \beta \times \pi_p$ where $\beta = 2 \times 10^{-5}$ and π_p is the momentum of the pion for that event. This distorts the MC as seen in Figure 6.12. It mimicks the behaviour of the data but to an intensified level. This MC is treated as if it were data with an true S-wave fraction of zero. The iterative method is used to find this true value.

An initial fit to this distorted MC with nominal acceptance, yields an S-wave fraction of $3.3 \pm 0.1\%$ as can be seen in the fit results in Table 6.4. After the third interation this reduces to zero and the P-wave amplitudes are consistent with the generated values. This shows that the method is effective at finding the true S-wave fraction.

Parameter	Nominal	Iteration 1	Iteration 2	Iteration 3
$\|A_\parallel\|^2$	0.246 ± 0.002	0.235 ± 0.002	0.238 ± 0.002	0.239±0.002
$\|A_\perp\|^2$	0.163 ± 0.002	0.156 ± 0.002	0.159 ± 0.002	0.160±0.002
$\delta_\parallel$ (rad)	-2.51 ± 0.01	-2.50 ± 0.01	-2.50 ± 0.01	-2.51±0.01
$\delta_\perp$ (rad)	3.31 ± 0.01	3.31 ± 0.01	3.31 ± 0.01	3.31 ±0.01
$\|A_S\|^2$	0.033 ± 0.001	0.0090 ± 0.0004	0.0025 ± 0.0002	0.00052± 0.00009
δ_s(rad)	-0.225 ± 0.02	-0.309 ± 0.04	-0.316 ± 0.08	-0.331 ± 0.17

Table 6.4: Fit results for distorted MC after each iteration of acceptance correction

For the second crosscheck, at generator level two MC11a samples have been produced (signal MC and phase space MC). To do this Gauss v41r1 was used. 1M events have been processed neglecting the detector description (generation phase only). The P-and S-wave parameters can effectively be changed by reweighting the pion momentum distribution using the same method as described above (event-by-event using the PDF). The following scenarios have been tested and the pion momentum distributions plotted for each:

- Adding S-wave to the MC with the value from the nominal fit (see Figure 6.13).
- Generating with S-wave and P-wave parameters from data (see Figure 6.14).
- The P-wave amplitudes set to the ones obtained on data (no S-wave) (see 6.15).
- $|A_\perp|^2$ increased from 0.16 to 0.27 and $|A_\parallel|^2$ from 0.24 to 0.39 (see 6.16)
- Taking a phase-space MC with $B_d \to J/\psi K\pi$ which allows to describe the S-wave component (without interference) (see 6.16).

Comparing the corresponding pion momentum distributions it can be seen that adding S-wave to the MC does change the distribution significantly but it is not sufficient to explain the difference we see between data and MC11a. Using the P-wave parameters as well from data does not have a measurable effect. As expected changing only the P-wave amplitudes to the ones obtained from data has almost no effect and even modifying the P-wave amplitudes by a large amount has only a small effect. The phase space MC has an effect to the opposite direction

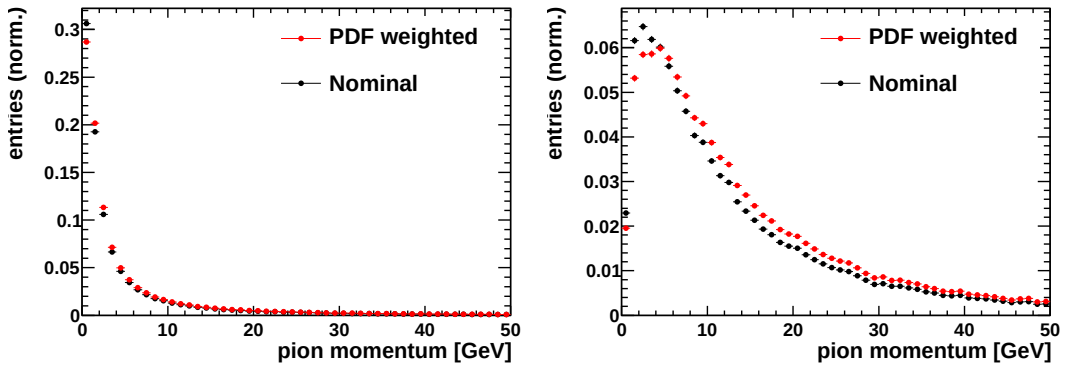

(a) no cuts (b) geometrical and basic kinematic cuts

Figure 6.13: Nominal MC pion momentum distribution (black) compared to MC with added S-wave as seen on data (red) for no cuts (left) and additional geometrical and kinematic cuts (right)

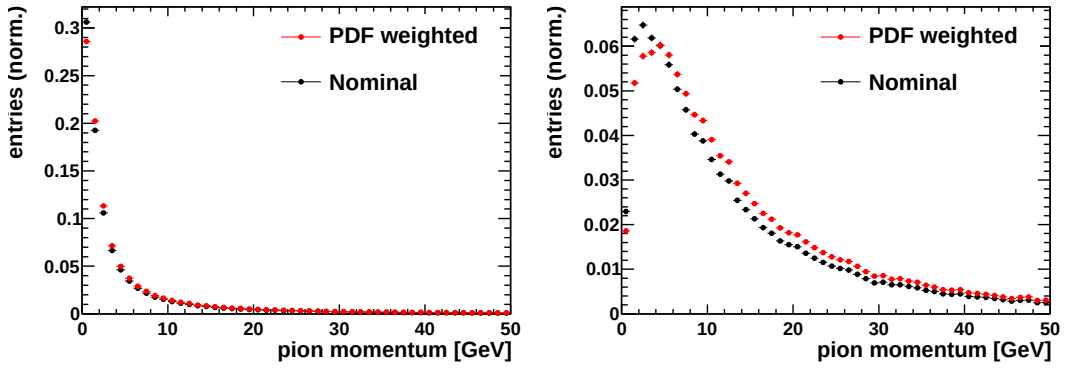

(a) no cuts (b) geometrical and basic kinematic cuts

Figure 6.14: Nominal MC pion momentum distribution (black) compared to MC with P- and S-wave parameters as seen on data (red) for no cuts (left) and additional geometrical and kinematic cuts (right)

as needed to decrease the difference between data an MC. Note that the phase space MC does not include interference effects.

To conclude, adding S-wave to the MC affects the pion momentum distribution significantly but only explains the difference observed in the fully reconstructed MC to a certain extent. A significant contribution therefore has to come from detector effects.

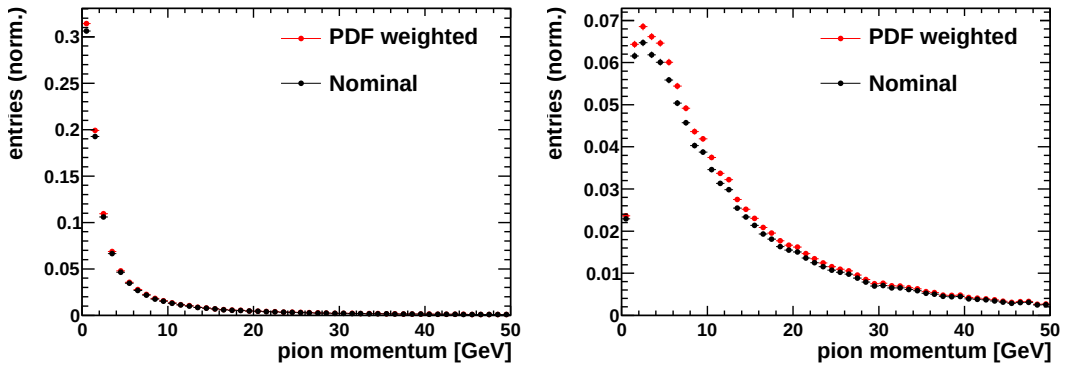

(a) no cuts (b) geometrical and basic kinematic cuts

Figure 6.15: Nominal MC pion momentum distribution (black) compared to MC with P-wave parameters as seen on data (red) for no cuts (left) and additional geometrical and kinematic cuts (right)

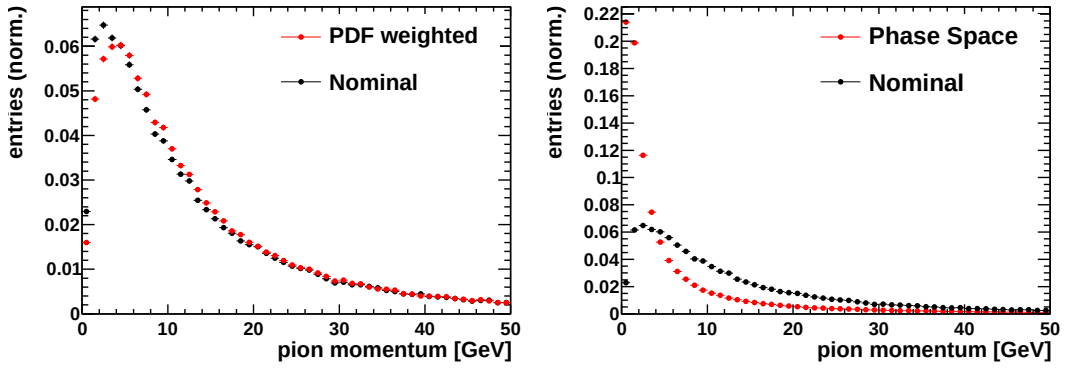

(a) (b)

Figure 6.16: Left: Nominal MC momentum distribution (black) compared to MC with $|A_\perp|^2$ increased to 0.27 and $|A_\parallel|^2$ increased to 0.39 (red); Right: Nominal MC momentum distribution (black) compared to phase space MC (red)

In summary one can say that both missing S-wave in the MC and detector effects can explain the difference in the pion momentum. If one only takes the remaining residual difference between data and MC after the iterative method to reweight the acceptance, then the systematics significantly decrease compared to the previous method taking the full difference between data and MC into account.

6.2 Systematic Uncertainties

The systematic uncertainties are summarised in Table 6.5.

Angular acceptance: Data/MC difference As described in Section 6.1, there are quite large discrepancies between data and MC in some of the kinematic distributions of the final state particles, especially in the pion momentum, or equivalently the decay angle $\cos\psi$. To account for systematic uncertainties, acceptance corrections were determined using MC which had been reweighted to include the S-wave component using an iterative method. The results from the final iteration are taken as the final results. The remaining discrepancy is then reweighted to calculate acceptance weights for the systematic uncertainty. Table 6.5 shows the uncertainties resulting from the data/MC difference. These are the dominating systematic errors.

Angular acceptance: Statistical error To check for systematic effects due to the statistical uncertainties of the acceptance corrections, each bin of the acceptance histogram was smeared independently with a Gaussian function whose width corresponds to the statistical error of the bin. The difference to the nominal physics parameters when the histogram is used in the fit is assigned as systematic error.

Backgrounds from *ghosts* As described in Section 5.2, the *ghosts* background in MC has a significantly different angular distribution compared to the signal. In the MC the ghosts background distribution in the invariant B^0 mass can be fit to with a double Gaussian function. To estimate the systematic error, the parameters of this fit and the yield in MC (shown in Table 5.5 to be 3.48 %) are fixed in the fit to data, and the angular distribution of these events is taken from MC. This mass fit to data is shown in Figure 6.17, where a logarithmic scale is used to show the contribution more clearly. The differences in the amplitudes and phases in the nominal fit compared to the one including ghosts background are used as a systematic error.

Combinatorial Background To account for systematic uncertainties due to the combinatorial background description, the full difference between the cFit

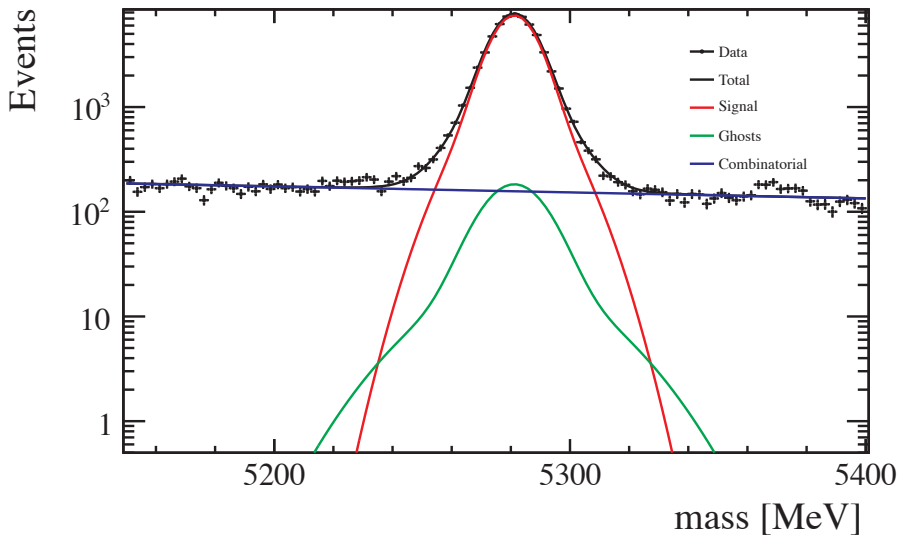

Figure 6.17: cFit to data including the ghosts background which are included for a systematic error. Note the logarithmic scale.

and the sFit is taken as systematic error. These are different methods of subtracting the combinatorial background and should be equivalent, which they are approximately.

Mass model To estimate systematic uncertainties due to the B^0 mass model, the PDF for the mass fit was changed from a double Gaussian to a single Gaussian. The difference to the nominal fit is assigned as systematic error. This was repeated separately with a Crystal Ball function, and the error is summed in quadrature for the systematic error.

The total systematic error is the quadratic sum of the single systematic uncertainties. In summary the precision of the results for $\delta_\perp$,$\delta_\parallel$, $|A_S|^2$ and δ_s are limited by the systematic errors. The dominating error comes from the Data/MC difference that is observed in the momentum distribution of the pion.

	$\lvert A_\parallel\rvert^2$	$\lvert A_\perp\rvert^2$	$\delta_\parallel$	$\delta_\perp$	$\lvert A_S\rvert^2$	δ_S
Data/MC	0.005	0.004	0.01	0.01	0.007	0.06
Statistical error acceptance	0.001	0.001	0.01	0.01	0.001	0.01
Ghost background	0.001	0.001	0.00	0.00	0.002	0.01
Background treatment	0.002	0.001	0.00	0.01	0.001	0.00
Mass Model	0.001	0.001	0.00	0.00	0.003	0.00
Quadratic Sum	0.006	0.004	0.01	0.02	0.008	0.06
Statistical Error	0.004	0.004	0.03	0.02	0.004	0.03

Table 6.5: Systematic uncertainties as described in the text.

Parameters	BaBar[78] (2007)	LHCb Previous [75] (2011)	LHCb preliminary (2012)
$\lvert A_\parallel\rvert^2$	$0.211 \pm 0.010 \pm 0.006$	$0.253 \pm 0.020 \pm 0.016$	$0.217 \pm 0.004 \pm 0.002$
$\lvert A_\perp\rvert^2$	$0.233 \pm 0.010 \pm 0.005$	$0.191 \pm 0.019 \pm 0.017$	$0.206 \pm 0.004 \pm 0.004$
$\delta_\parallel$ (rad)	$-2.93 \pm 0.08 \pm 0.04$	$-2.87 \pm 0.11 \pm 0.10$	$-2.98 \pm 0.03 \pm 0.01$
$\delta_\perp$ (rad)	$2.91 \pm 0.05 \pm 0.03$	$3.02 \pm 0.09 \pm 0.07$	$2.97 \pm 0.02 \pm 0.01$

Table 6.6: Results with no S-wave and comparison to BaBar and previous LHCb results which used the 2010 data set only.

6.3 Results

6.3.1 Without the S-wave component

As described in Chapter 4, results from previous experiments have not included the S-wave component, but have included it as a systematic uncertainty. For this reason the results with no S-wave component are initially presented for comparison. In Table 6.6, the preliminary result of this analysis is shown compared to the previous published LHCb results from 2011 which also excluded the S-wave component. This analysis and the previous LHCb analysis use independent data sets, the previous measurement using data from 2010 only. The most recent BaBar result is also shown which is the most precise published measurement to date. The statistical uncertainties are the first shown, and the systematic are the second. Within the errors both LHCb results are consistent. The BaBar results are consistent with the results presented here.

These results are also consistent with the previous results in Table 4.5. It is clear that both the statistical and systematic uncertainties are smaller than any

Parameters	Results (reduced dataset)
$\|A_\parallel\|^2$	0.236 ± 0.014
$\|A_\perp\|^2$	0.177 ± 0.019
$\delta_\parallel$ (rad)	-2.82 ± 0.12
$\delta_\perp$ (rad)	3.06 ± 0.09

Table 6.7: Fit results with dataset from 2010 only (36 pb^{-1}).

of the previous experiments. The results with no S-wave are statistically limited except for $|A_\perp|^2$ which has the same statistical and systematic error.

As an additional study, the dataset was replaced with the one from the previous LHCb result (36 pb^{-1}) in order to compare the results. The selection used was the same as for the previous analysis in [75] (the pion PID and the K^{0*} p_T cuts are not included and the B^0 mass range is reduced to a $\pm$45 MeV window). The angular acceptance is calculated from the same Monte Carlo sample as for the previous analysis, but due to a lack of information has not been reweighted in the distributions of the daughter particles. This is not expected to have a large effect. The peaking background from the previous analysis is not included in the fit due to a lack of information about this. The number of signal events in the dataset is 2656$\pm$42, consistent with the number in the previous analysis (2631$\pm$66). The results with statistical errors only are shown in Table 6.7. The central values are compatible with the results from the previous analysis, shown in Table 6.6.

6.3.2 Including the S-wave component

The results of the maximum likelihood fit including the S-wave are summarised in Table 6.8. The first uncertainty is the statistical and the second is systematic. The convention for the phases corresponds to the resolution of the ambiguity which is described later in this Chapter (section 6.5). The projection plots of the invariant mass, the proper time and the transversity angles can be seen in Figures 6.18 and 6.19. To show the stability of the errors Δ Log Likelihood scans of the physics parameters are shown in Figure 6.20. There are clear minima for each parameter. The correlation matrix of the fit in Table 6.9 shows that there is almost no correlation between the lifetime parameters $f_{\tau,1}^{\rm LL}$, $\tau_1^{\rm LL}$ and $\tau_2^{\rm LL}$ and

Parameter	Central Value ± stat. ± syst.
$\|A_\parallel\|^2$	0.221 ± 0.004 ± 0.006
$\|A_\perp\|^2$	0.198 ± 0.004 ± 0.004
$\delta_\parallel$ (rad)	-2.99 ± 0.03 ± 0.01
$\delta_\perp$ (rad)	2.92 ± 0.02 ± 0.02
$\|A_S\|^2$	0.037 ± 0.004 ± 0.008
δ_S(rad)	2.12 ± 0.03 ± 0.06

Table 6.8: Final fit results with S-wave including statistical and systematic errors.

the polarisation amplitudes or strong phases. A fit with and without the lifetime acceptance correction shows as expected, no difference in the angular amplitudes and phases.

A complete list of results for all other parameters floating in the fit can be found in Table 6.10: m_{B_d} is the mass of the B, $f^{\sigma}_{m,1}$, $\sigma^{sig}_{m,1}$ and $\sigma^{sig}_{m,2}$ are the fraction of the first Gaussian, the width of the first Gaussian and the width of the second Gaussian, respectively; α^{LL}_m is the exponential coefficient for the background description of the B mass; f_{sig} denotes the signal fraction; the two lifetimes and the fraction of the long lived background are described by τ^{LL}_1, τ^{LL}_2 and $f^{LL}_{\tau,1}$ respectively. In this Table (which shows the statistical error only), the fitted value of Γ is also included. This value is consistent with the world average value of $0.658 \pm 0.003\,\mathrm{ps}^{-1}$ [7].

6.4 Discussion of Results

It is clear that once the S-wave component is included the systematic errors become dominant for the strong phases, and the S-wave parameters. This is mainly due to the discrepancy between data and MC which has already been described. When the S-wave component is included in the fit, the values for $|A_\parallel|^2$ and $|A_\perp|^2$ and the strong phases are consistent with the results with no S-wave included. These results are also consistent with those from CDF, D0 and Belle. $|A_\perp|^2$ is not quite consistent with the BaBar result within the errors but the other parameters remain consistent. However, including an S-wave component is expected to change the value of $|A_\perp|^2$ which can be seen from the large correlation coefficient between $|A_\perp|^2$ and $|A_S|^2$ in Table 6.9.

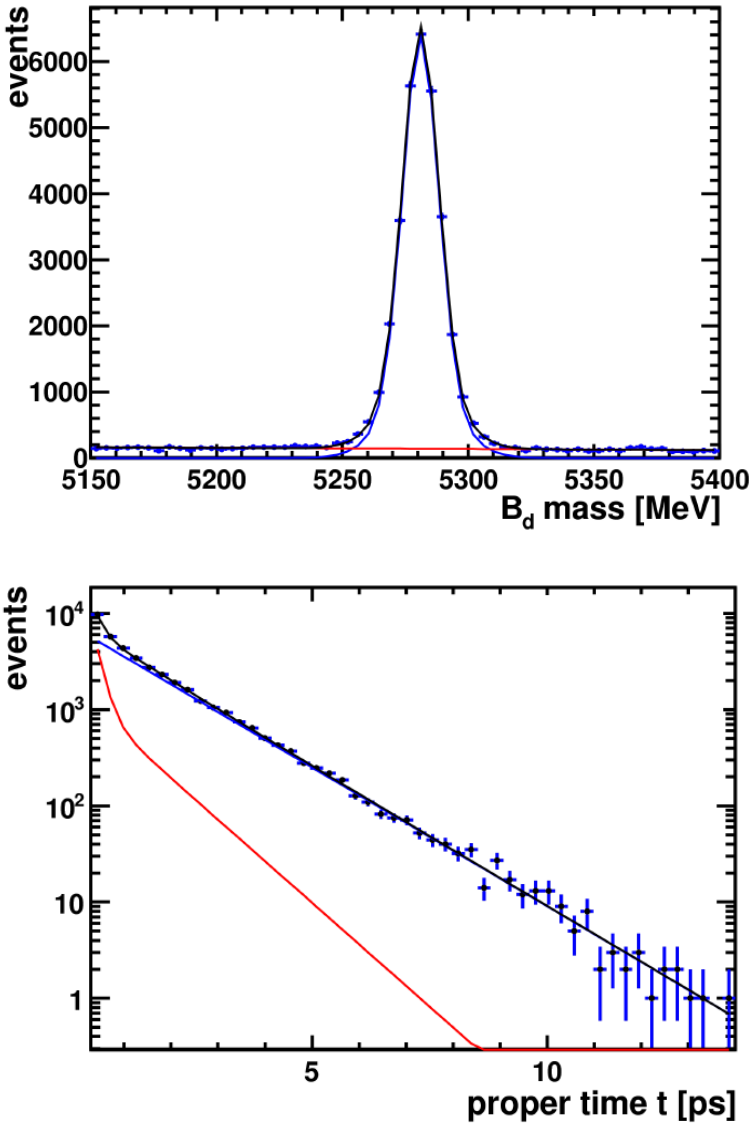

Figure 6.18: Invariant mass and proper time projection plots from fit to data. The black dots show the data points, the black curve the total fit, the blue curve the signal fit and the red curve the background fit.

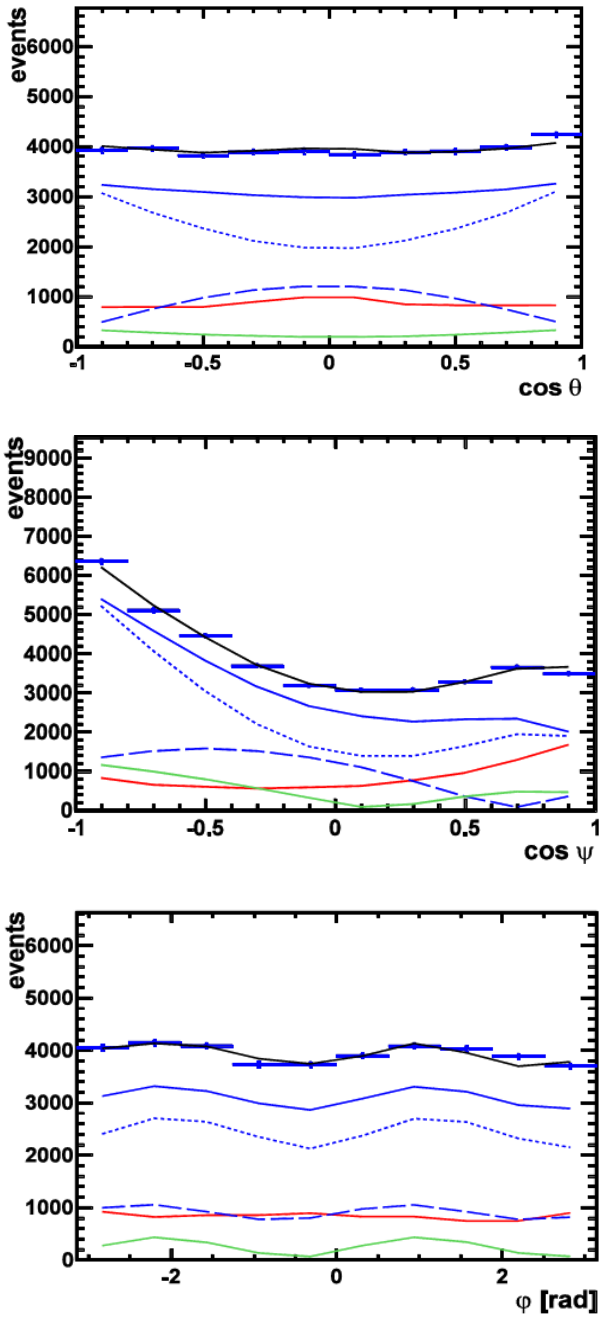

Figure 6.19: Projections of the transversity angles from fit to data. The black points show the data points, the black curve the total fit, the blue curve the signal fit (dotted blue CP-even contribution, dashed blue CP-odd contribution, the red curve the background fit and the green curve the S-wave contribution.

	Γ	$\lvert A_\parallel\rvert^2$	$\lvert A_\perp\rvert^2$	$\lvert A_s\rvert^2$	$\delta_\parallel$	$\delta_\perp$	δ_s	$f^{\sigma}_{\mathrm{m},1}$	$\sigma^{sig}_{\mathrm{m},1}$	$\sigma^{sig}_{\mathrm{m},2}$	m_{B_d}	$f^{\mathrm{LL}}_{\tau,1}$	τ^{LL}_1	τ^{LL}_2	α^{LL}_{m}	f_{sig}
Γ	1.00	-0.00	0.01	-0.01	0.00	-0.00	0.00	-0.00	0.00	0.01	0.00	0.03	0.00	0.05	0.01	0.07
$\lvert A_\parallel\rvert^2$		1.00	**-0.63**	0.01	-0.14	-0.08	0.00	-0.00	-0.00	-0.00	0.00	-0.00	0.00	0.00	-0.00	-0.01
$\lvert A_\perp\rvert^2$			1.00	**-0.47**	0.09	-0.09	-0.44	-0.00	0.00	0.00	-0.00	0.00	-0.00	-0.00	0.00	0.02
$\lvert A_s\rvert^2$				1.00	0.11	0.32	**0.81**	-0.00	-0.01	-0.01	0.00	-0.01	0.00	0.00	-0.01	-0.04
$\delta_\parallel$					1.00	**0.66**	0.18	0.00	0.00	0.00	-0.00	0.00	0.00	0.00	0.00	0.01
$\delta_\perp$						1.00	0.36	0.00	0.00	0.00	-0.00	-0.00	0.00	0.00	-0.00	-0.01
δ_s							1.00	0.00	0.00	0.01	0.00	0.00	-0.00	0.00	0.00	0.01
$f^{\sigma}_{\mathrm{m},1}$								1.00	**0.91**	**0.93**	-0.01	0.01	-0.02	-0.06	0.01	0.12
$\sigma^{sig}_{\mathrm{m},1}$									1.00	**0.8**	-0.01	0.01	-0.02	-0.05	0.01	0.11
$\sigma^{sig}_{\mathrm{m},2}$										1.00	-0.01	0.03	-0.02	-0.08	0.03	0.21
m_{B_s}											1.00	0.00	-0.00	0.00	0.03	-0.00
$f^{\mathrm{LL}}_{\tau,1}$												1.00	-0.45	0.35	0.01	0.05
τ^{LL}_1													1.00	**0.56**	-0.00	-0.02
τ^{LL}_2														1.00	-0.00	-0.03
α^{LL}_{m}															1.00	0.05
f_{sig}																1.00

Table 6.9: Correlation matrix for fit results in Table 6.8. The values in bold show the larger correlations. Note the value of -0.47 between $|A_\perp|^2$ and $|A_S|^2$.

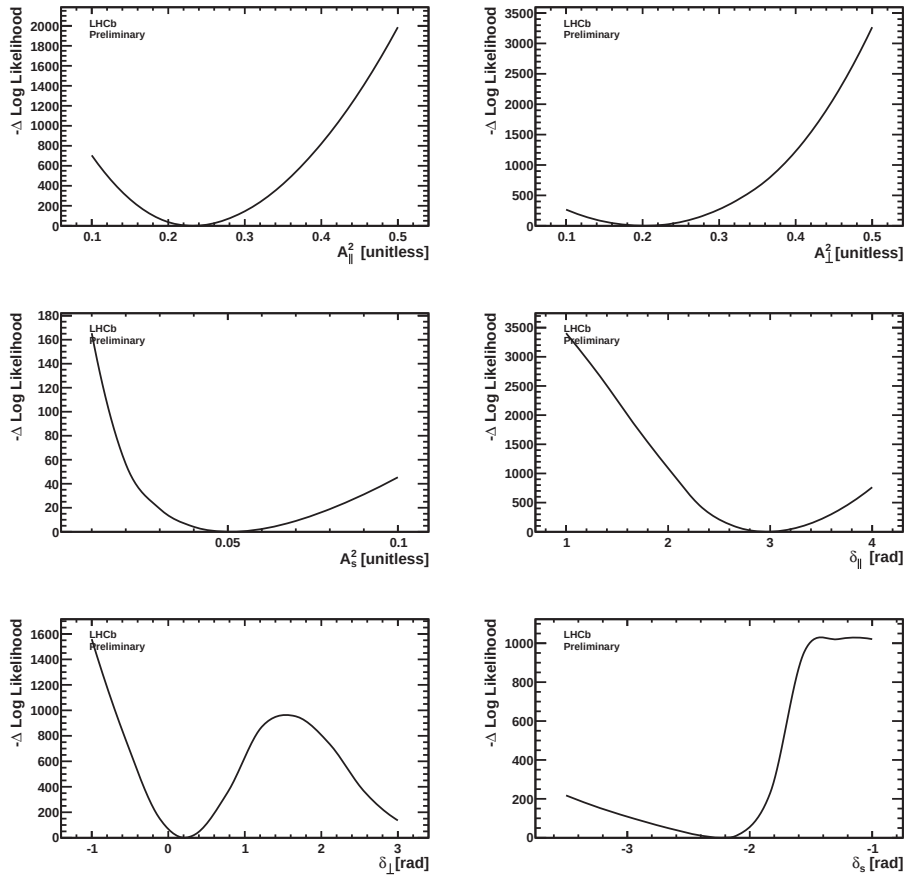

Figure 6.20: Δ Log Likelihood scans of the physics parameters.

In Chapter 4.3 it was hypothesised that the polarization angles for $B_s^0 \to J/\psi\phi$ should be similar to those for this analysis. The most recent LHCb results are shown in Table 6.11. Comparison with these results show that $|A_\parallel|^2$, $\delta_\parallel$ and $\delta_\perp$ are consistent, but $|A_\perp|^2$ is 2.8σ away from the central value. This is not a significant deviation but will be investigated further with more data.

It was also hypothesised that any deviation in strong phases from π or 0 is evidence for final state interactions (see Section 4.3.1). This was shown by BaBar [80] and Belle [79] to be the case. The results here show that $\delta_\parallel$ deviates from $\pm\pi$ by 0.15 ± 0.03 rad for $B^0 \to J/\psi K^{*0}$ and -0.24 ± 0.40 rad for $B_s^0 \to J/\psi\phi$. $\delta_\perp$ differs by -0.22 ± 0.03 rad for $B^0 \to J/\psi K^{*0}$ and by 0.0 ± 0.3 rad for $B_s^0 \to J/\psi\phi$. The results for $B^0 \to J/\psi K^{*0}$ clearly demonstrate the presence of final state interactions, whereas the $B_s^0 \to J/\psi\phi$ are inconclusive.

parameter	result
Γ	0.650 ± 0.003
m_{B^0}	5281.18 ± 0.04
$f^{\sigma}_{\mathrm{m},1}$	0.749 ± 0.020
$\sigma^{sig}_{\mathrm{m},1}$	7.11 ± 0.09
$\sigma^{sig}_{\mathrm{m},2}$	13.80 ± 0.37
f_{sig}	0.791 ± 0.002
$f^{\mathrm{LL}}_{\tau,1}$	0.545 ± 0.012
τ^{LL}_{1}	0.168 ± 0.005
τ^{LL}_{2}	1.021 ± 0.022
$\alpha^{\mathrm{LL}}_{\mathrm{m}}$	0.0012 ± 0.0001

Table 6.10: Values of the fitted detector and physics parameters (statistical error only)

Parameter	$B^0 \to J/\psi K^{*0}$ Result	$B^0_s \to J/\psi\phi$ Result [25]
$\lvert A_{\parallel}\rvert^2$	$0.221 \pm 0.004 \pm 0.006$	$0.231 \pm 0.012 \pm 0.027^*$
$\lvert A_{\perp}\rvert^2$	$0.198 \pm 0.004 \pm 0.004$	$0.246 \pm 0.010 \pm 0.013$
$\lvert A_0\rvert^2$	$0.581 \pm 0.006 \pm 0.007$	$0.523 \pm 0.007 \pm 0.024$
$\delta_{\parallel}$ (rad)	$-2.99 \pm 0.03 \pm 0.01$	$2.90 \pm 0.36 \pm 0.07$
$\delta_{\perp}$ (rad)	$2.92 \pm 0.02 \pm 0.02$	$[2.82, 3.47] \pm 0.13$

Table 6.11: Results of $B^0 \to J/\psi K^{*0}$ Angular analysis including S-wave (not quoted) compared to recent $B^0_s \to J/\psi\phi$ analysis by LHCb [25]. $^*|A_{\parallel}|^2$ has been calculated from the other amplitudes, with the errors propagated.

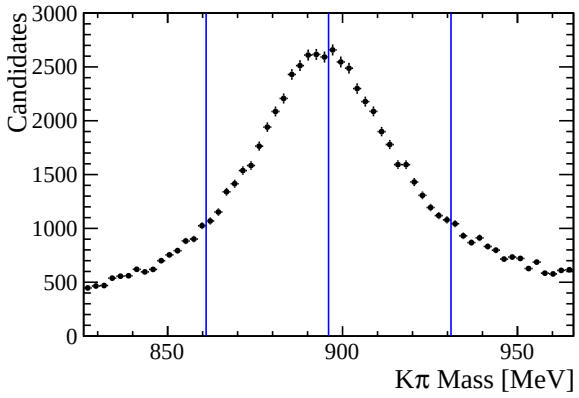

Figure 6.21: Bins of $K\pi$ mass.

The S-wave fraction is measured to be $3.7 \pm 0.4 \pm 1.5\%$ in a window of ± 70 MeV around the K^* mass. This is consistent with the measurement presented in the 2011 LHCb note which was 5.1 ± 2.2 %. BaBar [78] measured an S-wave fraction of 7.3 ± 1.8 % in a $K\pi$ mass range of 200 MeV.

6.5 Resolving the ambiguity in the phase

In order to resolve the ambiguity in the phase, a simultaneous fit in bins of the $K\pi$ invariant mass was carried out with the two different solutions of the phases. The $K\pi$ mass was split up into four equal bins which can be seen in Figure 6.21. New fitting parameters were defined, which are the same as in [91]. The P-wave component is defined as usual to be $A_p = A_0 + A_\perp + A_\parallel$, and the S-wave is defined as a fraction F_s. The new fitting parameters are defined below:

$$R_\perp^2 = \frac{A_\perp^2}{A_p^2}, \qquad R_\parallel^2 = \frac{A_\parallel^2}{A_p^2}, \qquad F_s = \frac{A_s^2}{A_p^2 + A_s^2}, \tag{6.1}$$

These parameters have the advantage that $R_\perp$ and $R_\parallel$ are independent of the $K^+\pi^-$ mass, and only the S-wave parameters vary with it. In the simultaneous fit F_s and δ_s are allowed to vary for each bin as well as the signal fraction. The fit results for one solution of δ_s are shown in Table 6.12, the other solution is the same but for the corresponding values of the phases. The two solutions for δ_s

are shown in Figure 6.22, the blue falling is the physical one, because the relative phase should decrease over the $K\pi$ mass (see section 4.3). This means we take the solution that δ_s is positive. The $B_s^0 \to J/\psi\phi$ analysis found the same solution and this validates their result [91].

Parameter	Result
Γ	0.650 ± 0.003 ps^{-1}
$\lvert R_\parallel \rvert^2$	0.224 ± 0.004
$\lvert R_\perp \rvert^2$	0.199 ± 0.004
$\delta_\parallel$	-2.99 $\pm$ 0.03 rad
$\delta_\perp$	2.92 $\pm$ 0.02 rad
m_{B_d}	5281.18 $\pm$ 0.04 MeV
$f_{\sigma_m{}^1}$	0.766 ± 0.018
$\sigma_m{}^1$	7.18 $\pm$ 0.08 MeV
$\sigma_m{}^2$	14.3 $\pm$ 0.4 MeV
f_{LL1}	0.971 ± 0.002
τ_{LL1}	0.166 ± 0.005 ps
τ_{LL2}	1.01 $\pm$ 0.02 ps
αM_{pr}	0.0012 ± 0.0001
$\lvert F_S{}^2 \rvert(1)$	0.076 ± 0.006
$\delta_S(1)$	3.19 $\pm$ 0.15 rad
$f_{sig}(1)$	0.642 ± 0.006
$\lvert F_s \rvert^2(2)$	0.029 ± 0.004
$\delta_s(2)$	2.55 $\pm$ 0.08 rad
$f_{sig}(2)$	0.849 ± 0.002
$\lvert F_s \rvert^2(3)$	0.039 ± 0.006
$\delta_S(3)$	1.73 $\pm$ 0.03 rad
$f_{sig}(3)$	0.846 ± 0.003
$\lvert F_s \rvert^2(4)$	0.096 ± 0.014
$\delta_S(4)$	1.32 $\pm$ 0.03 rad
$f_{sig}(4)$	0.659 ± 0.005

Table 6.12: Results of simultaneous fit in four bins of $K\pi$ invariant mass. Only the signal fraction and $|F_S|^2|$ and δ_S are varied for each bin. The parameters that are varied are shown under the double horizonal lines and the result for each bin is shown. The other solution involves the changes of all three phases shown in Equation 4.16. Only statistical errors are shown.

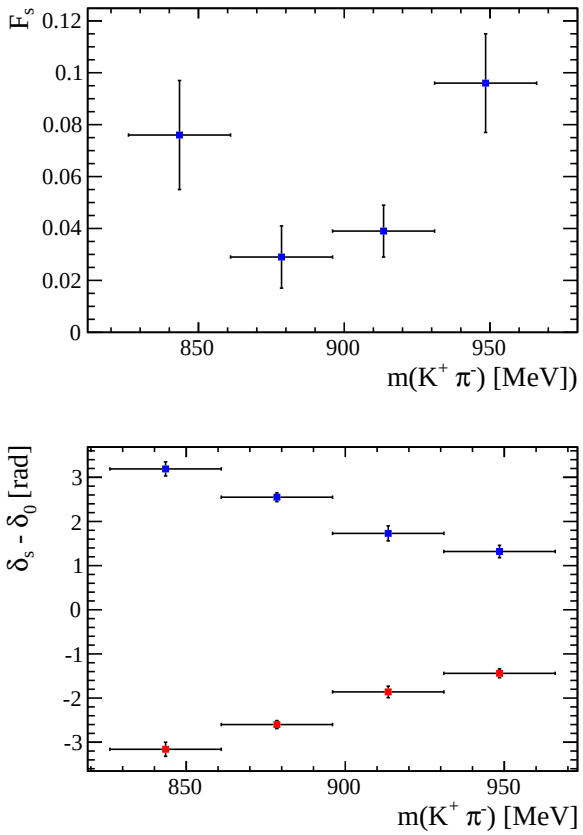

Figure 6.22: Variation of F_s and δ_s in the simultaneous fit in bins of $K\pi$ mass. Here both statistical and systematic errors are plotted.

(a) B^0 30838 signal events

Parameter	Fit result
$A_\parallel{}^2$	0.222 ± 0.005 ± 0.007
$A_\perp{}^2$	0.192 ± 0.006 ± 0.005
$A_S{}^2$	0.038 ± 0.006 ± 0.008
$\delta_\parallel$	-2.98 ± 0.03 ± 0.02
$\delta_\perp$	2.93 ± 0.03 ± 0.01
δ_S	2.17 ± 0.04 ± 0.04

(b) $\overline{B^0}$ 30423 signal events

Parameter	Fit result
$A_\parallel{}^2$	0.215 ± 0.005 ± 0.007
$A_\perp{}^2$	0.205 ± 0.006 ± 0.004
$A_S{}^2$	0.040 ± 0.006 ± 0.007
$\delta_\parallel$	-2.97 ± 0.03 ± 0.01
$\delta_\perp$	2.94 ± 0.03 ± 0.02
δ_S	2.12 ± 0.04 ± 0.05

Table 6.13: Direct CP violation measurement (systematics using iterative method)

6.6 Direct CP measurement

A direct CP measurement is also carried out by splitting the dataset into B^0 and $\overline{B^0}$ decays. Any significant deviation in the polarization amplitudes would indicate some physics effects beyond the SM. The results are shown in Table 6.13. The systematic uncertainties are calculated in the same way as described in section 6.2. The difference in the B^0 and $\overline{B^0}$ fit results are consistent for all polarization amplitudes and strong phases. There is no evidence for direct CP violation or New Physics effects in $B^0 \to J/\psi K^{*0}$ precise to approximately 5%. Belle's previous measurement for direct CP violation in this channel was precise to approximately 11% (see Table 4.7).

6.7 Conclusion

The first full angular analysis of $B^0 \to J/\psi K^{*0}$ which includes the S-wave component has been performed with $1\,\text{fb}^{-1}$ of data collected using LHCb in 2011. The polarization amplitudes $|A_\parallel|^2$, $|A_\perp|^2$ and $|A_s|^2$, and the strong phases $\delta_\parallel$, $\delta_\perp$ and δ_s have been measured with the highest precision to date. The results are systematically limited.

The results presented are consistent with previous results from the BaBar, Belle, CDF and D0 experiments. Evidence has been found for final state interactions in $B^0 \to J/\psi K^{*0}$ from the deviation from π in the measurement of the strong phases [80]. This has been previously seen by the BaBar and Belle

experiments.

The measurements of the polarisation amplitudes and strong phases have been compared with the most recent results from LHCb of the decay $B_s^0 \to J/\psi\phi$. They have been predicted to have similar values [97] and any deviation could be due to penguin diagrams or New Physics effects. They have been found to be consistent except for $|A_\perp|^2$ which shows a deviation of almost 3σ. This is not significant enough to make any firm conclusions and more data is required.

The ambiguity in the strong phases has been resolved with simultaneous fit in bins of $K\pi$ mass, concluding that the physical solution is the one with the positive δ_s value. This supports the similar analysis for $B_s^0 \to J/\psi\phi$ which found a positive physical value for $\Delta\Gamma_s$ [91].

Finally, a direct CP measurement has been made by performing the angular analysis on the B^0 and $\overline{B}^0$ decays separately. It was found that the polarization amplitudes and strong phases are consistent within a few percent providing evidence for CP conservation and no New Physics effects.

Appendix A

HPD timelines

The full analysis done on the timelines of RICH 1 and RICH 2 HPDs is presented here. As mentioned in the full text, the HPDs were split into groups according to their most recent HPD measurements (at the time). Their timelines were then overlaid both according to absolute date and HPD age. The RICH 1 plots are shown in Figure A.1 and those for RICH 2 are shown in Figure A.2. The increased gradient is more visible in the absolute date plots, indicating that the cause is environmental effects in the LHCb cavern.

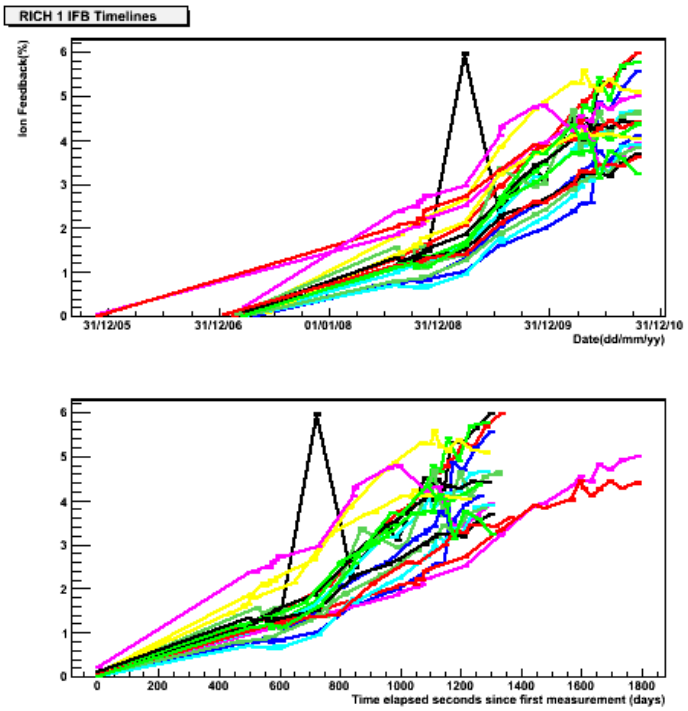

(a) RICH 1 Group 1

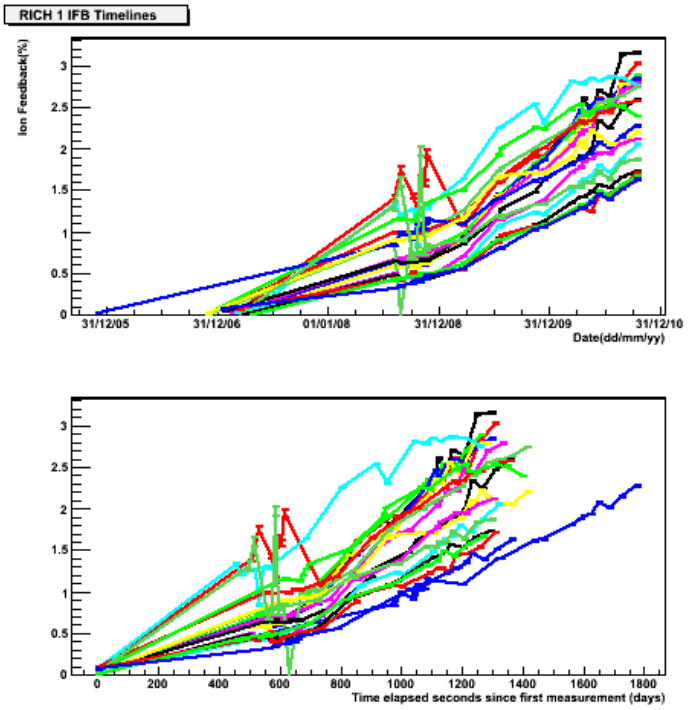

(b) RICH 1 Group 2

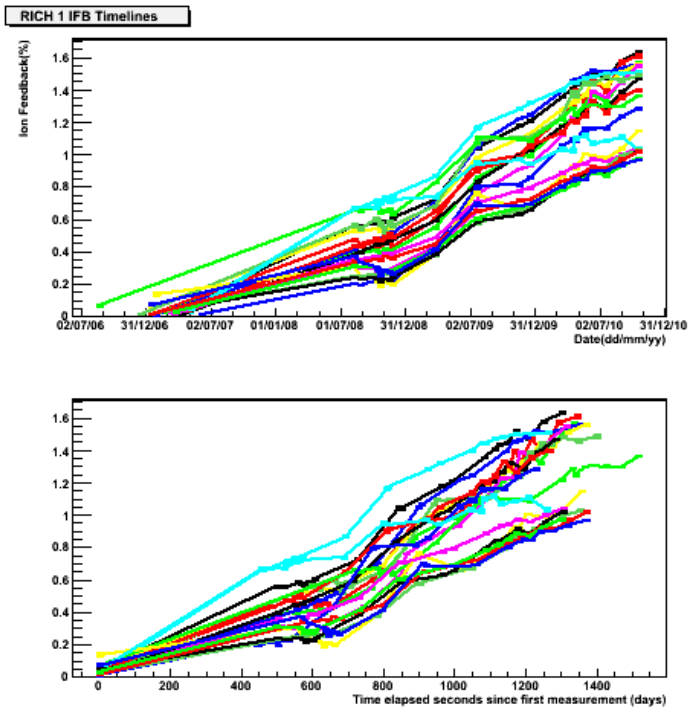

(c) RICH 1 Group 3

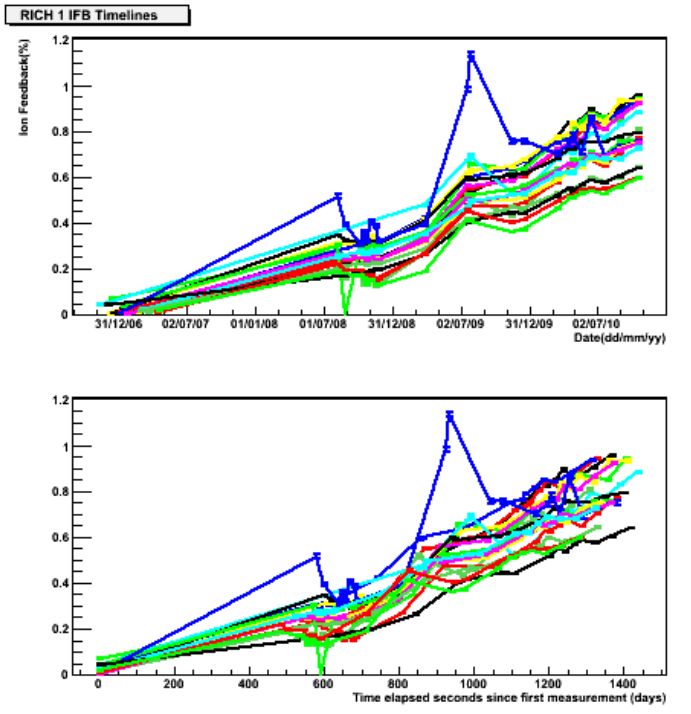

(d) RICH 1 Group 4

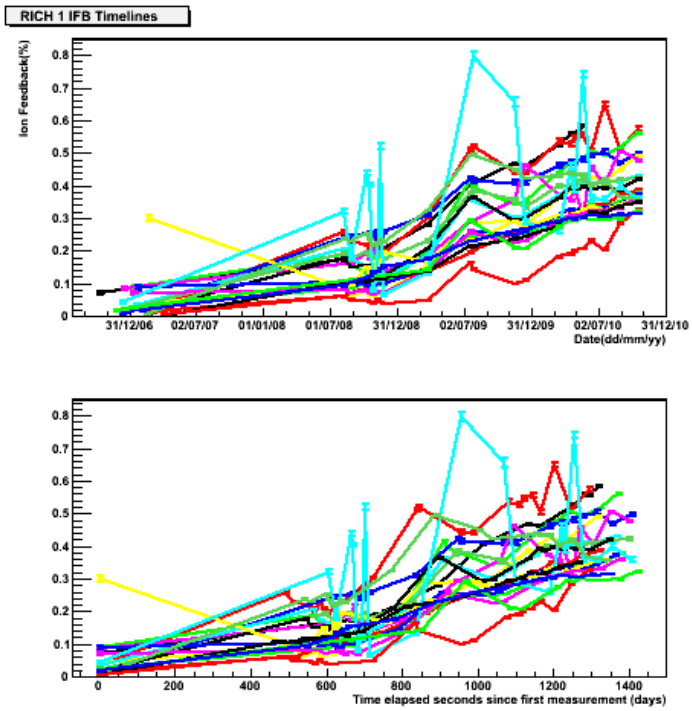

(e) RICH 1 Group 5

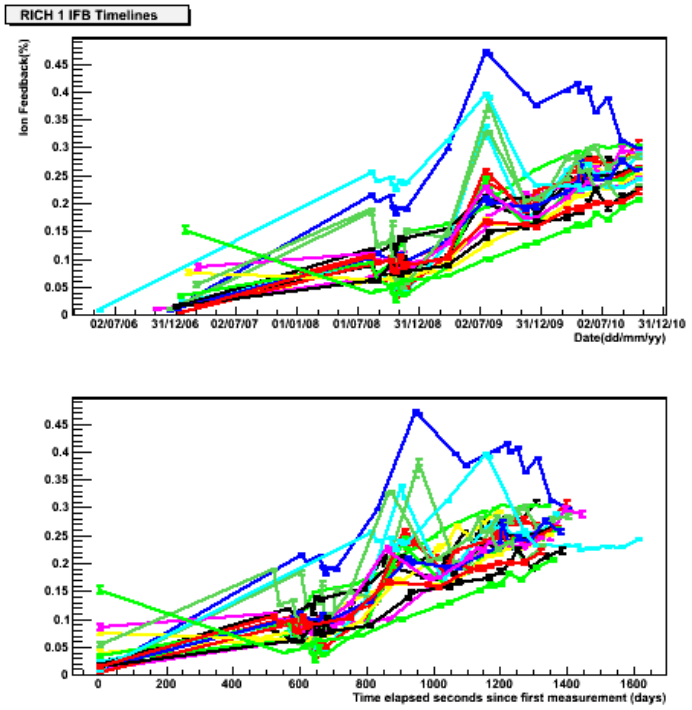

(f) RICH 1 Group 6

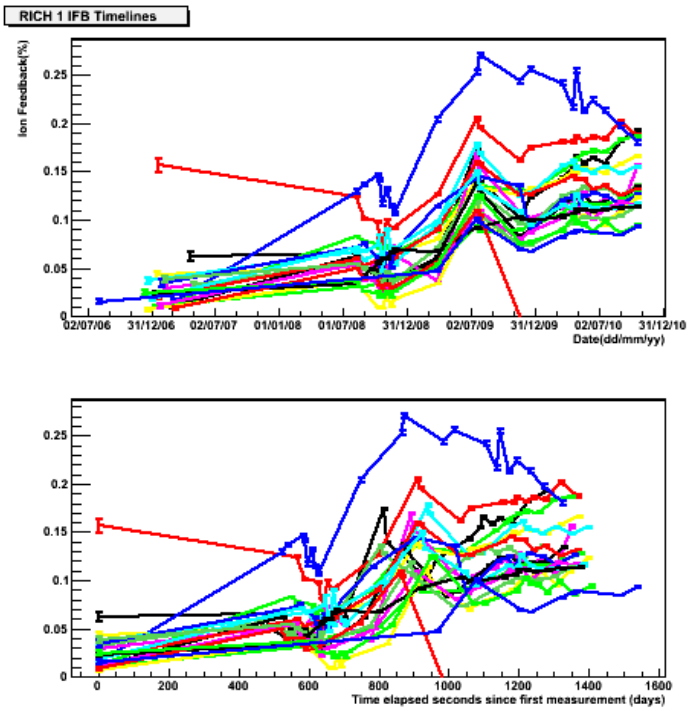

(g) RICH 1 Group 7

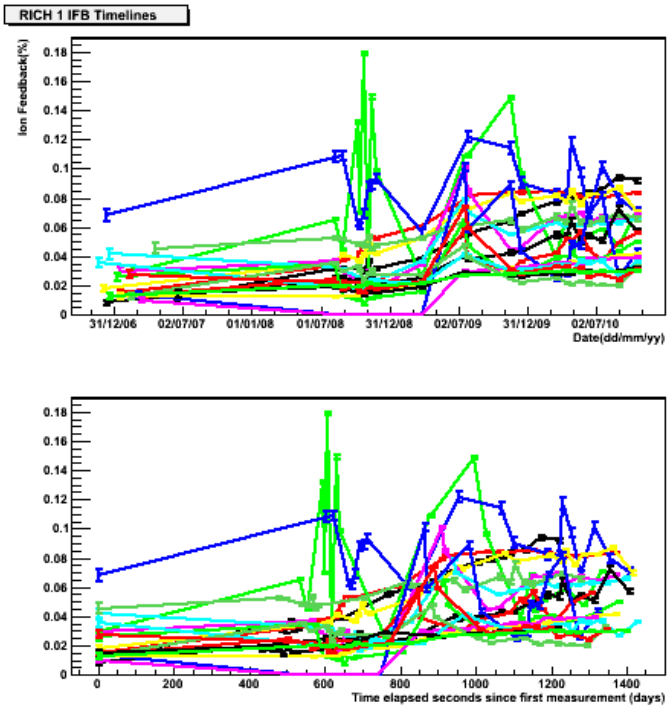

(h) RICH 1 Group 8

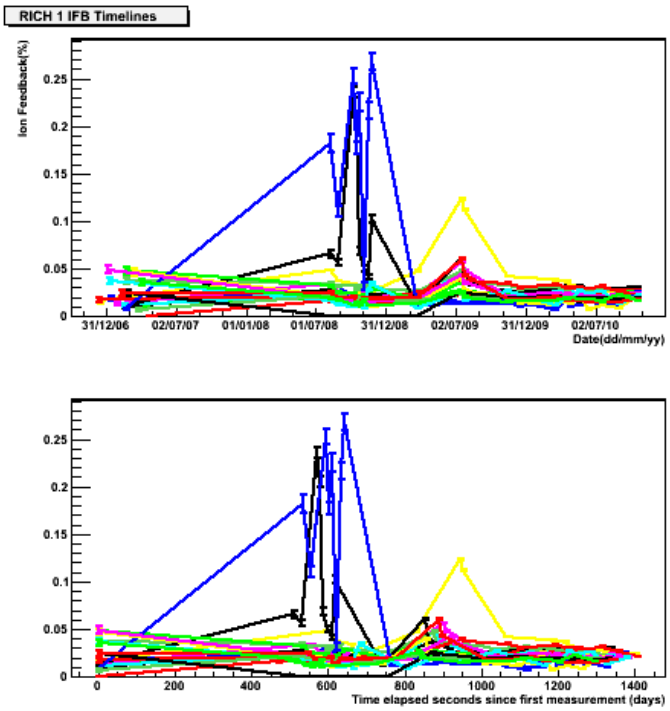

(i) RICH 1 Group 9

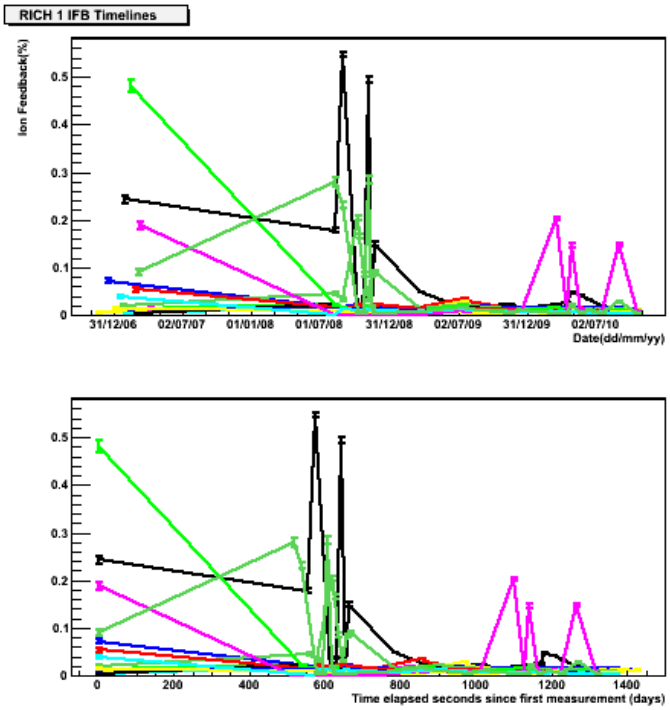

(j) RICH 1 Group 10

Figure A.1: Overlayed timelines for all groups of HPDs in RICH 1. RICH 1 Group 1 are those with the highest IFB measurement, and 10 are those with the lowest

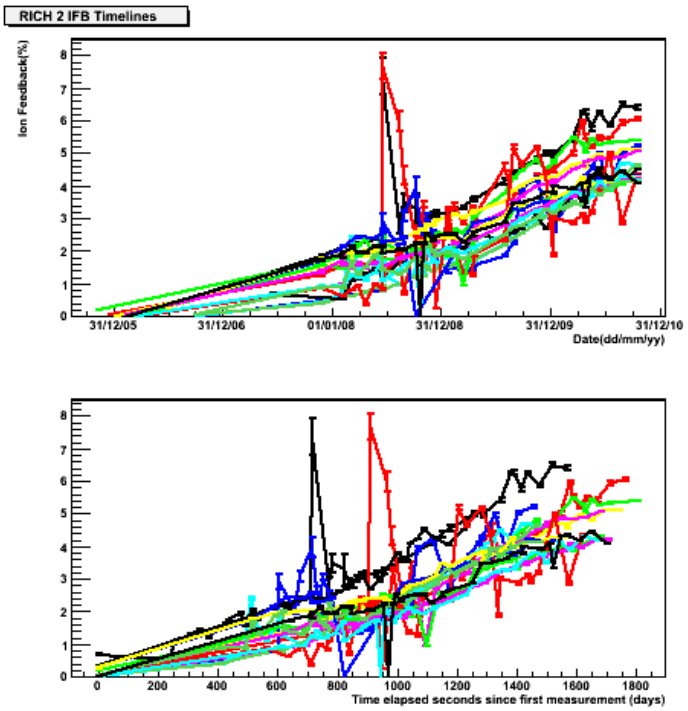

(a) RICH 2 Group 1

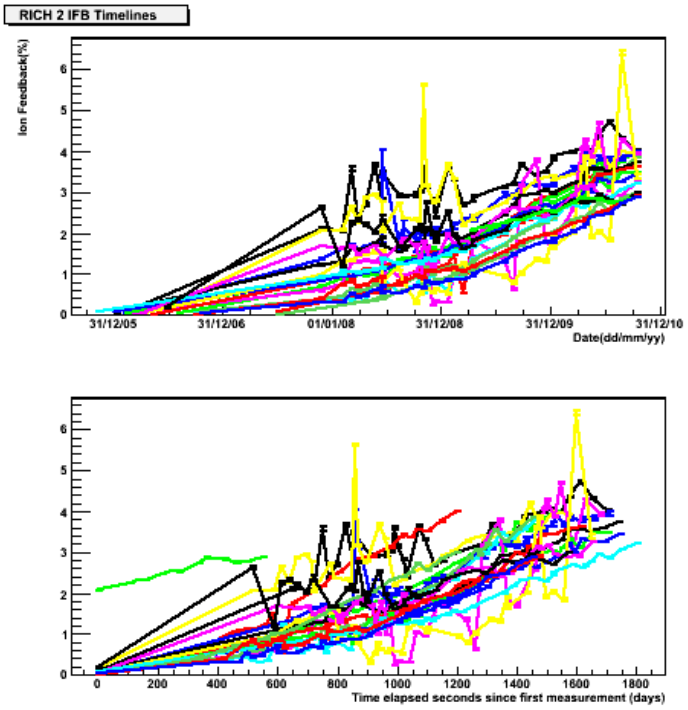

(b) RICH 2 Group 2

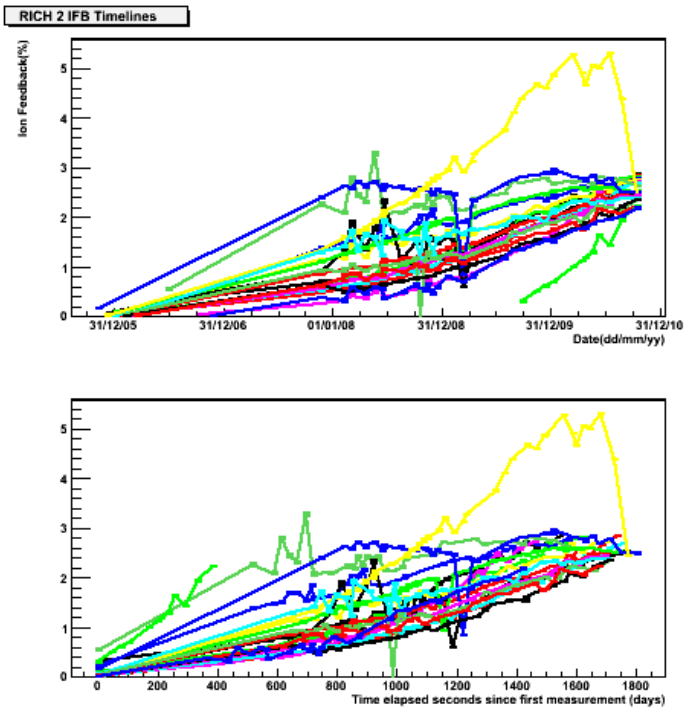

(c) RICH 2 Group 3

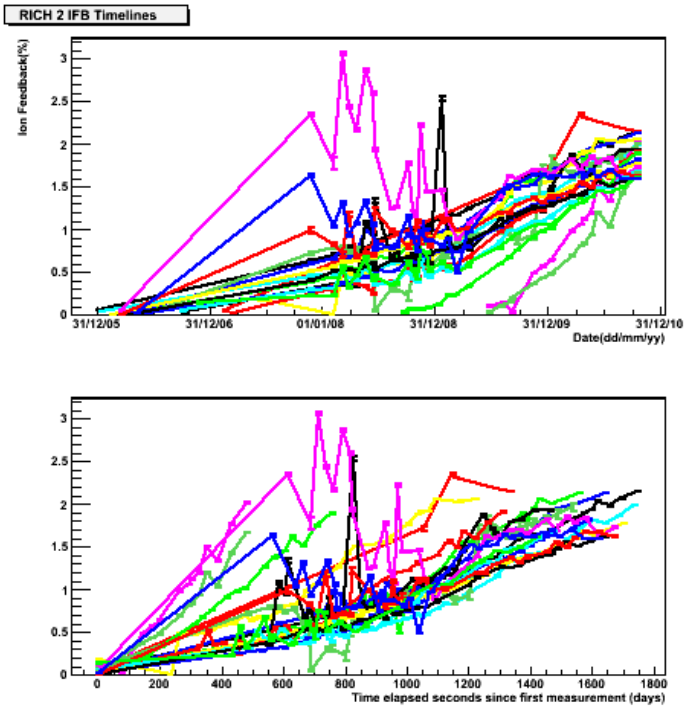

(d) RICH 2 Group 4

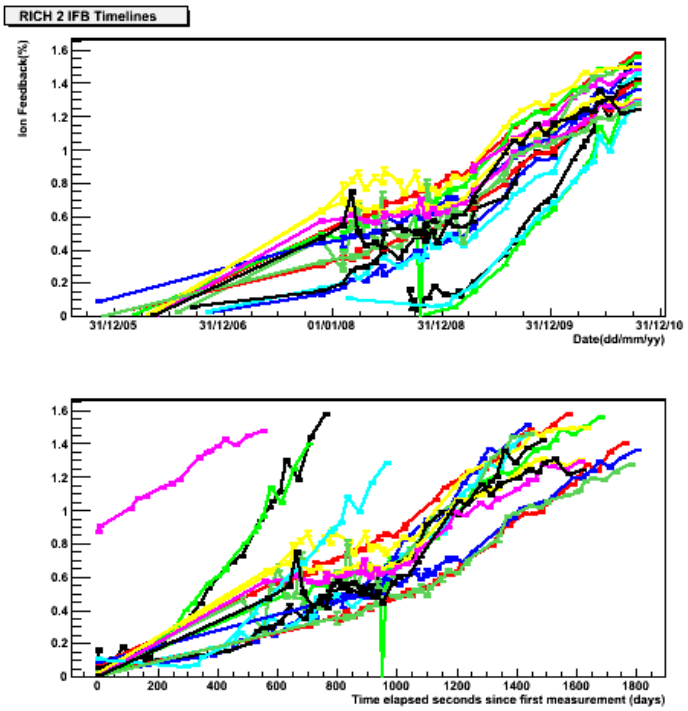

(e) RICH 2 Group 5

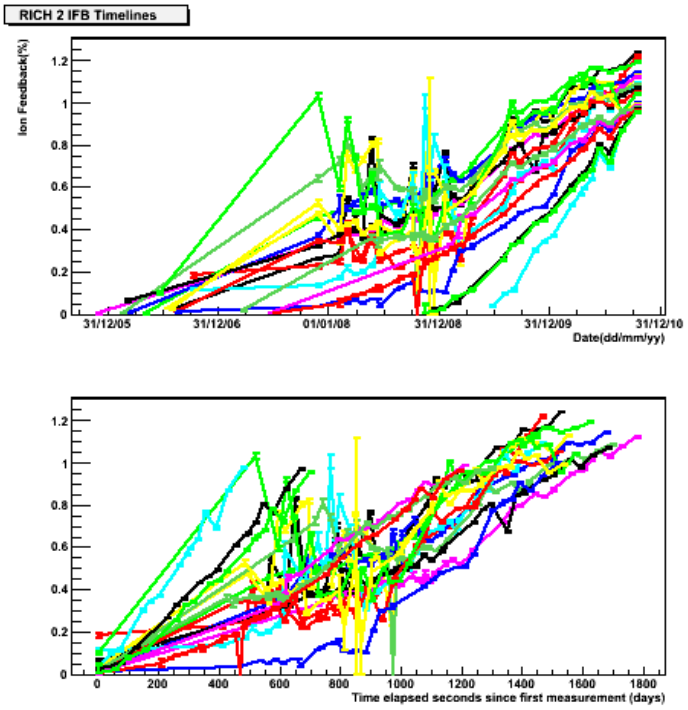

(f) RICH 2 Group 6

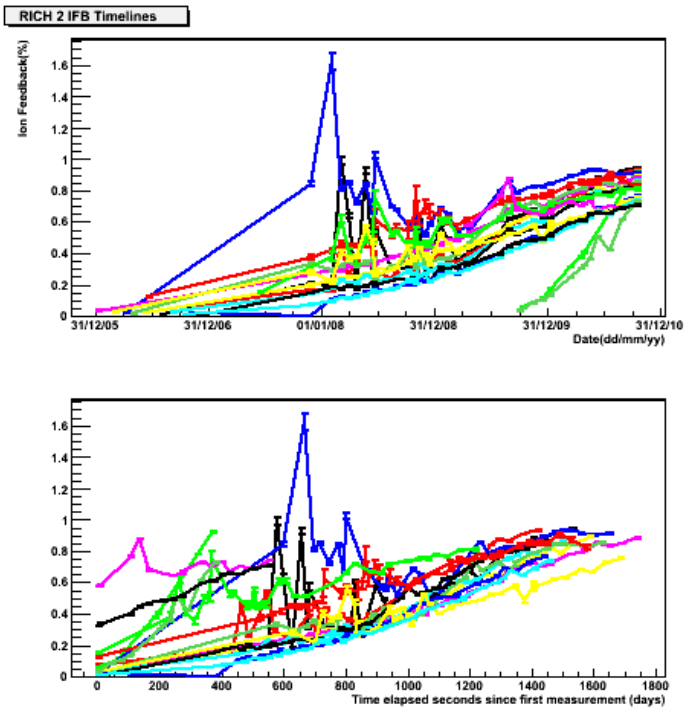

(g) RICH 2 Group 7

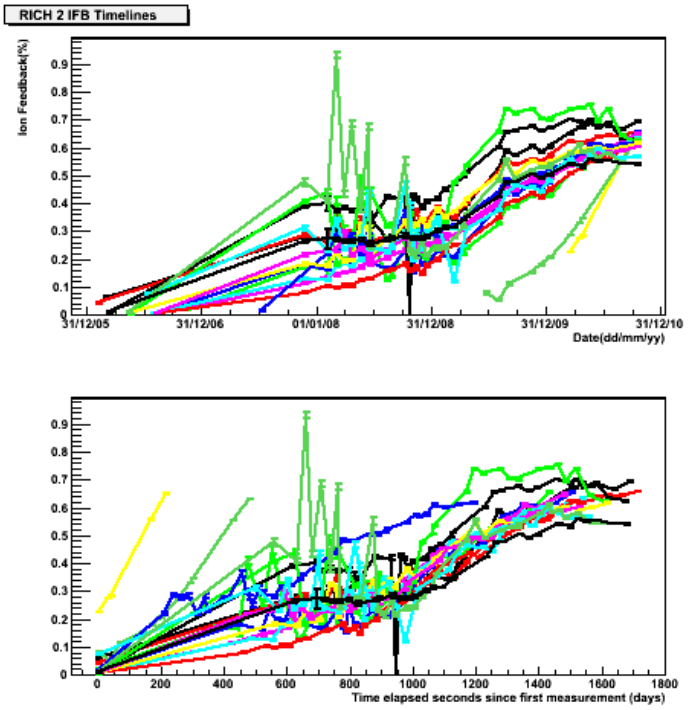

(h) RICH 2 Group 8

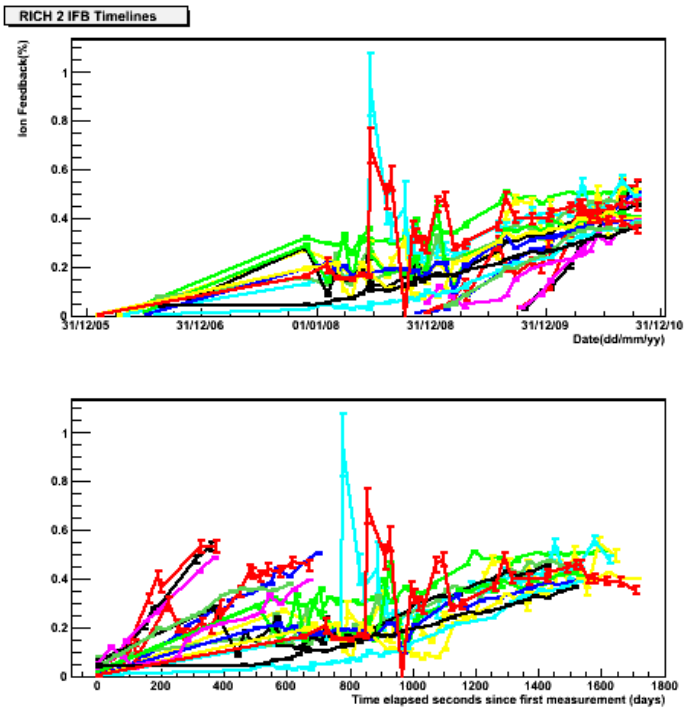

(i) RICH 2 Group 9

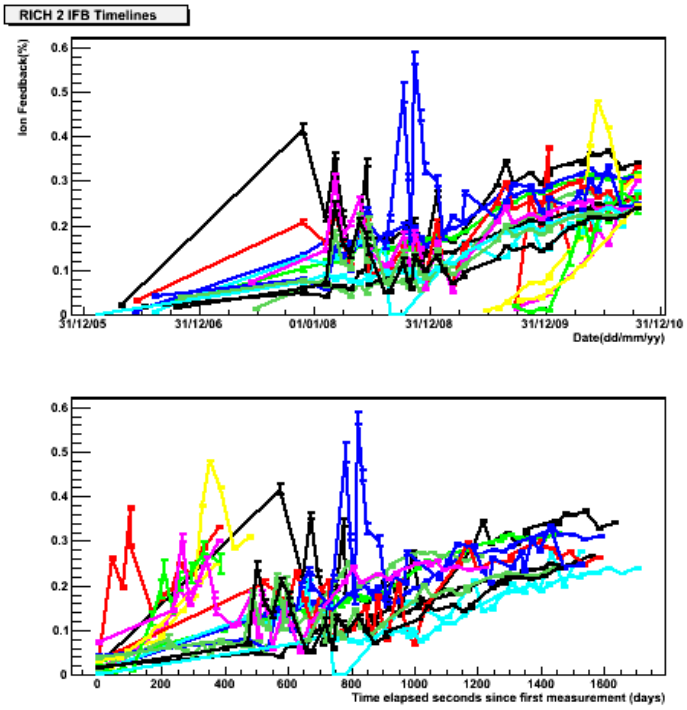

(j) RICH 2 Group 10

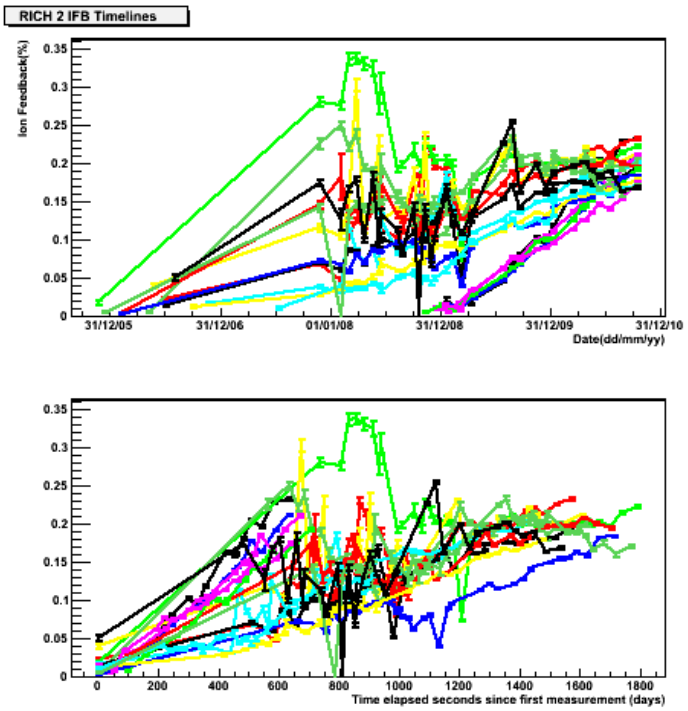

(k) RICH 2 Group 11

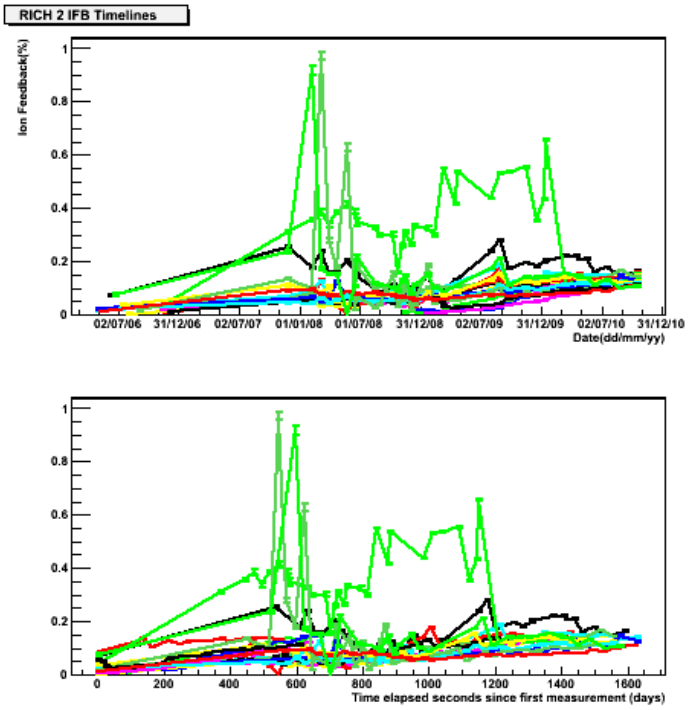

(l) RICH 2 Group 12

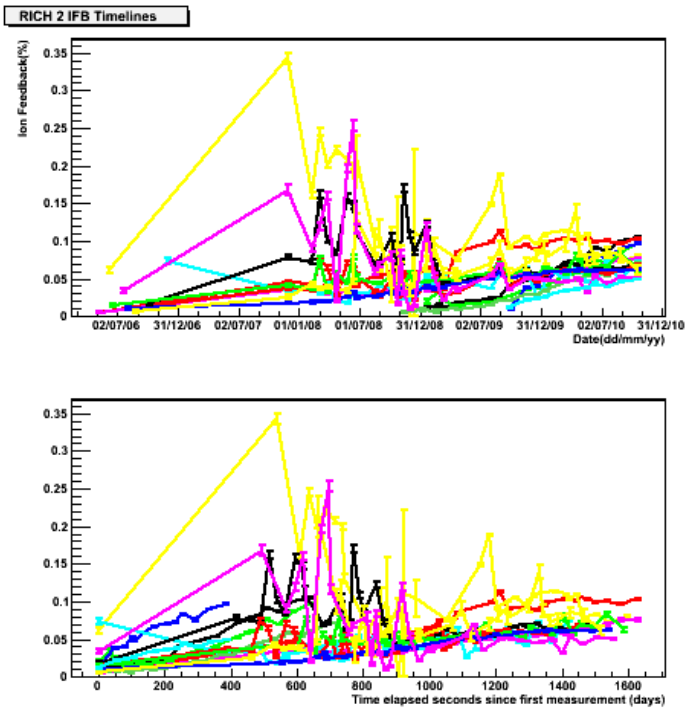

(m) RICH 2 Group 13

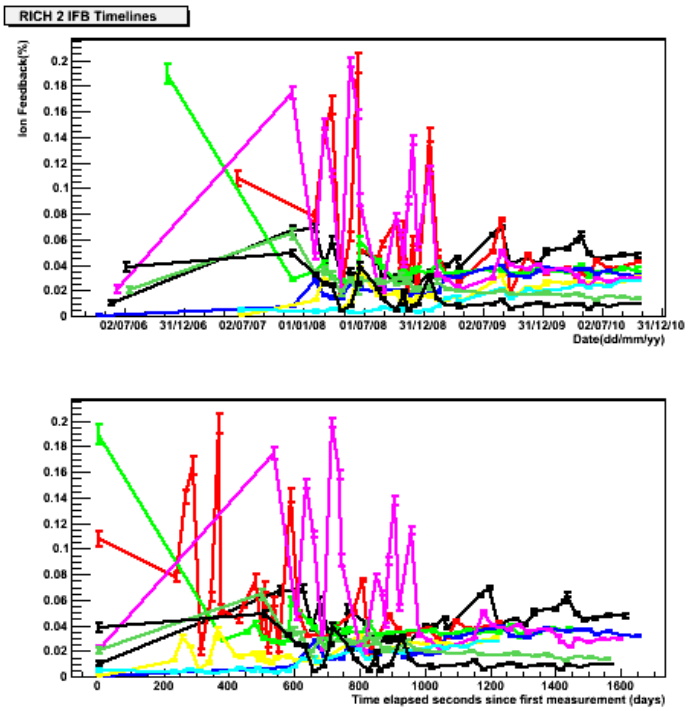

(n) RICH 2 Group 14

Figure A.2: Overlayed timelines for all groups of HPDs in RICH 2. RICH 1 Group 1 are those with the highest IFB measurement, and 14 are those with the lowest

Appendix B

Long Laser IFB Runs

As mentioned in the text the logarithm of the IFB measurement for each HPD in two different runs were plotted against each other to verify that taking the first three million events for the IFB measurement is valid. The plots are shown below:

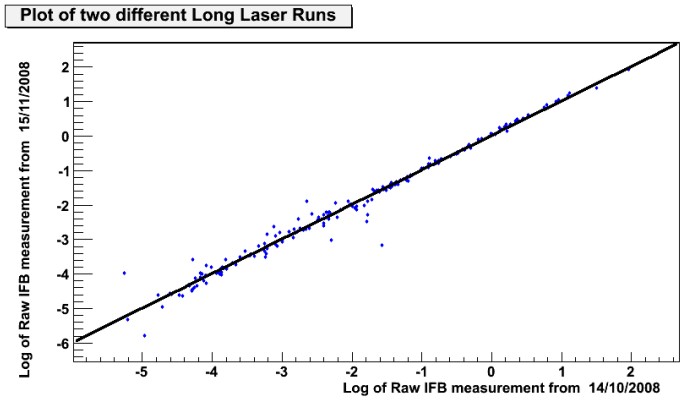

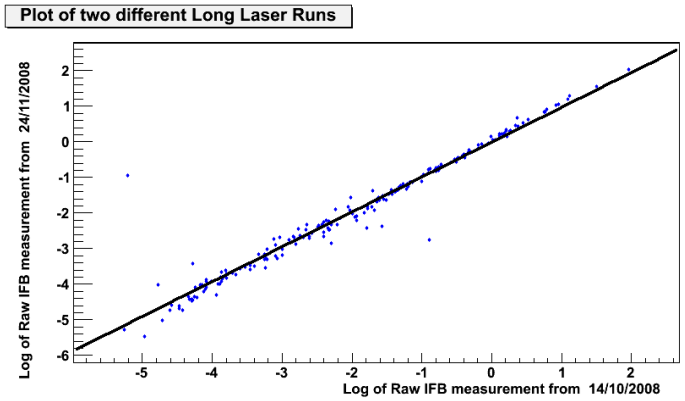

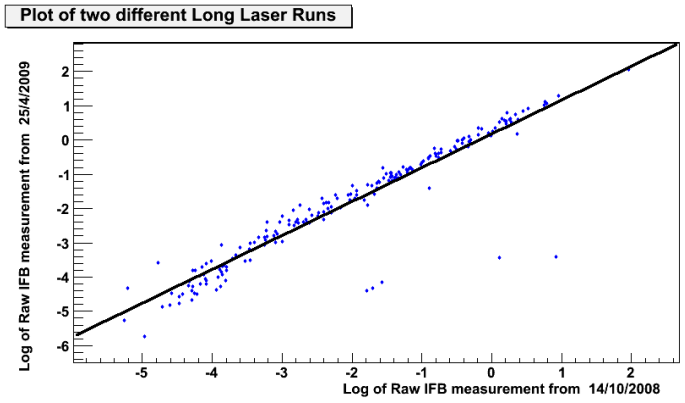
Plot of two different Long Laser Runs
Log of Raw IFB measurement from 25/4/2009
Log of Raw IFB measurement from 14/10/2008

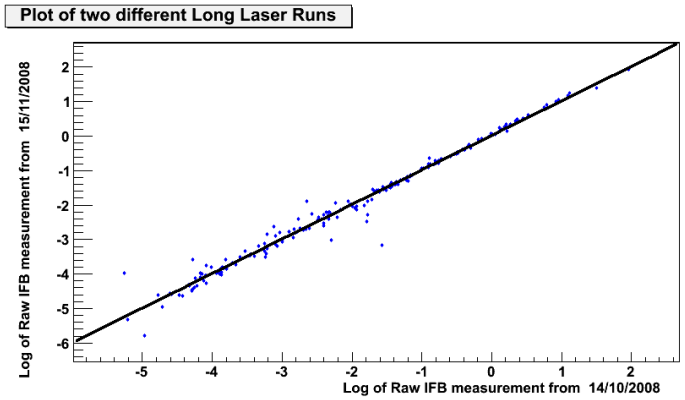
Plot of two different Long Laser Runs
Log of Raw IFB measurement from 15/11/2008
Log of Raw IFB measurement from 14/10/2008

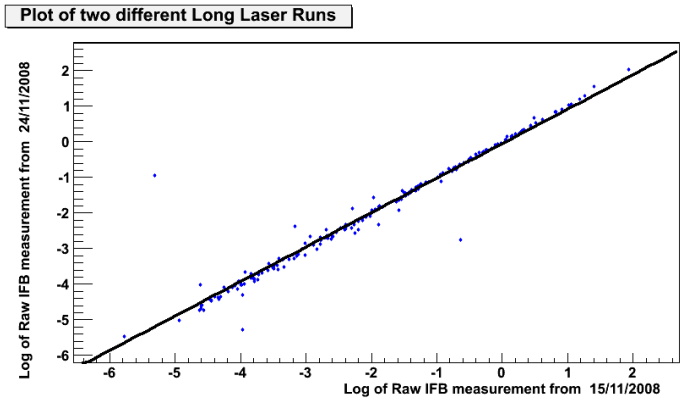
Plot of two different Long Laser Runs
Log of Raw IFB measurement from 24/11/2008
Log of Raw IFB measurement from 15/11/2008

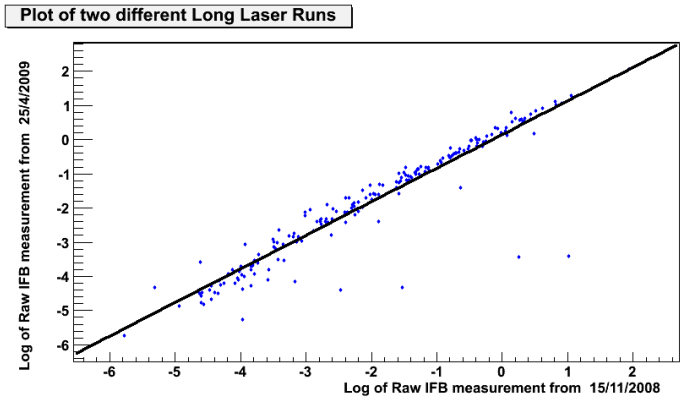
Plot of two different Long Laser Runs
Log of Raw IFB measurement from 25/4/2009
Log of Raw IFB measurement from 15/11/2008

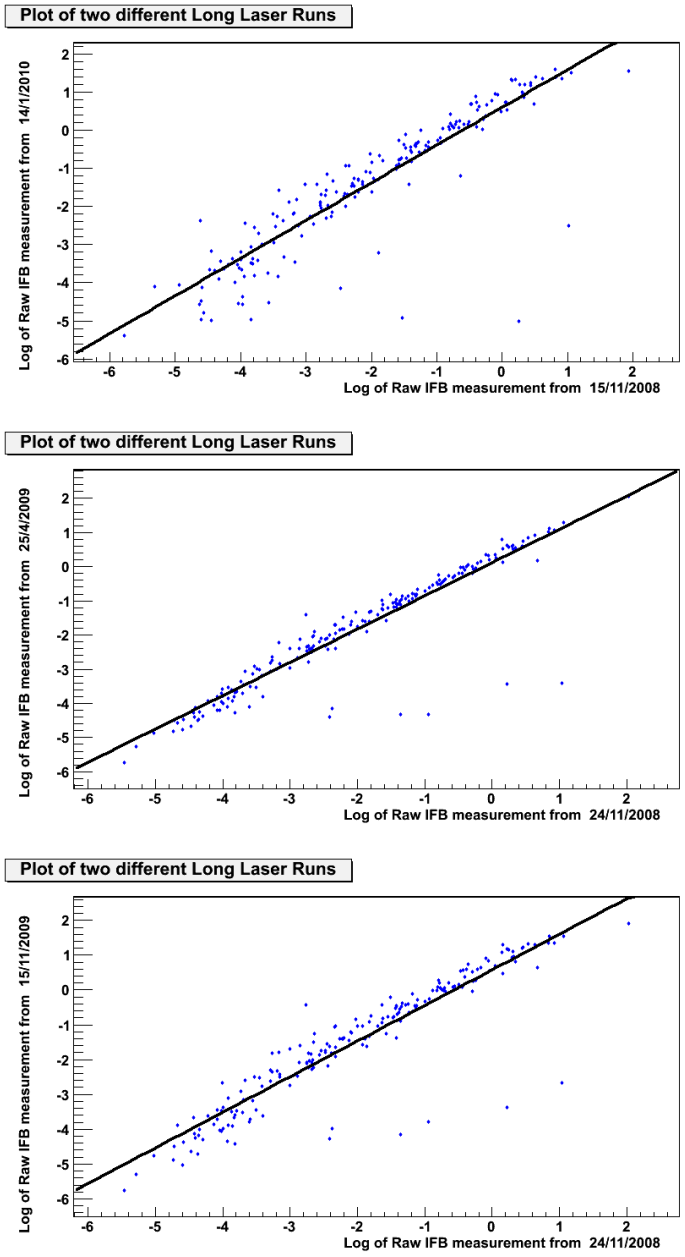

Figure B.1: The logarithm of the IFB measurements for two different runs plotted against eachother

As mentioned in the main text the range of the IFB values measured over long laser IFB runs were plotted as histograms shown here:

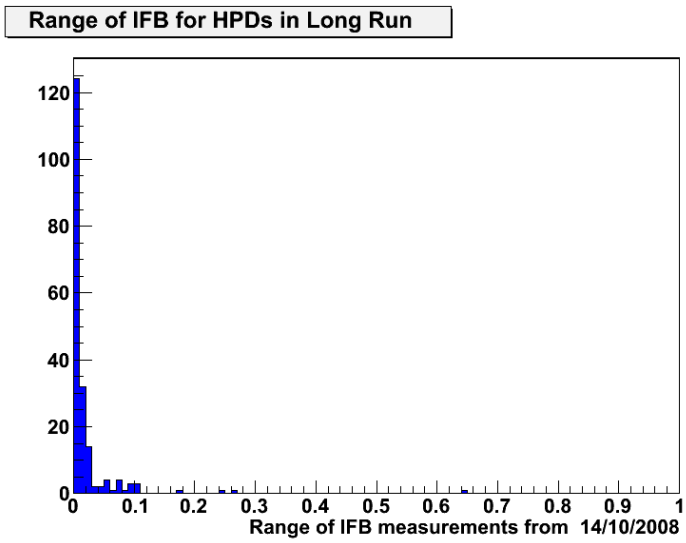

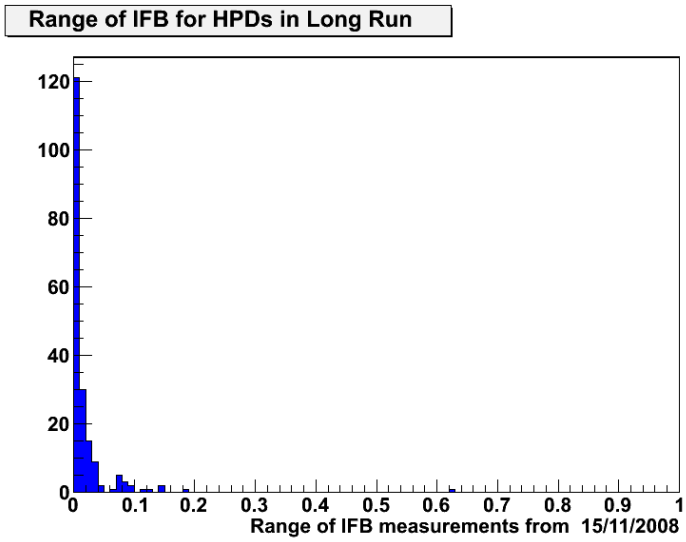

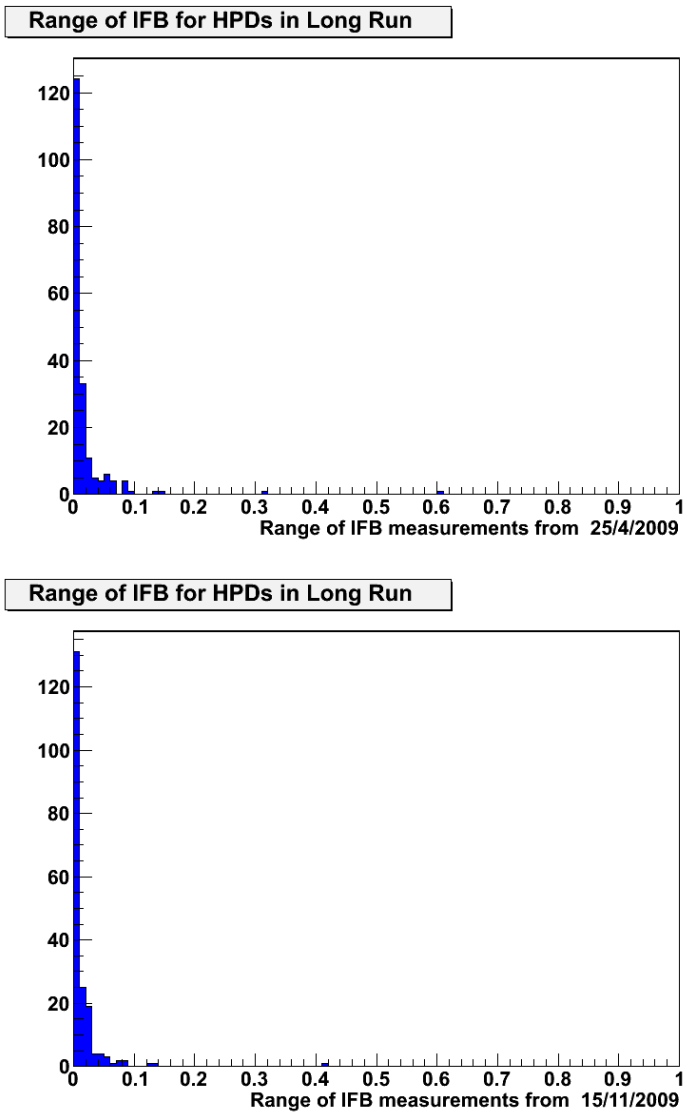

Figure B.2: Histograms of the range of the long laser runs

Appendix C

HPD investigations

Out of 196 HPDs in RICH 1:

- There are only 11 HPDs that have a positive gradient for every long laser run
- 72 HPDs that have a positive gradient for more than 4 of the long laser runs
- Only 4 HPDs have negative gradients for every run
- 53 HPDs have negative gradients for more than 4 of the long laser runs

The HPDs were then split into 3 different groups:

- High IFB gradient (> 5)
- Medium IFB gradient ($1 - 5$)
- Low IFB gradient (< 1)

The magnitude was taken so to include those with negative gradients. Observations were:

- No HPDs had a high IFB gradient for all long laser runs
- 7 HPDs had a high IFB gradient for more than 4 of the runs
- 31 HPDs had a low IFB gradient for all 6 runs
- 85 HPDs had a low IFB gradient for more than 4 of the runs

A study was done to see whether for each long laser run, the same HPDs are correlated or anti-correlated with average cluster rate:

- 1 HPD is correlated with average cluster rate for all 6 runs
- 0 HPDs were correlated with average cluster rate for 5 runs
- 1 HPD was correlated with average cluster for 4 runs out of 6

- 0 HPDs anti-correlated with averate cluster rate for all 6 runs
- 5 HPDs anti-correlated with average cluster rate for 5 runs out of 6
- 28 HPDs anticorrelated with average cluster rate for 4 or more runs out of 6

This suggests that as for the previous study, the HPDs do not seem to behave similarly between runs.

Bibliography

[1] D. Larson, J. Dunkley, G. Hinshaw, E. Komatsu, M. R. Nolta, C. L. Bennett, B. Gold, M. Halpern, R. S. Hill, N. Jarosik, A. Kogut, M. Limon, S. S. Meyer, N. Odegard, L. Page, K. M. Smith, D. N. Spergel, G. S. Tucker, J. L. Weiland, E. Wollack, and E. L. Wright. *Seven-year Wilkinson Microwave Anisotropy Probe (WMAP) Observations: Power Spectra and WMAP-derived Parameters. The Astrophysical Journal Supplement Series*, 192(2):16, 2011.

[2] A. D. Sakharov. *Violation of CP Invariance, C Asymmetry, and Baryon Asymmetry of the Universe. Pisma Zh. Eksp. Teor. Fiz.*, 5:32–35, 1967.

[3] Carl D. Anderson. *The Positive Electron. Phys. Rev.*, 43:491–494, Mar 1933.

[4] Owen Chamberlain, Emilio Segrè, Clyde Wiegand, and Thomas Ypsilantis. *Observation of Antiprotons. Phys. Rev.*, 100:947–950, Nov 1955.

[5] R. Feynman. *The Theory of Positrons. Physical Review*, 76(6):749–759, 1949.

[6] E. Stueckelberg. *Helvetica Physica Acta*, 14(51-80), 1941.

[7] K. Nakamura et al. (Particle Data Group). *The Review of Particle Physics. J.Phys. G*, 37(075021), 2011.

[8] R. Feynman. *Space-Time Approach to Quantum Electrodynamics. Physical Review*, 76(6):769–789, 1949.

[9] Julian Schwinger. *Quantum Electrodynamics. I. A Covariant Formulation. Physical Review*, 74(10):1439–1461, 1948.

[10] Tomonaga Tati. *A Self-Consistent Subtraction Method in the Quantum Field Theory. Progress of Theoretical Physics*, III(4):391–406, 1948.

[11] Steven Weinberg. *A Model of Leptons. Physical Review Letters*, 19(21):1264–1266, 1967.

[12] Abdus Salam and J. C. Ward. *Weak and electromagnetic interactions. Il Nuovo Cimento (1955-1965)*, 11(4):568–577, 1959.

[13] F J Hasert, S Kabe, W Krenz, C Conta, J Von Krogh, D Lanske, J G Morfín, K Schultze, H Weerts, G H Bertrand-Coremans, J Sacton, W K Van Doninck, P Vilain, U Camerini, Donald C Cundy, R Baldi, I A Danilchenko, W F Fry,

Dieter Haidt, S Natali, P Musset, B Osculati, R Palmer, John Bryan M Pattison, Donald Hill Perkins, Antonio Pullia, A Rousset, W A Venus, H W Wachsmuth, V Brisson, B Degrange, Maurice Haguenauer, L Kluberg, U Nguyen-Khac, P Petiau, E Belotti, S Bonetti, D Cavalli, Ettore Fiorini, M Rollier, Bernard Aubert, D Blum, L M Chounet, P Heusse, A Lagarrigue, A M Lutz, A Orkin-Lecourtois, J P Vialle, F W Bullock, M J Esten, T W Jones, J McKenzie, A G Michette, Gerald Myatt, and W G Scott. *Observation of neutrino-like interactions without muon or electron in the Gargamelle neutrino experiment. Nucl. Phys. B*, 73(1):1–22, 1974.

[14] S.-K. Choi. *Observation of a Narrow Charmonium-like State in Exclusive $B^{\pm} \to K^{\pm}\pi^{+}\pi^{-}J/\psi$ Decays. Physical Review Letters*, 91(26), 2003.

[15] Kiyotaka Shimizuand Makoto Takizawa Sachiko Takeuchi. *Charmonium and Meson–Molecule Hybrid Tetraquarks Vector Meson Width and the Isospin Breaking in the X(3872) Decay Clear. Few-Body Systems*, 2012.

[16] G. Hanson, G. S. Abrams, A. M. Boyarski, M. Breidenbach, F. Bulos, W. Chinowsky, G. J. Feldman, C. E. Friedberg, D. Fryberger, G. Goldhaber, D. L. Hartill, B. Jean-Marie, J. A. Kadyk, R. R. Larsen, A. M. Litke, D. Lüke, B. A. Lulu, V. Lüth, H. L. Lynch, C. C. Morehouse, J. M. Paterson, M. L. Perl, F. M. Pierre, T. P. Pun, P. A. Rapidis, B. Richter, B. Sadoulet, R. F. Schwitters, W. Tanenbaum, G. H. Trilling, F. Vannucci, J. S. Whitaker, F. C. Winkelmann, and J. E. Wiss. *Evidence for Jet Structure in Hadron Production by $e^{+}e^{-}$ Annihilation. Phys. Rev. Lett.*, 35:1609–1612, Dec 1975.

[17] Nicola Cabibbo. *Unitary Symmetry and Leptonic Decays. Phys. Rev. Lett.*, 10:531–533, Jun 1963.

[18] M Kobayashi and T Maskawa. *CP-Violation in the Renormalizable Thoery of Weak Interaction. Progress of Theoretical Physics*, 49(2):652–657, 1973.

[19] CKMfitterGroup (J.Charles et. al.). *http://ckmfitter.in2p3.fr/. Eur. Phys. J. C*, 41:1–131, 2005.

[20] C. S. Wu, E. Ambler, R. W. Hayward, D. D. Hoppes, and R. P. Hudson. *Experimental Test of Parity Conservation in Beta Decay. Phys. Rev.*, 105:1413–1415, Feb 1957.

[21] L. Landau. *On the conservation laws for weak interactions. Nuclear Physics*, 3(1):127 – 131, 1957.

[22] J. H. Christenson, J. W. Cronin, V. L. Fitch, and R. Turlay. *Evidence for the 2π Decay of the K_2^0 Meson. Phys. Rev. Lett.*, 13:138–140, Jul 1964.

[23] *Measurement of direct $\mathcal{CP}$ violation in charmless charged two-body B decays at LHCb.* 25eme Rencontres de Physique de La Vallee d'Aoste, La Thuile, Italy, Apr 2011. LHCB-CONF-2011-011.

[24] *Measurement of time-dependent CP violation in charmless two-body B decays*, number LHCb-CONF-2012-007. 47th Rencontres de Moriond on QCD and High Energy Interactions, La Thuile, Italy, Mar 2012.

[25] *Tagged time-dependent angular analysis of $B_s^0 \to J/\psi\phi$ decays at LHCb*. 47th Rencontres de Moriond on Electroweak Interactions and Unified Theories, La Thuile, Italy, Mar 2012. LHCb-CONF-2012-002.

[26] A. Lenz et al. *Anatomy of new physics in $B^0 - \overline{B^0}$ mixing. Physical Review D*, 83(3), 2011.

[27] The LHCb Collaboration. *Observation of CP violation in B+ to DK+ decays.* arXiv:1203.3662v1, 03 2012.

[28] The LHCb Collaboration. *Evidence for CP Violation in Time-Integrated $D^0 \to h^-h^+$ Decay Rates. Phys. Rev. Lett.*, 108:111602, Mar 2012.

[29] The LHCb Collaboration. *Measurement of $\sigma \to b\bar{b}X$ at $\sqrt{s} = 7$ TeV in the forward region. Physics Letters B*, 694(3):209 – 216, 2010.

[30] LHCb Collaboration. *LHCb Technical Proposal.* Number CERN-LHCC-98-004 in Tech. Proposal. CERN, Geneva, 1998.

[31] A.Augusto Alves et al. *The LHCb Detector at the LHC. JINST*, 3:S08005, 2008.

[32] *Performance of the LHCb Vertex Locator*, number LHCb-PROC-2011-087. PSD9: The 9th International Conference on Position Sensitive Detectors, Aberystwyth, UK, Sep 2011.

[33] *The LHCb Silicon Tracker Performance in pp Collisions at the LHC.* 13th ICATPP Conference on Astroparticle, Particle, Space Physics and Detectors for Physics Applications, Como, Italy, Oct 2011. Linked to LHCb-PROC-2011-051.

[34] *Tracking and Alignment Performance of the LHCb silicon detectors.* International Workshop on Vertex Detectors, Rust, Austria, Jun 2011. LHCB-PROC-2011-086.

[35] D. van Eijk, S. Bachmann, Th. Bauer, Ch. FÃrber, A. Bien, V. Coco, M. Deckenhoff, F. Dettori, R. Ekelhof, E. Gersabeck, T.M. Karbach, R. Koopman, A. Kozlinskiy, Ch. Langenbruch, Ch. Linn, M. Merk, M. Meissner, P. Morawski, A. Pellegrino, N. Serra, P. Seyfert, B. Spaan, S. Swientek, B. Storaci, M. Szczekowski, N. Tuning, U. Uwer, E. Visser, D. Wiedner, and M. Witek. *Radiation hardness of the LHCb Outer Tracker. Nuclear Instruments and Methods in Physics Research Section A: Accelerators, Spectrometers, Detectors and Associated Equipment*, 685(0):62 – 69, 2012.

[36] *The Performance of the Outer Tracker Detector at LHCb.* 13th ICATPP Conference on Astroparticle, Particle, Space Physics and Detectors for Physics Applications, Como, Italy, Oct 2011. LHCb-PROC-2011-058.

[37] I Machikhiliyan. *Current status and performance of the LHCb electromagnetic and hadron calorimeters.* Aug 2010. Journal of Physics http://iopscience.iop.org/1742-6596/293/1/012052/.

[38] Yu. Guz. *First Year of Running for the LHCb Calorimeter System.* Poster at NDIP 2011- New Developments in Photodetection, Lyon, 2011.

[39] LHCb Collaboration. *LHCb Muon System: second Addendum to the Techinical Design Report.* Number CERN-LHCC-2005-012 in Technical Design Report LHCb. CERN, Geneva, 2005.

[40] J A Hernando Morata, E Lopez Asamar, D Martinez Santos, H Ruiz-Pérez, and F Teubert. *Measurement of trigger efficiencies and biases.* Technical Report LHCb-2008-073. CERN-LHCb-2008-073, CERN, Geneva, Mar 2010.

[41] Roel Aaij and Johannes Albrecht. *Muon triggers in the High Level Trigger of LHCb.* Technical Report LHCb-PUB-2011-017. CERN-LHCb-PUB-2011-017, CERN, Geneva, Sep 2011.

[42] T. Sjostrand et. al. *High-energy-physics event generation with Pythia 6.1. Computer Physics Communications*, 135(2):238–259, 2001.

[43] David J. Lange. *The EvtGen particle decay simulation package. Nuclear Instruments and Methods in Physics Research Section A: Accelerators, Spectrometers, Detectors and Associated Equipment*, 462(2):152 – 155, 2001.

[44] S. Agostinelli et al. *Geant4 - a simulation toolkit. Nuclear Instruments and Methods in Physics Research Section A: Accelerators, Spectrometers, Detectors and Associated Equipment*, 506(3):250 – 303, 2003.

[45] F. James and M. Roos. *Minuit: A System for Function Minimization and Analysis of the Parameter Errors and Correlations. Comput. Phys. Commun.*, 10:343–367, 1975.

[46] Rene Brun and Fons Rademakers. *ROOT- An Object Oriented Data Analysis Framework.* In *Proceedings AIHENP'96 Workshop, Lausanne*, volume 389, pages 81–86. Nucl.Inst and Meth. in Phys.Res.A, 1996.

[47] Yuehong Xie. *sFit: a method for background subtraction in maximum likelihood fit.* Technical Report arXiv:0905.0724, May 2009. Comments: 8 pages.

[48] A Borgia, W Cameron, A Contu, C D'Ambrosio, C Frei, N Harnew, M Johen, G Lefeuvre, R Mountain, S Stone, D Websdale, and F Xing. *The Magnetic Distortion Calibration System of the LHCb RICH1 Detector.* Technical Report LHCb-PUB-2011-018. CERN-LHCb-PUB-2011-018, CERN, Geneva, Jun 2012.

[49] K. Wyllie et al. *A Pixel Readout Chip for Tracking at ALICE and Particle Identification at LHCb. Proceedings of the fifth workshop on Electronics for LHC Experiments, Snowmass, Colorado*, CERN/LHCC/99-33, September 1999.

[50] M.Moritz et al. *Performance Study of New Pixel Hybrid Photon Detector Prototypes for the LHCb RICH Counters. IEEE Transactions on Nuclear Science*, 51(3):1060–1066, June 2004.

[51] T. Gys. *Production of 500 pixel hybrid photon detectors for the RICH counters of LHCb. Nuclear Instruments and Methods in Physics Research Section A: Accelerators, Spectrometers, Detectors and Associated Equipment*, 567(1):176 – 179, 2006.

[52] Stephan Eisenhardt. *Production and tests of Hybrid Photon Detectors for the LHCb RICH detectors. Nuclear Instruments and Methods in Physics Research Section A: Accelerators, Spectrometers, Detectors and Associated Equipment*, 595(1):142 – 145, 2008. Proceedings of the Sixth International Workshop on Ring Imaging Cherenkov Detectors.

[53] Robert W Lambert. *LHCb Hybrid Photon Detectors and Sensitivity to Flavour Specific Asymmetry in Neutral B-Meson Mixing.* PhD thesis, Edinburgh U., Edinburgh, 2009. Presented on 07 Jan 2009.

[54] Graham Young-Min Kim. *RICH Particle Identification at the Present and Future LHCb Experiment.* PhD thesis, Edinburgh U., Edinburgh, 2011. Presented 23 Mar 2011.

[55] Cheng-Wei Chiang. *Observables in the decays of B to two vector mesons. Physical Review D*, 61(7), 2000.

[56] Amol S. Dighe, Isard Dunietz, Harry J. Lipkin, and Jonathan L. Rosner. *Angular distributions and lifetime differences in $B_s \to J/\psi\phi$ decays.* hep-ph/9511363v1.

[57] A S Dighe, Isard Dunietz, and Robert Fleischer. *Extracting CKM Phases and $B_s - \overline{B}_s$ Mixing Parameters from Angular Distributions of Non-Leptonic B Decays. Eur. Phys. J. C*, 6(hep-ph/9804253. CERN-TH-98-085. FERMILAB-PUB-98-093-T. IC-98-25):647–662. 31 p, Apr 1998.

[58] The LHCb Collaboration. *First Evidence of Direct CP Violation in Charmless Two-Body Decays of B_s^0 Mesons. Physical Review Letters*, 108(201601), 2012.

[59] M. Alam et. al. *Exclusive hadronic B decays to charm and charmonium final states. Phys. Rev. D*, 50:43–68, Jul 1994.

[60] The ARGUS Collaboration. *Measurement of the polarization in the decay $B \to J/\psi K^*$. Physics Letters B*, 340(3):217 – 220, 1994.

[61] Thomas Mannel, Winston Roberts, and Zbigniew Ryzak. *Factorization hypothesis and the non-leptonic decays of heavy hadrons. Physics Letters B*, 259(3):359 – 364, 1991.

[62] T E Browder, K Honscheid, and S Playfer. *A review of hadronic and rare B decays.* Technical Report hep-ph/9404314. CLNS-1261. HEPSY-93-10. OHSTPY-HEP-E-93-018. UH-511-778, Cornell Univ. Lab. Nucl. Stud., Ithaca, NY, Feb 1994.

[63] Kenneth M. Watson. *The Effect of Final State Interactions on Reaction Cross Sections. Phys. Rev.*, 88:1163–1171, Dec 1952.

[64] M Neubert, V Rieckert, B Stech, and Q P Xu. *Exclusive weak decays of B-mesons.* Number p.286 in World Scientific, Singapore. Heavy Flavours, 1992.

[65] A. Deandrea, N. Di Bartolomeo, R. Gatto, and G. Nardulli. *Two body non-leptonic decays of B and Bs mesons. Physics Letters B*, 318(3):549 – 558, 1993.

[66] R. Aleksan, A. Le Yaouanc, L. Oliver, O. Pène, and J.-C. Raynal. *Critical analysis of theoretical estimates for B -to-light-meson form factors and B →ψ K (K*) data using factorization. Phys. Rev. D*, 51:6235–6252, Jun 1995.

[67] C. Jessop. *Measurement of the Decay Amplitudes and Branching Fractions of $B \to J/\psi K^*$ and $B \to J/\psi K$ Decays. Physical Review Letters*, 79(23):4533–4537, 1997.

[68] CDF Collaboration. *Measurement of the Decay Amplitudes of $B^0 \to J/\psi K^{*0}$ and $B_s^0 \to J/\psi\phi$ Decays. Physical Review Letters*, 85(22):4668–4673, 2000.

[69] The BaBar Collaboration. *Measurement of the $B \to J/\psi K^*(892)$ Decay Amplitudes. Phys. Rev. Lett.*, 87:241801, Nov 2001.

[70] K. Abe et. al. *Measurements of branching fractions and decay amplitudes in $B^0 \to J/\psi K^*$ decays. Physics Letters B*, 538(1-2):11 – 20, 2002.

[71] Hai-Yang Cheng. *$B \to J/\psi K^*$ decays in QCD factorization. Physical Review D*, 65(9), 2002.

[72] Xuan Son Nguyen and Xuan-Yem Pham. *On the $B^0 \to J/\psi K^*$ Decay.* hep-ph/0110284v4.

[73] D. Melikhov. *Weak form factors for heavy meson decays: An update. Physical Review D*, 62(1), 2000.

[74] H.Y. Cheng, Y.Y. Keum, and K.C. Yang. *Angular distribution analysis of $B \to J/\psi K^*$ and resolving discrete ambiguities in the determination of ϕ_1. Int.J.Mod.Phys.*, A18:1437–1442, hep-ph/0112257, 2003.

[75] *Flavor-untagged angular analysis of $B_d^0 \to J/\psi K^*$ and $B_s^0 \to J/\psi\phi$ decays*, number LHCb-CONF-2011-002. 25eme Recontres de Physique de La Vallee d'Aoste, La Thuile, Italy, 2011.

[76] The CDF Collaboration. *Angular Analysis of $B_s \to J/\psi\phi$ and $B^0 \to J/\psi K^*$ Decays and Measurement of $\Delta\Gamma_s$ and ϕ_s. CDF note 8950*, 2007.

[77] D0 Collaboration. *Measurement of the angular and lifetime parameters of the decays $B_d \to J/\psi K^{*0}$ and $B_s^0 \to J/\psi\phi$. Phys.Rev.Lett.102, 032001*, 2009.

[78] The BaBar Collaboration. *Measurement of Decay Amplitudes of $B \to (c\bar{c})K*$ with an Angular Analysis, for $(c\bar{c}) = J/\psi, \psi(2S)$ and $\chi_c 1$. Phys.Rev.D 76, 031102*, 2007.

[79] The Belle Collaboration. *Studies of CP Violation in $B \to J/\psi K^*$ Decays. Phys. Rev. Lett.*, 95:091601, Aug 2005.

[80] The BaBar Collaboration. *Time-integrated and time-dependent angular analyses of $B \to J/\psi K\pi$: A measurement of* $\cos 2\beta$ *with no sign ambiguity from strong phases. Phys. Rev. D*, 71:032005, Feb 2005.

[81] T. Mannel S.Faller, R.Fleischer. *Precision physics with $B_s^0 \to J/\psi\phi$ at the LHC: The quest for new physics. Physical Review D*, 79(1), 2009.

[82] D. London, N. Sinha, and R. Sinha. *Probing New Physics via an Angular Analysis of B –> V1 V2 decays. EUROPHYS.LETT.*, 67:579, 2004.

[83] The BaBar Collaboration. *Measurement of Branching Fractions and Charge Asymmetries for Exclusive B Decays to Charmonium. Phys. Rev. Lett.*, 94:141801, Apr 2005.

[84] Wei-Shu Hou, Makiko Nagashima, and Andrea Soddu. *$B \to J/\psi K^*$ in a supersymmetric right-handed flavor mixing scenario. Phys. Rev. D*, 71:016007, Jan 2005.

[85] D. London, N. Sinha, and R. Sinha. *New Physics in $B \to J/\psi K^*$.* hep-ph/0207007v1.

[86] Michael Gronau and Jonathan L. Rosner. *Triple-product asymmetries in K, $D_{(s)}$, and $B_{(s)}$ decays. Phys. Rev. D*, 84:096013, Nov 2011.

[87] Xiao-Gang He. *Direct CP violation in the angular distribution of $B \to J\psi K^*$ decays. Physical Review D*, 58(11), 1998.

[88] Xiao-Gang He and Wei-Shu Hou. *CP violating phase difference between $B \to J/\psi K_S$ and $J/\psi K_S\pi^0$ from new physics. Physics Letters B*, 445(3):344 – 350, 1999.

[89] Alakabha Datta and David London. *Triple-Product correlations in $B \to V_1V_2$ decays and new physics. International Journal of Modern Physics A: Particles and Fields; Gravitation; Cosmology; Nuclear Physics*, 19(15):2505 – 2544, 2004.

[90] Eugene Wigner. *Lower Limit for the Energy Derivative of the Scattering Phase Shift. Physical Review*, 98(1):145–147, 1955.

[91] The LHCb Collaboration. *Determination of the Sign of the Decay Width Difference in the B_s^0 System. Phys. Rev. Lett.*, 108:241801, Jun 2012.

[92] Yuehong Xie, Peter Clarke, Greig Cowan, and Franz Muheim. *Determination of $2\beta_s$ in $B_s^0 \to J/\psi K^+K$ decays in the presence of a K^+K S-wave contribution. Journal of High Energy Physics*, 2009(09):074, 2009.

[93] J. Charles, O. Deschamps, S. Descotes-Genon, R. Itoh, H. Lacker, A. Menzel, S. Monteil, V. Niess, J. Ocariz, J. Orloff, S. T'Jampens, V. Tisserand, and K. Trabelsi. *Predictions of selected flavor observables within the standard model. Phys. Rev. D*, 84:033005, Aug 2011.

[94] The CDF Collaboration. *Measurement of the CP-violating phase β_s in$B_s^0 \to J/\psi\phi$ decays with the CDF II detector. Phys. Rev. D*, 85:072002, Apr 2012.

[95] The D0 Collaboration. *Measurement of the CP-violating phase $\phi_s \to J/\psi\phi$ using the flavor-tagged decay $B_s^0 \to J/\psi\phi$ in* 8 fb^{-1} *of $p\overline{p}$ collisions. Phys. Rev. D*, 85:032006, Feb 2012.

[96] The LHCb Collaboration. *Measurement of the CP-Violating Phase ϕ_s in the Decay $B_s^0 \to J/\psi\phi$. Phys. Rev. Lett.*, 108:101803, Mar 2012.

[97] Michael Gronau and Jonathan L. Rosner. *Flavor symmetry for strong phases and determination of $\beta_s, \Delta\Gamma$ in $B_s \to J/\psi\phi$. Physics Letters B*, 669(5):321 – 326, 2008.

[98] M.Calvi, B.Khanji, G.Lanfranchi, O.Leroy, and S.Poss. *Lifetime unbiased selection of $B_s \to J/\psi\phi$ and related control channels $B^0 \to J/\psi K^*$ and $B^+ \to J/\psi K^+$.* Technical Report LHCb-2009-025, CERN, Geneva, May 2009.

[99] S.Kullback and R.Liebler. *On Information and sufficiency.* Annals of Mathematical Statistics (79- 86), 1951.

[100] M Needham. *Clone Track Identification using the Kullback-Leibler Distance.* Technical Report LHCb-2008-002. CERN-LHCb-2008-002. LPHE-2008-002, CERN, Geneva, Jan 2008.

[101] Wouter Hulsbergen. *https://twiki.cern.ch/twiki/bin/view/LHCb/DecayTreeFitter.*

[102] B. Adeva et al. *Roadmap for selected key measurements of LHCb.* 0912.4179, 2009.

[103] Muriel Pivk and Francois R. Le Diberder. *SPlot: A Statistical tool to unfold data distributions. Nucl.Instrum.Meth.*, A555:356–369, physics/0402083, 2005.

[104] V Gligorov. *Reconstruction of the Channel $B_d^0 \to D^+\pi^-$ and Background Classification at LHCb (revised).* Technical Report LHCb-2007-044. CERN-LHCb-2007-044, CERN, Geneva, Jun 2007. revised version submitted on 2008-01-24 12:46:44.

[105] W.T. Vetterling B.P.Flannery W.H.Press, S.A.Teukolsky. *Numerical Recipies-The Art of Scientific Computing (Thrid Edition).* Cambridge University Press, 2007.

[106] The CDF Collaboration. *Observation of $B_s^0 \to J/\psi K^*(892)^0$ and $B_s^0 \to J/\psi K_S^0$ decays. Phys. Rev. D*, 83:052012, Mar 2011.

[107] *Evidence for the decay $B_s^0 \to J/\psi\overline{K}^{*0}$.* Jun 2011. LHCb-ANA-2011-025 LHCb-ANA-2011-071.

[108] Tristan du Pree. *Search for a Strange Phase in Beautiful Oscillations.* PhD thesis, Amsterdam: Nikhef, 2010. Ph.D. Thesis Advisors : Prof. Dr. M.H.M. Merk and Dr. H.G. Raven.

[109] N.D. Gagunashvili. *Comparison of weighted and unweighted histograms.* Technical Report arXiv:0605123v1, May 2006.